UNIVERSITY OF GENOA

POLYTECHNIC SCHOOL

DIME

DIME - Department of Mechanical, Energy, Management and Transportation Engineering

PhD thesis in Marine Science and Technologies
Curriculum Energy Systems and Machineries for the Sea
XXXV cycle

Innovative ship power plants for the energy transition in the maritime field

Supervisor:

Prof. Francesca Satta

Candidate: Alessandro Dotto

November 2022

Declaration

I hereby declare that, the contents and organization of this dissertation constitute my own original work and does not compromise in any way the rights of third parties, including those relating to the security of personal data.

Alessandro Dotto
2022

* This dissertation is presented in partial fulfillment of the requirements for **Ph.D. degree** in the University of Genoa.

Abstract

In the recent years, global awareness on climate change has been promoting energy transition towards sustainable development strategies. In this scenario, in order to limit GHGs and pollutants generated by the shipping field, even more stringent regulations and policies have been introduced. Specifically, two main strategies are receiving major attention in the scientific community to face energy transition in the maritime sector. First, the overall ship power plant efficiency is required to be improved by either further research on existing technologies and operating condition optimization. Second, innovative and greener solutions for the maritime sector appear necessary pathways to complete energy transition and cope with long-term environmental regulations. Optimization of vessel operating conditions and installation of efficient waste heat recovery systems currently appear promising technologies able to lower primary energy utilisation onboard. Instead, among innovative solutions, major research efforts are payed on alternative fuels and hybrid-electric configurations.
In this context, the present work aims to investigate innovative power plant configurations enabling both primary energy savings and long-term reduction of GHG and pollutant emissions from the maritime sector. Where the pathway on existing technologies is concerned, the benefits provided by COmbined Gas Electric and Steam (COGES) plants installed onboard are investigated. Specifically, engine room operating conditions and waste heat recovery systems have been numerically optimized focusing on configurations coupling COGES plants with small-size reciprocating engines. Within the second pathway, attention is paid to GHG and pollutant emission reduction enabled by emerging alternative fuels and hybrid-electric power plants. In details, the applicability and pros/cons offered by Liquefied Natural Gas (LNG), methanol, ammonia and hydrogen are investigated under different temporal horizons. Furthermore, performances obtained by hybrid-electric power plants are analysed considering various optimized energy management strategies. Owing to their benefits in terms of energy savings and fuel flexibility enhancement, the second pathway is assessed focusing on engine room configurations based on both COGES plants and reciprocating engines. Either pathways have been investigated focusing on modern cruise-ferries and large-size cruise ships. Since challenging decisions are needed by the ownerships in a dynamically evolving regulation

context to remain cost competitive, all the investigations have been indiscriminately carried out under energetic, economic and environmental point of views. Thus, complete insight on the major solutions available in a short-, mid- and long-term energy transition scenario is provided. In order to numerically perform computation, various codes and optimization tools have been developed in Fortran and MATLAB/Simulink languages. Specifically, quasi-static, dynamical and Mixed-Integer Linear Programming (MILP) models have been implemented and gradient-descent, Multi-Objective Genetic Algorithms (MOGA), full-factorial and Linear Programming optimization tools have been set up. In details, optimization algorithms have been repeatedly used to assess component and power plant design, as well as to optimize engine room operating conditions by various objective functions. Overall, results demonstrated that COGES plants can play a significant role in the energy transition in the maritime sector. Specifically, combining COGES plants with small-size reciprocating engines resulted to be a viable solution by energetic, economic and environmental point of views, independently from the time horizon considered for energy transition. Further GHG and pollutant emission reduction can be achieved by alternative fuels and hybrid-electric power plants, mainly due to the mature fuel flexibility and high energy efficiency of COGES plants.

Contents

List of Figures

List of Tables

Nomenclature

Roman Symbols

$\dot{m}$	Mass flow, kg/s
$\dot{q}$	Heat flux, W
$\tilde{B}$	Baffle spacing, m
$\tilde{C}$	Maximum charge rate, W
$\tilde{c}$	Minimum charge rate, W
$\tilde{D}$	Maximum discharge rate, W
$\tilde{d}$	Minimum discharge rate, W
$\tilde{E}$	Energy, J
$\tilde{e}$	Specific energy, J/kg
$\tilde{p}$	Price, $€/Wh$
$\tilde{R}$	Capacity ratio
$\tilde{T}$	Set of time intervals
$\tilde{V}$	Volume, m^3
$\tilde{W}$	Weight, kg
$\tilde{X}$	Binary variable
$\tilde{x}$	Steam quality
$\tilde{Y}$	Binary variable
A	Cross-sectional area, m^2
AFC	Fuel cost, €
AMC	Maintenance cost, €
C	Capacity
c_p	specific heat at constant pressure, $J/(kgK)$
C_t	Tube clearance, m
c_v	specific heat at constant volume, $J/(kgK)$
CEM	Carbon emission cost, €
CF	Fuel cost, $€/kg$
CG	Grid electricity cost, $€/Wh$
CH_3OH	Methanol
CM	Maintenance cost, $€/Wh$
CO	Carbon monoxide
CO_2	Carbon dioxide
CRF	Capital Recovery Factor
CT	Carbon Tax, $€/kg_{CO_2}$
D	Power demand, W
d	Diameter, m

Em	CO_2 emissions, g
$Emno$	NO_x emissions, g
F	Fuel consumption, kg/s
H	Height, m
H_2	Hydrogen
Jh, JH	Heat transfer factor
L	Length, m
LHV	Lower Heating Value, J/kg
Li	Lithion
m	Mass, kg
N	Rotational speed, rpm
n	Number
NB	Number of batteries
NH_3	Ammonia
NO_x	Nitrogen oxide
NT	Number of tube
Nu	Nusselt number
O	Obstruction coefficient
P	Power, W
p	Pressure, Pa
P_b	Brake power, W
P_o	Propeller power, W
Pr	Prandtl number
Pt	Tube pitch, m
Pt_p	Parallel tube pitch, m
Re	Reynolds number
RI	Dirt factor on tube side
RO	Dirt factor on shell side
S	Surface area, m^2
SO_x	Sulfur oxide
T	Temperature, °C
U	Thermal transmittance, $W/m^2/K$
u	Internal energy, J/kg
V	Velocity, m/s
W	Width, m
$B3$	Set of boilers producing steam at 3 bar
$B9$	Set of boilers producing steam at 9 bar
G	Set of COGES plants
R	Set of reciprocating engines

Greek Symbols

β	Compression ratio
χ	Discount rate
Δt	Temporal discretization step, s
ΔT_{pp}	Pinch Point, °C
ΔT_{sub}	Subcooling, °C
Δx	Discretization step along x, m
ε	Expansion ratio
η_B	Boiler efficiency

η_{AC-DC} AC-DC converter efficiency

η_a alternator efficiency

η_{DC-AC} DC-AC converter efficiency

η_{el} Electrical efficiency

η_g Cogeneration efficiency

η_r propeller rotative efficiency

γ_{CO_2} CO_2 emission factor, gCO_2/g_{fuel}

λ Thermal conductivity, $W/(mK)$

μ Dynamic viscosity, Pas

ρ Density, kg/m^3

θ IGV opening angle

$\tilde{\alpha}$ Numerical coefficient

$\tilde{\beta}$ Numerical coefficient

$\tilde{\varepsilon}$ Heat exchanger efficiency

$\tilde{\mu}$ Numerical coefficient

$\tilde{\Pi}$ Maximum power, W

$\tilde{\pi}$ Minimum power, W

$\tilde{\tau}$ Numerical coefficient

ξ Convective heat transfer coefficient, $W/(m^2K)$

Acronyms / Abbreviations

$LMTD$ Logarithmic mean temperature difference

NTU Number of transfer units

PM Particulate matter

AE Auxiliary engine

CAPEX CAPital EXpenditure, €

COGES COmbined Gas Electric and Steam

DF Dual-Fuel engine

EEDI Energy Efficiency Design Index, $gCO_2/(t\ nm)$

EG Electrical Generator

EM Electrical Motor

EVA Evaporator

GB Genoa-Barcelona

GP Genoa-Palermo

GT Gas Turbine

HE Heat exchanger

HFO Heavy Fuel Oil

HP High pressure

HRSG Heat Recovery Steam Generator

HT High temperature

IGV Inlet Guide Vane

IP Intermediate pressure

LNG Liquefied Natural Gas

LP Low pressure

LT Low temperature

MDO Marine Diesel Oil

ME Main engine

MGO	Marine gas oil
MOGA	Multi-Objective Genetic Algorithm
NC	Naples-Catania
NG	Natural Gas
NP	Naples-Palermo
OPEX	OPerational EXpenditure, €
SFC	Specific Fuel Consumption, g/kWh
SH	Superheater
ST	Steam Turbine
TIT	Gas Turbine Inlet Temperature, K
TOT	Gas Turbine Outlet Temperature, K
WHR	Waste Heat Recovery

Subscripts

0	Nominal
$1c$	Cold flow inlet
$1h$	Hot flow inlet
$2c$	Cold flow outlet
$2h$	Hot flow outlet
β	Bundle
ϕ	Related to fins
τ	Time instant index
$\tilde{c}$	Charge
$\tilde{d}$	Discharge
all	Overall number
avg	Average
b	Boiler index
bat	Battery
BT	Boiling tubes
c	Cold
$calc$	Calculated
$cand$	Candidate
E	Related to large-size RE
e	Equivalent
e	Related to small-size RE
eff	Effective
el	Electrical
er	Engine room
ES	Energy storage
$film$	Film
$fuel$	Related to the main fuel
g	Gas turbine index
$grid$	Grid
h	Hot
I	Internal
id	Ideal state
in	Entering
max	Maximum value
min	Minimum value

O	External
out	Exiting
pm	Prime movers
pol	Polytropic
$prop$	Propeller
ps	Passages
pt	Discretization points
r	Reciprocating engine index
REQ	Requested
rw	Rows
S	Shell
se	Steam extraction
sea	Sea water
sf	Surface
T	Tube
$th3$	Related to thermal energy at 3 bar
$th9$	Related to thermal energy at 9 bar
$wall$	Wall
c	Compressor
cc	Combustion chamber
COND	Condenser
ECO	Economizer
el	Electrical
eq	Equivalent
ex	Exhaust gas
i	Inlet value
mecc	Mechanical
net	Net
o	Outlet value
P	Pump
PT	Power turbine
R	Reference value
s	Steam
sat	Saturation value
ship	Ship
t	Turbine
TGG	Gas generator turbine
th	Thermal
w	Water

Superscripts

$B3$	Related to boiler producing steam at 3 bar
$B9$	Related to boiler producing steam at 9 bar
el	Electrical
ES	Energy storage
$fuel$	Related to the main fuel
G	Related to gas turbines
R	Related to reciprocating engine
$th3$	Related to thermal energy at 3 bar
$th9$	Related to thermal energy at 9 bar

Chapter 1

Introduction

The relationship mankind has had with energy, punctuated by shifts from one resource to another, has and continues to play a pivotal role in the trajectory of societies. In the recent years, the development of a global energy consciousness and the need to reduce climate change in a sustainability perspective have promoted energy transition. Maritime transportation plays an important role for world trade, with about 90% of world's good transported by ships, typically powered by Heavy Fuel Oil (HFO). Consequently, the shipping industry is one of the major fossil fuel consumers with 330 million metric tons of fuels annually, hence its contribution to air pollution and climate change cannot be ignored. Specifically, from 2007 to 2012, the average annual emissions of sulphur oxides (SO_x), nitrogen oxides (NO_x) and carbon dioxide (CO_2) from the maritime field reached 11.3, 20.9 and 1016 million tonnes, respectively, which overall amounted to 13%, 15% and 2.8% of the annual anthropogenic emissions [38]. Since the largest part of ship emissions occurs within 400 km of land ($\approx$ 70%), shipping significantly contributes to air pollution in coastal communities [39], whereas GHGs trigger climate change leading to environmental degradation [40]. Furthermore, during the period from 2008 to 2018 a 4.6% average annual growth in the number of vessels (5% by tonnage) occurred [41] and the demand for marine fuel is estimated to double by 2030, with unquestionable intensification of air pollution and GHG emissions [42, 43]. Accordingly, in order to limit emissions from the shipping field, various international and national regulations entered into forced in the last decades. Particularly, progressive amendments to the International Convention for the Prevention of Pollution from Ships (MARPOL) have been issued by the International Maritime Organization (IMO) [44, 45] to phasing out progressive reduction of emissions of SO_x, NO_x and GHGs. Aiming at reducing SO_x emissions, MARPOL Annex VI imposed limits on the sulphur content of marine fuels and introduced Sulphur Emission Control Area (SECA) (e.g., the North Sea), where more stringent limits were

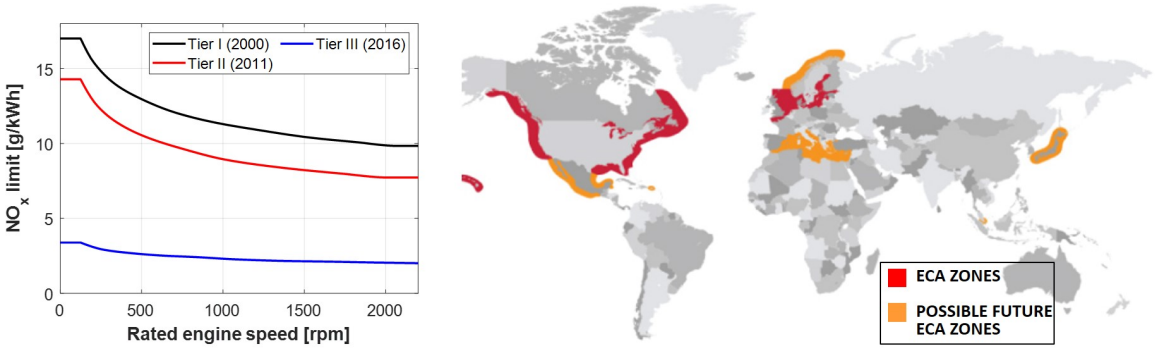

Fig. 1.1 IMO Tier limits for reciprocating engines (left) and evolution of ECA zones (right) [1].

imposed [46, 47] (see figure 1.1). Analogously, IMO regulations set NO_x caps depending on the ship construction date, Diesel engine speed and operation area. Where GHGs reduction is concerned, MARPOL Annex VI identifies improving energy efficiency through the adoption of various technical and operational measures as the main pathway. Either using low sulphur fuels (i.e. low sulphur heavy fuel oil, LSHFO, marine diesel oil, MDO or marine gas oil, MGO) or installing exhaust gas cleaning systems were employed to control SO_x emissions, whereas Selective Catalytic Reduction (SCR) and improvements in engine technology assessed NO_x reduction. Instead, energy efficiency enhancement through waste heat recovery systems able to partially cover the ship thermal and/or electric energy demand without further fuel energy consumption represented the prominent solution to reduce GHG emission [48, 49]. In order to fulfil the energy responsibility of the shipping sector, the carbon intensity of international shipping and its annual GHG emissions were ambitiously stated to be reduced by 2050 by 70% and 50% compared to 2008, respectively, on 13 April 2018 by the Initial IMO Strategy [50]. Towards this end, the Energy Efficiency Design Index (EEDI) for new ships and the Ship Energy Efficiency Management Plan (SEEMP) for all the existing ships have been additionally introduced as mandatory mechanisms to improve ship energy efficiency and mitigate CO_2 emissions [44, 51]. However, most of the power plants installed onboard ships do not operate optimally, with consequent increase in fuel consumption and emissions per kWh [52]. Thus, in order to guarantee a more strict control on existing ships and their operating conditions, extensive new CO_2 regulations were introduced by IMO in June 2021 focusing on the Energy Efficiency eXisting ship Index (EEXI) and the Carbon Intensity Indicator (CII) rating scheme [53] (see figure 1.2). Specifically, the EEXI consists in a one-time certification targeting technical efficiency on design parameters, while the CII addresses the actual GHG emissions during ship operation, i.e. how efficiently a ship transports goods or passengers in terms of $gCO2$ per cargo capacity. In details, the CII requirements will impact on all cargo, RoPax and cruise vessels above 5000 Gross Tonnage

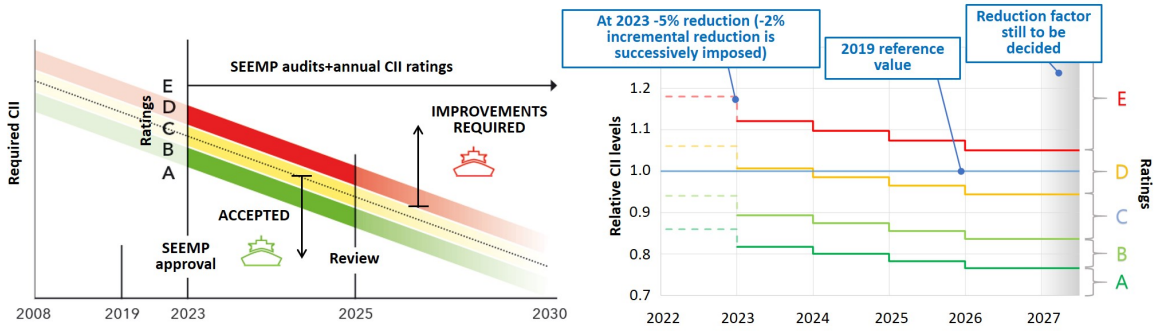

Fig. 1.2 Schematic view of the Carbon Intensity Indicator regulation (left) [2] together with its progressive rating updating (right) [3].

and will come into force in 2023, as shown in figure 1.2. The ship is given an annual rating ranging from A to E on its operational CO_2 emissions, with required index level C or above (see the left side of figure 1.2), and increasingly stringent thresholds for rating are imposed towards 2030, as shown by descending steps in the right side of figure 1.2. Since the existing technological and operational measures revealed inadequate to achieve the ambitious levels stated in the Initial IMO Strategy [54], new technologies (i.e. batteries, Flettner rotors, Air Lubrication Systems (ALS),...) and low or zero-carbon fuels were identified by IMO as necessary pathways in addition to those previously proposed. In addition to IMO regulations, Europe is recently introducing more strict roadmap to carbon neutrality of the maritime sectors with the FuelEU, ETS and ETD directives [55–57] as part of the Fit for 55 package and the European Green Deal [58]. Specifically, carbon pricing will soon entry into force to accelerate energy transition in shipping. In this scenario, technologies aimed at both increasing energy savings and abating carbon impact are recently obtaining major attention in the maritime sector, with changes in terms of prime movers, power plant configurations and fuels. Nowadays, most of marine vessels utilise reciprocating engines to cover power demand onboard. However, combining a gas turbine (GT) with a bottoming steam power cycle is an option commonly used in terrestrial power plants in COmbined Gas Electric and Steam (COGES) engine room architecture can play a role in a more efficient energy utilisation strategy [59]. Indeed, the large amount of thermal power available in exhaust gas from GT can be profitably used to partially cover both electrical and thermal power demand onboard ships, with no further primary energy consumption. Overall, COGES plants guarantee higher energy efficiency compared to reciprocating engines for sizes exceeding 10 MW [60] and they can offer benefits in terms of reduced maintenance costs and higher power/volume and power/weight ratios. In addition, fuel flexibility is guaranteed by them since decades. Where alternative fuels are concerned, both abatement and elimination strategies are currently emerging as viable options to oil-based fuels on different temporal horizons. Liquefied

Natural Gas (LNG) has great potential to drastically cut GHG emissions from shipping sector, owing to its low carbon-to-hydrogen ratio [61]. Thus, LNG is presently evaluated as a clean and reliable fuel for ship propulsion in comparison to heavy or distillate fuels [44, 62] and currently appears the most prolific with around 300 ships in operation around the globe and in most ship segments. However, it represents viable solution in a short-term perspective, except for synthesizing it from renewable sources. Recently, methanol, ammonia and hydrogen are accepted as promising marine alternative fuels. Indeed, they are potentially able to eliminate or drastically abating GHG and pollutant emissions, despite technology is still mostly under development to improve combustion properties as well as storage and handling methods [63–65]. Specifically, physical-chemical characteristics, availability, costs, safety and ability to meet future emission requirements deeply influence the contribution of each alternative fuel to energy transition in a short- , mid- or long-term perspectives. Nevertheless, renewables spreading in the energy market is expected to enable methanol, ammonia and hydrogen synthesis in a zero-emission power-to-fuel strategy. Furthermore, electrification of the propulsion with the possible use of hybrid power systems [66] is now emerging as a potential solution to reduce airborne emissions and achieve the 2050 goals [23]. Indeed, installing battery systems onboard ships in place of reciprocating engines can produce no GHGs during the voyage and provide lower maintenance costs [59], despite their low capacity/volume ratios limit operation on the short-sea segment for offshore and passenger ships/ferries [67, 68], otherwise coupling with traditional power sources is required. Aiming at charging batteries while being at berth, cold-ironing is also emerging in Europe [69, 70]. This work aims to investigate innovative power plant configurations enabling energy transition in the maritime sector in line with the Initial IMO Strategy. Specifically, power plants enabling both energy efficiency increase and GHG and pollutant emission abatement are analysed. Where the first pathway is concerned, the benefits in terms of efficient energy utilisation offered by combining COGES plants with small size reciprocating engine are demonstrated under flexible ship operating conditions. Instead, within the second strategy, attention is paid to GHG and pollutant emission reduction enabled by emerging alternative fuels and hybrid-electric power plants. In details, the potential and challenges related to LNG, methanol, ammonia and hydrogen are comparatively assessed in terms of applicability and regulation compliance under different temporal horizons. In this scenario, the shipping industry is facing challenging decisions concerning what investments are needed now for new ships to enable compliance with both short- and long-term emission regulations, while remaining economically competitive. Thus, investigations embedded in this work are thoroughly carried out under energetic, economic and environmental point of views, such to provide a complete insight of the major solutions in a sustainability perspective. Various static and dynamic

models as well as optimization tools have been numerically developed to carry out analyses reported in this thesis. Detailed road-map of the case studies considered in this thesis and extensively analysed in the following sections is shown in figure 1.3. Finally, all the pathways studied are expected to mature during the next five to ten years [59], despite important role appears played by environmental regulations and incentive schemes implemented in future.

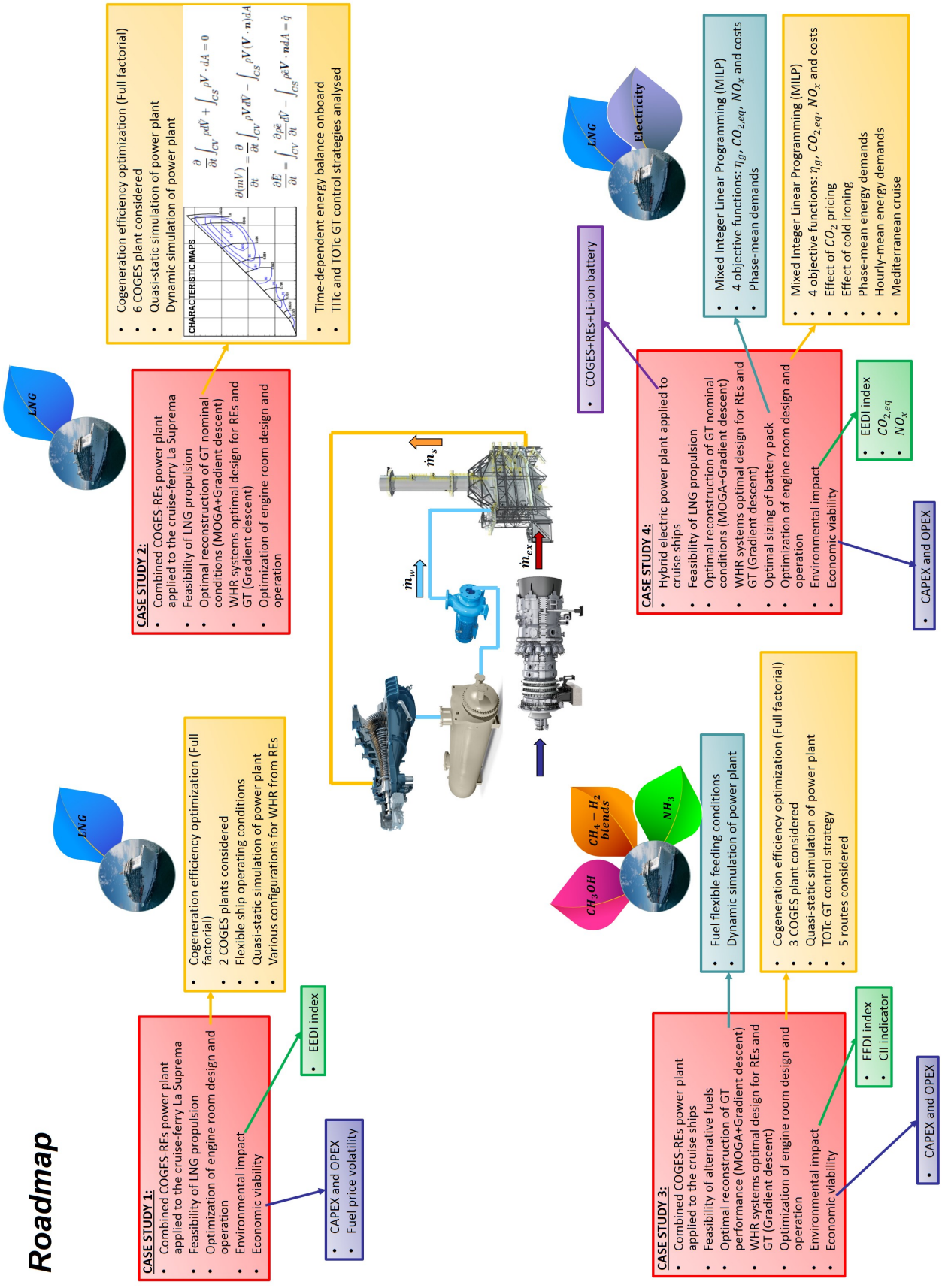

Fig. 1.3 Road-map of the case studies considered in the present thesis.

Chapter 2

Prime movers applied within the marine field

2.1 Gas turbines

2.1.1 Merchant field

Due to their quite high specific fuel consumption in comparison to Diesel engines and to its unexperienced reliability, GTs were characterized by a slow introduction within the merchant navy sector. The real behaviour of gas turbines on board existing ships was first investigated replacing Diesel engines, while successively newly designed vessels powered by them were built. In the 50s and 60s, the UK and US were the main nations to first equip merchant ships with aeroderivative and heavy-duty GTs, respectively. In 1952, UK replaced one of the four Diesel engines installed onboard the oil tanker Auris with a 860 kW aeroderivative GT dealing with a regeneration power plant configuration. The maximum temperature of the cycle was limited to only 650 °C by materials and fuel composition dealing with sodium, vanadium and sulphur contents, with an overall 20% efficiency. Nevertheless, this test showed how GTs could reliably work in marine environment: indeed, in case of repeated failure to 1 or 2 Diesel engines onborad Auris, the 860 kW GT guaranteed the safety return to port of the ship. Due to these benefits, after 20000 hours of GT operation with no issue generated, a 4.1 MW GT from the British Thompson-Houston company was installed onboard Auris to replace all the Diesel engines in 1959. On the other hand, the US replaced the steam power plant installed onboard the ship SS John Sergeant with a heavy-duty gas turbine from General Electric (GE) dealing with 4.85 MW nominal power and 317 g/kWh specific fuel

(a)

(b)

Fig. 2.1 The container vessel Eurofreighter (a) [4] and the LNG carrier Lucian (b) [5].

consumption. The high temperature corrosion was avoided by purifying the Bunker C fuel from the sodium content as well as adding inhibitors of vanadium. From this first test on, GE became the main company selling heavy-duty GTs for the marine sector. On the other hand, in 1968 the US installed two 14.7 MW Pratt-Whitney FT4A-2 aeroderivative gas turbines onboard the roll-on/roll-off ship Callaghan, which transported freights and trucks for the US Army between New York and Bremerhaven. Due to a maximum ship speed equal to 26 knots, the Callaghan resulted the fastest ship of the period and continued to work up to 1991. Successively, installation of gas turbines was considered for newly built merchant ships where specific characteristics offered by GTs could provide significant benefits for the ownerships. In particular, drawbacks provided by GTs in terms of *SFC* in comparison to Diesel engines lost relevance for ships requiring high capital costs or, alternatively, where reduced maintenance costs and high power/volume ratio were needed. The main types of merchant ships where GT installation was considered before the 1970 is reported below.

- Container vessels: since they transport finished products ready to be sold, they need to operate with high ship speed ($\approx$ 27 knots) and high power/volume ratios. Interestingly, both these two specific requirements well fit with gas turbines. In the 70s, four container ships (i.e. Euroliner, Eurofreighter, Asialiner and Asiafreighter) each powered by two Pratt-Whitney FTA4-12 gas turbines started working (see figure 2.1). Each GT delivered 22.38 MW with *SFC* 332 g/kWh and mechanically drove a controllable pitch propeller by means of two stage gearbox. Overall, GTs provided a 12% higher volume available onboard for freights in comparison with steam power plants dealing with comparable sizes and a ship speed V_{ship} equal to 26 knots was ensured.

- Tankers: in 1975, six different tankers dealing with 35000 tonn Gross Tonnage start working, the first one being the Chevron Oregon. Each tanker was equipped with a

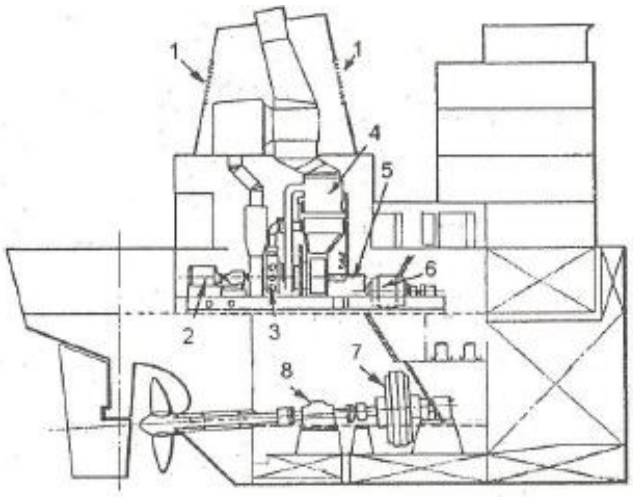

Fig. 2.2 Propulsion plant installed onboard the tanker Chevron Oregon. Air intakes (1), start-up motor (2), gas turbine (3), regenerator (4), reduction gearbox (5), alternator (6), electric motor (7), thrust bearing (8) [6].

regenerative GE MS3002 9.325 MW gas turbine enabling a 15 knots navigation ship speed. A 2.2 MW Ruston TB 3000 gas turbine was additionally installed onboard to guarantee the safety return to port in case of failure involved with the main GT. An electric propulsion configuration was adopted instead of the mechanical one, hence it was possible to install GTs on a higher deck in the hull with respect to electric motors driving propellers, with reduced volumes required by air intake and discharge ducts.

- Liquefied Natural Gas (LNG) carriers: Since GTs could operate on natural gas without combustion issues which instead arose for reciprocating engines, they were installed on many LNG carriers. As an example, the 29000 m^3 LNG carrier Lucian built in 1975 was equipped with a 15 MW MM5212R regenerative gas turbine from GE (see figure 2.1). Propulsion plant was able to guarantee 20 knots navigation speed and both boil off gas (BOG) and heavy fuel oil could be burned in the combustion chamber.

- Roll-on/Roll-off ships: in 1975, two roll-on/roll-off ships (i.e. Seaway Prince and Seaway Princess) dealing with an integrated electric power plant configuration based on GTs started sailing. A 9 MW MM3012R regenerative gas turbine from GE was installed within the engine room and enabled a 18 knots ship speed.

- Bulk carriers: in 1977, the bulk carrier Iron Carpentaria was equipped with 8 MW MS3002R regenerative GT from GE and a ship speed of 15 knots was guaranteed. An epicicloidal gearbox was used to reduce the gas turbine rotational speed (6556 rpm) to the propeller one (112 rpm).

- Ferries: in 1977, the Finnjet, i.e. the first ferry powered by GTs started working. It was able to transport 1532 passengers and 350 cars and it operated in the Baltic Sea between Helsinki (Finland) and Travemunde (Germany). The journey lasted 22 hours, thanks to a navigation ship speed of 30.5 knots. Propulsion power was supplied by two FT4C-1DLF Pratt Whitney gas turbines, each delivering 28 MW. A controllable pitch propeller rotating at 171 rpm was mechanically connected with the GTs by means of a tree-stage gearbox with a 22.2:1 reduction ratio. Quick start ability (under few minutes), deep reliability and reduced maintenance stop periods (2 hours of maintenance every 22 hours of operation) were required to complete more than 150 trips per year. Successively, the Finnjet was equipped with an additional 14.5 MW medium-speed Diesel engine to reduce fuel consumption in season where lower demand was present.

Although it was perfectly expected that the GT would not undermine the consolidated performance of Diesel engines and steam power plants, its application in the 70s was penalized by its high specific fuel consumption and need for cleaner fuels than residual oils. On the contrary, at the end of the 60s, the quality of the residual fuel which could be burned by Diesel engines considerably worsened to limit operational costs. Successively, in 1974 the energy crisis and the consequent increase in the fuel price dealt a severe blow to the GT installations onboard ships. Initially, GT-powered ships operated at reduced speeds to lower fuel consumption. E.g. the four container ships built by Seatrain Lines Inc (i.e. Euroliner, Eurofreighter, Asialiner and Asiafreighter) reduced navigation speed from 26 to 20 knots. However, since GT performance deteriorate at part-loads, reduced savings were obtained. Thus, ship power plants based on GTs were successively converted by replacing gas turbines with Diesel engines. The Euroliner, Eurofreighter, Asialiner and Asiafreighter were equipped with two medium-speed four-stroke Diesel engine SWD TM620, each delivering 12 MW. Analogous conversion took place for the iron Carpentaria bulk carrier, where in 1983 the heavy-duty GT was replaced by two medium-speed Diesel engine Wärtsilä Wasa 12V32, each delivering 8 MW at 720 rpm. Instead, the LNG carrier Lucian was equipped with a low-speed two-stroke 7RND76M Sulzer engine in 1980. Therefore, from 1980 onwards, few merchant vessels where GTs initially offered economic benefits, remained powered by them. However, in the meantime, GTs were technically improved in both power generation and aviation fields. Specifically, the maximum cycle temperature and turbomachinery efficiency were significantly increased, with consequent benefits in terms of *SFC* and power/volume ratio. For this reason, application of GTs into the naval field was re-launched when new needs arose in the 90s. Specifically, one of the main drivers was the need for inter-city or coastal ship routes, with high speed sailing conditions (around 40 knots) as well as installed

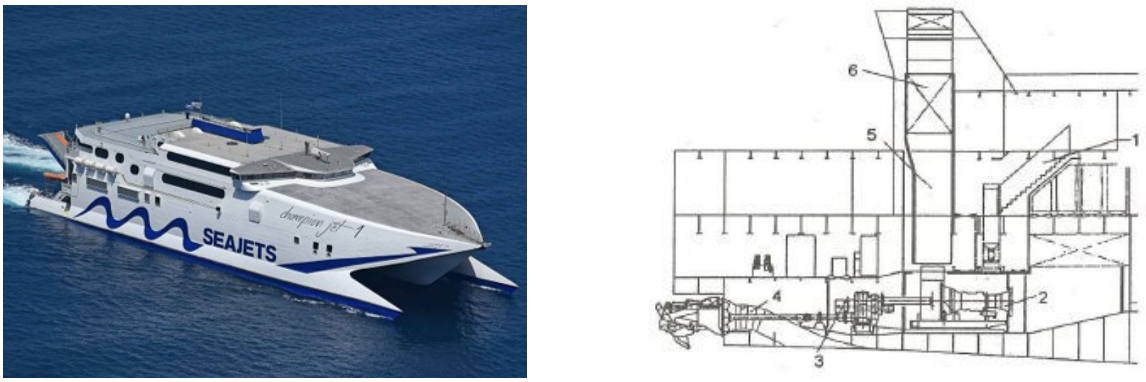

(a) (b)

Fig. 2.3 The fast ferry Seajet 250 (a) [7] together with schematic view of propulsion plant it dealt with (b) [6]. Air intake (1), gas turbine (2), reduction gearbox (3), waterjet (4), exhaust duct (5), silencer (6).

power larger than 60 MW required. In order to reduce ship drag and increase the payload, most of the attention was paid on thin hulls, resembling those of catamarans, as well as on prime movers dealing with high power/volume ratio. In this scenario, GTs were installed onboard fast ferries operating in the North Sea, English Channel and Mediterranean Sea. E.g., the fast ferry Seajet 250 was equipped with two LM1600 GTs, each delivering 14.92 MW with an efficiency of 36%, to reach 44 knots ship speed. The duration of the journey passed from 1 hour and 45 min provided by Diesel engines to 45 min. Similarly, in 1996-1997 Stena Line started operating three new fast ferries HSS1500 powered by GTs, targeting the maritime transport between England, Holland and Ireland. HSS1500 ferries were 125 m long and 40 m wide, and they were able to transport 1500 passengers together with 375 cars at a 40 knots ship speed. These ferries were equipped with two 20.2 MW LM2500 and two 13.1 MW LM1600 gas turbines.

Finally, in recent decades, complex power plant architectures grounded on GTs have been installed onboard few cruise ships (e.g., Millennium and Infinity from Celebrity or Radiance of the Seas from the Royal Caribbean). However, despite the compactness of GT guarantees more volume and weight available for passengers or freights, few applications have been developed in the civil maritime sector. Since environmental aspects and more sustainable fuels are increasingly important in recent years, the benefit of burning low-grade fuels, which leaded reciprocating engines to dominate the maritime sector through reduced operational costs, inevitably loses its relevance in favour of the mature fuel flexibility provided by GTs.

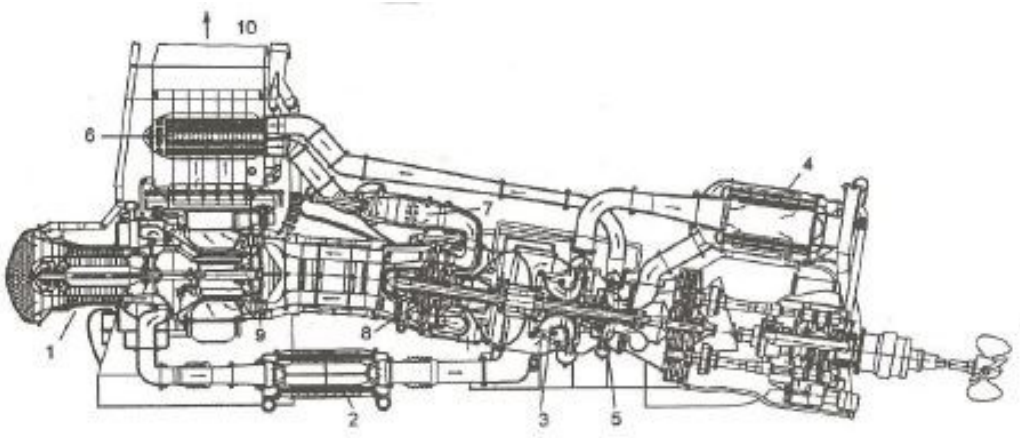

Fig. 2.4 Rolls-Royce RM60 intercooled and regenerated gas turbine. LP axial compressor (1), first intercooler (2), IP centrifugal compressor (3), second intercooler (4), HP centrifugal compressor (5), regenerator (6), combustion chamber (7), HP turbine driving IP and HP compressors together with propeller (8), LP turbine driving the axial compressor (9), outlet duct (10).

2.1.2 Military field

In the military forces, the spreading of aeroderivative GTs started in the 50s and has successively experienced a monotonic growth, owing to their high power/volume and power/weight ratios, their quick start ability and their easy replacement in case of failure. In 1953, the Royal Navy first replaced the steam power plant installed onboard the gun boat HMS Grey Goose by 9 MW RM60 from Rolls-Royce. As can be seen from the schematic view reported in figure 2.4, regenerator 6 and intercoolers 2-4 were coupled with RM60 to improve electrical efficiency. In 1958, the Brave class of coastal guard ships of the Royal Navy was equipped with the 3.35 MW Rolls Royce Proteus gas turbine and analogous propulsion plant was successively adopted by the Danish and Swedish Navies, for a total number of 40 sailing units. Since these first two tests in the Royal Navy revealed the high reliability and compactness of GTs, the UK government ruled in 1968 that engine rooms based on GTs would be installed onboard all the military ships of the Navy, independently from the ship type. E.g., in the 1975, the Sheffield destroyer, equipped with two 21 MW Olympus and two 3.2 MW Tyne gas turbines entered the Royal Navy and, successively, other 5 twin ships were built. The power plant installed onboard allowed to reach 28 knots speed within 58 seconds from the turning-on.

Where the US Navy is concerned, in the 70s GE opened a venture with FIAT Avio with the aim of adapting the aeroengine TF39/CF-6 to marine applications. As a main result, the aeroderivative gas turbine LM2500, able to deliver 20.51 MW at SFC =230 g/kWh, was produced. This GT model has gained great interest in the military field, hence many

improved versions have been developed up to now. E.g., the destroyer Spruance, with a 64 MW installed power supplied through four LM2500 GTs, entered into service in the US Navy. The maximum ship speed available consisted in 30 knots and 30 ships of this class were globally built. In the 1978 analogous venture developed the LM500 GT from the TF34 aeroengine. In table 2.1 the main aeroderivative gas turbines produced by GE and Rolls-Royce and used in military field are reported. It must be remarked that power

Gas Turbine Model	*Power* **[MW]**	$Efficiency$	$\dot{m}_a + \dot{m}_f$**[kg/s]**	T_4**[°C]**
R-R Tyne	4	0.292	-	-
R-R Spey	19.5	0.374	67	458
R-R Olympus	22	0.291	-	-
R-R RB211	27	0.361	-	-
R-R WR21	25.2	0.42	73	355
R-R MT30	36	0.41	-	440
GE LM 500	4.47	0.312	16	565
GE LM 1600	14.92	0.367	47	510
GE LM 2500	25.06	0.371	70	566
GE LM 2500+	27.6	0.385	81	516
GE LM 2500+G4	35.3	0.413	93	549

Table 2.1 Aeroderivative gas turbines produced by GE and Rolls-Royce and traditionally installed onboard military ships [6].

plants combining GTs and Diesel engines are currently installed onboard modern warships, with the aim of lowering fuel consumption at reduced navigation speeds [71, 72]. Indeed, cruise conditions of military ships usually relate to 15-18 knots, which correspond to 60% of the power load required to reach maximum speed (see figure 2.5). Furthermore, maximum ship speed operating conditions last for only 10-15% of the useful life of the vessel. Thus, combining different prime movers can result useful to keep the efficiency high in both cruise and maximum ship speed conditions.

2.1.3 Operating principles of gas turbines

Aeroderivative gas turbines are aircraft engines, where nozzle is replaced by power turbine. Since they are lighter and low volume requiring than heavy-duty GTs, they are commonly used for marine applications, as explained in details in section 2.1. For this reason, in the present thesis aeroderivative configuration is considered, whose thermodynamic cycle in the (T,s) diagram is reported in figure 2.6. In the rest of the thesis, the nomenclature reported in figure 2.6 is adopted. The air intake is enabled by the compressor, which increases pressure and temperature levels of the flow from station 2 to 3. Then, the air flow passes through the combustion chamber, where the fuel is injected and combustion takes place in order to improve the energetic content of the flow before expansion in the turbine modules.

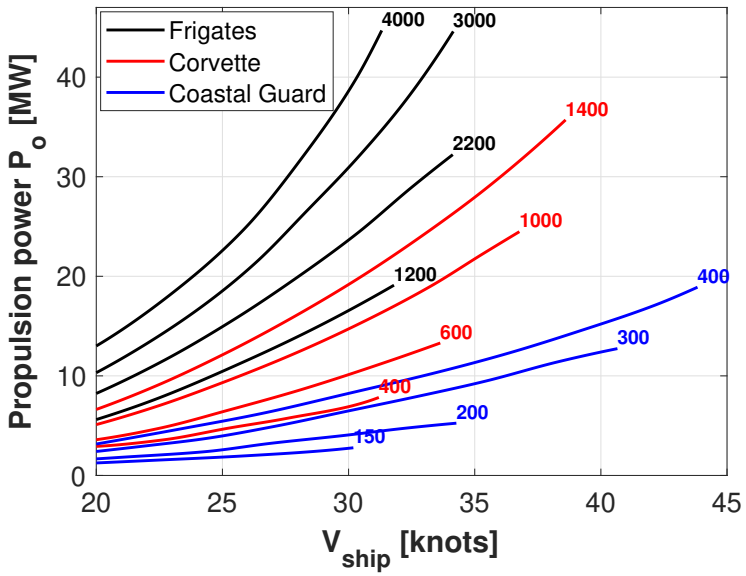

Fig. 2.5 Power requested for propulsion in military ships dealing with different tonnage (indicated in tonn next to the curves) [6].

Specifically, the flow exiting combustion chamber first expands in the gas generator (GG) turbine module, which mechanically drives the compressor. Successively, residual energy content of the flow is utilised in the power turbine (PT) module to generate electrical power. In simple-cycle architectures (see figure 2.6), the exhaust gas exiting PT is then released into the ambient. Despite significant progress has enhanced the thermal efficiency of simple-cycle GTs from 25% in 1960 to the current 40% [73], more complex cycles were developed in the maritime sector aiming at approaching the low SFC enabled by large size Diesel engines. Specifically, three main architectures were developed to improve efficiency and power output of gas turbines in both nominal and part-load operating conditions:

- Intercooled cycle : Compression is split into two parts, each one characterized by reduced pressure ratio β. An intercooler is added between high-pressure and low-pressure compressors with the aim of reducing the overall power requested for compression. Specifically, increase in net power output is achieved and possibly also thermal efficiency benefits occur in case thermodynamic parameters are optimized.
- Recuperated cycle : a recuperator recovers waste thermal power from the exhaust gases of GT and transfers it to the compressed flow before it enters the combustion chamber. In this way, less primary energy is used within the combustion process to reach a certain target value of temperature T_4. Overall, benefits in terms of both thermal efficiency and net power may be obtained.

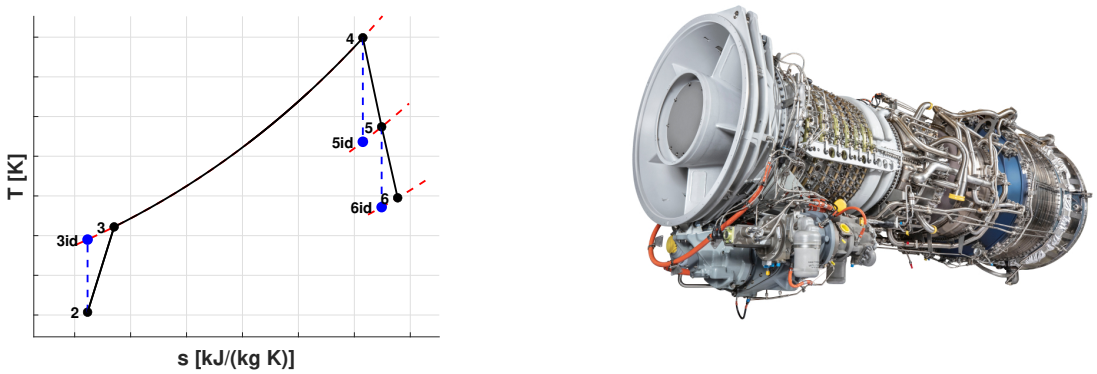

Fig. 2.6 Thermodynamic cycle for aeroderivative gas turbine (left side) and the LM2500 GT (right side) [8].

- Combined cycle : since high thermal power is available from the exhaust flow exiting GTs, recovering it in a bottoming steam cycle guarantees a more efficient exploitation of primary energy. Indeed, thermal energy at high temperature is not wasted, since it is used to generate more electrical power by steam turbine.

Parametric studies were carried out by GT manufacturers to establish the optimum performance each cycle configuration may provide, mainly varying temperature T_4 and pressure ratios. Furthermore, performances obtained combining intercooled and recuperated cycles were also assessed. This strategy was applied in the Rolls-Royce WR-21 ICR gas turbine and enabled a 42% thermal efficiency across 70% of the GT operating range. However, complexity and some correlated issues arising in the marine environment thwarted its commercial success, despite it was proved to be reliable and highly efficient over brief service. Further drawbacks from the ICR configuration consisted in high costs and volumes. Overall, the highest thermal efficiency and net power were obtained by the combined cycle layout. However, within the maritime sector, the major drawback of combined cycles consists in additional volumes and weights required by the Heat Recovery Steam Generator (HRSG). Nevertheless, in recent decades marine applications of gas-steam combined power plant architectures are currently receiving attention due to their operational flexibility, low environmental impact and reduced fuel consumption rate, with consequent benefits within a energy transition scenario [74–77].

2.2 Steam turbines

In the maritime sector, steam turbines played a significant role in the 50s-60s when they replaced reciprocating steam engines onboard ships dealing with $\geq$20-30MW power demand (see figures 2.8 and 2.7). Successively, the number of new vessels powered by steam turbines increased constantly up to 1975, due to novel trends growing in the maritime sector in that period. Specifically, some new types of ships, such as bulk carriers, supertankers and LNG carriers started to widespread and their operational characteristics appeared well suited to install onboard steam power plants. Furthermore, in order to limit cost penalties generated by the closure of the Suez Canal, ship owners were induced to build even larger oil tankers and bulk carriers, with installed power up to 60 MW. Similarly, the capacity and installed power of container ships increased: in the 60s their maximum capacity was 1500 TEU with a corresponding maximum ship speed of 22 knots; successively, vessels dealing with 2300 TEU and 25-30 knots speed were designed, with an overall installed power reaching 80 MW.

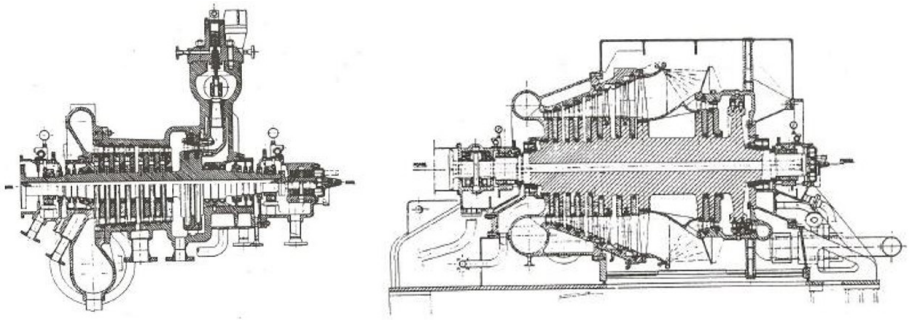

Fig. 2.7 HP (left) and LP (right) modules of a 28.5 MW steam turbine from TOSI for naval application [6].

Since steam turbines were able to reliably deliver such high power levels, they experienced an increasingly widespread onboard these types of ships. However, thin hulls were necessary to reduce ship drag at high ship speeds, hence the volume and positioning of the steam power plants onboard needed to be carefully chosen in order to increase the number of freights transported. Between 1965 and 1975, steam turbines were also applied to LNG carriers and nowadays they continue to represent the most common solution for these vessels [78], since the boiler of a steam power plant can be fed by BOG produced while sailing with no combustion issues. Table 2.2 summarises the main features of the steam power plants installed onboard ships during the 60s-70s together with the manufacturers' details. As visible in table 2.2, the pressure and temperature levels at the steam turbine inlet (i.e. $p_{i,HPT}$ and $T_{i,HPT}$) resulted quite increased in comparison to the corresponding values adopted in the first steam turbine installed onboard ships during the 50s (i.e. $p_{i,HPT}$ =40

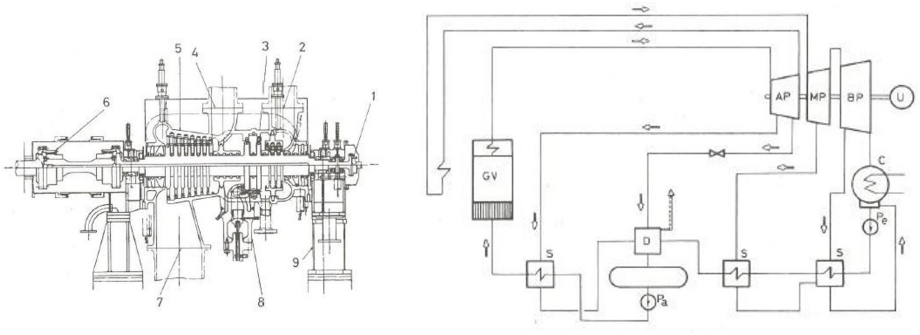

Fig. 2.8 HP and IP modules of steam turbine installed in a multiple superheating UR steam power plant from Kawasaki (left) and a schematic view of the entire plant (right) [6]. Left side: clutch (1), exit of HP steam turbine towards reheater (2), HP steam turbine (3), inlet of reheated steam into the IP steam turbine (4), IP steam turbine (5), flexible joint (6), exit of IP steam turbine towards LP module (7), inlet valve for HP steam turbine (8), flexible support (9). Right side: steam generator (GV), HP steam turbine (AP), IP steam turbine (MP), LP steam turbine (BP), users (U), condenser (C), pumps (P_e and P_a), regenerator (S), deaerator (D).

Properties	**IHI R-802**	**Kawasaji**	**Mitsubishi**	**GE**	**Pametrada**	**Stal-Laval**
P_{el} [MW]	24.619	22.38	22.38	22.38	22.691	21.177
N_{prop} [rpm]	101	80-100	0	80	110	-
$p_{i,HPT}$ [bar]	84.4	100	88-102	102	70	100
$p_{o,RSH}$ [bar]	6	20	-	18.5	14.8	22
$T_{o,RSH}$ [°C]	520	520	510-538	510	538	507
η_{boiler} [-]	0.89	0.9	0.9	0.9	0.9	0.9
N_{se}	4	5	5	5	5	5
SFC[g/kWh]	261	239	241	237	239	244

Table 2.2 Thermodynamic features of the steam power plants installed onboard ships during the 60s-70s [6].

bar and $T_{i,HPT}$ =450 °C). However, weaker increase was promoted by manufacturers on the maximum temperature, since Cr-Mb steals continued to be used for the superheater pipes and the first stages of turbine, otherwise the more expensive austenitic steal would have been necessary. It must be underlined that increasing maximum pressure level at nearly fixed maximum temperature implies reduced specific volume in the first rows of the steam turbines (i.e. lower height of blades) and more water droplets generated in the final part of flow expansion. To mitigate these drawbacks as well as improve thermal efficiency of the cycle, the multiple superheating was commonly adopted, as visible in table 2.2. The number of steam extractions N_{se} was kept equal to 4 and 5 for power plant configurations dealing with single or multiple superheating, respectively, with the aim of optimizing electrical efficiency. Technical improvements summarised in table 2.2 with respect to the steam power plants commercially available in the 50s provided SFC≈238 g/kWh and electrical efficiencies around 35%. Overall, the main driver for these modifications derived from the contemporary

diffusion of large-size Diesel engines in the maritime sector, which undermined STs in their typical applications.
In the following, the main types of vessels powered by steam turbines in 70s are reported, adopting a treatment by examples.

- Bulk carriers: in 1970 began service Universe Kure, the largest bulk carrier in the world, aimed at transporting salts from Mexico to Japan and dealing with a 155000 tonn capacity. It was equipped with a 20 MW IHI-GE-JM steam turbine guaranteeing 15.5 knots ship speed. Steam was generated by two IHI-Foster-Wheeler boilers at 42 bar and 463 °C.

- Oil tankers: in 1972 the oil tanker Nissek-Haru, dealing with 372698 tonn Gross Tonnage, started sailing. Propulsion power was supplied by a 30 MW IHI steam turbine, mechanically coupled with a 90 rpm propeller and enabling a 15 knots ship speed.

- LNG carriers: in 1972 the LNG carrier LNG Gadinia started sailing for the Shell Tankers company. It was able to transport 75000 m^3 of LNG and was equipped with a 5.5 MW steam power plant manufactured by Atlantique Stal-Laval, which guaranteed a 19 knots ship speed.

- Container ships: table 2.3 summarises the container ships exceeding 2000 tonn capacity built between 1971 and 1973. Overall, the reported container vessels operated at 25-30 knots and were characterized by installed power around 44-88 MW. Among all the 38 ships, 24 were powered by steam turbines, 10 by two-stroke Diesel engines and 4 by gas turbines. As an example, the Tokyo-Bay, dealing with a 2000 TEU capacity, was equipped with two Stal-Laval steam turbines fed by steam at 65 bar and 513 °C.

In 1974, the strong increase in fuel cost due to the energy crisis imposed a significant reduction in fuel consumption onboard ships. Thus, as a first strategy, the ship speed was reduced. However, deeper effects of the energy crisis on the power plants installed onboard occurred only beyond 1977. Indeed, from the 1977 on, there was a significant reduction of new ships powered by steam turbines, since two-stroke turbocharged Diesel engines were able to burn the same low-quality fuels used in steam power plants but with higher thermal efficiency. This triggered the installation of Diesel engines onboard ship types, where steam turbines previously had the monopoly during the 70s. Table 2.4 shows a comparison between two-stroke Diesel engines and steam turbines in terms of costs: benefits concerning maintenance, lubrication and reliability guaranteed by steam turbines were not

Ship	Year	DWT	Knots	Engine	Engine Type	MW
Asialiner	1971	28400	26	Pratt-Whitney	GT	2x22.38
Asiafreighter	1972	28400	26	Pratt-Whitney	GT	2x22.39
Benalder	1972	35000	26.5	AEI	ST	2x32.38
Benavon	1973	35000	26.5	AEI	ST	2x32.38
Bremen Express	1972	43800	26	Stal-Laval	ST	2x29.44
Cardigan Bay	1973	35000	26	Stal-Laval	St	2x29.44
City of Edinburgh	1973	35000	26.5	AEI	St	2x32.38
Elbe Maru	1972	34550	25	B&W	D	1x25.215
Eurofreighter	1971	27984	26	Pratt-Whitney	GT	2x22.38
Euroliner	1971	27984	26	Pratt-Whitney	GT	2x22.38
Hamburg Express	1972	42100	26	Stal-Laval	ST	2x29.44
Hong Kong Express	1973	43800	26	Stal-Laval	ST	2x29.44
Jutlandia	1972	32200	26	B&W	D	1x22.38
Kamakura Maru	1971	29200	26	Mitsubishi	ST	2x29.44
Kiso Maru	1973	32300	25.3	Sulzer	D	2x25.96
Kitano Maru	1972	29150	26	Mitsubishi	ST	2x29.44
Korrigan	1973	35000	26.5	AEI	ST	2x32.38
Kurobe Maru	1973	32300	25.3	Sulzer	D	2x25.96
Kurama Maru	1972	29200	26	Mitsubishi	ST	2x29.44
Kowloon Bay	1972	35000	26	Stal-laval	ST	2x29.44
Liverpool Bay	1972	35000	26	Stal-laval	ST	2x29.44
Nedlloyd Dejima	1973	34000	26	Stal-laval	ST	2x29.44
New Jersey Maru	1973	32850	26	B&W	D	2x25.96
Nihon	1972	26500	26	Gotaverken	D	1x21.04
Remuera	1973	26500	23	AEI	ST	2x17.66
Oasaka Bay	1973	35000	26	Stal-laval	ST	2x29.44
Rhine Maru	1971	29300	26.1	Mitsubishi	ST	2x29.44
Sealandia	1972	32200	26	B&W	D	1x22.38
Sea-Land Commerce	1973	25700	30	GE	ST	2x44.16
Sea-land Echange	1973	26500	30	GE	ST	2x44.16
Sea-Land Galloway	1972	25700	30	GE	ST	2x44.16
Sea-Land Maclean	1972	26500	30	GE	ST	2x44.16
Sea-Land Trade	1973	26500	30	GE	ST	2x44.16
Tokyo Bay	1971	35000	26	Stal-laval	ST	2x29.44
Tokyo Express	1973	43800	26	Stal-laval	ST	2x29.44
Toyama	1973	27200	26	B&W	D	1x22.38
Verrazzano Bridge	1973	34900	25.9	MAN	D	2x29.84
New York Maru	1973	32850	25.3	Sulzer	D	2x25.96

Table 2.3 Container ships exceeding 2000 tonn capacity built between 1971 and 1973 [6].

compensated by the cost penalties caused by higher fuel consumption. Thus, major steam turbine manufacturers spent lots of efforts in increasing the thermal efficiency of their steam turbines. Specifically, in 1978 Stal-Laval started the Very Advanced Propulsion (VAP) research project aimed at improving steam power plant performance. Thanks to changes in thermodynamic cycle configurations, turbine blades and reduction gearboxes, steam turbines returned competitive with Diesel engines for $\approx$ 20 MW sizes. Maximum temperature and pressure consisted in 600 °C and 126 bar, respectively, and multiple superheating at 600 °C and 28 bar was present. The flow expansion was performed by means of three STs working at high (HP), intermediate (IP) and low (LP) pressures, all dealing with high rotational speeds (i.e. 12000-14000 rpm) to reduce volumes. In order to avoid corrosion instigated

OPEX term	ST[%]	Diesel[%]
Fuel cost	86	64
Lubrication cost	1	2
Maintenance cost	5	8

Table 2.4 Comparison between two-stroke Diesel engines and steam turbines in terms of costs [6].

by exhaust gas at high temperature, Fluidized Bed Combustion (FBC) guaranteed steam heating during each superheating process. Despite the VAP project obtained significant energy savings (i.e. a 5% reduction of SFC), steam turbines were not re-launched in the maritime sector. Specifically, less than 10 new ships built in the 80s were equipped with steam turbines. Particularly, LNG carriers and oil tankers remained the only vessel types onboard which steam power plants continued to be installed. This mainly derived from both possible combustion of BOG in boilers for LNG carriers and large amount of steam necessary for cleaning tanks and heating petroleum in tankers (e.g. see the case study of the LNG Methania reported above). On the other hand, where ships built before the 80s and powered by steam turbines are concerned, their operating ship speed was reduced from 21-30 knots to 16-18 knots with the aim of lowering fuel consumption, despite drawbacks on efficiency. However, since two-stroke Diesel engines simultaneously reached $SFC \approx 200$ g/kWh, ship owners started replacing steam power plants onboard existing vessels to gain cost benefits, especially for oil tankers and container ships. E.g., the oil tanker Mobil Hawk, built in 1976 and dealing with a 27 MW GE steam turbine, was equipped with two four-stroke Diesel engines SEMT Pielstick and more than 60 tonn of fuel per day were saved, due to SFC reduction from 277 g/kWh to 187 g/kWh. However, the lubrication oil consumption was increased from 15 kg/day to 780 kg/day. Due to the economic benefits obtained, the Mobil company decided to convert other 4 oil tankers, previously powered by steam turbines, to Diesel engines. Nevertheless, also other ship types experienced analogous conversions. This

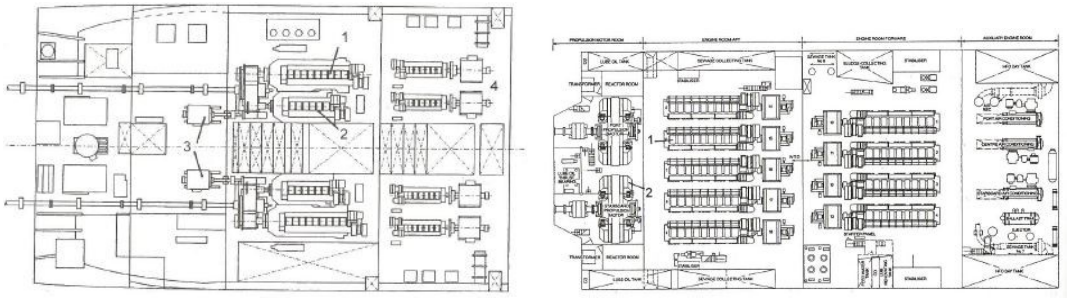

(a) (b)

Fig. 2.9 Schematic view of the power plant installed onboard the cruise ships Galaxy (a) and Queen Elizabeth 2 (b) [6]. Left side: large-size Diesel engine (1), small-size Diesel engine (2), electric generator (3), Diesel generator (4). Right side: Diesel engine (1) and electric motor (2).

was the case of the cruise ship Queen Elizabeth 2, where two 21 MW steam turbines were replaced by nine four-stroke Diesel engines MAN B&W 9L58/64 delivering an amount of 88 MW (see figure 2.9). Nowadays, steam power plants are unused within the merchant navy, whereas they continue to be installed on aircraft carriers, nuclear submarines and some frigates. Recently, the use of steam turbines in the marine sector was re-launched in the form of gas-steam combined power plants, currently used on some container (CMA CGM) and cruise (Radiance of the Seas, Jewel of the Seas, Celebrity Constellation, Celebrity Summit,...) ships.

2.3 Reciprocating engines

Diesel engines were introduced in the marine sector since the dawn of the 1900 and successively experienced a constant growth up to reach the current monopolistic position for ship propulsion [79]. The first ship powered by Diesel engines normally sailing was the river boat Petit Pierre, which entered into service in august 1903 transporting freights along Rhene and Marna. Propulsion load was supplied by a controllable pitch propeller driven by a 18.6 kW four-stroke Diesel engine rotating at 360 rpm. First, both two-stroke and four-stroke Diesel engines from the terrestrial transport sector were installed onboard ships. However, in 1905 the first two-stroke Diesel engine specifically designed by Sulzer for marine applications was commercially available. It was able to ensure a 65 kW net power when rotating at 375 rpm, with a mean effective pressure MEP=4.41 bar. From 1911 up to 1930, few modifications were introduced to improve scavenging, filling coefficient, intake and exhaust strokes (for four-stroke configurations). Furthermore, the bore was increased up to 900 mm and double-acting pistons were introduced as response to the increasingly high power demands requested by ship owners. In this context, in 1943 Sulzer introduced the SD engine class, which dealt with a single wash pump for each cylinder to reduce volumes. Then, in 1954, the RSD class introduced rigid arms instead of oscillating levers to improve simplicity and reliability of the valve operating system. Focusing on both SD and RSD classes, the delivered power was increased adopting larger bores (nearly 1000 mm) and slightly higher rotational speed, whereas the MEP experienced weak variations passing from 4.9 bar to 5.4 bar. In parallel, in 1954 the first boosted Diesel engine entered production from Sulzer. Specifically, the SD72 engine was coupled with a pulse-type turbocharger which increased MEP up to 6.24 bar, with consequent benefits in terms of power, whose value passed from 514 kW to 662 kW. In 1959, Sulzer launched the first Diesel engine specifically designed to include turbocharging, i.e. the RD90 engine. The main characteristics of the RD90 engine were 900 mm bore,

1550 mm piston stroke, $MEP = 8.65bar$ and 1.69 MW/cylinder. Aimed at achieving higher thermodynamic performances without losing reliability, in 1968 the constant pressure type turbocharging was introduced by Sulzer in the RND105 engine together with improvements in the bore cooling system. From 1950 to 1970, in order to reduce the impact of charter rate on the final price of freights, gigantism strategy for bulk carriers and oil tankers was followed by the major maritime companies and the trend was intensified after the Suez Canal closing. In those years, Ultra Large Crude Carriers up to 560000 DWT and container ships started to spread. High propulsion power demands requested onboard these vessels ($\geq$ 30 MW) could not be supplied by reciprocating engines, which also provided lower thermal efficiencies in comparison to steam power plants. When large size two-stroke Diesel engines were designed thanks to supercharging, steam turbines continued to be preferred on specific types of vessels where volumes and weights were particularly relevant. Then, in 1973-1974 the energy crisis moved research efforts from increasing power/cylinder ratio to reducing their SFC. Furthermore, to increase propulsion efficiency the diameter of propellers was increased, hence the rotational speed of Diesel engines, directly coupled with them, was also lowered. Thus, two-stroke Diesel engines characterized by high stroke/bore ratios ($C/D \approx 2.1$) were introduced in 1980-1982 (e.g. the RLB series from Sulzer). Thanks to the longer time available for burning fuel, combustion process was significantly improved and SFC=182 g/kWh was achieved. This determined the spreading of two-stroke Diesel engines onboard ships traditionally powered by steam turbines. Reinforcing of this trend was instigated by the further increase in fuel prices which occurred during the Iranian revolution and Iran-Iraq war, where super-long stroke engines were adopted (e.g., the RTA84M engine, dealing with SFC =158 g/kWh). During 2000s the main target of research concerning reciprocating engines became reducing production costs. Consequently, the power/cylinder ratio was increased from 3.46 MW/cylinder (RTA84M) to 5.72 MW/cylinder (RTA96C). Finally, from 2005 on, off-design performances of reciprocating engines have been improved by means of electronic control systems.

On the other hand, focusing on four-stroke Diesel engines, they were the first type of reciprocating engine developed within the terrestrial transport and power generation fields. Successively, the small size of four-stroke Diesel engines appeared well fitted for submarine propulsion during the World War II. Around 1950, the medium-speed four-stroke Diesel engines start spreading onboard ships for two main reasons: all the merchant vessels destroyed during the war needed to be re-built as well as new types of ships such as Roll-on/Roll-off, Fast Reefer ships, Lighter Aboard ships (LASH), Ropax and ferries appeared over the seas. Specifically, these new ship classes required high navigation speed, low engine room volume, high propeller rpm and low hull draft. Similarly to the two-stroke Diesel engines, the energy

crisis imposed a change of route: lowering specific fuel consumption and enabling the possibility of burning low-quality fuels became the new targets for four-stroke Diesel engines, instead of increasing power/weight ratio. Specifically, in order to deal with low-quality, cheaper fuels, the feeding system was improved by increasing injection pressure ($\approx$ 1300 bar), reducing diameter of pulverizer holes and adopting alloys resilient to vanadium and sulphur corrosion (i.e. Nimonic). Then, in the 2000s the target switched to lowering the investment cost of four-stroke Diesel engines, hence the power/cylinder ratio was increased up to 2 MW/cylinder and the bore diameter settled around 600 mm. Table 2.5 summarises the main geometrical and operational parameters for medium-speed four-stroke Diesel engines commercially available a decade ago. As can be seen, the MEP reaches 25-26 bar, whereas maximum pressure for combustion is around 200 bar (see the MAN B&M 18V48/60B). Thus, in order to improve thermo-mechanical resistance of the engine, technical tricks previously developed for two-stroke engines were implemented (e.g. bore cooling). All the four-stroke Diesel engines were equipped with turbochargers and intercooling was performed after pre-compression of the new charge outside the cylinder. Overall, SFC reached 175 g/kWh. Today, high-speed four-stroke engines ($\geq$ 1000 rpm) are also commercially available. Compared to the medium-speed ones, they deal with higher MEP, higher SFC but triple power/weight ratio. As final evolutionary step, in recent decades even more stringent regulations concerning

Properties	**MAN9L58/64**	**MAN18V48/60B**	**Wärtsilä 9L64**	**MaK M43C**
N_{cyl}	9	18	9	9
C **[m]**	640	600	900	610
D **[m]**	580	480	640	430
C/D	1.1	1.25	1.4	1.42
N **[rpm]**	428	514	333.3	514
MEP **[bar]**	23	25.8	25	26.4
MW/cyl	1.39	1.2	2.01	1
SFC **[g/kWh]**	177	176	175	177

Table 2.5 Main geometrical and operation parameters for medium-speed four-stroke Diesel engines [6].

both pollutant and GHG emissions are entered into force in the maritime sector [50, 80, 81] with the aim of gradually implementing energy transition. Thus, extensive research on reciprocating engines is currently underway by the major marine engine companies to allow for alternative fuel combustion. Specifically, reciprocating engines running on typical high-grade fuels such as natural gas (e.g., dual-fuel or natural gas engines) have been recently introduced to cope with the ECA zones [82, 83]. In addition, reciprocating engines working on greener fuels than natural gas (e.g., ammonia, hydrogen,...) are currently under study in a long-term energy transition perspective.

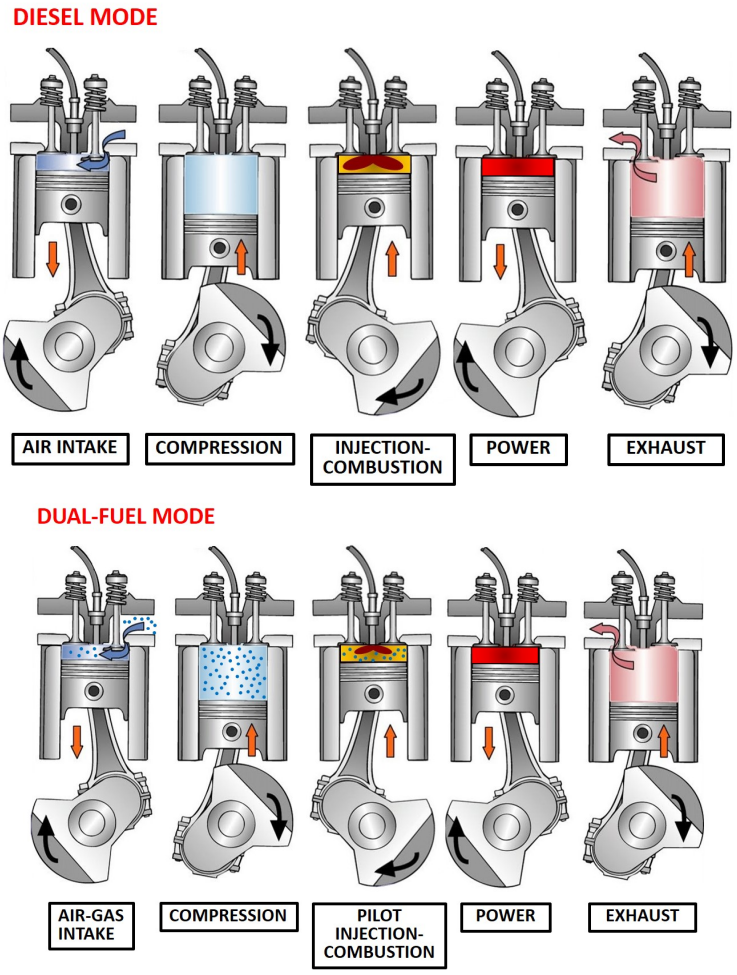

Fig. 2.10 General operating principle of Diesel (top) and DF (bottom) engines.

2.3.1 DF engine operation

Dual-fuel (DF) engines are compression ignited engines able to run in either natural gas or Diesel mode [84]. When operating on gas, a lean combustion process takes place, as shown in figure 2.10 for four-stroke engines. In details, during the intake stroke, new charge is formed mixing gas with air upstream of the inlet valves and, then, sucked into the combustion chamber. The compression stroke increases pressure and temperature levels achieved inside the combustion chamber and, successively, a small amount of liquid pilot fuel ($\approx 2\%$) is pressurized and injected into the cylinder by a common rail feeding system to ignite the lean premixed air-gas mixture. Then, the working stroke takes place and useful torque at the crankshaft is generated. When piston gets closer to the inferior dead point, the cylinder is emptied of exhaust gases through exhaust valve blow-out. Then, the inlet valves open and the process starts again. A backup fuel feeding system based on camshaft-operated fuel oil

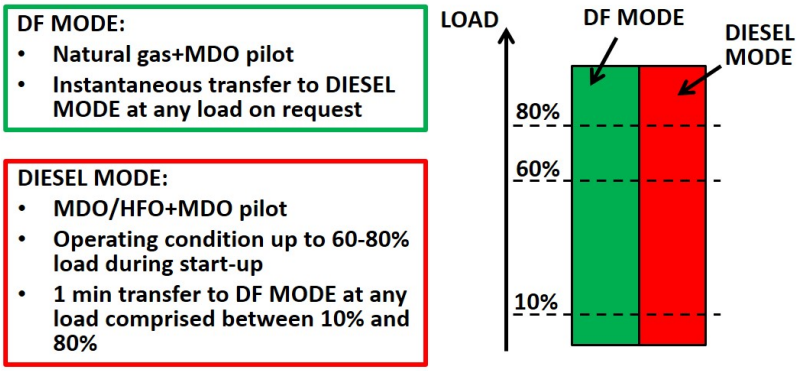

Fig. 2.11 Details on the switching capabilities of DF engines between Diesel and gas modes [9].

pumps is included to allow for 100% fuel oil operation, when unstable combustion of natural gas mode is surveyed during maneuvering or port conditions. Particularly, stable combustion during natural gas mode must be attained under those main circumstances:

- Operating conditions during switch from natural gas to Diesel mode and vice versa
- Rapid load variations
- Minimum load condition

Thanks to the lean combustion occurring during gas mode, the injection timing needs to be optimized and the compression ratio to be increased. Overall, benefits in terms of higher thermal efficiencies and reduced peak temperatures (i.e. reduced NO_x emissions) are achieved in comparison to Diesel engines [83, 85]. Since pilot flame is generated by diffusive combustion with negative influence on NO_x emissions, the amount of fuel oil injected within the combustion chamber should be small ($\approx 2\%$). In case a spark plug is used for ignition instead of pilot injection of Diesel fuel, the natural gas (NG) engines are obtained, working with lean natural gas-air blends. Focusing on the transition occurring between gas and Diesel mode in DF engines, two main scenarios can arise (see figure 2.11 for reference):

1. Switch from the Diesel to the gas mode: the Diesel mode is always used in the starting procedure and it remains enabled up to 60-80% of the nominal engine speed, when stable combustion of natural gas is ensured. Within 2 min after the switch-over command, the full gas mode is achieved, with minimal effects on either the engine power and rpm.
2. Switch from the gas to the Diesel mode: in case natural gas supply stops or failure occurs, the gas mode is switched over to the Diesel mode in less than 1 s and a

camshaft-operated injection system is enabled. Due to the instantaneous switch, drops in power and rpm are avoided.

Chapter 3

Ship propulsion plant configurations

Mechanical and electric propulsion are traditionally distinguished in the maritime sector. By an historical point of view, mechanical propulsion was the first to be developed: its major benefit consists in securing high reliability with reduced risk of failures, whereas high energetic efficiency is only guaranteed at nearly nominal operating conditions. Instead, electric propulsion have been successively introduced with the aim of preserving energy efficiency over wide operating conditions with less prime movers installed onboard. Within mechanical propulsion category, prime movers are linked to propellers through shafts and gearboxes, whereas electrical grid and motors are adopted in electric propulsion configurations (see figures 3.1 and 3.2). It must be remarked that in mechanical propulsion, distinct engines supply propulsion and hotel service power demands, whereas each engine can cover them in the electric propulsion configuration, allowing for energetic optimization. In this framework, combined (or hybrid) power plants for ships are based on coupling different prime movers in a single engine room installed onboard. This allows for enhancing benefits and weakening drawbacks from each prime mover, obtaining energy savings over the whole velocity range the ship sails. Combined power plants were born essentially for warship applications, where mechanical propulsion is always preferred. However, operation flexibility can be further enhanced in case combined power plants are configured for electric propulsion. Both arrangement and type of prime movers included within the engine room determine the acronyms traditionally used to differentiate combined power plants. Classification of the most common configurations, available in both mechanical and electric propulsion layouts, is reported below.

- COmbined Steam And Gas (COSAG): this configuration consists in combining steam and gas turbines, both of them fed by fuel and enabled to transfer power to the

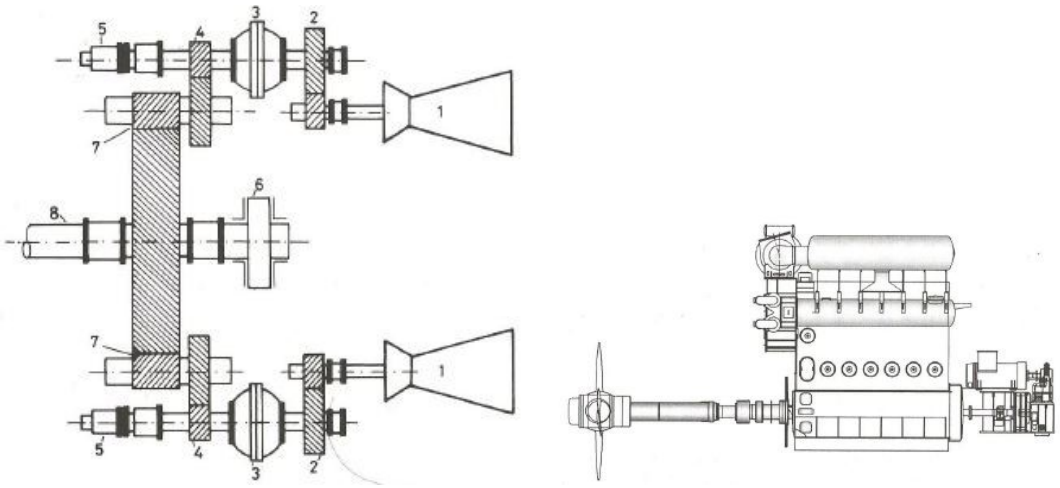

(a) (b)

Fig. 3.1 Three-stage reduction gearbox currently installed onboard the aircraft carrier Garibaldi of the Italian Navy (a) [6]. LM2500 gas turbine (1), first stage reduction gearbox (2), reversing clutch (3), second stage reduction gearbox (4), synchro-self-shifting clutch (5), thrust bearing (6), third stage reduction gearbox (7), propeller shaft (8). Schematic view of mechanical propulsion plant based on reciprocating engine directly coupled with the propeller (b).

propellers. Reduction gearboxes and clutches are necessary in order to switch from simultaneous to individual operating condition for turbines. The base-load power is delivered by steam turbine, whereas the maximum ship speed is guaranteed by additionally turning on gas turbines. As examples, the frigates Ashanti of the Royal Navy are powered by a 8.8 MW steam turbine coupled with a 6.5 MW gas turbine, whereas the guided missile destroyer Devonshire deals with COSAG including a 11 MW steam turbine and two 6.5 MW gas turbines.

- COmbined Gas And Steam (COGAS): the same prime movers of the previous configuration are included within the engine room. However, the exhaust gases from the gas turbine feed the steam turbine by means of HRSG. Thus, a better utilisation of energy is achieved in comparison to COSAG, with consequently lower SFC.

- Diesel And Diesel (DAD): this configuration covers propulsion demand combining different Diesel engines, whose mechanical connection with propellers can be enabled or disabled through a series of clutches and transmission mechanisms (see figure 3.3). Thus, small-size engines are turned on for reduced ship speeds to lower fuel consumption. The high-speed four-stroke Diesel engines are traditionally adopted for these power plant configurations, with MEP reaching 20-30 bar. Example of this configuration are installed onboard small military ships as those of the Cost Guard.

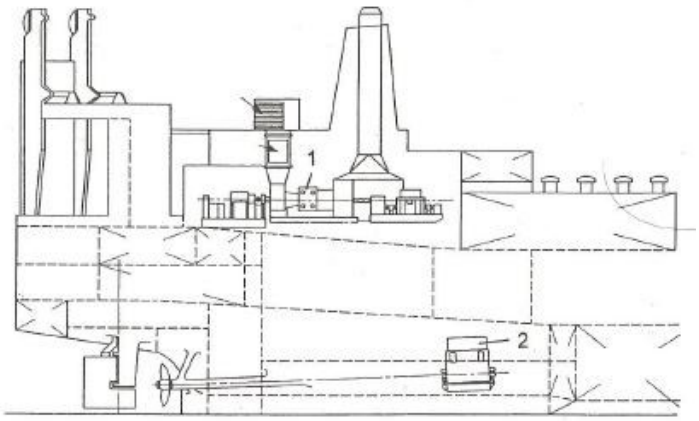

Fig. 3.2 Schematic view of electric propulsion plant based on gas turbine (1) driving the electrical motor (2) which delivers power to propeller [6].

- COmbined Diesel And Gas (CODAG) and COmbined Diesel Or Gas CODOG: the base-load power in cruise conditions is provided by one or more Diesel engines, whereas the maximum ship speed is achieved by turning on gas turbines. If GTs are able to cover the entire power demand for the maximum ship speed, the configuration is referred to CODOG: as an example, the F122 frigates of the German Navy are powered by two 2.8 MW MTU20VTB92 Diesel engines and by a GE LM2500 18.38 MW gas turbine. Similar power plants were installed on the Italian Navy frigates Maestrale, Lupo, Sagittario, Perseo and Orsa. In case power is withdrawn from both GTs and Diesel engines during the maximum ship speed condition, the configuration is refferred to CODAG. The corvettes Köln of the German Navy were powered by CODAG plants based on two 2.2 MW Diesel engines and a 9.5 MW gas turbine, whereas the Italian frigates Carabiniere (see figure 3.4) and Alpino are powered by two Diesel engine delivering 2.65 MW each and a 5.5 MW gas turbine. A schematic view of the CODAG configuration is reported in figure 3.3.

- COmbined Gas And Gas (COGAG) and COmbined Gas Or Gas (COGOG): these power plants are applied on large-size ships and are based on one or more GTs able to guarantee high efficiency in cruise condition and one or more GTs to boost operating condition. In case the base-load GT is not operating at maximum ship speed, the configuration is called COGOG (see figure 3.3). E.g., this configuration was installed on the HMS Exmotuh and on the destroyer Sheffield of the Royal Navy. In case base-load GTs also work during the maximum ship speed condition, the configuration is called COGAG. As an example, the aircraft carrier Garibaldi is powered by four

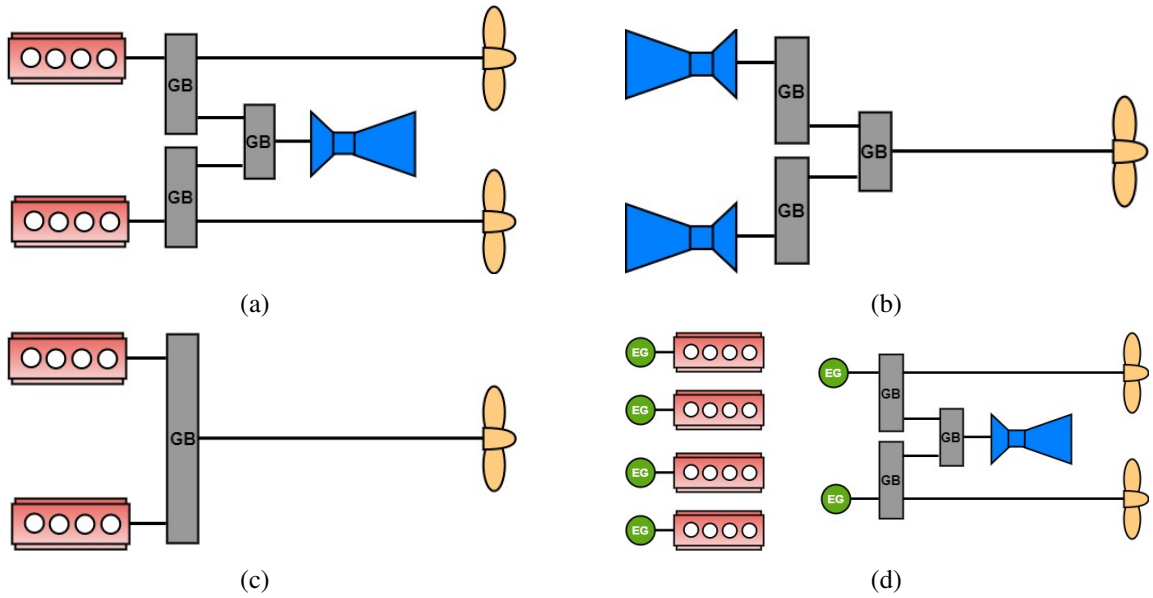

Fig. 3.3 Schematic view of CODAG (a), COGOG (b), CODAD (c) and CODLAG (d) power plants.

LM2500 GTs for a total installed power of 70 MW and maximum ship speed 29.5 knots (see figure 3.4).

- COmbined Diesel eLectric And Gas (CODLAG): this configuration is based on two electric motors driving propellers and moved by Diesel engines or gas turbines. Thus, it only belongs to the electric propulsion category, not to mechanical one. Diesel engines are able to cover power demand during port, maneuvering and low ship speed navigation, whereas gas turbines are turned on at mid or high speeds. Differently from previous configurations, the same prime movers can be used for propulsion and for hotel service, hence further benefits in terms of energy savings and number of installed prime movers (i.e. investment costs) can be obtained. CODLAG systems are currently installed on submarines and anti-submarine vessels. A schematic view of the CODAG configuration is reported in figure 3.3.

- COmbined Gas Electric and Steam (COGES): similarly to CODLAG, this configuration only applies to the electric propulsion category. Indeed, electric motors are interposed between prime movers and propellers. In this case, gas and steam turbines represent the only prime movers installed onboard. Specifically, thermal power available within the exhaust gases of GT is recovered by a bottoming steam power plant through HRSG. Furthermore, also in this case all the prime movers are enabled to cover both propulsion and hotel service power demand, hence energy benefits are guaranteed. COGES plants were installed on some cruise ships, where high thermal power required onboard can

(a)

(b)

Fig. 3.4 The frigate Carabiniere (a) [10] and the aircraft carrier Garibaldi (b) [11].

be covered through part of the large amount of thermal power available from exhaust gas from GT. Indeed, typical thermal power demand onboard cruise ships cannot be supplied by only Diesel engines, due to reduced mass flow rate and temperature feeding the waste heat recovery (WHR) system. A schematic view of the COGES plant installed onboard the Millenium cruise ship is shown in figure 3.5, whereas comparison between COGES and Diesel power plants in terms of occupied volume onboard cruise ships is shown in figure 3.6.

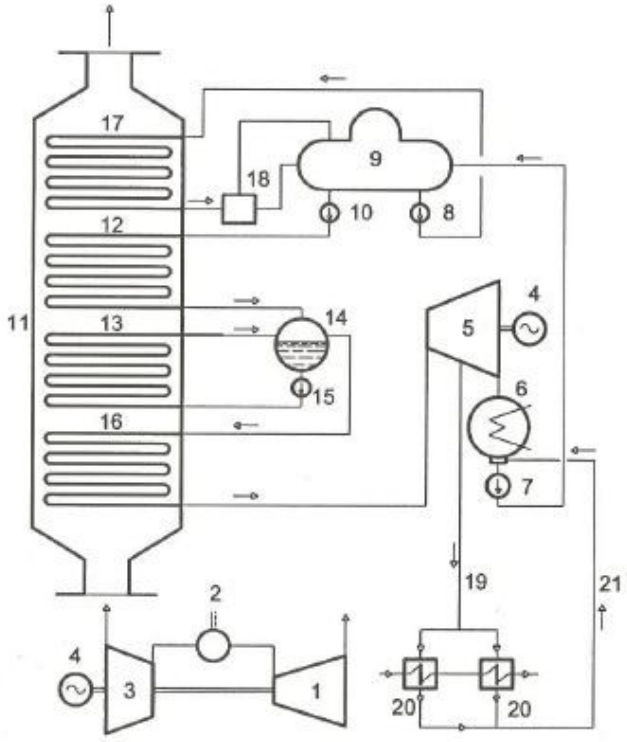

Fig. 3.5 Schematic view of the COGES plant installed onboard the Millenium cruise ship [6]. Compressor (1), combustion chamber (2), turbine (3), alternator (4), steam turbine (5), condenser (6), pumps (7,8,10,15), deaerator (9), HRSG (11), economizer (12), evaporator (13), cylindrical drum (14), superheater (16), LP economizer (17), separator (18), extracted steam (19), thermal users (20), condensate loop (21).

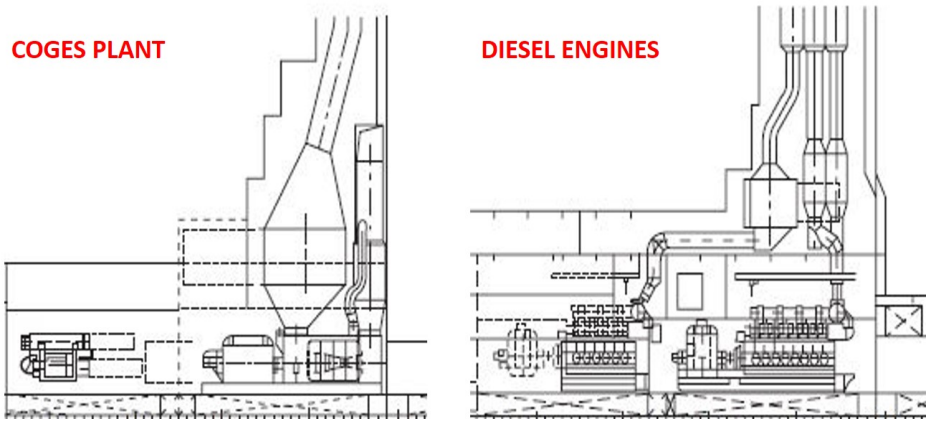

Fig. 3.6 Comparison between COGES and Diesel-electric power plants in terms of volume occupied onboard cruise ships [6].

Chapter 4

Fuels

4.1 Marine Gas Oil (MGO), Marine Diesel Oil (MDO) and Heavy Fuel Oil (HFO)

Crude oil is a mixture of many different hydrocarbons, hence it deals with a very wide boiling range. Furthermore, crude oil composition is significantly affected on source as well as on geographical area. For these reason, petroleum refineries constitute complex systems of multiple operations, which vary depending on both desired product slate and characteristics of crude oil. The processing scheme of a complex refinery can be divided into two parts [12]:

- Crude oil distillation (atmospheric and vacuum distillation): the crude oil fraction boiling below 360 °C are distilled off under reflux in atmospheric distillation columns. Typical products recovered are naphtha, kerosene, and light/heavy gasoil. However, since maximum temperature for atmospheric distillation is limited to 360 °C with the aim of avoiding coking, large amount of residual fuel oil is recovered. Thus, vacuum distillation is performed to distill off heavier components without exceeding the 360 °C limit.
- Catalytic and thermal cracking processes: the distillate fractions of the vacuum distillation are entered into a catalytic cracking unit (e.g., fluidized-bed catalytic cracking, FCC), where high temperature and crystalline aluminum silicate catalyst are adopted to break large molecules into lighter hydrocarbons (light cycle oil, which increases gasoil produced by refinery). On the other hand, residual fractions from the vacuum distillation are conveyed to the visbreaker, where mild thermal cracking operation

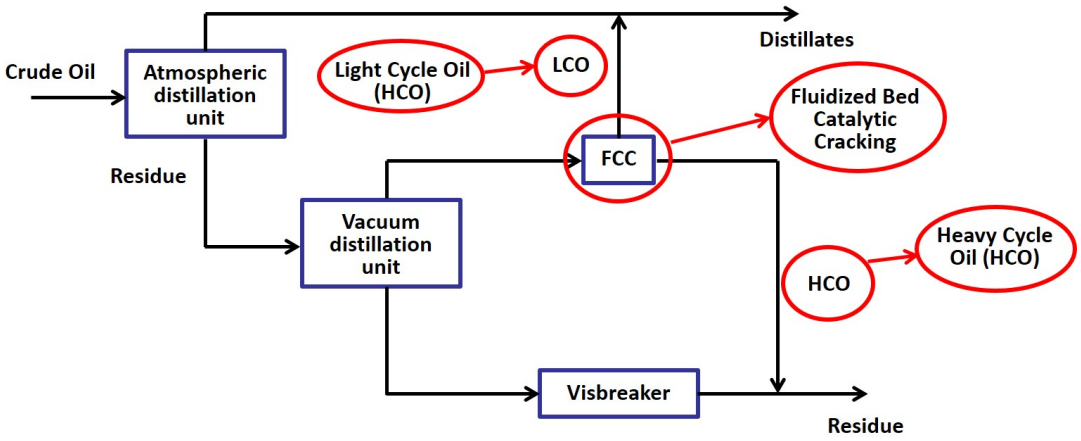

Fig. 4.1 Schematic view of the working principle of a complex refinery [12].

is performed to obtain 20% of light products which increase the amount of gasoil generated by the refinery (the remaining part is residual fuel oil).

Since 1987, the international ISO standard ISO8217 defines the requirements for fuels to be used onboard ships, before conventional onboard treatment (settling, centrifuging, filtration,...) is made.

In figures 4.2, 4.3 the last updated release for specification is reported. Specifically, the ISO 8217 divides marine fuels into two families: distillate marine fuels (first letter D, figure 4.2) and residual marine fuels (first letter R, figure 4.3). Each family is successively classified in several grades, depending on composition of the fuel. Overall, residual marine fuels are collectively referred to Heavy Fuel Oils (HFOs) and represent the residual fraction from the distillation process described above. On the other hand, DMA and DMB correspond to Marine Gas Oil (MGO) and Marine Diesel Oil (MDO), respectively, and are mainly manufactured from kero, naphtha and light/heavy gasoil fractions. Specifically, MGO consists in a high-quality marine fuel which is exclusively made of distillates, whereas MDO is a distillate blended with low quantities of residual fuel oil. As can be seen from figures 4.2 and 4.3, passing from the right to the left side of the reported grades, viscosity, density, flash point temperature and sulfur content reduce. Indeed, heavy fuel oils deal with $\geq 960\ kg/m^3$ density at 15 °C and $\geq 30\ mm^2/s$ kinematic viscosity due to the high content of long-chain, heavy molecules, whereas MDO and MGO are characterized by lower values.
Since the share of the fuel cost is around 30-50% of the total operating costs for a vessel, low-grade, cheaper fuels (i.e. HFO) have been used for decades in the maritime sector. However, HFO combustion in reciprocating engines emits a large amount of harmful pollutants, such as black carbon, sulfur dioxide, nitrogen oxides and particulate matter [86–88]. Furthermore,

Limit	Parameter	DMX	DMA	DFA	DMZ	DFZ	DMB	DFB
Max.	Viscosity at 40°C (mm^2/s)	5.500	6.000		6.000		11.00	
Min.	Viscosity at 40°C (mm^2/s)	1.400	2.000		3.000		2.000	
Max.	Micro Carbon Residue at 10% Residue (% m/m)	0.30	0.30		0.30		-	
Max.	Density at 15°C (kg/m3)	-	890.0		890.0		900.0	
Max.	Micro Carbon Residue (% m/m)	-	-		-		0.30	
Max.	Sulphur (% m/m)	1.00	1.00		1.00		1.50	
Max.	Water (% V/V)	-	-		-		0.30	
Max.	Total sediment by hot filtration (% m/m)	-	-		-		0.10	
Max.	Ash (% m/m)	0.010	0.010		0.010		0.010	
Min.	Flash point (°C)	43.0	60.0		60.0		60.0	
Max.	Pour point in Winter (°C)	-	-6		-6		0	
Max.	Pour point in Summer (°C)	-	0		0		6	
Max.	Cloud point in Winter (°C)	-16	Report		Report		-	
Max.	Cloud point in Summer (°C)	-16	-		-		-	
Max.	Cold filter plugging point in Winter (°C)	-	Report		Report		-	
Max.	Cold filter plugging point in Summer (°C)	-	-		-		-	
Min.	Calculated Cetane Index	45	40		40		35	
Max.	Acid Number (mgKOH/g)	0.5	0.5		0.5		0.5	
Max.	Oxidation stability (g/m^3)	25	25		25		25	
Max.	Fatty acid methyl ester (FAME)	-	-	7.0	-	7.0	-	7.0
Max.	Lubricity, corrected wear scar diameter (wsd 1.4 at 60°C) (um)	520	520		520		520	
Max.	Hydrogen sulphide (mg/kg)	2.00	2.00		2.00		2.00	
	Appearance	Clear & Bright					-	

Fig. 4.2 Distillate marine fuel standard from ISO [13].

heavy fuel oils present larger GHG impact (emission factor 1.34 gCO_2/kWh) in comparison to distillates (e.g., MDO emission factor is equal to 0.33 gCO_2/kWh). Thus, even more stringent IMO environmental regulations have been enforced with the aim of curtail CO_2, NO_x and SO_x emissions and the Marine Environmental Protection Committee (MEPC) has been established. In this scenario, Emission Control Areas (ECAs) have been creating worldwide, where Heavy Fuel Oil (HFO) is not allowed yet. For this reason, since 2015 less residual oil is produced by refineries and even more ships are converted to distillate fuels [89, 90].

4.2 LNG

Liquified Natural Gas (LNG) is natural gas that has been converted into liquid form for the ease and safety transport. Thus, LNG consists in a mixture of hydrocarbons, whose composition depends on the natural gas reservoir source and affects its chemical-physical properties. Nevertheless, LNG predominately consists in methane (88-99%) along with a few percent ethane (5-8%), even less propane and butane, and trace amounts of nitrogen [33].

Limit	Parameter	RMA 10	RMB 30	RMD 80	RME 180	RMG 180	RMG 380	RMG 500	RMG 700	RMK 380	RMK 500	RMK 700
Max.	Viscosity at 50°C (mm^2/s)	10.00	30.00	80.00	180.0	180.0	380.0	500.0	700.0	380.0	500.0	700.0
Max.	Density at 15°C (kg/m^3)	920.0	960.0	975.0	991.0	991.0				1010.0		
Max.	Micro Carbon Residue (% m/m)	2.50	10.00	14.00	15.00	18.00				20.00		
Max.	Aluminium + Silicon (mg/kg)	25	40		50	60						
Max.	Sodium (mg/kg)	50	100		50	100						
Max.	Ash (% m/m)	0.040	0.070			0.100				0.150		
Max.	Vanadium (mg/kg)	50	150			350				450		
Max.	CCAI	850	860			870						
Max.	Water (% V/V)	0.30	0.50									
Max.	Pour point (upper) in Summer (°C)	6	30									
Max.	Pour point (upper) in Winter (°C)	0	30									
Min.	Flash point (°C)	60.0										
Max.	Sulphur (% m/m)	To comply with statutory requirements as defined by purchaser										
Max.	Total Sediment, aged (% m/m)	0.10										
Max.	Acid Number (mgKOH/g)	2.5										
	Used lubricating oils (ULO): Calcium and Zinc; or Calcium and Phosphorus (mg/kg)	The fuel shall be free from ULO, and shall be considered to contain ULO when either one of the following conditions is met: Calcium > 30 and zinc > 15; or Calcium > 30 and phosphorus > 15.										
Max.	Hydrogen sulphide (mg/kg)	2.00										

Fig. 4.3 Residual marine fuel standard from ISO [13].

Boiling point	-161.5 °C at 1 atm
Freezing point	-182.6 °C at 1 atm
Density	450 kg/m^3
Flammability limits	5-15 by volume
Ignition temperature	538 °C at 1 atm
Octane number	120-130
Laminar burning velocity	0.374 m/s
Energy density	22.2 MJ/l

Table 4.1 Chemical and physical properties of LNG [33].

The main properties of natural gas are summarised in table 4.1. Specifically, LNG is non-corrosive, colorless and odorless. Despite gaseous release from LNG may cause asphyxiation in case of unventilated areas, it is nontoxic. Boiling and melting point at ambient pressure corresponds to -161.5 °C and -182.6 °C, respectively. Furthermore, natural gas can be ignited when mixed with air in certain concentrations: the superior and inferior flammability limits for methane/air mixtures coincide with 15 and 5% by volume, respectively [33]. When natural gas concentration in air exceeds the upper flammability limit, too little oxygen is present to start burning. On the contrary, when the natural gas concentration is below the lower flammability limit, too much air is present. The first scenario occurs in closed storage tanks where the vapor forms but not sufficient air is present for ignition. Instead, the second situation typically happens in case of small amount of LNG vapors leakages in ventilated

areas, where the mixture rapidly reaches concentration lower than the inferior flammability point [91]. Interestingly, only vapors of LNG mixing with air can generate explosive and flammable gaseous mixtures, whereas explosion and firing should not be considered as potential hazards in liquid state. Low laminar burning velocity (0.374 m/s) [92] and high ignition temperature (538 °C) relative to other hydrocarbons are shown by vaporized LNG. Owing natural gas presents low energy density per unitary volume in comparison to other fuels, either liquefaction and compression are performed to reduce volumes for storage and transport. Specifically, energy density provided by LNG (22.2 MJ/l) is 2.5 times higher than that of compressed natural gas (9 MJ/l at 250 bar and ambient temperature) [34], hence transporting natural gas in liquid form reveals more economically and energy efficient [93]. For this reason, LNG as marine fuel is typically stored onboard ships at ambient pressure and reducing temperature just below its corresponding boiling point (-162 °C). Consequently, the following challenges need to be addressed:

- materials able to provide high resistance at very low temperatures
- highly performing types of insulation (with low thickness)
- special provisions to avoid shrinkage of the case.
- safety measures to control LNG evaporation and leakage
- positioning and large volumes for containment systems

Where the LNG storage onboard ships is concerned, particular cryogenic tanks traditionally adopted on LNG carriers are used. LNG tanks can be classified into two different types [33]:

- Membrane containment systems: they consist in double-layer tanks integrated into the hull with the aim of optimizing space available onboard for passengers or freights. Since they contribute to the strength of the hull, they are considered structural elements. A thin layer of metal constitutes the primary barrier, which is sequentially surrounded by insulation, secondary membrane barrier and further insulation. Primary barrier is made by high-nickel-content (36%) steel (Invar) or 18% chrome/8% nickel stainless steel. Membrane tanks are designed in such a way that thermal expansion or contraction is compensated for without increasing stresses. Between the two barriers, gas detector and nitrogen atmosphere are usually positioned for safety reasons. Since membrane containment systems cannot limit the BOG to the amount useful for propulsion, adequate re-liquefaction plants are necessary [94]. In figure 4.4 a schematic view of membrane containment systems is reported. Example of membrane containment

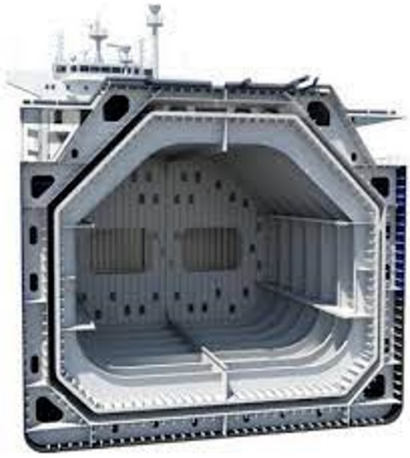

Fig. 4.4 LNG carrier (left) and its corresponding membrane containment system (right) [14, 15].

systems consist of the GT No 96 and Mark III membrane tanks, which have been almost exclusively applied to LNG carriers for decades.

- Self-supporting containment systems: three main categories, namely Type A, B and C, are usually distinguished. Type A self-supporting tanks deal with prismatic shape and are usually installed onboard fully-refrigerated LPG carriers. Basic stress analysis and materials not crack propagation resistant are usually used in the design procedure. The tank is surrounded by insulation materials (e.g. perlite) and a secondary barrier is added to ensure safety in case of leakage. Specifically, the IGC Code imposes that secondary barrier must contain tank leakage for 15 days. Type B tanks are often characterized by spherical shape (Kvaerner-Moss) and a more detailed stress analysis, accounting for fatigue life and crack propagation, is carried out during the design procedure. Thanks to its enhanced design, only a drip tray partially performs as secondary barrier. A thick layer of foam insulation surrounds the tank and a thin layer containing nitrogen atmosphere to check for leakage. Furthermore, since cool down or warm up of Type B containment systems can cause significant contraction and expansion ($\approx 0.6m$), flexible bellows are adopted to connect pipeline to the tank. The Kvaerner-Moss tank type is exclusively adopted on LNG and LPG tankers. However, in the future, it is expected to be installed on large container ships requiring more than 2000-3000 m^3 of fuel [95], due to their lower volume-specific cost in comparison to Type C tanks [96]. Finally, Type C tanks are characterized by cylindrical shape (mono- or bi-lobed), which allows for high internal pressures (up to 20 bar) but poor utilisation of the hull volume. Tanks can be installed either horizontally or vertically onboard ships and are designed according to the conventional pressure vessel code, with detailed stress

Fig. 4.5 Type B (left) [16] and Type C (right) [17] self-sustaining containment systems.

analysis to guarantee high fatigue strength. For this reason, no secondary barrier is required, despite concentric-shell structure is anyway present. Inner shell made of austenitic stainless steel contains LNG, whereas secondary shell prevents leakage. The space gap between the inner and outer shell is filled by either insulating materials (i.e. perlite) or is kept under vacuum conditions. Type C tanks are currently the most widely used storage method for LNG-fuelled ships, where a typical pressure around 5 bar is adopted to make the gas spontaneously flow towards the power supply of the engines, with the benefits of no dedicated pumps needed. Furthermore, reduced tank capacity are enabled (i.e. $\leq$500 m^3) [95].

Since the insulation cannot prevent all external heat from reaching the LNG tank, some of the liquid boils off during the voyage. Independently from the containment system used, the LNG boil off gas (BOG) is typically generated at the rate of about 0.10% to 0.15% of the ship volume per day and accumulates in the atmosphere above the liquid, causing the tank pressure to increase in time and favouring even more evaporation. Thus, for structural integrity and safety reasons, BOG must be removed to keep the tank at a constant pressure. Specifically, the BOG can be vented out, used as fuel in the engine room, burned in auxiliary boilers to produce steam or re-liquefied. In the first LNG carriers, BOG was burned with HFO in steam boilers, while the excess was vented out. Recently, strategies for using BOG that guarantee greater efficiency from an energy point of view have been developed for both LNG carriers and LNG fueled vessels [97, 98].
Three main types of bunkering infrastructures exist for LNG fueled ships (see figure 4.6):

- Truck-to-Ship (TTS): the LNG truck is connected to the vessel on the quayside by means of a flexible hose. Due to the still limited demand for LNG bunkering and its relatively low investment costs for operators, TTS represents the most widely used bunkering method, as a provisional solution. E.g., in 2008, 50% of the Norwegian

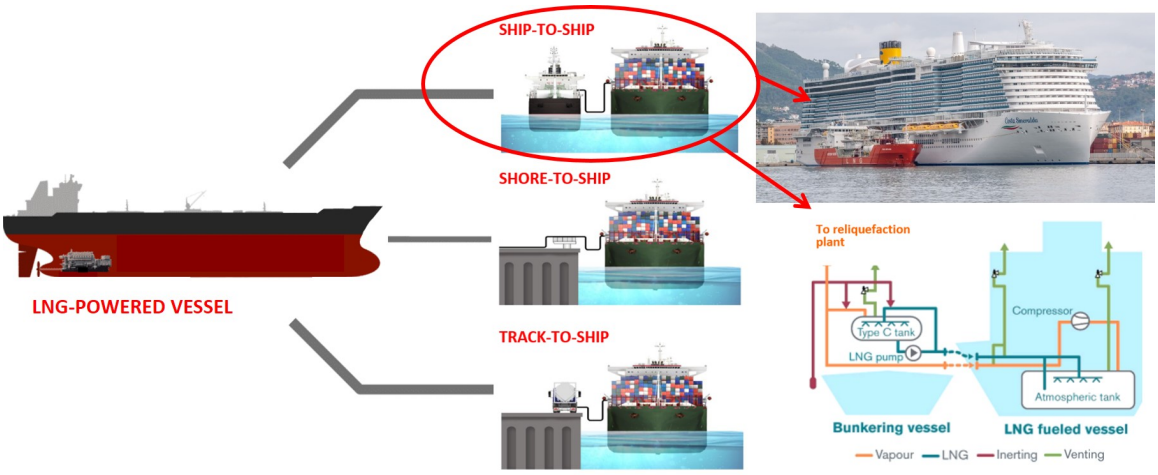

Fig. 4.6 LNG bunkering options (left) and detailed view of the ship-to-ship method (right) [18, 19].

LNG-powered ferries were regularly supplied by trucks. Furthermore, tanker trucks can be used also for LNG distribution to users different from ships. However, the limited capacity of tanker trucks ($\approx$ 40-80 m^3) represents the main drawback of TTS and makes it suitable only for small-size LNG-fuelled ships (i.e. dealing with 50 tonn maximum tank capacity). Additionally, bunkering completion takes nearly 1 hour due to the reduced flow rate which can be conveyed from truck to ship ($\approx$ 1000 l/min). Finally, road connection, space necessary and safety requirements clearly impact other quayside activities in port (i.e. either cargo and passenger handling). Nevertheless, TTS results suitable for ships requiring limited bunker volumes (coastguard ships, small passenger vessels,...) in absence of particular safety restrictions (i.e. the passenger vessel Viking Grace is refuelled through ship-to-ship system by Seagas).

- Ship-to-Ship: It can take place indifferently at sea, at anchor or along the quayside and involves bunkering capacity ranging from 1000 to 10000 m^3, with consequent high flexibility ensured. Safety port regulation often allow simultaneous cargo handling during bunkering, since ship-to-ship relies on mooring the bunker vessel with LNG-fuelled ship. Two are the main drawbacks of ship-to-ship bunkering. First, LNG bunker vessels can experience limited operation since LNG demand does not reach a relevant levels, hence their high investment cost can be hardly paid back. Second, LNG bunker vessels need authorization to enter in non-petroleum ports, depending on their safety regulations. Overall, ship-to-ship bunkering is expected to play a major role in future for ships equipped with $\geq$ 100 m^3 tank capacity (i.e. RoPax, RoRo, bulk carriers and container vessels) thanks to its operational flexibility.

- Shore-to-Ship: it consists in bunkering LNG-fuelled ships from tanks or terminals in port through pipelines, guaranteeing high bunkering rate (3000 l/min). Stable and long-term bunkering demand in ports is required to be cost effective. The main drawbacks consist in high investment costs and large space requirements in port, where limited berth access for shore-ship bunkering can be present.

Until a few years ago, TTS was the most frequently used bunkering configuration, due to difficulties in developing business case for the other two methods. However, infrastructures for ship-to-ship and shore-to-ship bunkering are under development worldwide, since they can offer benefits in terms of capacity, operational flexibility and safety requirements. Independently from the bunkering options, few issues must be faced. First, since LNG is at -162 $^{\circ}$C, portable pipes and connections used to transfer it must freeze gradually in order to avoid ruptures or brittle fracture causing leakage and spillage of LNG. In this case, human contact should be carefully avoided, since it lead to frostbite and cryogenic burns, whereas fire and explosion hazards are limited thanks to the ice formation at the leak.
In the recent years, Liquefied Natural Gas (LNG) is emerging as a clean source of energy for the maritime sector and definitely appears a viable option in bridging energy transition to sustainability. Indeed, combustion of natural gas generates nearly null particulate matter (PM) emissions due to impurities and low NO_x may be achieved in case of lean-premix flames reducing peak temperatures. Furthermore, since methane chemically presents the lowest hydrogen/carbon ratio among all hydrocarbons, significant carbon dioxide emission reduction can be obtained. Finally, sulphur content in LNG is drastically reduced during the liquefaction process, hence approximately null SO_x emissions are generated. Many works exist in the literature addressing the extent of emission reduction attained by LNG combustion rather than burning MDO. The overall trends are reported below [82, 83, 85]:

- 25 - 30% lower carbon dioxide (CO_2)
- 85% lower nitrogen oxides (NO_x)
- $SO_x \approx 0$ - almost all the sulfur is removed during purification process
- $PM \approx 0$
- No sludge deposits, hence engine life extended.

Owing LNG allows to cope with current environmental regulations in ECA zones, even more attention is paid by ownerships to it, with consequent thrust on developing adequate bunkering infrastructures. At 2020, 53 ports where LNG bunkering is available and 37 ports

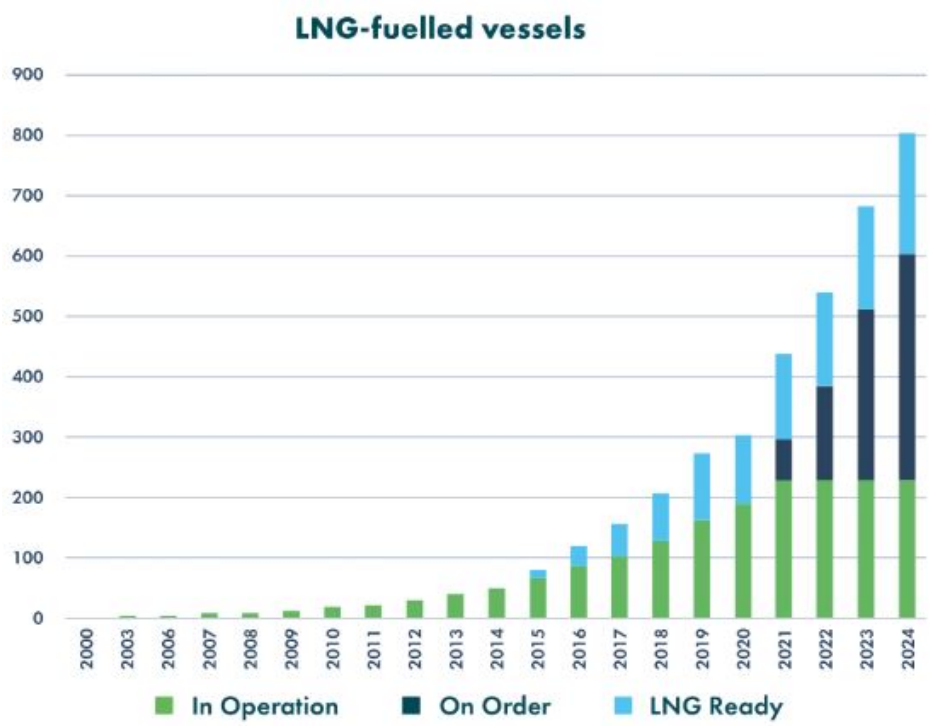

Fig. 4.7 Global development of LNG-fuelled fleet [20].

where LNG bunkering facilities are under development were available in Europe. The first LNG fuelled ship other than LNG carriers started sailing in the Norwegian seas in 2000 [99]. Successively, vessels designed for short-sea routes (e.g. small ferries and Platform Support Vessels, PSV) came into service powered by LNG [100, 101]. Recently, also tankers, cruise ships, cargo vessels, Ro-Ro ships and tug boats fueled by LNG have entered into operations [102]. At the 1 January 2022, DNV estimated the global fleet of LNG-fuelled vessels at 654 units (251 in operation and 403 on order), together with additional 210 LNG-ready vessels. Overall, LNG-fuelled vessels recently amount to 13% of the new-build order book [103]. On the other hand, focusing on the ultra-large container vessel segment, nearly 50% of the new-build book consists in either LNG-fuelled or LNG-ready ships.
In order to reduce GHG impact, production of bio-LNG from bio-methane i.e. CH_4 coming from renewable resources, is currently receiving major attention. Two main pathways and various feedstocks are available for bio-methane production:

- Anaerobic digestion: organic waste, manure, municipal waste and other residues can be used to produce a mixture of CH_4 and CO_2 through anaerobic digestion. Then, the CH_4 mixture can be upgraded to reach minimal amounts of impurities.

- Gasification of biomass: synthetic natural gas is produced from biomass and, then, upgraded.
- Electrolysis of water: surplus electricity from intermittent renewable power generation can be used to produce H_2 and, then, synthetic natural gas

Overall, agriculture and waste sectors constitute the two largest potential feedstocks for bio-methane production. By an environmental point of view, these feedstocks for bio-methane enable huge reduction in GHG emissions, with a twofold benefit [104]:

- prevent methane emissions from the agriculture and waste sectors, which would otherwise occur naturally without being used to produce renewable energy source
- displace fossil fuels by means of bio-methane

Since bio-LNG is simply liquefied methane, is interchangeable with LNG as a fuel in existing engines and can be transported, stored and bunkered in ports utilising existing LNG infrastructure. Burning bio-LNG, initially as a drop-in fuel, can provide 92% reduction of GHG emissions compared with fossil LNG, with even further benefits possible depending on the origin of the bio-LNG. E.g., in 2018 Biokraft started operating the world's largest facility performing biogas production, biogas upgrading (to bio-methane) and bio-methane liquefaction. The facility converts the biogas produced by anaerobic digestion of fishery waste and residual paper mill slurry into 250 GWh/year bio-LNG, which was first used as vehicle fuel in Norway for busses and heavy trucks. Since 2019, the bio-LNG produced by the facility is also used to supply cruise ships of the Hurtigruten fleet. Residues from the bio-LNG production facility are currently supplied to farmers as bio-fertiliser. Analogously, the world's largest LNG bunkering operation occurred in Rotterdam in November 2020, i.e. 17300 m^3 of LNG supplied to CMA-CGM ultra-large container vessel named JACQUES SAADE, comprised 13% of bio-LNG [105]. Furthermore, 100% renewable bio-LNG is used to bunker the dry bulk carrier Viiki from ESL Shipping in Finland [106], two LNG-fuelled tankers chartered by the Preem company work with 10% bio-LNG blend in Sweden and two high-speed ferries from the Destination Gotland operator are currently powered by bio-LNG blends. This shows how bio-LNG presents a very viable business case for ship bunkering in Europe.

4.3 Methanol (CH_3OH)

Methanol (CH_3OH) is one of the simplest alcohols, commonly referred as methyl alcohol or wood alcohol in the chemical field. Under the current environmental and regulatory challenges, many factors show its suitability as a viable solution for the maritime sector. Indeed, combustion of methanol is able to provide lower emissions when compared to HFO or MDO. Specifically, less than 0.01 g/kWh soot and particulate matter are generated by CH_3OH in Diesel engines, against the 0.1 g/kWh shown by HFO [107]. Then, laboratory and field tests proved that nitrogen oxide emissions from methanol-fuelled reciprocating engines are low (i.e. 2-4 g/kWh), despite they slightly exceed the IMO Tier III limit. Additionally, since methanol is sulfur-free, it avoids sulfur oxide emissions. Due to its similarity to Diesel fuels regarding transportation requirements, methanol currently appears the best replacement for gasoline in the future. Indeed, methanol is liquid at ambient pressure and temperature (boiling point at 64.7 °C, melting point at -97.6 °C), hence it is easier to handle in comparison to LNG or hydrogen [108] and can be stored in ordinary tanks with few modifications. Handling and transporting methanol as a chemical, both in tank trucks and bulk vessels, were widely experienced in Europe during the last decades, due to its traditional adoption in industry: it traditionally represents a feedstock to synthetize chemicals derivatives such as formaldehyde, acetic acid, ... [109]. For example, it must be remarked that CH_3OH was the dominant bulk liquid handled in Finnish ports in 2008 and 2009 and is commonly transported in ports of Baltic Sea [110]. Overall, CH_3OH represents still now one of the leading chemicals in terms of volumes transported and distributed in Europe. Where the economical feasibility of methanol is concerned, many studies exist in the literature showing that costs for adapting marine Diesel engines to methanol are significantly lower than those involved for the transition to LNG [111, 112]. However, CH_3OH can be burned in various types of prime movers for ship propulsion, such as two- and four-stroke Diesel engines, Otto engines, gas turbines and fuel cells [108]. Though it requires an ignition enhancement (usually provided by small amount of Diesel oil), methanol shows good combustion properties and energy efficiency. Methanol-air mixtures have a higher laminar burning velocity than gasoline (0.455 m/s), as well as lower and upper flammability limits equal to 6.7% and 36%, respectively [113, 114]. Therefore, when methanol concentration in air exceeds 36%, too little oxygen is present to instigate combustion. Instead, when the methanol concentration is below 6.7%, too much air is present. Similarly to LNG, methanol is a low flash-point fuel, i.e. vaporizes and forms a flammable mixture with air at relatively low temperatures, hence this issue need to be addressed in the safety assessment.

However, the main drawback of CH_3OH coincides with its lower energy content per unitary volume in comparison to traditional fuels (see table 4.3 below). Industrial methanol production has three main steps [115, 116]:

- Production of synthesis gas containing H_2
- Conversion of the synthesis gas into methanol
- Processing and distillation of crude methanol

The first step may rely on different feedstocks for generating synthesis gas, including natural gas, coal and wood biomass. Chemical and physical properties are not affected by the type of source used [112], whereas the accounting process of GHG emissions related to the production phase strongly depends on the feedstock used. Specifically, the maximum abatement potential of equivalent carbon dioxide emissions is achieved by bio-methanol, i.e. methanol generated from biomass. On the other hand, production of 1 tonn of methanol from fossil resources generates 0.6-1.5 tons of CO_2 [117, 118]. Nowadays, most of CH_3OH available on the market derives from natural gas and, secondly, from coal. China uses coal to produce methanol for domestic use, whereas residual fractions from refineries and HFO are currently playing minor role for production purposes [119]. On the other hand, chemical industry showed how various kinds of biomass (waste wood, forest thinning and even municipal solid waste) are an effective source of the renewable synthesis gas when gasified. For example, black liquor produced from pulps and paper mills is used to generate methanol and bio-Di methylether (DME) in Sweden [119, 120]. Furthermore, the widespread of renewables in the electricity market, excess power generation from wind or photovoltaic plants could be used to produce methanol, which operates as a "liquid battery" (power-to-fuel strategy) [119, 121]. Specifically, hydrogen produced by water electrolysis is used to performed the catalytic reaction:

$$3H_2 + CO_2 \longrightarrow CH_3OH + H_2O \tag{4.1}$$

which is facilitated by CuO, ZnO or Al_2O_3 catalyzers and takes place at 250-300 °C and at 50-100 bar [122, 123]. However, costs of renewable methanol is estimated to be 40% higher than that obtained for the fossil-based one [119, 124]. Nevertheless, independently from the production source, pilot projects are underway to test the performance of methanol fueled passenger ferries, such as Stena Germanica, which sails between Gothenburg (Sweden) and Kiel (Germany). Specifically, the engine room retrofit concept was gradually developed using CH_3OH engines developed by Wärtsilä. Overall, the economic feasibility of a methanol-fuelled ferries was shown, despite disappointing results not able to cope with IMO Tier III

were surveyed for the NO_x emissions. Indeed, experimental tests of Wärtsilä and MAN on methanol-fuelled reciprocating engines showed 60% and 3-4% reductions in NO_x emissions and SFC in comparison to HFO, respectively [125, 126]. Furthermore, other works in the literature found a 8% reduction in the exhaust gas temperature over the entire working range, when CH_3OH feeding conditions are enabled [127].
On the other hand, the ability of GTs to burn methanol has been proven for decades. Specifically, Turbo Power and Marine pioneered methanol combustion experimental tests in a 20 MW gas turbine at the Bayboro Station of Florida Power Corporation [128]. Methanol was shown to guarantee 74% NO_x emission reduction in comparison to heavy distillate fuels. Successively, full operational tests on a 26 MW Turbo Power and Marine GT were performed by EPRI and Southern California Edison Company [129]. In comparison to dynamic off-design performance available from CH_4, unaffected ability to start, stop, accelerate, decelerate and perform synchronization was surveyed under CH_3OH feeding conditions. Since gravimetric energy density of CH_3OH is lower than that of CH_4, feeding GT with methanol was shown to increase power output and electrical efficiency, thanks to the higher mass flow rate available in turbine. Furthermore, methanol combustion achieved a 59% NO_x emission reduction in comparison with CH_4, for analogous GT operating conditions [130]. Successively, GE conducted methanol combustion tests on an E-class heavy-duty gas turbine equipped with a MS7001 DLN combustor. Results shown 30% NO_x lower emissions provided by CH_3OH feeding system with respect to CH_4 [131]. Analogous tests on methanol combustion were successfully carried out on a 3.25 MW Allison 501-KB gas turbine at the University of California (Davis) [132] and on a 30 MW GT by Tokyo Electric Power at Yokosuka [133].

4.4 Hydrogen (H_2)

Hydrogen (H_2) is the lightest element and does not exist in nature in pure form, hence it is commonly considered an energy carrier rather than an energy source [134]. Hydrogen is odorless, colorless and nontoxic. However, it is highly flammable [135], hence very low energy is sufficient to ignite it in air mixtures. Chemical and physical properties of H_2 are reported in table 4.2. Though the energy content of 1 kg of hydrogen is far higher than that available from other fuels, its low volumetric energy density in MJ/m^3 currently appears the main issue, limiting the range able to be covered by ships (see table 4.3). Where sources are concerned, hydrogen can be produced by several methods, despite sustainability is not always guaranteed. Since H_2 is usually found in combination with oxygen in water and with carbon in hydrocarbons, the principal production methods are the following:

Color, odor	Colorless, odorless
Toxicity	none (asphyxiant)
Density	0.07 g/cm^3 (liquid)
Liquid to gas expansion ratio	1:848 (at 1 atm)
Boiling point	-253 °C
LHV	120MJ/kg
Adiabatic flame temperature	2107 °C
Flammability	4-75%
Laminar flame velocity	3.06 m/s
Auto ignition temperature	585 °C
Octane number	>130

Table 4.2 Chemical and physical properties of hydrogen [34].

- Splitting hydrocarbons: hydrogen can be produced by splitting hydrocarbon molecules [136]. In case Carbon Capture and Storage (CCS) systems are not available, GHG emissions are present and affect sustainability over the entire Life Cycle Assessment (LCA) of the fuel [134]. Fossil fuels mostly used consist in coal and natural gas. Specifically, the chemical process commonly adopted is the steam reforming reaction, which relies on providing thermal energy to hydrocarbons by means of steam at 700-1000 °C to produce a H_2-rich synthetic gas:

$$C_nH_m + nH_2O \longrightarrow nCO + (\frac{m}{2} + n)H_2 \tag{4.2}$$

  Catalysts based on Nickel and Magnesium oxides are needed to facilitate the reaction. Then, the shifting reaction is performed to increase the amount of H_2 obtained via exothermic reactions between steam and carbon monoxide:

$$nCO + nH_2O \longrightarrow nCO_2 + nH_2 \tag{4.3}$$

  Finally, bio-methane generated by bio- and waste resources such as biomass and wastewater can be effectively adopted to produce H_2 by steam reforming with reduced carbon footprint [137].

- Gasification of coal: gasification of coal is accomplished by mixing pulverized coal with an oxidant (usually steam) with the aim of turning it into synthesis gas (i.e. syngas), which is mainly composed of carbon monoxide CO, hydrogen H_2 and carbon dioxide CO_2. Syngas is generated at high temperature ($\approx$ 1800 °C) and, second, shifting reaction is typically performed to increase H_2 content [138].

- Renewable sources: both electricity from the grid or self-generated electric power deriving from renewable sources (solar, wind, hydro, geothermic and biomass) can be used to produce H_2 through electrolysis of water (see figure 4.8 for the main types of

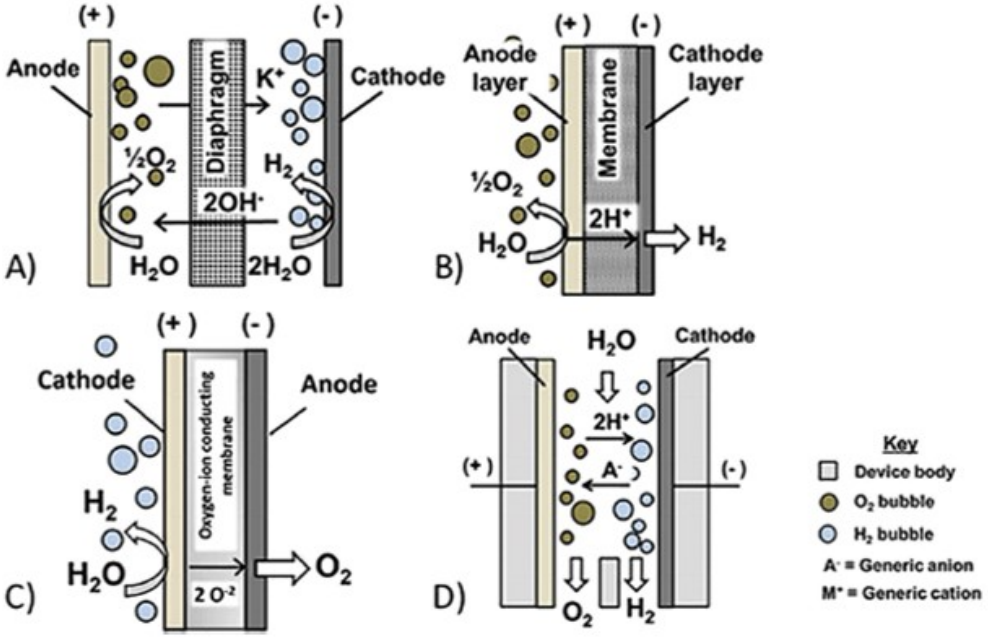

Fig. 4.8 Schematic view of different types of electrolysis: alkaline (A), proton-exchange membrane (B), solid oxide (C) and membraneless (D) [21].

electrolysis). By means of electricity, the electrolysis splits water into its two elements, i.e. H_2 and O_2 [139]. In case only energy from renewables is used, the environmental impact of the H_2 production process may be nearly zero [134]. Furthermore, electrolysis of water provides high-purity H_2 (99.99%), which is particularly relevant when hydrogen is used in fuel cells to avoid failures. Indeed, lower grade H_2 causes fuel cells replacements after few years, hence additional costs are gained. Similar high grade hydrogen cannot be achieved by steam reforming of fossil fuels [140]. Hydrogen generated by electrolysis is currently more expensive than that derived from the steam reforming reaction, since investment cost for electrolyzers is still high. The main types of electrolyzer consist in alkaline, proton exchange membrane and solid oxide.

- Synthesized hydrogen carriers: since the containment of H_2 is particularly challenging, hydrogen can be indirectly produced as synthesized H_2 carriers (methanol, ammonia and synthetic fuels), which successively deliver it during preliminary reforming reactions [141] or the combustion process [139].

In recent years, the global production of H_2 reached 65 million tons per year, with about 48% coming from the steam reforming of methane, 30% from oil, 18% from coal and only 4% from electrolysis [140]. However, some countries produce H_2 almost entirely by electrolysis,

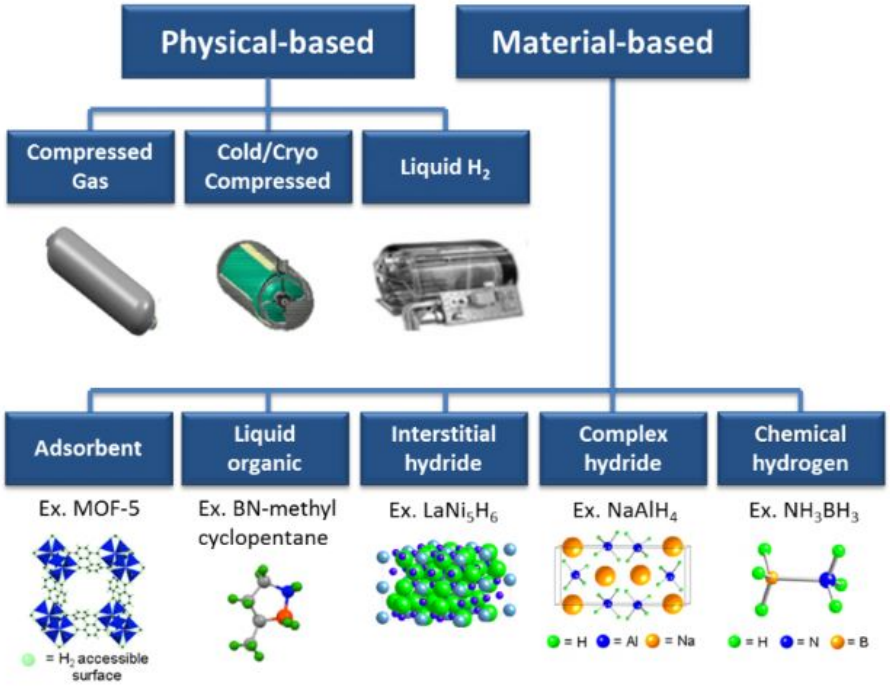

Fig. 4.9 H_2 storage systems [22].

e.g. Norway. According to Züttel [142], H_2 can be stored in 6 different ways (refer to figure 4.9) [22]:

- Compressed H_2: gaseous hydrogen is normally stored in high-pressure cylindrical tanks at 350 or 700 bar and ambient temperature [143]. Due to the extremely high pressure levels adopted, tanks dealing with particularly thick skin are necessary to avoid explosion hazards. Type 4 tanks made of polymeric materials incorporating carbon-fibers let wall-thickness reduction [144]. Nevertheless, high pressure levels determine high volumes required onboard for H_2 storage, because of the low MJ/M^3 energy density obtained. In case of storage below deck, strict regulations regarding ventilation are necessary to avoid accumulation within the engine room [145]. By an economical point of view, costs around 400-2100$ per kg of hydrogen stored [146] are achieved by compressed H_2. Compressed H_2 at 700 bar is currently used for terrestrial Fuel-Cell Electrical Vehicles (FCEV), whereas hydrogen fueled buses are equipped with 350-bar tanks [140]. Recently, two hydrogen-powered ferries from the Norwegian shipowner Torghatten Nord will enter into service in the next months. Specifically, CO_2 emissions will be reduced by fuel cells fed by a minimum 85% green hydrogen content and reciprocating engines running on CH_4-hydrogen blends. These two ferries will be equipped with compressed H_2 storage systems [147].

- Liquid hydrogen: hydrogen is stored as liquid in cryogenic tanks maintaining a temperature of -253 °C at least [148]. Since only 20 °C separate the storage temperature from the absolute zero (i.e. -273.15 °C), the liquefaction process is particularly high-energy consuming and traditionally performed with gas expansion techniques [142]. Liquid H_2 deals with higher energy density in MJ/m^3 than compressed hydrogen [149], hence it represents the most widely used solution for H_2 storage. By an economical feasibility point of view, costs for liquid H_2 are comprised within the range 20-400$ per kg of hydrogen stored [150], with consequent benefits in comparison to compressed H_2 systems. Recently, MSC and Fincantieri announced the construction of two cruise vessels (i.e. Explora V and VI) powered by 6 MW fuel cells running on hydrogen. Specifically, emissions-free power for the hotel services will be enabled in port and each ship will sport a containment system for liquid hydrogen. Explora V and VI are expected to be operational in 2027 and 2028, respectively [151]. Analogously, the MF Hydra ferry from the Norled A/S will enter into service in Norway. It will be the first liquid hydrogen-powered ferry, equipped by two 200kW fuel cells from Ballard Power Systems.

- Cryo-compressed hydrogen: is a compromise of the two previous solutions, i.e. compressed H_2 and liquid H_2

- Absorbed hydrogen in materials dealing with a large specific surface area: specifically, metal-organic frameworks (MOFs) are two- or three-dimensional porous crystalline materials which are characterized by approximately infinite lattices. Thus, ultra-high surface area ($\geq 2500\ m^2/g$) is available [152, 153].

- Absorbed in metal hydrides: hydrogen can be stored in metal hydrides, in a very space efficient way. Specifically, the small dimension of H_2 molecules allows for storage in interstizial space of metal hydrides [154, 155]. However, the energy density by unitary weight is relatively low (i.e. 5-7%), with consequent high weights installed onboard and drawbacks for ship stability. Thus, hydrogen storage in hydrides is traditionally used only for submarines, where increase in weight reveals useful for underwater operation. The release of H_2 from the hydride matrix can be simply obtained by heat exchange with low temperature sources (≈200 °C). Costs for metal hydride storage are 200-750 $ for 10 m^3 of H_2 stored [156].

- Reforming: hydrocarbons can be considered as hydrogen chemical storage, able to successively deliver H_2 by steam reforming and water gas shifting reactions.

Regarding the ability to use hydrogen in prime movers, it can potentially be use in GTs, reciprocating engines and fuel cells. Specifically, in recent years, research activity from GT manufacturers targeted fuel flexibility enhancement and developed new design procedures to face challenges arising from burning H_2 [157, 158]. Specifically, since the laminar flame speed of hydrogen in stoichometric mixtures is an order of magnitude greater than that of CH_4, burners need to be carefully designed to avoid the flame propagating upstream from the combustion zone into the premixing zone (flash back). At the same time, lean homogeneous mixtures are needed to limit rapid NO_x formation, which are negatively affected by H_2 due to its high adiabatic flame temperature. Furthermore, nearly triple volumetric flows need to be conveyed by the fuel feeding system when operating on 100% H_2, in comparison to natural gas, due to the low volumetric energy content provided by hydrogen. For these reasons, advanced Dry Low NO_x (DLN) combustors were developed for hydrogen-enriched fuels considering hydrogen volumetric concentration up to 85% [157, 158]. They resulted able to guarantee stable lean-premixed combustion at part-loads without exceeding regulation limits on NO_x emissions. Particularly, in order to enable fast premixing process and reach high level of homogeneity for the mixture, GE designed the DLN 2.6e burner based on small-scale jet-in-crossflow mixing. Siemens developed a similar burner to face combustion instability and thermal NO_x formation for blends containing up to 65% hydrogen [158], whereas Ansaldo Energia [159, 160] and Mitsubishi [161] developed sequential combustors and ammonia cracking combustors, respectively, for the same purpose. Alternatively to DLN combustors, wet combustion can be performed to lower the NO_x formation when H_2 is burned in GTs. Since thermodynamic properties and density of steam are quite different from those of air, Wet Lean NO_x (WLN) combustion significantly affects GT performance. Combustion systems based on H_2-rich fuel dilution by steam, water (WLN) or nitrogen were investigated by Chiesa et al. [162] and three main control strategies were identified to maintain high performance, depending on maximum temperature, inlet guide vane position or compressor pressure ratio.

On the other hand, reciprocating engines fed by CH_4-H_2 blends are currently under experimental tests by the major manufacturer companies in the maritime field [163, 164]. Overall, a maximum 30% volumic content of hydrogen has been considered by manufacturers [165]. Recent works in the literature found out a nearly 2% electrical efficiency increase while feeding spark and compressed ignited engines with CH_4-H_2 blends [166–169]. However, Sandalci et al. [170] and Karagöz et al. [171] underlined that optimization of control maps is required in compressed ignited engines to gain benefits in terms of electrical efficiency, otherwise drawbacks in combustion performance may occur. This agrees with experimental results concerning H_2 injection into DF and NG engines found out by Wärtsilä [165]. Fur-

thermore, Chen et al. [172] and Mariani et al. [173] observed that feeding reciprocating engines with CH_4-H_2 blends provides a 5% increase in all the cylinder temperature levels, with a consequent +30% on NO_x emissions [174, 173].
Finally, fuel cells are currently receiving great attention as possible hydrogen users, since they are able to generate electricity through H_2 and O_2 electrochemical reaction. However, only small size fuel cells currently appear viable, due to their particularly low energy density in kWh/m^3.
Focusing on the existing applications in the maritime sector, many pilot projects installing hydrogen-fed prime movers onboard ships were developed in recent years. As a result of the industrial cooperation initiated in 2003 by DNV, Eidesvik, Wärtsilä and MTU, a 330 kW fuel cell system was installed on the supply vessel Viking Lady and regularly operated for approximately 18500 hours: 52% electrical efficiency was developed at full load and low-emissions were surveyed. Hydrogen is currently burned in PEM fuel cells installed on board Type 212 submarines operating in the Germany and Italian Navies. The size of the fuel cell stack is around 120 kW, whereas more than 14 days underwater operation is guaranteed by H_2 storage in metal hydrides [140]. In 2017, a zero-emission ferry for Scandlines' Vogelfluglinie sailing at 17 knots between Puttgarden (Germany) and Rødby (Denmark), was designed including 8.3 MW high-temperature fuel cells. Hydrogen is stored in 140 m^3 C-type tanks and provide 48 hours endurance. A 2.4 MWh battery system was additionally installed onboard, since high temperature fuel cells provide slow response to load variations and excess power with respect to demand is often generated [175]. The ship builder estimated that only 25% increase in investment cost would be reached in comparison to conventional technologies [176]. However, by an infrastructural and logistics point of view, rare hydrogen bunkering stations for maritime usage are available within ports of countries in the forefront [177].

FUEL	**Energy density** [MJ/kg]	**Energy density** [GJ/m^3]	**Storage Pressure** [bar]	**Storage Temperature** [$°C$]	**Density** [kg/m^3]
MGO	42.8	36.6	1	15	890
LNG	50	23.4	1	-162	423
CH_3OH	19.9	15.8	1	15	805
NH_3	18.6	12.7	1	-34	683
Liquid H_2	120	8.5	1	-253	71
Compressed H_2	120	7.5	700	15	42

Table 4.3 Comparison between fuels for ship propulsion [35].

Color, odor	colorless, pungent
Toxicity	Toxic
Density	0.703 g/l (1 atm, 25 °C)
Boiling point	-33 °C
LHV	18.8 MJ/kg
Adiabatic flame temperature	1800 °C
Flammability	15-28%
Laminar flame velocity	0.015 m/s
Auto ignition temperature	651 °C
Octane number	>130

Table 4.4 Chemical and physical properties of ammonia [36].

4.5 Ammonia (NH_3)

Ammonia was firstly used as fuel during the World War II, when a shortage of Diesel fuel occurred in the US. Nowadays, ammonia is mostly used as fertilizer in agriculture [178]. Where ammonia production from renewable energy sources is concerned, production plants located in Norway exist for at least 40 years [178], hence proving the feasibility of green ammonia. On the other hand, the application of ammonia in the maritime sector for vessel propulsion has recently sparked interest as a part of the IMO solution within a GHG reduction strategy. Combustion of ammonia can take place independently into gas turbines, reciprocating engines and fuel cells [179]. Ammonia storage is well established by a technical point of view and derives from the NH_3 carriers know-how. Thermodynamic conditions of the stored NH_3 stay below the boiling point temperature, which coincides with -33 °C. Thus, differently from liquid H_2, minimal cooling is required for maintaining temperature in the storage system [178]. Ammonia can be used as a fuel itself or as hydrogen carrier. In the second case, ammonia is decomposed into N_2 and H_2 through a reformer included within the engine room, and then hydrogen is conveyed to prime movers [180, 181]. The main properties of ammonia are reported in table 4.4. As can be seen, the energy density in MJ/m^3 of ammonia is significantly higher than that of H_2, hence more space for the payload is available onboard. However, one of the major barriers which limited the use of ammonia as a fuel for ships consists in its toxicity. Indeed, low concentrations of NH_3 ($\leq 1700 ppm$) may cause coughing, whereas higher ones ($\geq 2500 ppm$) lead to death [182, 183]. Thus, specific measures are needed to avoid NH_3 leakage onboard vessels in addition to standard safety requirements. For the same reasons, maintenance activities can be problematic, since they represents a safety risk for both workers and crew on board. Furthermore, leaking of NH_3 into the sea could definitely damage the marine biological environment, since ammonia presents comparable comparable density with respect to water, hence they may easily mix. Ammonia is not odorless, hence low concentrations can be detected by humans. NH_3 deals

with narrow flammability range coupled with high energy levels necessary to ignite it, with consequent lower explosion risks in comparison to other alternative fuels. Energy to ignite NH_3 is traditionally provided by Diesel oil or, more often, by hydrogen generated through cracking NH_3 molecules, such the pilot flame is always lighted on to stabilize combustion [184]. Where the environmental point of view is concerned, low flammability implies real risk for NH_3 unburned emissions. Furthermore, due to the nitrogen content in the NH_3 molecule, higher NO_x emissions are produced compared to traditional fuels (HFO, MDO), hence selective catalytic reduction is necessary to comply with the IMO Tier III regulation. However, no CO_2 emissions are provided by NH_3 combustion, since no carbon content is chemically present in ammonia. Finally, due to the corrosive properties of NH_3, fuel supply and power generation system have to be designed without materials such as brass, titanium, copper and zinc alloys, rubber and neoprene [185].

Methods for producing NH_3 mainly distinguish for the source of the H_2 content [185]. Nowadays, almost the entire NH_3 commercially available is synthesized by means of hydrogen reformed from methane (48%), oil (30%) or coal (18%), within conventional Haber Bosch plants [186]. Other production systems for H_2 currently cover minor amount of NH_3 (4%). Depending on the energy source used to produce H_2, NH_3 is named gray, blue or green. Specifically, gray ammonia is produced by fossil fuels with no carbon capture included, whereas blue ammonia maintains the same H_2 source but considers CO_2 sequestration. Finally, green ammonia uses electricity from renewable energy sources to produce H_2 by electrolysis [187]. Though grey ammonia currently dominates, future investments in renewable energies can significantly increase the green NH_3 contribute [178]. This would be a key point from an environmental point of view, since 1.8% of global CO_2 emissions derives from ammonia production [188].

Regarding the ability o burn ammonia into prime movers, the first tests on NH_3 combustion in GTs were developed during the 1960's [189–191], proving that higher ignition energy is necessary to burn NH_3, owing to its low reactivity. Successive tests showed that the slow chemical reaction rate of ammonia requires reduced flow velocity within the combustion chamber [192], with negative effects on turbulent mixing [191]. Furthermore, experiments conducted by Solar and UC Berkeley found out similar performances when burning NH_3 and JP-4 [193]. In order to optimize performances, two GT control schedules were tested. First, injecting into the combustion chamber an ammonia mass flow rate corresponding to the JP-4 energy input yielded lower turbine inlet temperature and similar power output. Second, keeping constant the turbine inlet temperature provided nearly 10% higher power and, consequently, higher electrical efficiencies. Recently, similar experimental campaign on NH_3-fed GTs was carried out by the Italian company ENEL and benefits in terms of power

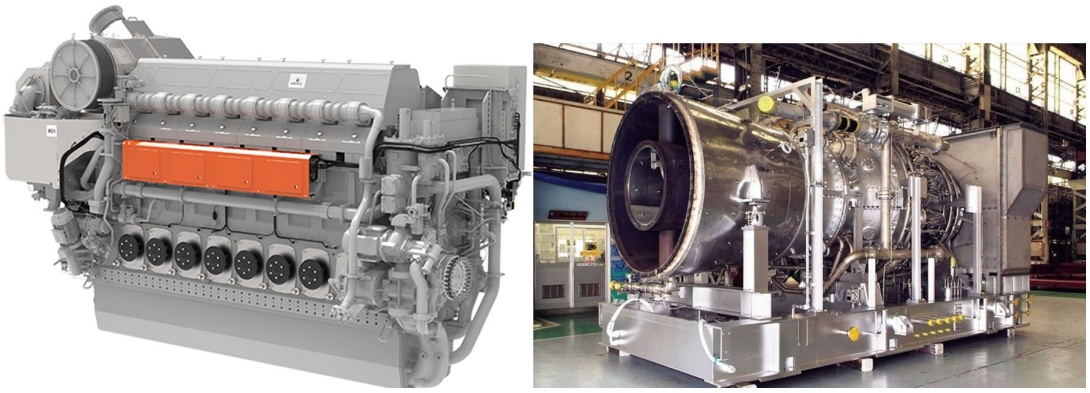

Fig. 4.10 The Wärtsilä 25 engine (left), used by Wärtsilä to develop ammonia combustion technology (technology concept readiness slated for 2023) and the 100% ammonia capable H-25 series from Mitsubishi Power (right).

production and efficiency were confirmed, though high NO_x emissions were obtained [194]. On the other hand, the main manufacturer companies producing marine engines are currently carrying out research on ammonia combustion. From research activities, MAN claimed that some DF engines can burn ammonia with few modifications [195]. Similarly, Wärtsilä has recently started to test ammonia combustion in reciprocating engines in collaboration with ownerships [196]. However, reciprocating engines running on ammonia are not commercially available yet, since experimental campaigns by manufacturers are still needed before installing them in full-scale vessels. Indeed, owing to the low combustion efficiency and higher flammability energy required by NH_3, a 5% electrical efficiency decrease occurs and all the temperatures levels within the cylinder are reduced by 13% [197]. Furthermore, due to the nitrogen content inside the NH_3 molecules, the amount of NO_x emissions reaches 2.5 times that of DF engines [198, 199, 185].

Where NH_3 fueled ships are concerned, in 2021 Yara International has signed an intention agreement with the trading company Trafigura Pte to both produce and commercialize green and blue ammonia as fuel in the marine sector [178].

Chapter 5

Batteries for ship propulsion applications

In the last few decades, even more strict regulations on emissions from the maritime sector have been enacted. In this context, hybrid-electric propulsion, based on including electrical energy storage onboard, is becoming a feasible solution to reduce emissions and enhance energy savings onboard (see figure 5.1). Many types of batteries are commercially available for electrical energy storage. Since energy and power densities determine potential and limits of different electrical energy storage systems, figure 5.2 shows their classification in a comparison perspective. In the following the main categories are analysed [200]:

- Lead-acid batteries: they are characterized by Pb anode and PbO_2 cathode immersed in an aqueous H_2SO_4 electrolyte. They represent one of the most popular, mature and cheap battery type within the transport and industrial sectors. In order to optimize volumes, battery stacks including 6-12 cells are formed, each delivering 12-24 V. Each cell capacity can reach 10000 Ah with charge/discharge efficiency around 70-85% [201]. Specific energy density of 15-40 Wh/kg is provided with increased weights and volumes. However they suffer from capacity reduction after low number of charging-discharging cycles (less than 500-1000), hence replacement is needed in 2-3 years [202]. Furthermore, they cannot be discharged more than 80% capacity.

- Ni-Cd batteries: often used in industrial and military sector, as well as on train. They ensure reliability for ambient temperature ranging from -50 to +60 °C. However, they present low charge/discharge efficiency (60-70%), low energy density (50-75 Wh/kg) high investment costs (1000 $\$/MWh$) and they must cope with strict disposal regulations due to pollution issues [203, 204]. Useful life approximately consists in 1500-2500 cycles [205].

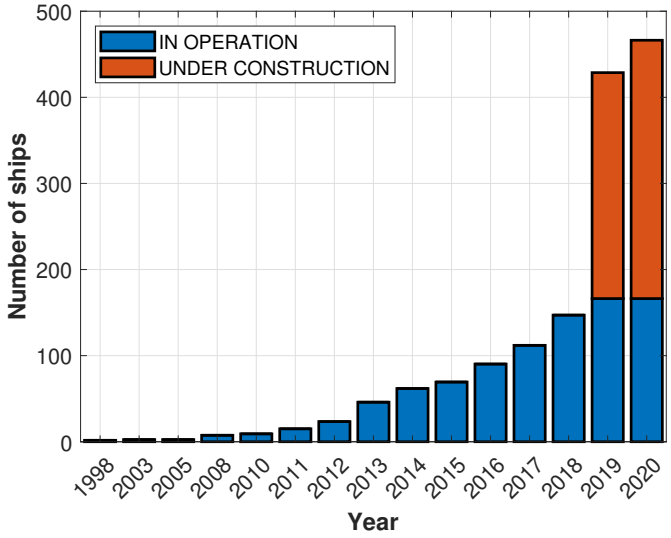

Fig. 5.1 Global growth for the number of ships equipped with hybrid-electric propulsion in recent years [23].

- Ni-metal hydrides (Ni-MH): they present similar features to Ni-Cd batteries, except for their reduced environmental impact and alkaline electrolyte. Ambient temperature range securing reliable operating conditions coincides with [-50 +70] °C, whereas efficiency is currently limited to 70-90% [206]. They require low investment cost and their useful life extends for 1200 charging/discharging cycles [204]. They were first applied to the power electronics field and for hybrid-electric transport.

- Flow batteries: they consist of electrochemical cell - accounting for anode, cathode and selective membrane - integrated with two tanks, each containing a distinct electrolyte. The main flow batteries are zinc bromide ZnBr and vanadium redox (see the schematic view reported in figure 5.3 for vanadium flow battery) [207]. Interestingly, as a main advantage, energy and power densities are governed by two different elements in flow batteries. Indeed, the volume of electrolyte tanks determines energy density, while materials and size of the electrochemical cell decide power density (i.e. voltage and current levels per unitary surface area). This feature of flow batteries makes them particularly suitable for large size electrical energy storage in the power generation field, where volumes can be significantly increased to match grid flexibility requirements [208]. However, two main penalties can be identified by an economic point of view: inclusion of circulation pumps and flow control systems imply higher maintenance costs; precious redox materials and electrocatalysts increase their investment cost [209, 205]. Though energy content per unitary weight is low (25 Wh/kg) and normal

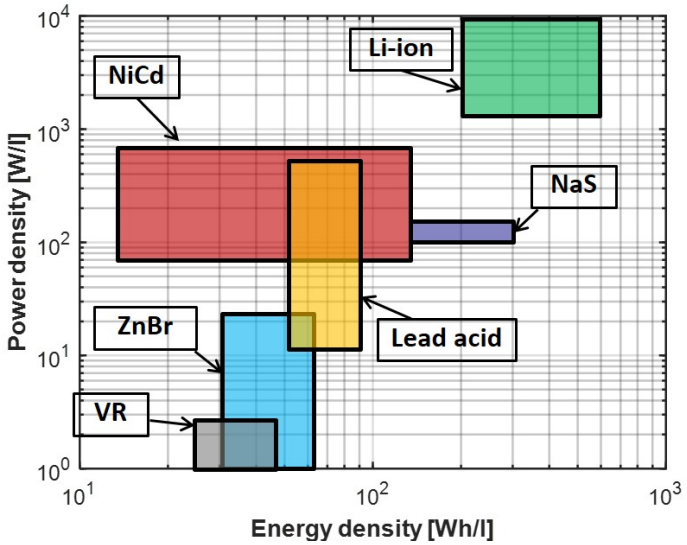

Fig. 5.2 Comparison between energy and power densities provided by different energy storage systems [24]. VR indicates vanadium redox flow batteries.

operation is ensured within strict range of ambient temperature (0-40 °C), useful life provided by flow batteries is particularly long (≈10000 cycles) [210, 211].

- Na/S batteries: they offer high redox potential thanks to sodium (-2.71 V), high energy density (150-240 Wh/kg), intermediate useful life (maximum 4500 cycles) and quite high charge/discharge efficiencies (75-90%) [205]. However, they require high working temperature (around 270 °C) and heating systems, since sodium becomes liquid above 98 °C. Furthermore, high capital costs are necessary (350€/kWh) [212]. They are used coupled with renewable power plants.

- Li-ion batteries: they represent the most promising battery type, due to their benefits in terms of high specific energy (≈ 90-250 Wh/kg, long useful life (1500-5000 cycles) and high charge/discharge efficiencies (85-98%) [213, 214]. Electrolyte is organic, either liquid or polymeric, whereas anode and cathode usually consist of lithiated graphite and lithium oxides, respectively. Safety, sustainability and circular economy of Li-ion batteries have been assessed by Mossali et al. [215] and Mauger et al. [216]. They are widely used in the power electronics, hybrid-electric transport and power generation fields.

Since they currently represent the most promising electrical energy storage technology for the hybrid-electric propulsion of ships, many works investigated the pros and cons of installing Li-ion batteries onboard ships [217]. Ancona et al. [218] formulated a genetic algorithm to

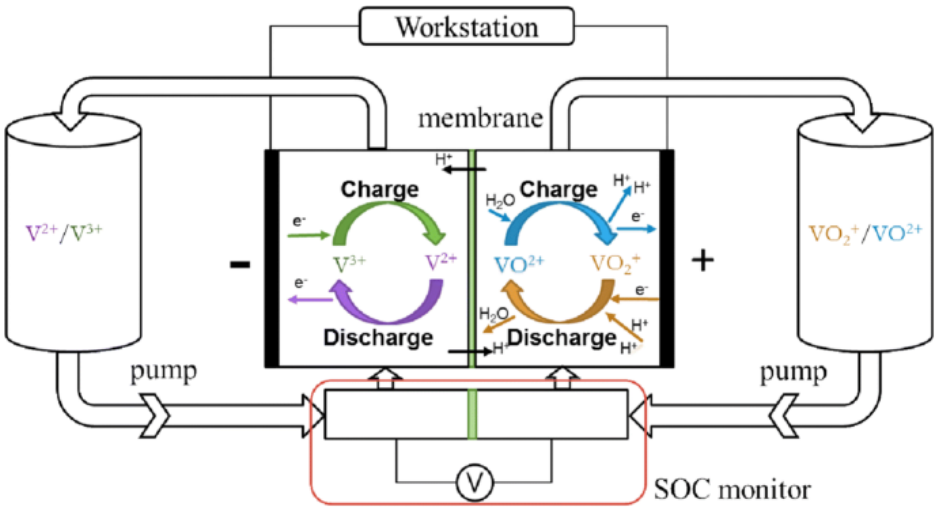

Fig. 5.3 Schematic view of the working principle for a vanadium redox flow battery [25].

optimally govern engine room including various energy sources, comprising Li-ion batteries, with the aim of minimizing the fuel consumption onboard a cruise vessel. Optimal design of oil tanker power plant including photovoltaic panels, Diesel generators and batteries was studied by Lan et al. [219]. Both costs and CO_2 emissions were considered as objective functions. Misyris et al. [220] introduced a system identification approach to estimate the state of charge (SOC) for batteries installed onboard, whereas potential of 14% reduction in CO_2 equivalent emissions was found by Dedes et al. [221] for bulk carriers powered by batteries and Diesel engines. However, few works exist in the literature warning that energy efficiency of the engine room can be maximized only adapting battery capacity to specific mission profiles [222, 223]. With the aim of increasing their useful life or grid energy savings, various studies proposed specific control strategies of batteries to perform peak-shaving and spinning-reserve [224–227]. By a prototype point of view, the MF Ampere project first investigated the feasibility of fully electric ships [228]. Nowadays, some battery packs are currently installed onboard cruise ships [229], to cover weak fluctuations of electrical power demands, or onboard submarines [230, 231], to guarantee propulsion under air-independent operation.

Chapter 6

Dynamic models

Dynamic modeling of power plants installed onboard ships represents a necessary tool for at least three primary reasons:

- the theoretical assessment of the dynamic behaviour of the power plant under time-dependent ship operating conditions. Specifically, increasingly strict environmental regulations on pollutant and GHG emissions require accurate measurements and modeling of prime mover operating conditions.
- defining and testing the control system, in order to ensure precise governing strategy for prime movers. Thus, safe component operation is guaranteed and risks for either electrical or mechanical failures onboard caused by unbalanced power are reduced.
- the investigation of the start-up and shut-down procedures for every prime mover. This provides useful insights on thermo-fluidynamics phenomena, such as surge, which may occur during strong transient acceleration and deceleration conditions.

Where COmbined Electric and Steam (COGES) power plants are concerned, they include many components, each governed by peculiar working principles. Thus, accurately assessing the operating conditions of COGES plants is particularly challenging and comprises various variables to be monitored. Therefore, in the last decades significant efforts have been paid by the scientific community to develop models aimed at predicting dynamic and transient operating conditions of gas-steam combined cycles. Dynamic simulation strategies for gas turbines were first introduced by Fawke et al. [232], whereas Schobeiri et al. [233] focused their attention on 1-D modeling of turbomacinery and combustors. A detailed description of the transient phenomena induced within surge working conditions for gas

turbines was assessed by Pilidis and Macallum [234] and Garrard [235]. A modular tool for microturbine simulation in conventional and innovative configurations was developed by Traverso [26]. Since characteristic maps of most components are usually not available from the manufacturers, both physically-based models and transfer function approaches have been developed within the literature. Kim et al. [236] found out that turbomachinery map scalings resulting from performance adaptation approaches can efficiently reproduce aeroengine transient performances as well as improve thermal control loops installed within them. Similarly, improvements in performance prediction and diagnostics for GTs obtainable from novel compressor map tuning methods were shown by Tsoutsanis et al. [237], whereas benefits deriving from a linearization approach were investigated by Hadroug et al. [238]. Wang et al. [239] compared physically-based models of fuel feeding systems for GTs with transfer function methods and concluded that higher accuracy can be reached by ODEs equations. In order to realize safe and efficient operation of gas-steam combined cycles, fast Model Predictive Control (MPC) was successfully adopted by Hou et al. [240] and Rua et al. [241], both by a thermodynamic and structural integrity point of view. In the recent few years, also machine learning techniques have been applied to dynamic modeling. Specifically, black or gray box approaches were implemented to investigate GT dynamics [242, 243] or for maintenance prediction purposes [244]. Where dynamic models for steam power plants are concerned, Cooke [245] was one of the first to predict the stage-by-stage pressure drops in a back-pressure steam turbines operating in off-design conditions by means of the Stodola's Ellipse Law. A mixed algebraic-differential mathematical framework was developed by Ray [246] to physically represent various ST configurations and similar lumped volume approach was applied by Zhao et al. [247] for steam power plants coupled within the nuclear power generation field. Similarly, a nonlinear, semi-empirical model of large-size steam turbine were developed in Chaibakhsh and Ghaffari [248], whereas time-dependent behaviour of HRSGs installed within combined cycles was analytically investigated by Alobaid et al. [249]. Crosa et al. [250, 251] performed the dynamic simulation of a combined cycle based on a 65 MW heavy-duty gas turbine reproducing the compressor and turbine operating conditions by means of a stage by stage numerical scheme. No mutual interaction between speed and exhaust temperature control loops were accounted for, since the entire model was linearized. More recently, a dynamic simulation tool for combined power plants equipped with one pressure level HRSG was implemented in Dymola by Benato et al. [252] aiming to address thermo-mechanical fatigue. Where steam turbine control systems are concerned, Pondin et al. [253] proved that that novel actuation technologies are required to meet fast-load cycling of combined cycles within the current power generation sector. Beiron et al. [254] analysed the economic feasibility of Combined Heat and Power (CHP) cycles, showing that higher

cost savings can be obtained improving flexibility on electrical and thermal power supply. Similarly, Sun et al. [255] proved that lowering steam turbine inlet temperature for 5-7% with respect to nominal value implies larger amount of power from CHP under flexible operating conditions. Within a combined cycle flexibility study, time-dependent response of once-through and natural circulation evaporator included within HRSGs was compared by Mertens et al. [256].

6.1 Matlab/Simulink code

In this thesis, a flexible and modular tool for the dynamic simulation of COmbined Gas Electric and Steam (COGES) plants has been developed in MATLAB/Simulink. The program is mainly divided into two parts, assessing different issues. Specifically, the first part is developed in MATLAB and aims at obtaining the entire thermodynamic performance of commercially available GTs in nominal operating conditions, not available from manufacturers. On the other hand, the second part is developed in MATLAB/Simulink and aims to reproduce time-dependent behaviour of combined gas-steam power plants, focusing the attention on different control strategies governing the gas turbine engine. Nevertheless, aeroderivative architecture for GT is analysed, since it is traditionally used in marine applications, as mentioned above. In the following sections, both parts are presented.

6.1.1 Matlab code: nominal conditions reconstruction

GT manufacturers generally publish only global performance data in nominal operating conditions, such as net power P_{net}, electrical efficiency η_{el}, exhaust gas temperature T_{ex} and air mass flow rate $\dot{m}_a$. However, complete information on thermodynamic parameters in nominal operating conditions is necessary to accurately simulate GT dynamic behaviour. Thus, in order to obtain information not available within technical sheets of GT manufacturers, the entire thermodynamic performances of commercially available gas turbines under nominal conditions of load, ambient temperature and fuel are reconstructed through a two-step optimization procedure. Precisely, GT nominal conditions refer to 100% load, 15 °C ambient temperature and natural gas feeding system. A schematic view of the algorithm underlying the code is shown in figure 6.1 for clearness. Firstly, a thermodynamic cycle is computed to initialize the optimization procedure. Solution of thermodynamic cycle is grounded on the following assumptions:

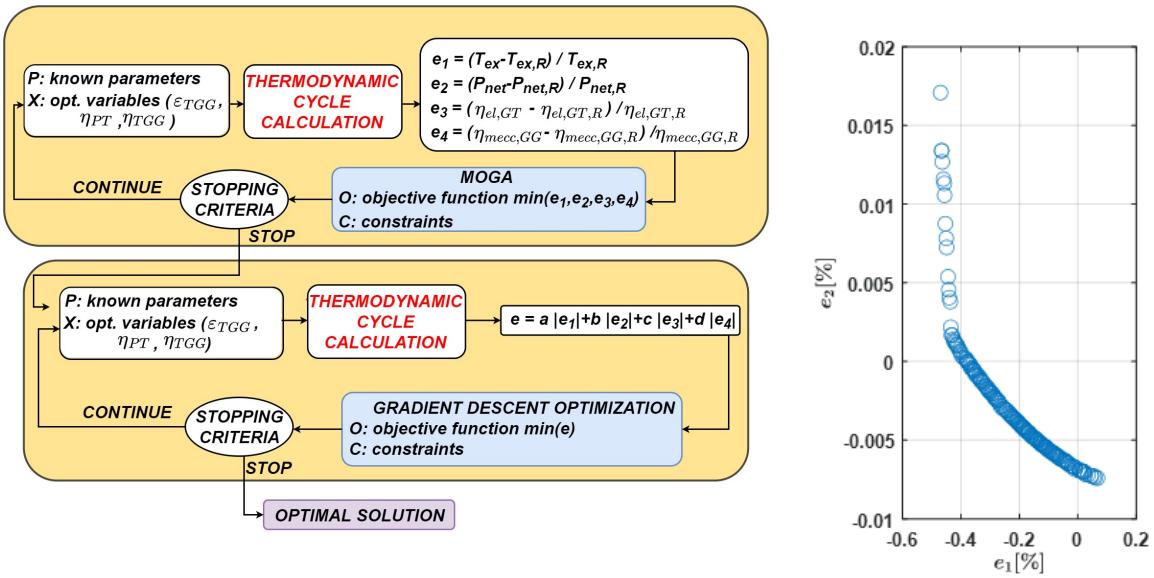

Fig. 6.1 Optimization scheme for GT performance reconstruction (left) and example of Pareto front obtained (right).

- Fluid coincident with air (ideal gas)
- Adiabatic turbomachines
- Thermodynamic transformations are considered globally, with solution computed only at inlet and outlet sections

Thermodynamic properties have been assessed by means of the open source software Coolprop and they all refer to the total states of the working fluids. Inputs required from the thermodynamic cycle computation are yielded from data sheets and consist of:

- P: operational parameters known from the manufacturer (β_c, $\dot{m}_a$, P_{net}, η_{el}, ...)
- X: optimization variables, coinciding with η_{TGG}, η_{PT}, ε_{TGG}. Their values are not known a priori, thus the purpose of the optimization procedure is to find out them by minimizing certain objective function.

The relationships used for the gas turbine cycle computation are summarised below (see figure 6.2 for nomenclature):

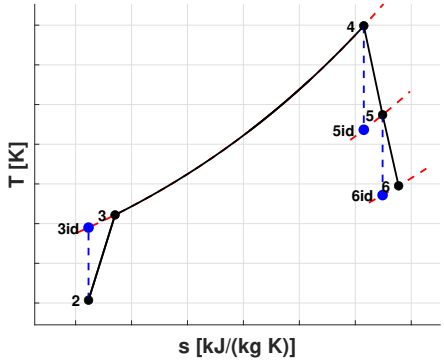

Fig. 6.2 Nomenclature for thermodynamic cycle of aeroderivative gas turbine.

- Point 2:

$$\begin{aligned} T_2 &= T_{amb} \\ p_2 &= p_{amb} \\ s_2 &= s(T_2, p_2) \\ h_2 &= h(T_2, p_2) \end{aligned} \tag{6.1}$$

- Point 3:

$$\begin{aligned} s_{3id} &= s_2 \\ p_3 &= \beta_c p_2 \\ h_{3id} &= h(s_{3id}, p_3) \\ h_3 &= h_2 + (h_{3id} - h_2)/\eta_c \\ s_3 &= S(h_3, p_3) \\ T_3 &= T(h_3, p_3) \end{aligned} \tag{6.2}$$

- Point 4:

$$\begin{aligned} h_4 &= (\dot{m}_a h_3 + \dot{m}_f LHV\, \eta_{CC})/(\dot{m}_a + \dot{m}_f) \\ p_4 &= p_3/\varepsilon_{CC} \\ T_4 &= T(h_4, p_4) \\ s_4 &= s(h_4, p_4) \end{aligned} \tag{6.3}$$

- Point 5:

$$\begin{aligned} p_5 &= p_4/\varepsilon_{TGG} \\ \varepsilon_{PT} &= p_5/p_6 \\ s_{5id} &= s_4 \\ h_{5id} &= h(S_{sid}, p_5) \\ h_5 &= (h_{5id} - h_4)\eta_{TGG} + h_4 \\ s_5 &= s(h_5, p_5) \\ T_5 &= T(h_5, p_5) \end{aligned} \tag{6.4}$$

- Point 6:

$$\begin{aligned} s_{6id} &= s_5 \\ h_{6id} &= h(s_{6id}, p_6) \\ h_6 &= (h_{6id} - h_5)\eta_{PT} + h_5 \\ s_6 &= S(h_6, p_6) \\ T_6 &= T(h_6, p_6) \end{aligned} \tag{6.5}$$

- Global relations:

$$\begin{aligned} T_{ex} &= T_6 \\ P_{net} &= (\dot{m}_f + \dot{m}_a)(h_5 - h_6)\eta_{mecc}\eta_a \\ \eta_{el} &= P_{net}/(\dot{m}_f LHV) \\ \eta_{GG,mecc} &= \dot{m}_a(h_3 - h_2)/((\dot{m}_f + \dot{m}_a)(h_4 - h_5)) \end{aligned} \tag{6.6}$$

As a main result from cycle computation, the global performance parameters, whose real values are traditionally available from the manufacturers (i.e. P_{net}, η_{el}, T_{ex}, η_{mecc}) are obtained. Since the first-hypothesis values for the optimization variables X are initially considered, the computed global performance parameters in all probability do not coincide with the reference ones reported in datasheets. For this reason, all the thermodynamic parameters yielded by the preliminary calculation are successively used as initial conditions for a two-step optimization process, aimed at minimizing the existing gap which arises between computed and reference values of P_{net}, η_{el}, T_{ex} and η_{mecc}.
The first step of the optimization process consists in formulating a Multi-Objective Genetic Algorithm (MOGA). In detail, the relative errors e_1, e_2, e_3 and e_4 defined as:

$$\begin{aligned} e_1 &= (P_{net,R} - P_{net})/P_{net,R} \\ e_2 &= (\eta_{el,R} - \eta_{el})/\eta_{el,R} \\ e_3 &= (T_{ex,R} - T_{ex})/T_{ex,R} \\ e_4 &= (\eta_{mecc,R} - \eta_{mecc})/\eta_{mecc,R} \end{aligned} \tag{6.7}$$

are considered as objective functions to be minimized by varying the optimization variables X within certain ranges. In eqs. (6.7) the subscript "R" refers to the reference values available from the manufacturers' datasheets. Variations of X are limited by constraints C, which represent both minimum-maximum values assumed from the literature and equations used in cycle computation (i.e. conservation equations and thermodynamic relations, e.g. $h = f(T, p)$). Positioning of the initial point within the (X_1, X_2, X_3) space is provided by cycle computation preliminary performed. Interestingly, in a genetic algorithm framework, a single combination of $X = (X_1, X_2, X_3)$ represents a gene of a certain individual, i.e. candidate thermodynamic

cycle corresponding to X. Furthermore, an ensemble of thermodynamic cycles consists in a generation, whereas more generations form a population. Therefore, summarising the working principle of MOGA, the algorithm starts identifying a population of individual dealing with various X combinations, then computes the corresponding thermodynamic cycles, checks the gap arising for objective functions and, finally, moves to a successive generation through mutation and crossover. Precisely, in order to explore the entire domain (Design Of Experiments, DOE), next generations are obtained by adopting many evolutionary strategies. Thus, a certain evolutionary strategy can prefer to minimize e_1 and let e_2 high and an other the opposite. The algorithm described above is iterated on many generations and, finally, the Pareto front, i.e. the ensemble of non-dominant solutions minimizing objective functions under different evolutionary strategies, is obtained. In figure 6.1 an example of Pareto front resulting from 50 generations computed by the MOGA algorithm for the LM2500 GT is reported. It must be underlined that figure 6.1 only focuses on the e_1 and e_2 errors to improve visualization, despite the full Pareto front develops in the 4-D space (e_1, e_2, e_3, e_4). Figure 6.1 clearly shows significantly low (<0.5%) relative errors e_1 and e_2, thus indicating the accuracy in reproducing reference nominal conditions. Analogous orders of magnitude for errors have been achieved for e_3 and e_4, independently from GT considered. The choice of the best solution from the Pareto front depends on user's priorities: a solution minimizing a specific subset of errors or providing comparable values of all the objective functions can be selected. Therefore, as a main result of the MOGA algorithm, the best individual is chosen by the user from the Pareto front and successively entered as input within the second step of the optimization procedure. Specifically, the solution space around the best individual obtained from the MOGA algorithm is explored by a gradient descent optimization procedure. It must be remarked that such a definition of the two-step optimization process allows to exploit the main benefits of both multi-objective and single objective optimization algorithms used. Indeed, the MOGA procedure ensures the exploration of the complete solution space (X_1, X_2, X_3), hence it may reliably determine the global minimum in the 4-D domain (e_1, e_2, e_3, e_4) discarding the local ones. Instead, the gradient descent optimization is more accurate than the MOGA in locally exploring the solution space (X_1, X_2, X_3) around the global minimum, such that the optimality of the solution for (e_1, e_2, e_3, e_4) found by MOGA is verified. Focusing on the second step of the optimization procedure, it consists in defining a single-objective gradient descent algorithm. Specifically, a single cost function taking into account all the relative errors for η_{el}, P_{net}, T_{ex} and η_{mecc} is formulated, as reported in eq. (6.8):

$$e_{tot} = w_1 |e_1| + w_2 |e_2| + w_3 |e_3| + w_4 |e_4| \tag{6.8}$$

where w_1, w_2, w_3 and w_4 represent weights, aimed at increasing or reducing the relevance of each relative error in the optimization convergence. As was for the MOGA, conservation equations and thermodynamic relations (i.e. $h = f(T,p)$, $s = f(T,p)$, ...) represent constraints to be satisfied. Firstly, the thermodynamic cycle is solved for the triple (X_1, X_2, X_3) related to the best individual resulted from MOGA. Then, eq. (6.8) is evaluated as the optimization algorithm slightly moves in the (X_1, X_2, X_3) space with the aim of further minimizing objective function (see figure 6.3). In case lower objective function is gained, the triple (X_1, X_2, X_3) becomes the new optimal solution as well as the new starting point within the X space for a successive iteration step. This process is repeated many times, in all the possible directions belonging to the $X = (\eta_{TGG}, \eta_{PT}, \varepsilon_{TGG})$ space (figure 6.3 illustrates the case of 1-D X space for simplicity). Figure 6.3 shows a schematic view of the operating conditions

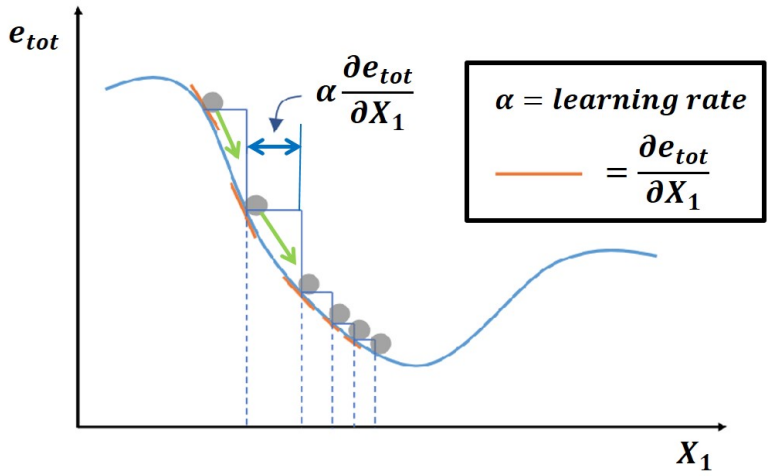

Fig. 6.3 Schematic view of the operating principle of a gradient descend algorithm.

underlying the gradient descent algorithm. The magnitude of the changes detected on the objective function determines the extent of the next moving step in (X_1, X_2, X_3). Specifically, reduced variations on e_{tot} imply lower moving steps, since the the objective function appears nearly flat around the global minimum. Finally, in case no reduction in objective function is achieved by successive moving steps, the global optimal solution is found. In particular, the entire GT thermodynamic cycle reproducing the global performance parameters provided by manufacturers as well as complying with both state-of-the-art values and physical relationships is known. Overall, the two-step optimization procedure is able to reconstruct GT nominal condition within 1% relative error for global performance parameters P_{net}, η_{el}, T_{ex} and η_{mecc}. The nominal condition found is successively used to initialize dynamic simulation of GTs, which is successively performed in Simulink by means of the code described in the following section.

6.1.2 MATLAB code: nominal conditions reconstruction under fuel flexible operating conditions

The reconstruction of the GT nominal operating condition illustrated in section 6.1.1 works in case the simulated gas turbine operates fed by the designed fuel (i.e. typically CH_4). On the other hand, when operating on hydrogen as well as on other alternative fuels, information concerning the GT performance at 100% load is not even partially present in technical datasheets from manufacturers. However, assessing the influence on the turbomachinery matching as well as changes concerning global performance parameters (P_{net}, η_{el}, ...) are of fundamental importance to address fuel flexibility. Towards this end, a MATLAB code aiming at reconstructing the full-load operating condition of GTs fed by alternative fuels, such as CH_4-H_2 blends, CH_3OH and NH_3, has been developed. has been developed. Since components do not change under fuel flexible conditions, their performance maps result unaffected. Indeed, it is well known from the main GT manufacturers that modern feeding systems can work on different fuels or, alternatively, only few changes are needed in the burner to enhance fuel flexibility [28, 131, 158]. In order to completely identify new component matching occurring at 100% GT load, the MATLAB code presented in this section implements a numerical optimization procedure based on Multi-Objective Genetic Algorithm (MOGA) coupled with a gradient descent algorithm. An overall view of the

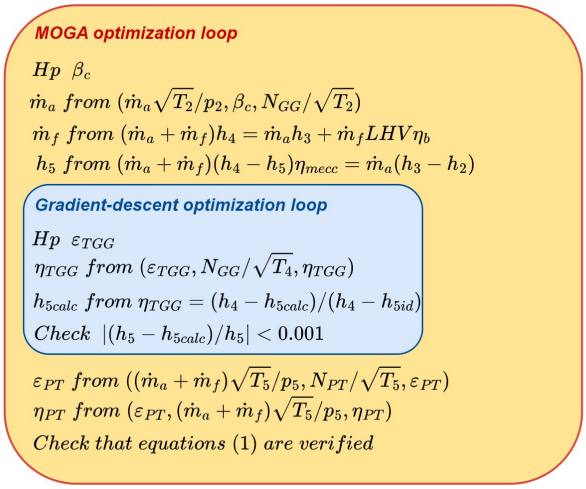

Fig. 6.4 Schematic view of the optimization procedure used to solve for the 100% load operating condition of GTs fed by alternative fuels.

numerical scheme adopted is shown in figure 6.4. The main hypotheses used are summarised below:

1. Gas generator and power turbines both working in choked conditions. This hypothesis is in good agreement with the traditional design procedure adopted by manufacturers, where choked conditions are always imposed to obtain higher performances from the expansion phases [257]. In choked condition, the mass flow rate through a turbine or nozzle can be only modified enabling throat area variation or increasing upstream energetic content of the flow (i.e. p or T), as stated by equation (6.9) for isentropic flows [258]:
$$\dot{m} = \frac{A_g p}{RT}\sqrt{k}\left(\frac{k+1}{2}\right)^{-\frac{k+1}{2(k-1)}} \tag{6.9}$$
where A_g represents the cross-flow area at the throat, R is the universal gas constant and k is the ratio between the specific calorific values at constant pressure and volume. In real accelerating transonic and supersonic flows eq. (6.9) is traditionally assumed valuable [257].

2. $k = c_p/c_v$ assumed constant with respect to chemical composition of exhaust gas. Since the amount of fuel used within gas turbines is nearly 1-2% of the air mass flow rate independently from feeding conditions, small variations on the exhaust gas composition is achieved by the combustion process. Therefore, slight variations on k can be effectively neglected with no accuracy issue.

3. Maximum cycle temperature T_4 is retained constant under fuel flexible feeding conditions, in order to preserve the thermo-mechanical integrity of the first rows of gas generator turbine.

4. The reduced mass flow rate $\dot{m}\sqrt{T}/p$ disposed of by turbine modules is considered unaffected by alternative fuels. Indeed, as mentioned above, turbines are designed to work in choked condition to maximize their adiabatic efficiency and no changes in turbomachinery geometry are required to operate on variable fuel [157]. Furthermore, k is assumed constant (see hypothesis 2). Therefore, the reduced mass flow rate result unaffected by fuel flexible operating conditions. The conservation of the reduced mass flow rate between CH_4 or alternative fuel feeding conditions for both turbine modules included in aeroderivative architectures is imposed:
$$\begin{aligned}
\frac{(\dot{m}_a+\dot{m}_f)\sqrt{T_4}}{p_4}\Big|_{H_2} &= \frac{(\dot{m}_a+\dot{m}_f)\sqrt{T_4}}{p_4}\Big|_{CH_4} \\
\frac{(\dot{m}_a+\dot{m}_f)\sqrt{T_5}}{p_5}\Big|_{H_2} &= \frac{(\dot{m}_a+\dot{m}_f)\sqrt{T_5}}{p_5}\Big|_{CH_4}
\end{aligned} \tag{6.10}$$

where $\dot{m}_a$ and $\dot{m}_f$ are the fuel and air mass flow rates, subscripts 4 and 6 indicate the inlet of GG and power turbine, respectively. Focusing on eqs. (6.10), since T_4 is retained constant (see hypothesis 3), the main parameters varying under fuel flexible operating conditions consist of p_4 and $\dot{m}_a + \dot{m}_f$. Interestingly, the overall mass flow rate $\dot{m}_a + \dot{m}_f$ directly depends on the LHV of the fuel, with consequent variations on p_4 needed.

5. Rotational speed of gas generator and power turbine shafts at 100% GT load unaffected by feeding conditions. Otherwise, the distance from over-speed limit can be exceeded, with negative consequences from a mechanical point of view. Thus, safe margin from the over-speed limit is guaranteed and increase in centrifugal forces experienced by rotor blades is avoided.

6. The Inlet Guide Vane is considered full-opened at 100% GT load independently from the fuel considered. This preserve the governing ability of IGV at part-loads.

Focusing on the numerical algorithm reported in figure 6.4, an external optimization loop aimed at computing the compressor operating point is performed by MOGA optimization, whereas a gradient descent procedure is applied internally to compute the corresponding matching between compressor and gas generator turbine. The first step shown in figure 6.4 consists in assuming a p_4, i.e. $beta_c$, preliminary value. Then, the reduced mass flow rate at compressor inlet is evaluated by the $(\dot{m}_a\sqrt{T_2}/p_2, \beta_c, \theta_{IGV}, N_c/\sqrt{T_2})$ characteristic map. Specifically, rotational speed as well as IGV angle are imposed by the hypotheses 5 and 6, respectively. From the reduced mass flow rate, the air flow $\dot{m}_a$ is computed for T_2 =15 °C and p_2 =1 atm. Similarly, the compressor efficiency η_c is derived from the corresponding map $(\dot{m}_a\sqrt{T_2}/p_2, \beta_c, \theta_{IGV}, \eta_c)$ using as inputs β_c, the IGV angle and the reduced mass flow rate within compressor. Enthalpy and entropy at the compressor inlet are computed by thermodynamic relations $h_2, s_2 = f(T_{amb}, p_{amb)}$. Then, enthalpy for the point 3 can be obtained:

$$h_3 = h_2 + (h_{3id} - h_2)/\eta_c \tag{6.11}$$

where $h_{3id} = f(p_3, s_2)$ represents enthalpy of the corresponding isoentropic state. At this stage, the hypothesised operating point of compressor is completely known. Successively, energy conservation within the combustion chamber:

$$(\dot{m}_a + \dot{m}_f)h_{o,cc} = \dot{m}_a h_{i,cc} + \dot{m}_f LHV\,\eta_{cc} \tag{6.12}$$

is solved for the fuel mass flow rate compatible with h_3, h_4 and LHV. Lower heating value in eq. (6.12) relates to alternative fuel, whereas h_4 and s_4 are computed as $f(p_4, T_4)$. It must be

remarked that p_4 is obtained from p_3 subtracting cold and hot total pressure losses within the combustion chamber, overall assumed equal to 5%. Thus, point 4 is entirely known. Successively, the enthalpy h_5 is derived from the power balance on the gas generator shaft between compressor and turbine:

$$(\dot{m}_a + \dot{m}_f)(h_4 - h_5)\eta_{TGG} = \dot{m}_a(h_3 - h_2)\eta_c \tag{6.13}$$

From now on, the internal optimization loop based on gradient descent algorithm is enabled to compute the operating condition of the gas generator turbine matching with the previously evaluated compressor point. Specifically, focusing on on the $(\varepsilon_{TGG}, N_{GG}/\sqrt{T_4}, (\dot{m}_a + \dot{m}_f)\sqrt{T_4}/p_4)$ GG turbine map, the expansion ratio ε_{TGG} can be found by interpolation. Indeed, rotational speed of GG and temperature T_4 are known from the mechanical and thermal resistance constraints, respectively (see hypothesis 4 and 5), as well as reduced mass flow rate is assumed equal to that occurring for methane to preserve adiabatic efficiency. However, since the gas generator turbine works in choking conditions, ε_{TGG} can not be found unequivocally, due to the non-bijective dependency existing between reduced mass flow rate and expansion ratio. Therefore, iterative procedure governed by gradient descent optimizer is necessary. Specifically, hypothesis on ε_{TGG} is first made and temperature T_5 is derived as $T_5 = f(h_5, p_5)$ (h_5 is known from eq. (6.13)). Then, ε_{TGG} and $N_{GG}/\sqrt{T_4}$ are used to interpolate GG turbine efficiency from the $(\varepsilon_{TGG}, N_{GG}/\sqrt{T_4}, \eta_{TGG})$ map. Since h_{5id} is known from the thermodynamic relation $h_{5id} = f(s_4, p_4)$, the definition of GG turbine efficiency is used to compute h_{5calc}, i.e. a check value of h_5:

$$\eta_{TGG} = (h_4 - h_{5calc})/(h_4 - h_{5id}) \tag{6.14}$$

At this point, h_5 deriving from the GG-shaft power balance and h_{5calc} related to the hypothesized value for ε_{TGG} are compared. In case $|(h_5 - h_{5calc})/h_5| \geq 10^{-3}$, the gradient descent optimizer moves to a different ε_{TGG} and iterates until convergence is reached. In this way, the mechanical and fluid dynamic matching between compressor and GG turbine is assured and point 5 is completely known. Finally, the power turbine module is solved. Specifically, since $(\dot{m}_a + \dot{m}_f)\sqrt{T_5}/p_5$ is known from the above steps and $N_{PT}/\sqrt{T_5}$ derives from hypotheses, the characteristic map $((\dot{m}_a + \dot{m}_f)\sqrt{T_5}/p_5, N_{PT}/\sqrt{T_5}, \varepsilon_{PT})$, is used to find the expansion ratio ε_{PT}. Then, the adiabatic efficiency of power turbine is obtained interpolating the $(\varepsilon_{PT}, (\dot{m}_a + \dot{m}_f)\sqrt{T_5}/p_5, \eta_{PT})$ map, whereas the exhaust gas enthalpy h_6 and temperature T_6 are computed by means of $\eta_{PT} = (h_5 - h_6)/(h_5 - h_{6id})$ and thermodynamic relation $T_6 = f(p_6, h_6)$, respectively. The net power delivered by GT at 100% load and its

corresponding electrical efficiency are obtained from:

$$P_{net} = (\dot{m}_f + \dot{m}_a)(h_5 - h_6)\eta_{mecc}\eta_a \tag{6.15}$$

$$\eta_{el} = \frac{P_{net}}{\dot{m}_f LHV} \tag{6.16}$$

At this point, the overall thermodynamic cycle of aeroderivative GT operating with alternative fuels is entirely solved through mechanical and fluid-dynamics compatibility equations. However, the constraints (6.10) on reduced mass flow rate within turbines have not been verified yet. Therefore, the equality (6.10) of the reduced mass flow rates resulting from the above procedure with the corresponding values referring to CH_4 feeding system is queried:

$$\begin{aligned} G_1 &= \frac{(\dot{m}_a + \dot{m}_f)\sqrt{T_4}}{p_4}|_{H_2} - \frac{(\dot{m}_a + \dot{m}_f)\sqrt{T_4}}{p_4}|_{CH_4} \\ G_2 &= \frac{(\dot{m}_a + \dot{m}_f)\sqrt{T_5}}{p_5}|_{H_2} - \frac{(\dot{m}_a + \dot{m}_f)\sqrt{T_5}}{p_5}|_{CH_4} \end{aligned} \tag{6.17}$$

In case numerical gaps arise in equations (6.17) (i.e. G_1 and G_2 exceed a certain threshold), the MOGA algorithm iterates on the pressure p_4 (i.e. β_c), which was initially hypothesised at the beginning of the procedure. Indeed, an equilibrium condition for the entire aeroderivative GT not satisfying eqs. (6.10) (i.e. hypotheses 1, 2 and 3) obtained. Objective functions for the MOGA algorithm consist in the relative errors E_1 and E_2 defined on the reduced mass flow rates:

$$\begin{aligned} E_1 &= \left(\frac{(\dot{m}_a + \dot{m}_f)\sqrt{T_4}}{p_4}|_{H_2} - \frac{(\dot{m}_a + \dot{m}_f)\sqrt{T_4}}{p_4}|_{CH_4}\right) \Big/ \frac{(\dot{m}_a + \dot{m}_f)\sqrt{T_4}}{p_4}|_{CH_4} \\ E_2 &= \left(\frac{(\dot{m}_a + \dot{m}_f)\sqrt{T_5}}{p_5}|_{H_2} - \frac{(\dot{m}_a + \dot{m}_f)\sqrt{T_5}}{p_5}|_{CH_4}\right) \Big/ \frac{(\dot{m}_a + \dot{m}_f)\sqrt{T_5}}{p_5}|_{CH_4}) \end{aligned} \tag{6.18}$$

whereas constraints coincide with thermodynamic relations, component maps and compatibility equations. Convergence threshold for the MOGA algorithm is fixed at 1% relative error on equations (6.18). In order to quantitatively assess variations in terms of nominal operating condition for GTs fed by alternative fuels, relative errors related to the main thermodynamic parameters are reported in table 6.1. Specifically, relative errors are defined as $(V_R - V_{af})/V_R$, where V_R and V_{af} are the values corresponding to methane and alternative fuel feeding conditions, respectively. As alternative fuels, CH_4-H_2 blends (with 85% of H_2 volumic content [157]), CH_3OH and NH_3 are considered in the analysis, whereas variations are assessed for the LM2500 gas turbine. In comparison with GT fed by pure CH_4, lower η_{el} and P_{net} are obtained for CH_4-H_2 blends, opposite to performances related to CH_3OH and NH_3. It must

Table 6.1 Alternative fuel effect on the GT performances. Nominal operating conditions: CH_4 fuel, T_{amb}=15°C, p_{amb}=1 atm, P_{net}=24.31 MW, η_{el}=36%, $\dot{m}_a+\dot{m}_f$=70.3 kg/s, T_{ex}=566°C

Parameter	CH_4-H_2	CH_3OH	NH_3
η_{el}	-0.1%	+1.6%	+1.7%
P_{net}	-1.3%	+6.8%	+7.6%
T_{ex}	+0.1%	-0.8%	-0.8%
$\dot{m}_f$	-38.0%	+160.6%	+181.0%
$\dot{m}_a$	0.0%	0.0%	0.0%
$\dot{m}_a+\dot{m}_f$	-0.7%	+3.1%	+3.5%
β_c	-0.7%	+3.1%	+3.2%
ε_{TGG}	+0.3%	-2.3%	-2.9%
ε_{PT}	-0.9%	+5.6%	+6.3%

be underlined that benefits and penalties provided by alternative fuels in terms of η_{el} and P_{net} well agree with experimental results available in the literature, obtained imposing T_4 equal to that provided by CH_4 [129, 130, 193, 194]. Overall, η_{el} and P_{net} results reported in table 6.1 appear to mainly derive from variations experienced by β_c and $\dot{m}_a+\dot{m}_f$ evolving within the turbine modules. Indeed, the strong differences in terms of LHV significantly affect the fuel mass flow rate required to achieved T_4. Specifically, since CH_3OH and NH_3 are characterized by lower energy content per unit mass, more fuel must be injected in the combustion chamber to keep T_4 unvaried, hence the mass flow rate $\dot{m}_a+\dot{m}_f$ evolving within TGG and PT increases and higher P_{net} is generated. Opposite to CH_3OH and NH_3 combustion processes, mass flow rate evolving within turbine modules is observed to reduce for CH_4-H_2 blends. However, small variations are surveyed for CH_4-H_2 mixtures with respect to the methane feeding condition. Indeed, high volumic concentrations of H_2 in CH_4-H_2 blends correspond to far lower mass percentage because of the low hydrogen density (e.g. 80% volumic concentration of H_2 corresponds to nearly 33% content in mass). Furthermore, table 6.1 shows how CH_3OH and NH_3 raise β_c. Globally, this moves the compressor point towards region dealing with higher η_c. As a consequence, reduced expansion ratio is required by TGG to drive compressor and more enthalpy in the fluid can be used to generate power in the power turbine. This also guarantees energy benefits in terms of η_{el}. For analogous reasons, an opposite behaviour is surveyed for CH_4-H_2 blends, due to β_c reduction. Finally, where CH_3OH and NH_3 feeding is concerned, it must be remarked that surge margin limit is not exceeded despite β_c increases at constant rotational speeds N_{GG} and N_{PT}. Thus, safety operating conditions are ensured for compressor.

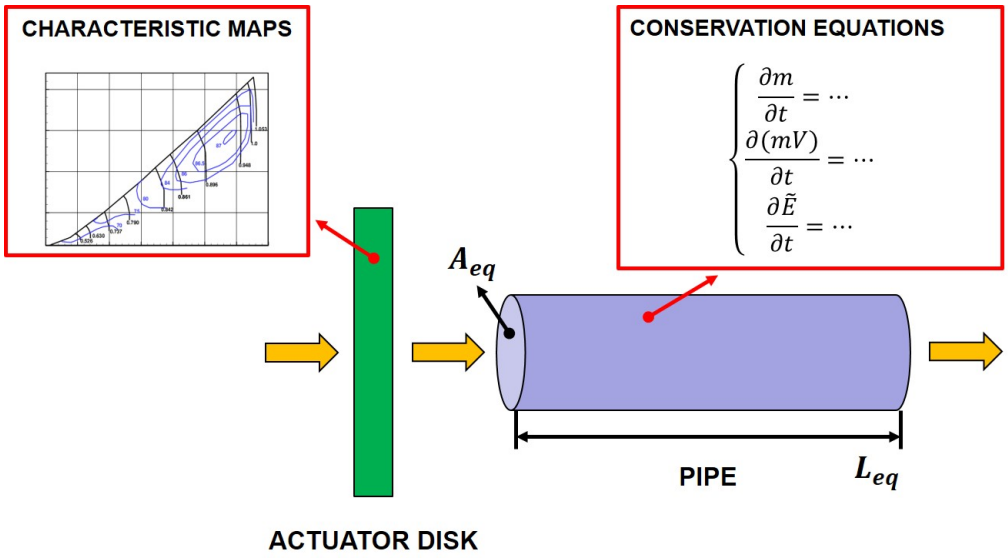

Fig. 6.5 Schematic view of the lumped volume approach [26].

6.2 Simulink code: dynamic simulation of COGES plants

The MATLAB/Simulink code used for dynamic simulating gas-steam combined power plants mainly consists of a nonlinear lumped volume model, despite few components of the steam power plant are based on a dynamic finite-difference approach. Specifically, a set of linear/nonlinear algebraic and partial/ordinary differential equations physically governing combined power plants is solved at each time step in order to investigate the transient operating condition of all the components. Where the lumped-volume models of components are concerned, the approach firstly developed in Traverso [26] is adopted in this thesis and reported in figure 6.5. Specifically, components modeled within a lumped volume approach are represented numerically by separating the quasi-static off-design performance from transient behavior. The first information is provided by an actuator disk, which provides a rigid response of the component to off-design operating conditions by means of performance maps involving the most relevant thermodynamic parameters. E.g. where turbomachinery components are concerned, the compressor working point is assessed through the maps $(\dot{m}_a\sqrt{T_2}/p_2, \beta_c, N_{GG}/\sqrt{T_2}, \theta_{IGV})$ and $(\eta_c, \beta_c, N_{GG}/\sqrt{T_2}, \theta_{IGV})$, as well as turbine static performances are obtained from $((\dot{m}_a + \dot{m}_f)\sqrt{T}/p, \varepsilon_t, N/\sqrt{T})$ and $(\eta_t, \varepsilon_t, N/\sqrt{T})$ diagrams [259]. The maps used in this thesis have been obtained from previous works available in the literature and successively scaled with respect to the nominal operating condition reconstructed according to section 6.1.1. Specifically, maps of machines dealing with size and architecture similar to those reproduced in this work have been used, hence dynamic

behaviour results comparable. Interestingly, maps do not introduce temporal information, i.e. time delays or dead times modeling thermal, mechanical and fluid inertia of components. Instead, transient behaviour is dynamically assessed by an equivalent duct, i.e. a duct characterized by cross-sectional area A_{eq} and length L_{eq} able to reproduce physical delays and dead-times. If the geometry of the component is known from CAD, A_{eq} and L_{eq} can be accurately estimated, otherwise they need to be evaluated from data available in the literature. The time-dependent behaviour of the equivalent duct is obtained by solving the conservation of mass, momentum and energy as reported in general form in equations (6.19), (6.20) and (6.21), respectively:

$$\frac{\partial}{\partial t}\int_{CV}\rho d\tilde{V}+\int_{CS}\rho V\cdot dA=0 \tag{6.19}$$

$$\frac{\partial(mV)}{\partial t}=\frac{\partial}{\partial t}\int_{CV}\rho V d\tilde{V}-\int_{CS}\rho V(V\cdot n)dA \tag{6.20}$$

$$\frac{\partial\tilde{E}}{\partial t}=\int_{CV}\frac{\partial\rho\tilde{e}}{\partial t}d\tilde{V}-\int_{CS}\rho\tilde{e}V\cdot ndA=\dot{q} \tag{6.21}$$

where U indicates 1-D flow velocity, $\tilde{E}$ total energy, $\tilde{e}$ total energy per unit of mass, ρ density, CV control volume, m mass, A surface and n the vector locally normal to the control surface. Furthermore, it must be underlined that the energy conservation equation is solved for both fluid and solid domains, hence both heat losses to the environment and thermal storage within the metal are accounted for [26]. Finally, superposition of the effects for the quasi-static and time-dependent performances is introduced to model the complete off-design behaviour of components. Indeed, the actuator disk responds rigidly to inputs, then the equivalent duct delays variations on mechanical and thermodynamic parameters. Where the interconnecting protocol between two adjacent components is concerned, interconnecting plena approach is adopted to regulate information flow, hence intermediate volumes have been inserted between adjacent components whose inputs/outputs do not numerically match. As was for the equivalent duct, conservation of energy, momentum and mass is solved within each interconnecting plena included in the model, whose volume is set to reproduce transition ducts existing between two adjacent components (e.g. between compressor and combustion chamber). Overall, the interconnecting plena approach guarantees that compatible boundary conditions are imposed in the entire model, avoiding numerical inconsistency or instability.

6.2.1 Dynamic model of gas turbines

A schematic view of the dynamic model for aeroderivative GTs is shown in figure 6.6. The following physical-based subsystems can be identified:

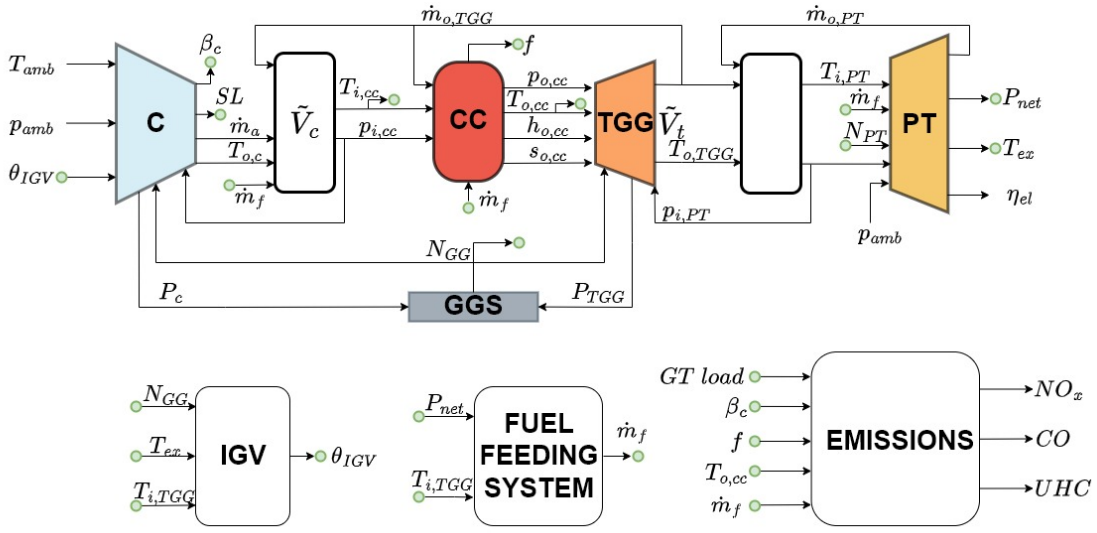

Fig. 6.6 Block diagram of gas turbine dynamic model.

- Compressor (C)
- Interconnecting plena between compressor and combustion chamber ($\tilde{V}_c$)
- Combustion chamber (CC)
- Gas-generator turbine (GGT)
- Gas generator shaft (GGS)
- Interconnecting plena interposed between gas-generator and power turbines ($\tilde{V}_t$)
- Power turbine (PT)

Additionally, two subsystems are included to govern fuel mass flow rate and IGV angle. The lumped volume strategy introduced in figure 6.5 is implemented in all the components, whereas the presence of the intermediate plena $\tilde{V}_c$ and $\tilde{V}_t$ clearly derives from the adopted interconnecting protocol approach. Specifically, the intermediate volume $\tilde{V}_c$ guarantees that the outputs from the compressor block match the inputs of the combustion chamber, as $\tilde{V}_t$ performs the same function between the gas generator and power turbines. Conservation equations solved within the intermediate volumes $\tilde{V}_c$ and $\tilde{V}_t$ allows to model the transient mass storage as well as the temperature and pressure fluctuations experienced by the flow. In the following, the main subsystems are analysed in details, focusing the attention on the input/output quantities together with component characteristic maps.
Figure 6.7 shows a schematic view of the compressor block together with the corresponding

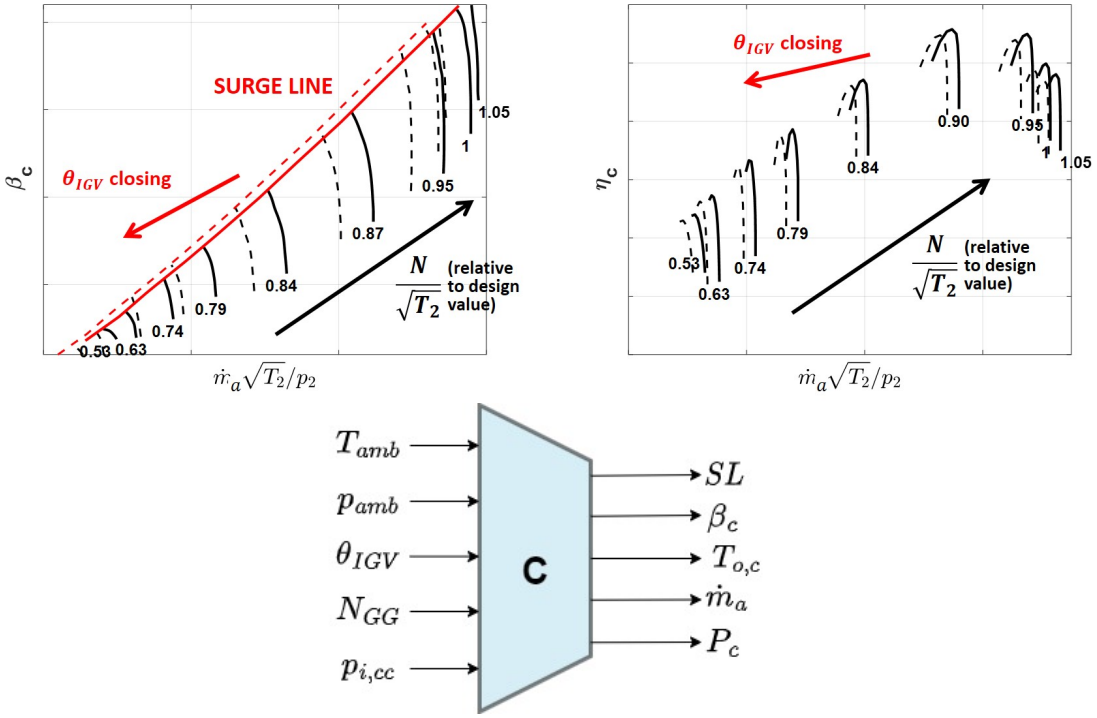

Fig. 6.7 Characteristic maps for compressor and inputs/outputs related to its corresponding block.

characteristic map implemented to get rigid response. Maps reported in figure 6.7 derives from the literature concerning the LM2500 gas turbine [260]. Five inputs are shown to enter the subsystem: pressure and temperature ambient conditions; the IGV opening angle θ_{IGV}, withdrawn from the specific controller; the rotational speed of the gas generator shaft deriving from the dynamic balance between compressor C and turbine TGG; outlet pressure p_3, computed from the interconnecting volume $\tilde{V}_c$, which accounts for mass storage. On the other hand, the surge limit (SL), the outlet temperature T_3, the power P_c absorbed by the compressor, the pressure ratio β_c and the air mass flow rate $\dot{m}_a$ are computed as output. Specifically, the surge limit is computed following the work of Klapproth et al. [260] where the distance of the operating point, dealing with generic pressure $p(t)$, from the surge line (i.e. surge pressure p_{surge}) is computed along a $\dot{m}_a = const$ line:

$$SL(t) = \frac{p_{surge} - p(t)}{p(t)} \tag{6.22}$$

The mass flow rate $\dot{m}_a$ is obtained interpolating the map reported in figure 6.7 in function of the reduced rotational speed, β_c and θ_{IGV}. Specifically, the effect played by the stagger angle of the IGV row on the reduction of the mass flow rate evolving within the compressor clearly depends on the blade geometry and aerodynamic load. However, a scaling approach

is commonly adopted in the literature, since it often approximates actual operating conditions available from manufacturers with good agreement [261, 262, 77]. Therefore, following Hashmi et al. [262], the reduction of $\dot{m}_a$ triggered by a θ_{IGV} variation has been modeled as:

$$\dot{m}_a = \dot{m}_{a,0}(1 - a_{IGV}(\theta_{IGV} - \theta_{IGV,nom})), \quad a_{IGV} = \frac{\partial \dot{m}_a}{\partial \theta_{IGV}} \tag{6.23}$$

where a_{IGV} is the rate of change of the mass flow rate with θ_{IGV} and $\dot{m}_{a,0}$ is the air flow in case IGV is fully open, assuming the same conditions of β_c and $N_{GG}/\sqrt{T_2}$. Equations yielding pressure ratio and absorbed power from the compressor are reported below:

$$\beta_c = \frac{p_3}{p_2} \tag{6.24}$$

$$P_c = \dot{m}_a \eta_c / (h_3 - h_{2id}) \tag{6.25}$$

where the compressor adiabatic efficiency η_c is obtained by interpolating the $\dot{m}_a\sqrt{T_2}/p_2$, θ_{IGV} and $N_{GG}/\sqrt{T_2}$ map shown in figure 6.7. Particularly, the influence played by the IGV angle on η_c is accounted for according to Hashmi et al. [262]:

$$\eta_c = \eta_{c,0}(1 - b_{IGV}(\theta_{IGV} - \theta_{IGV,nom})^2) \tag{6.26}$$

with $\eta_{c,0}$ being the compressor efficiency in full-open IGV conditions at the same β_c, $\dot{m}_a$ and $N_{GG}/\sqrt{T_2}$, while b_{IGV} is the rate of variation experienced by η_c with respect to IGV angle (i.e. $b_{IGV} = \frac{\partial \eta_C}{\partial \theta_{IGV}}$). Indeed, though closing IGV maintains nearly unvaried η_c due to the adjustment of blade stagger angle to the incidence of inlet flow, aerodynamic performance of compressor rows is negatively affected by off-design operating conditions on air mass flow rate. Finally, the outlet temperature $T_{o,c}$ is obtained from the thermodynamic relation $T = f(h, p)$.

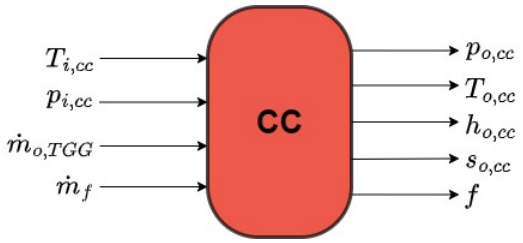

Fig. 6.8 Inputs/outputs for the combustion chamber block.

Where the combustion chamber is concerned, figure 6.8 reports the numerical scheme adopted. The pressure and temperature levels obtained from the interconnecting plenum $\tilde{V}_c$, $\dot{m}_f$ and the mass exhaust mass flow rate represent input parameters. Outputs consist in the complete

thermodynamic state of the flow at the exit of the combustion chamber. The equations implemented within the block mainly follow the thermodynamic cycle computation reported in section 6.1.1. Specifically, the enthalpy $h_{o,cc}$ of exhaust gas generated from the combustion process is obtained from eq. (6.27):

$$(\dot{m}_a + \dot{m}_f) h_{o,cc} = \dot{m}_a h_{i,cc} + \dot{m}_f LHV \eta_b \tag{6.27}$$

where a burner efficiency $\eta_b = 0.99$ and total pressure losses coefficient ε_{CC}=0.95 are assumed [259]. Within the combustion chamber module, GHG and pollutant emissions are computed depending on the operating point the GT is working at. Two numerical procedures are available to compute pollutant emissions:

- Correlation approach: thermodynamic parameters are inserted into emission correlations available from the literature.
- Operating curves: emission curves provided by manufacturers are used.

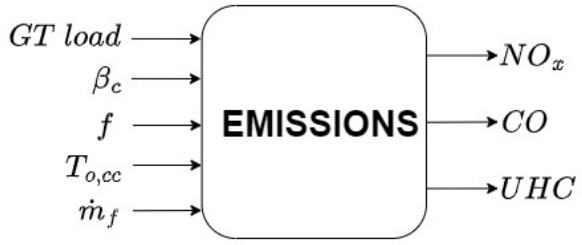

Fig. 6.9 Inputs/outputs for the block computing emissions.

Focusing on the first approach, a schematic view of the block performing emission computation is shown in figure 6.9. Inputs consist of β_c, combustion chamber inlet temperature, $\dot{m}_f$ and the fuel-to-air ratio $f = \frac{\dot{m}_f}{\dot{m}_{TGG} - \dot{m}_f}$. Following the work of Rokke et al. [263], the NO_x correlations reported below are considered:

$$\begin{aligned} NO_x &= 13.717\,(\beta_c)^{1.42}\,\dot{m}_a f^{0.72} && [ppmv] \\ NO_x &= 1.106\,(\beta_c)^{1.42}\,\dot{m}_a f^{0.72} && [gNO_x/kg fuel] \end{aligned} \tag{6.28}$$

Eqs. (6.28) are obtained for dry air dealing with 15% volumic O_2 content and apply to 1.5-34 MW commercially available GTs fed by natural gas. As can be seen, NO_x production is express in function of the compressor pressure ratio, air mass flow rate (i.e. GT size) and air-to-fuel ratio. Despite the simplified nature of the approach, it must be underlined that the

influence of both fuel type and rich-lean working conditions on NO_x is taken into account through f. As suggested by Altosole et al. [264], the numerical coefficient present within eq. (6.28) is calibrated to reproduce the NO_x emissions stated by manufacturers for various GTs. Though the main source of NO_x is thermal, no adiabatic flame temperature is present in eq. (6.28), since its effect is implicitly accounted for in p_3 and f. On the other hand, CO emissions are evaluated by means of the correlation proposed by Rizk e Mongia [265], successively corrected by Altosole et al. [264] to match with marine gas turbine size:

$$CO = \frac{11.42 \cdot 10^9 e^{\frac{7800}{T_{ad}}}}{p_3^2 (43 \dot{m}_f^{0.07})^{0.1} \left(\frac{\Delta p_{cc}}{p_3}\right)^{0.5} f} \quad [gCO/kgfuel] \tag{6.29}$$

where T_{ad} is the adiabatic flame temperature and Δp_{cc} represents total pressure losses in the combustion chamber. As was above for NO_x, the influence of fuel type and combustion characteristics is taken into account by the fuel-to-air ratio f. The adiabatic flame temperature is estimated by means of the open source Cantera software in function of pressure and temperature levels within the combustion chamber together with the equivalence ratio $ER = f/f_{stech}$, whose value is derived from typical laws $ER = f(load)$ available in the literature [250, 264]. Multiplying eq. (6.29) by $1.07 \cdot 10^3 f$, the CO production in ppm can be found. Furthermore, calibration analogous to that for NO_x has been performed with data from the manufacturers in nominal condition. Finally, the unburned hydrocarbon (UHC) emissions generated by either reduced residence time in the combustion chamber or localized low temperatures are estimated by the following correlation [265, 264]:

$$UHC = \frac{2.29 \cdot 10^{11} e^{\frac{9756}{T_{ad}}}}{p_3^{2.3} (43 \dot{m}_f^{0.07})^{0.1} \left(\frac{\Delta p_{cc}}{p_3}\right)^{0.6} f} \quad [gUHC/kgfuel] \tag{6.30}$$

As can be seen, the main dependencies visible in eq. (6.30) for UHC are similar to those considered for CO emissions. Indeed, these two pollutant species can form in similar working conditions. Multiplying equation (6.30) by $1.886 \cdot 10^3 f$, the corresponding ppm level is obtained. Finally, CO_2 emissions are obtained assuming complete fuel oxidation at equilibrium and, then, subtracting UHC and CO concentrations. Combustion reaction for a general hydrocarbon C_xH_y at equilibrium condition is reported in eq. (6.31):

$$C_xH_y + a(O_2 + 3.76N_2) \longrightarrow xCO_2 + \frac{y}{2}H_2O + 3.76aN_2 \tag{6.31}$$

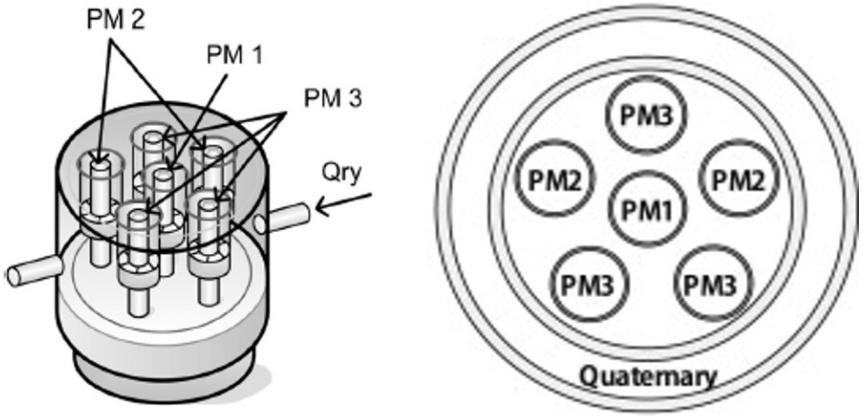

Fig. 6.10 Schematic view of the DLN2.6e combustor [27, 28].

with $a = x + \frac{y}{4}$.

On the other hand, the second approach aimed at computing emissions relies on the manufacturer-provided maps of NO_x, CO and UHC related to CH_4 combustion. Specifically, the emission curves provided by GE for the recent DLN2.6 combustor have been used independently from the GT simulated. Since almost all the GT combustors commercially available work under lean-premix conditions to reduce NO_x and comply with emission regulations, this hypothesis appears reasonable.

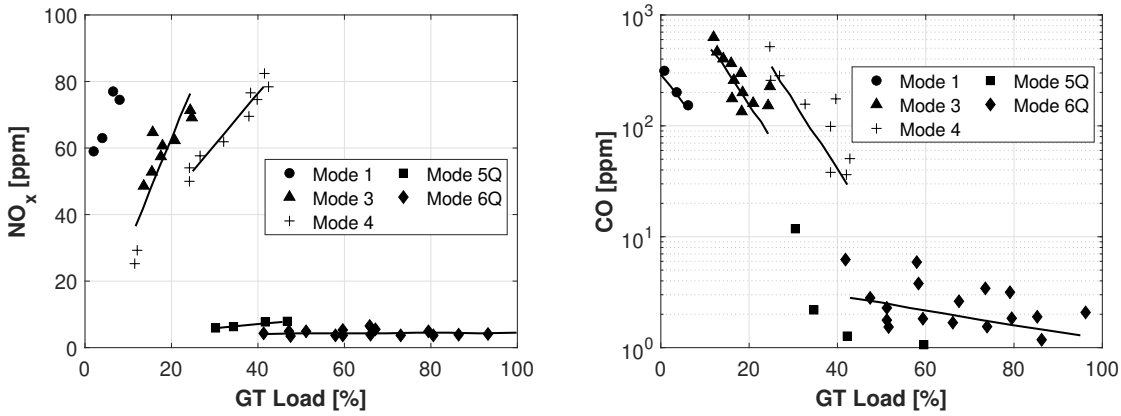

Fig. 6.11 NO_x and CO emissions generated by the DLN2.6 combustor under natural gas feeding conditions [28].

A schematic view of the DLN2.6 combustor is depicted in figure 6.10. During a start-up procedure, the combustor is sequentially operated passing from mode 1, where a reduced number of nozzles work on rich blends, to modes 5Q and 6Q, where all the burners operate with lean-premix mixtures. Mode 6Q is traditionally used from 50% of the GT load on [27, 28]. Curves related to NO_x and CO emissions from DLN2.6 are reported in figure 6.11

[28]. As can be seen, in the lean-premix working condition starting at 50% of the GT load, NO_x and CO emissions do not exceed 15 ppm and 25 ppm, respectively, in compliance with current regulations. At reduced loads, higher CO and NO_x are achieved due to the rich blends the combustor works on, aimed to guarantee stable combustion. When DLN2.6 is

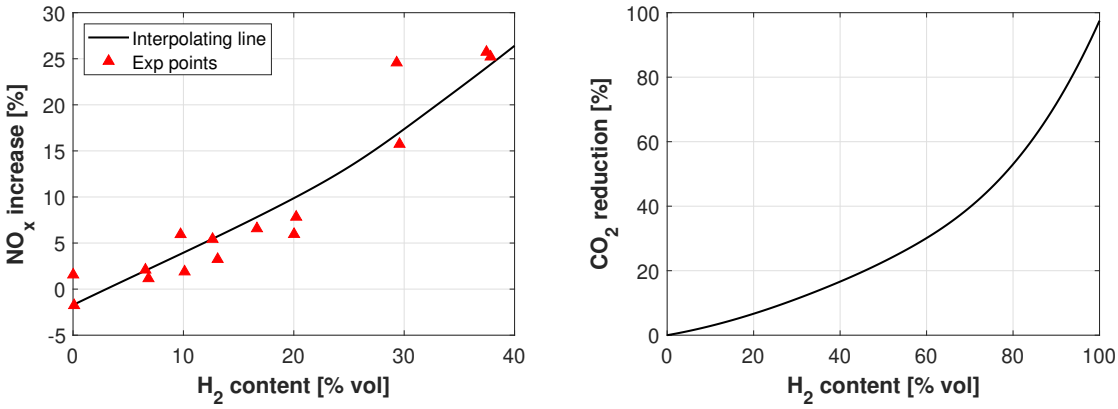

Fig. 6.12 NO_x increase and CO_2 reduction in % volume obtained by feeding the DLN2.6e combustor with $CH_4 - H_2$ blends [28].

fed by alternative fuels (e.g., $CH_4 - H_2$ blends in the DLN2.6e cobmsutor), the emissions curves reported in figure 6.11 are scaled by correction factors obtained from previous experimental works concerning fuel flexibility enhancement in GTs [157, 128, 130, 194, 193]. Particularly, results assessing the increase in NO_x production and the reduction of CO_2 emissions which were obtained by GE feeding the DLN2.6e combustor with $CH_4 - H_2$ blends are reported in figure 6.12. Where the GG turbine block is concerned, figure 6.13 reports the corresponding numerical scheme implemented together with characteristic maps. The turbine subsystem receives as inputs the entire thermodynamic state at the exit of the combustor, together with both the rotational speed of gas generator shaft N_{GG} and pressure downstream the interconnecting plena $\tilde{V}_t$. In detail, the entropy at the combustion chamber outlet and the pressure $p_{i,PT}$ are used to obtain ideal enthalpy level at the GG turbine exit, which in turn is used for computing h_5 by means of adiabatic efficiency definition. The main outputs consist in delivered power, exhaust gas temperature T_5 and mass flow rate $\dot{m}_{TGG}$. Similarly to compressor, the exhaust mass flow rate is derived from the characteristic map $(\varepsilon_{TGG}, N_{GG}/\sqrt{T_4}, (\dot{m}_a + \dot{m}_f)\sqrt{T_4}/p_4)$, entering with ε_{TGG} and $N_{GG}/\sqrt{T_4}$. Then, power delivered by GG turbine can be computed as:

$$P_{TGG} = \dot{m}_{TGG}(h_4 - h_{5id})\eta_{TGG} \tag{6.32}$$

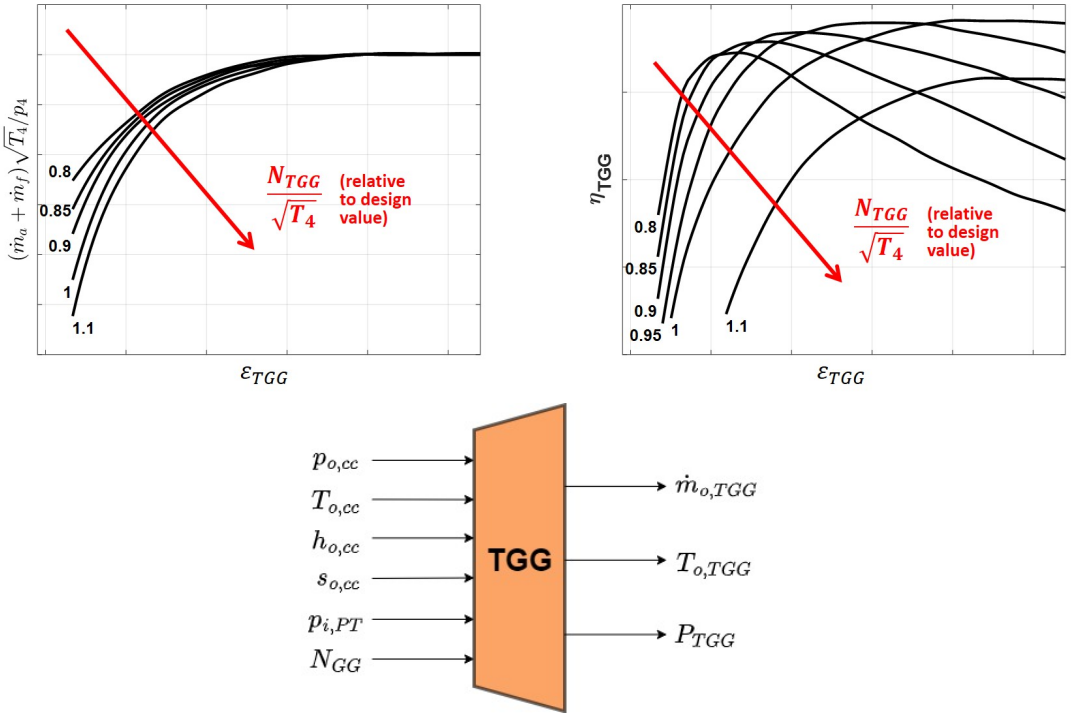

Fig. 6.13 Characteristic maps for GG turbine and inputs/outputs related to its corresponding block.

where η_{TGG} represents the adiabatic efficiency of gas generator turbine, whose value is withdrawn from the map $(N_{GG}/\sqrt{T_4}, (\dot{m}_a+\dot{m}_f)\sqrt{T_4}/p_4, \eta_{TGG})$ in function of $N_{GG}/\sqrt{T_4}$ and $(\dot{m}_a+\dot{m}_f)\sqrt{T_4}/p_4$. Finally, the exit temperature T_5 (i.e. $T_{o,TGG}$) is obtained from the thermodynamic relation $T_5 = f(h_5, p_5)$.

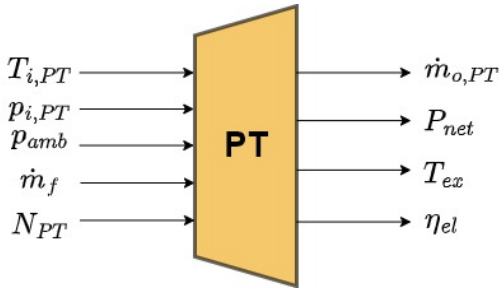

Fig. 6.14 Inputs/outputs for the power turbine block.

Similarly, numerical scheme adopted for the power turbine is reported in figure 6.14. No characteristic maps for mass flow rate or efficiency are shown, since they are qualitatively analogous to those previously shown in figure 6.13 for the GG turbine. The inputs required from PT consist in the entire thermodynamic state computed from the interconnecting volume $\tilde{V}_t$ together with ambient pressure p_{amb}, fuel mass flow rate $\dot{m}_f$ and N_{PT}. The main outputs

are the exhaust temperature at the GT outlet, the exhaust mass flow rate evolving within the power turbine and, finally, P_{net} and η_{el} delivered by the entire aeroderivative GT. The mass flow rate is derived from $(\varepsilon_{PT}, N_{PT}/\sqrt{T_5}, (\dot{m}_a + \dot{m}_f)\sqrt{T_5}/p_5)$ characteristic map analogous to that reported in figure 6.13, whereas exhaust gas temperature T_6 (i.e. T_{ex}) is computed by thermodynamic relations $T_6 = f(p_6, h_6)$, with h_6 obtained from η_{PT} definition. On the other hand, net power is computed as:

$$P_{net} = (\dot{m}_f + \dot{m}_a)(h_5 - h_6)\eta_{mecc}\eta_a \tag{6.33}$$

where a mechanical efficiency $\eta_{mecc} = 0.99$ and alternator efficiency $\eta_a = 0.97$ have been considered, according to the literature [259]. Finally, the electrical efficiency of gas turbine is calculated as:

$$\eta_{el} = \frac{P_{net}}{\dot{m}_f LHV} \tag{6.34}$$

where LHV is the lower heating value of the fuel.

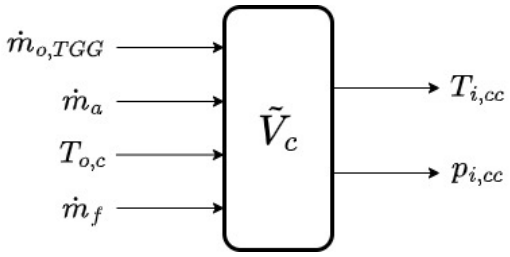

Fig. 6.15 Inputs/outputs for the interconnecting plenum $\tilde{V}_c$ block.

Focusing the attention on the interconnecting plena $\tilde{V}_c$, figure 6.15 shows its numerical scheme, in order to assess inputs and outputs. The air and fuel mass flow rates $\dot{m}_a$ and $\dot{m}_f$, respectively, together with the flow exiting the GG turbine and temperature T_3 (i.e. $T_{i,cc}$), are received in input. Instead, pressure and temperature levels entering the combustion chamber are provided as outputs. Specifically, the conservation equations (6.19), (6.20) and (6.21) written for a perfect gas are used to model mass storage and pressure variation within $\tilde{V}_c$. Then, variations in temperature follow from the perfect gas law:

$$p\tilde{V}_c = \bar{n}R_u T \tag{6.35}$$

where the volume $\tilde{V}_c$ is estimated from the either the GT CAD or the literature, R_u is the universal gas constant and $\bar{n}$ the number of moles. The operating principle remains the same also for the $\tilde{V}_t$ plena, since only changes in inputs/outputs acronyms are present.
Where the gas generator shaft is concerned, figure 6.16 reports the numerical scheme adopted.

Fig. 6.16 Inputs/outputs for GG shaft block.

Specifically, power absorbed by compressor and delivered by GG turbine is supplied as input, whereas rotational speed is computed by the time-dependent conservation of angular momentum:

$$J\omega\frac{d\omega}{dt} = P_{TGG} - P_c \tag{6.36}$$

where J represents the polar moment of inertia of the shaft, assumed from 10-40 MW GTs [266, 262]. Analogous equation governs the shaft dynamics for power turbine, where resistance power is represented by alternator. Finally, the effect played by the ambient

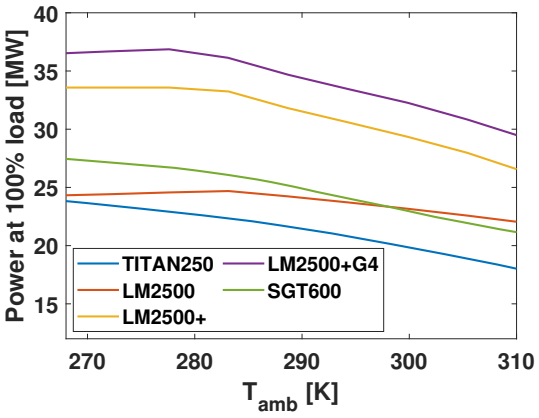

Fig. 6.17 Mechanical power dependency from variable ambient temperature for various GTs.

temperature in reducing GT performance is modeled by means of (P_{net}, T_{amb}) curves from the manufacturers (see figure 6.17). As shown in figure 6.17, the net power significantly reduces for increasingly high ambient temperatures, whereas it remains nearly constant in cold environments.

6.2.2 GT control strategies

Figure 6.18 shows the numerical scheme related to blocks which perform IGV and fuel mass flow rate control. Focusing on the IGV control, the inlet temperature T_4 to GG turbine, the exhaust gas temperature T_{ex} and GG rotational speed are supplied as inputs to determine θ_{IGV}. Indeed, the main purpose of the IGV control is to align the stagger angle of the first

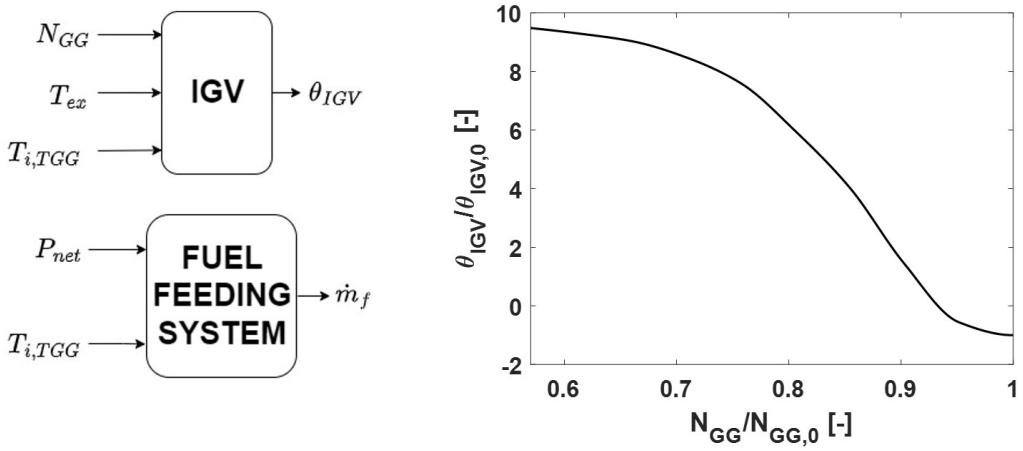

Fig. 6.18 Fuel and IGV control blocks (left) together with the default governing strategy for IGV during start-up procedure (right).

statoric row within the compressor to the velocity triangles, depending on GT load. Since this regulation guarantees high η_c levels under flexible GT operating conditions, IGV is traditionally governed in this way during start-up or shut-down schedules [242]. Diagram showing the default governing strategy for IGV installed on LM2500 GT is reported in figure 6.18. As can be seen, IGV starts fully opened at 100% load (i.e. nominal $N_{GG} = N_{GG,0}$) and is gradually closed for increasingly lower loads (i.e. $N_{GG} < N_{GG,0}$). However, in case specific control on some thermodynamic parameters (i.e. GG turbine inlet temperature TIT, turbine outlet temperature TOT, ...) is necessary, different IGV governing schedules are implemented, which consist in imposing positive/negative off-set angle to the default one. In this case, a positive/negative off-set angle is added to the value obtained from the curve reported in figure 6.18. On the other hand, focusing on the fuel mass flow controller, the GG turbine inlet temperature together with power generated by the alternator are supplied as inputs, whereas $\dot{m}_f$ is determined. In this thesis, the IGV and fuel mass flow rate controls may implement two governing strategies, which are traditionally adopted for combined cycles in the power generation field:

- $TIT = const$: aimed at maximizing GT efficiency at part-loads. In the following the acronym TITc is used for this strategy
- $TOT = const$: in order to limit off-design operating conditions experienced by the bottoming steam power plant at GT part-loads. Specifically, safety and energy savings are ensured for HRSG under variable GT load. In the following the acronym TOTc indicates this strategy

From the power generation field, it is well established that TOTc strategy allows to reach maximum performance of the overall gas-steam combined cycle [267, 268]. However, during COGES plant operation, some further control need to be assessed parallel to either the TITc or TOTc strategies. Specifically, power generation must balance energy demand onboard, hence the following-load service - typical of combined power plants - is required to avoid grid failures. Furthermore, safety controllers monitoring over-temperature at point 4 and GG shaft over-speed reduce risks of thermo-mechanical damages during transient GT operation. Therefore, all these additionally required governing strategies have been implemented within the controller blocks shown in figure 6.18. Specifically, looking at the inputs schematically reported in figure 6.18 for the IGV control, the actuated value of θ_{IGV} is determined coupling TITc or TOTc strategy with over-temperature and GG over-speed controls. Thus, TITc and TOTc methods, which are mutually excluding, always work parallel to safety conditions for T_4 and N_{GG}. In each GT operating condition, the minimum value for θ_{IGV} queried by enabled controllers is actuated, since it represent the most urgent provision of regulation. On the other hand, the following-load service, which is typical of combined power plants, is guaranteed by the fuel feeding controller, in compliance with the over-temperature and over-speed safety regulations as well as with the TITc or TOTc strategy adopted. In details, the net power generated by the power turbine is compared with the electrical power demand and the resulting error enters a controller to find out candidate fuel mass flow rate for the next time instant. This value is successively compared to candidate fuel mass flow rate obtained by over-temperature controller and, finally, the minimum value of $\dot{m}_f$ is actuated. Overall, it must be underlined that controller architectures for fuel and IGV angle shown in figure 6.18 are traditionally adopted in the power generation sector. Moving attention to the fuel controller, the actuated $\dot{m}_f$ is determined coupling TITc or TOTc strategy with all the over-temperature, over-speed and load-following regulations. Analogously to the IGV control, the minimum fuel mass flow rate queried by multiple governing strategies is actuated. Where the numerical architecture of controllers is concerned, regulation is performed by means of Proportional Integral Derivative (PID) controllers, whose Single Input Single Output (SISO) schematic view is shown in figure 6.19. R represents the reference signal, which is compared with the actual system response Y to compute error E. Then, the actuation input U is provided by the controller to efficiently govern the dynamical system. The actuation input $U(t)$ determined by PID controllers contains proportional, integral and derivative contributes with respect to the error $E(t)$:

$$U(t) = K_p E(t) + K_i \int_0^t E(\tau)\, d\tau + K_d \frac{dE(t)}{dt} \tag{6.37}$$

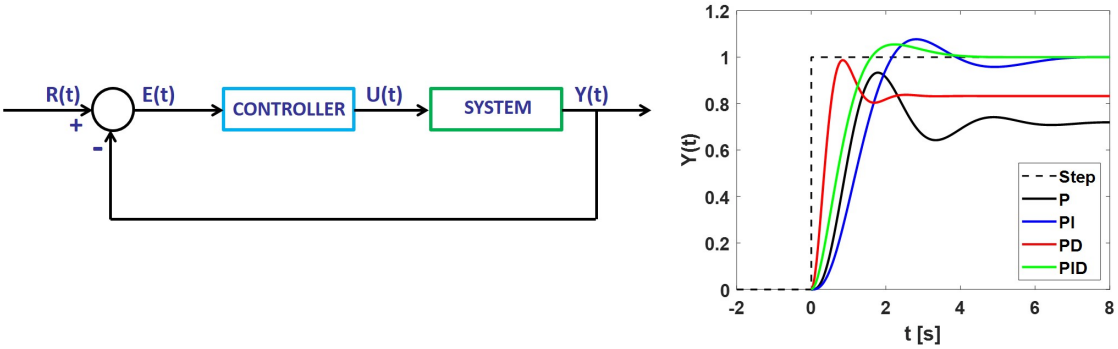

Fig. 6.19 Schematic view of a SISO control system (left) together with step responses obtained by different types of controller (right).

where the K_p, K_i and K_d coefficients correspond to the proportional, integral and derivative constants, respectively. As visible in figure 6.19, the response of closed-loop systems dealing with P controller is fast, despite offset error for $t \to \infty$ and significant overshoot is provided. On the other hand, adding the integral part to the controller (i.e. PI) can delete offset error at regime, while reducing the response speed and increasing overshoot. Instead, since derivative term anticipate variations in E, the PD controller guarantees high speed. However, offset error is still present and small oscillations in E can be amplified. Finally, PID controller takes the best of all the terms.

In case the physics of the system requires to limit the input signal U and, at the same time, the sign of E does not change for a long time, the integral term continues to increase its contribute. Then, when the error suddenly changes sign, the large accumulated contribute of the integral term is slightly reduced. The slow discharging process of the integral term temporarily compromises the sign of U and, consequently, the effectiveness of the control in a certain time interval. This phenomenon is commonly named wind-up and only derives from numerical issues. Two principal methods, i.e. clamping and back-calculation, are usually adopted to limit wind-up. Clamping consists in stopping the integral contribution when U saturates at its the maximum/minim level. On the other hand, an additional term proportional to the difference between pre-saturation and saturated signal U is added in eq. (6.37) within the back-calculation approach, hence the over-sizing of the integral contribution is avoided a-priori (see figure 6.20).

6.2.3 Dynamic model of bottoming steam power plants

The dynamic model of the bottoming steam power plant included within COGES is schematically depicted in figure 6.21, where the following physical-based subsystems can be identified:

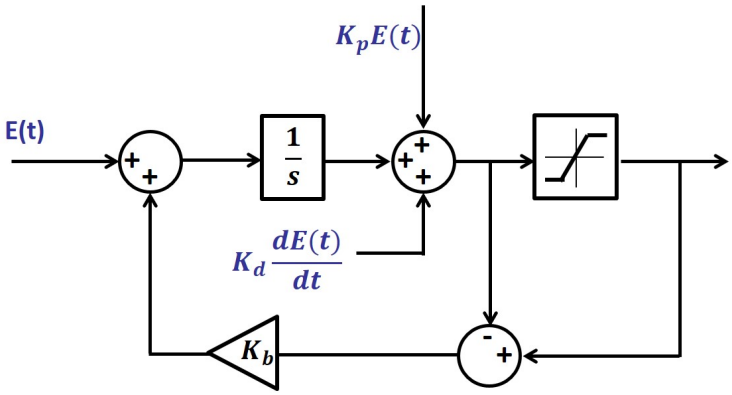

Fig. 6.20 Back-calculation PID numerical scheme to avoid wind-up.

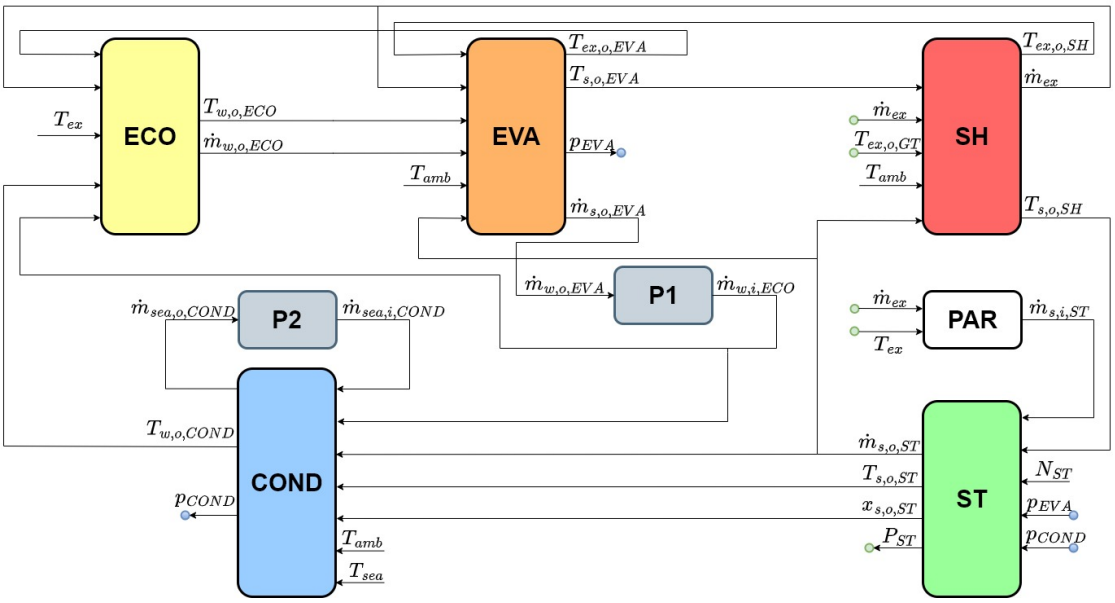

Fig. 6.21 Block diagram of the dynamic model concerning the bottoming steam power plant included within COGES.

- Economizer (ECO)
- Evaporator (EVA)
- Recirculating pump (P1)
- Superheater (SH)
- Steam turbine (ST)
- Condenser (COND)
- Sea water pump (P2)

Additionally, the PAR subsystem is included to assess the partialization control of steam turbine. The model shown in figure 6.21 relies on mixed lumped volume-dynamic approach. Specifically, a nonlinear lumped volume scheme analogous to that explained above for GT is adopted for turbomachinery components (pumps and steam turbine). On the other hand, heat exchangers (HE) included within HRSG as well as condenser are solved by a 2-D dynamic approach, based on spatial finite differences and temporal ODE system. No interconnecting plena are visible in figure 6.21, due to the mixed lumped volume-dynamic approach. Indeed, mass storage and pressure/temperature fluctuations are accounted for in the cylindrical drums of evaporator and condenser. In the following, the main subsystems are analysed in details, focusing the attention on the input/output quantities together with finite difference schemes used for heat exchangers.

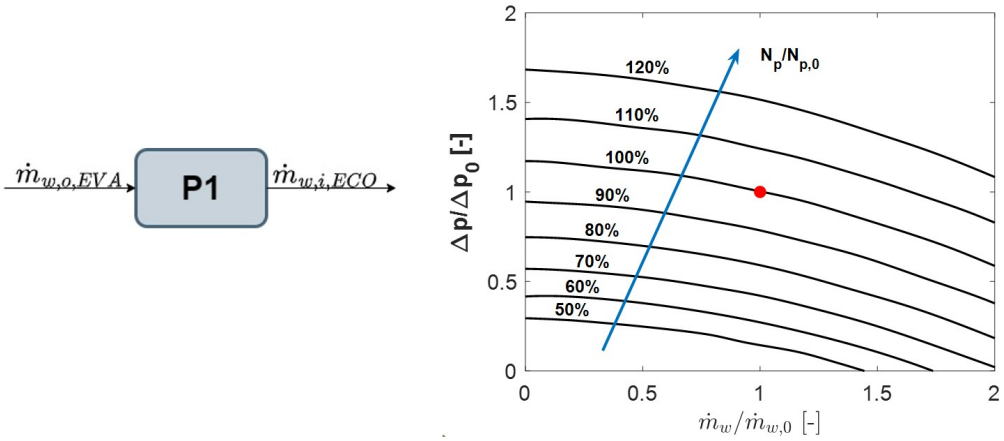

Fig. 6.22 Inputs/outputs for the pump P1 block (left) and its corresponding characteristic map (right).

Figure 6.22 shows a schematic view of the pump block P1 related to the main feed-water system (left side), together with the corresponding characteristic maps implemented (right side), where N_P indicates rotational speed of the pump, Δp are pressure losses, $\dot{m}_w$ the water mass flow rate and the subscript 0 refers to nominal point. As can be seen from figure 6.22, the pump controller inserted within block P1 provides as output the water mass flow rate $\dot{m}_w$ supplied to economizer ECO, depending on the steam flow generated by the evaporator. Indeed, inside the block P1 the physical-based operating condition of the pump provided by the $(N_P, \Delta p, \dot{m}_w)$ map is coupled with a controller, which aims to maintain liquid level within EVA constant, reducing risks of either burning EVA tubes or flooding SH. Specifically, the PID controller of pump P1 decides the pump rotational speed N_P, which is successively used as input in map $(N_P, \Delta p, \dot{m}_w)$ to find $\dot{m}_w$. Other input to the map $(N_P, \Delta p, \dot{m}_w)$ consists in

pressure losses recovered within the steam/water circuit, which can be computed as:

$$\Delta p = f_D \frac{L}{D} \frac{\rho V^2}{2} + \sum_j K_{L,j} \frac{\rho V_j^2}{2} \tag{6.38}$$

where the first and second terms represent concentrated and distributed pressure losses, respectively. Furthermore, the power required by pump P1 is obtained considering the enthalpic gap provided, i.e. $P_{P1} = (h_{i,ECO} - h_{o,COND})\dot{m}_{w,i,ECO}$.
Analogous numerical scheme is adopted for the pump P2. However, the sea water pump P2 is coupled with a PID controller targeting steady level of condensed water within COND. Thus, the sea water mass flow rate aiming at cooling steam is determined based on the condensed water level achieved in the condenser. Characteristic map used for P1 is qualitatively analogous to that of the main feed water pump P, hence is not reported for conciseness.

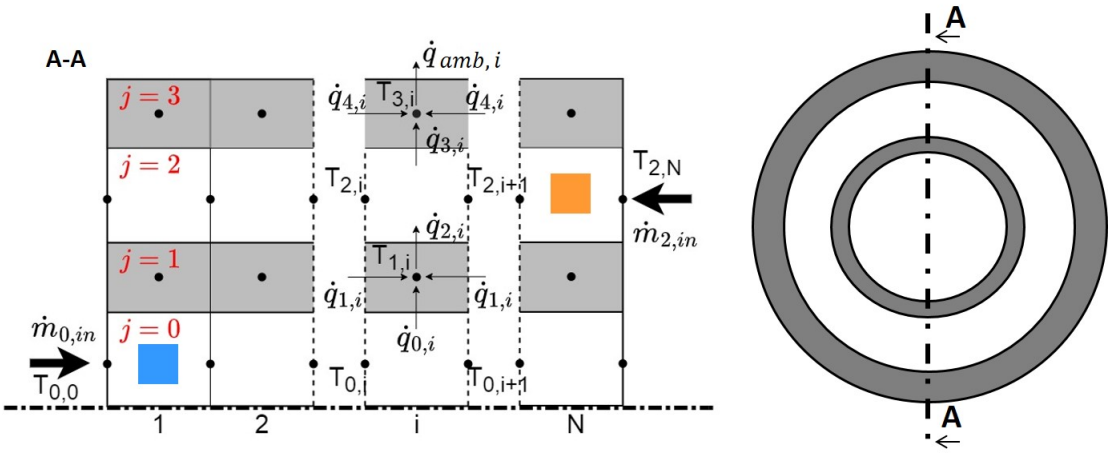

Fig. 6.23 Schematic view of discretized numerical model for single-phase heat exchangers.

Focusing on heat exchangers, the following treatment distinguishes single-phase from phase-change HEs since relevant differences arise by a numerical point of view. Where single phase heat exchangers are concerned (i.e. economizer and superheater), figure 6.23 shows details on the finite difference scheme adopted in space. Specifically, a second-order central finite difference scheme is adopted for space discretization, hence the Partial Differential Equations (PDEs) representing the conservation of energy are changed into temporal Ordinary Differential Equations (ODEs). Furthermore, the numerical scheme in figure 6.23 is aimed to reproduce a shell-and-tube heat exchanger configuration. The steam/water working fluid passes in the internal pipe for both economizer and superheater, whereas exhaust gas evolves

between shell and tube. Following the work of [252], no mass storage is accounted for in superheater SH and economizer ECO to correctly impose interconnecting boundary condition protocol between adjacent components. Thus, SH and ECO are modeled as pipe.

The discretised energy equations for the fluid and solid domains valuable for SH and ECO are written as follows, according to the index notation:

$$\begin{aligned}
\rho_{0,i}c_{v,0}A_{0,i}\frac{T_{0,i}^{n+1}-T_{0,i}^{n}}{\Delta t} &= \dot{m}_0 c_{p,0}\frac{T_{0,i-1}^{n+1}-T_{0,i}^{n+1}}{\Delta x}-\frac{\dot{q}_0}{\Delta x}\\
\rho_{2,i}c_{v,2}A_{2,i}\frac{T_{2,i}^{n+1}-T_{2,i}^{n}}{\Delta t} &= \dot{m}_2 c_{p,2}\frac{T_{2,i+1}^{n+1}-T_{2,i}^{n+1}}{\Delta x}+\frac{\dot{q}_2-\dot{q}_3}{\Delta x}\\
m_{1,i}c_{v,1}\frac{T_{1,i}^{n+1}-T_{1,i}^{n}}{\Delta t} &= \frac{2\dot{q}_1+\dot{q}_0-\dot{q}_2}{\Delta x}\\
m_{3,i}c_{v,3}\frac{T_{3,i}^{n+1}-T_{3,i}^{n}}{\Delta t} &= \frac{2\dot{q}_4+\dot{q}_3-\dot{q}_a}{\Delta x}
\end{aligned} \tag{6.39}$$

where q indicates the conductive/convective heat flux exchanged on the pipe or shell boundaries (i.e. radiation fluxes are neglected). In case heat fluxes are expressed as:

$$\begin{aligned}
\dot{q}_{0,i} &= \xi_0 S_{0,i}\left(\frac{T_{0,i+1}+T_{0,i}}{2}-T_{1,i}\right)\\
\dot{q}_{1,i} &= \lambda_1 A_1\frac{T_{1,i-1}-T_{1,i}}{\Delta x}+\lambda_1 A_1\frac{T_{1,i+1}-T_{1,i}}{\Delta x}\\
\dot{q}_{2,i} &= \xi_1 S_{1,i}\left(T_{1,i}-\frac{T_{2,i+1}+T_{2,i}}{2}\right)\\
\dot{q}_{3,i} &= \xi_2 S_{2,i}\left(\frac{T_{2,i+1}+T_{2,i}}{2}-T_{3,i}\right)\\
\dot{q}_{4,i} &= \lambda_3 A_3\frac{T_{3,i-1}-T_{3,i}}{\Delta x}+\lambda_3 A_3\frac{T_{3,i+1}-T_{3,i}}{\Delta x}\\
\dot{q}_{amb,i} &= \xi_4 S_{3,i}\left(T_{3,i}-T_{amb}\right)
\end{aligned} \tag{6.40}$$

eqs. (6.41) for temperature grid are obtained:

$$
\begin{aligned}
&\rho_{0,i}c_{v,0}A_{0,i}\frac{T_{0,i}^{n+1}-T_{0,i}^{n}}{\Delta t} = \dot{m}_0 c_{p,0}\frac{T_{0,i-1}^{n+1}-T_{0,i}^{n+1}}{\Delta x} - \frac{\xi_0 S_{0,i}}{\Delta x}\left(\frac{T_{0,i-1}^{n+1}+T_{0,i}^{n+1}}{2} - T_{1,i-1}^{n+1}\right)\\
&\rho_{2,i}c_{v,2}A_{2,i}\frac{T_{2,i}^{n+1}-T_{2,i}^{n}}{\Delta t} = \dot{m}_2 c_{p,2}\frac{T_{2,i+1}^{n+1}-T_{2,i}^{n+1}}{\Delta x} - \frac{\xi_2 S_{2,i}}{\Delta x}\left(\frac{T_{2,i+1}^{n+1}+T_{2,i}^{n+1}}{2} - T_{3,i-1}^{n+1}\right)\\
&- \frac{\xi_1 S_{1,i}}{\Delta x}\left(-\frac{T_{2,i+1}^{n+1}+T_{2,i}^{n+1}}{2} + T_{1,i}^{n+1}\right)\\
&m_{1,i}c_{v,1}\frac{T_{1,i}^{n+1}-T_{1,i}^{n}}{\Delta t} = \xi_0 S_{0,i}\left(\frac{T_{0,i+1}^{n+1}+T_{0,i}^{n+1}}{2} - T_{1,i}^{n+1}\right) - \xi_1 S_{1,i}\left(-\frac{T_{2,i+1}^{n+1}+T_{2,i}^{n+1}}{2}\right.\\
&\left. + T_{1,i}^{n+1}\right) + \frac{\lambda_1 A_{1,i}\Delta t}{\Delta x}\left(T_{1,i-1}^{n+1} + 2T_{1,i}^{n+1} + T_{1,i+1}^{n+1}\right)\\
&m_{3,i}c_{v,3}\frac{T_{3,i}^{n+1}-T_{3,i}^{n}}{\Delta t} = \xi_2 S_{2,i}\left(\frac{T_{2,i+1}^{n+1}+T_{2,i}^{n+1}}{2} - T_{3,i}^{n+1}\right) - \xi_3 S_{3,i}\left(T_{3,i}^{n+1} - T_{amb}\right)\\
&+ \frac{\lambda_3 A_{3,i}}{\Delta x}\left(T_{3,i-1}^{n+1} + 2T_{3,i}^{n+1} + T_{3,i+1}^{n+1}\right)
\end{aligned}
\tag{6.41}
$$

where λ is the metal conductivity, ξ the convective heat transfer coefficient (depending on temperature and fluid phase) and c_v the calorific value at constant volume of metal/fluid. Instead, S represents the heat exchange surface area and A_j indicates the overall cross-sectional areas of the $j-$th element belonging to shell or tube, depending on the domain considered. Finally, Δx is the discretisation step along the streamwise direction (i.e. the axial direction of the shell-and-tube heat exchanger). As visible in figure 6.23, the numerical grid within the solid domains is staggered with respect to nodes in the fluid domains. This ensures numerical stability as well as accuracy, with limited computational costs [26]. Indeed, each solid cell belonging to the domains $j = 1,3$ exchanges heat with the average temperature obtained from two adjacent fluid cells in the $j = 0,2$ domains.

Where phase-change heat exchangers are concerned (i.e. EVA and COND), figure 6.24 shows the finite difference scheme adopted for evaporator. As was for ECO and SH, a second order central finite difference scheme is adopted for space discretization, to transform PDEs in a system of ODEs. The shell-and-tube configuration is assumed, with shell containing changing phase fluids, i.e. condensing steam for COND, evaporating water for EVA. Thus, as visible in figure 6.24, tubes where the hot exhaust gas passes are submerged within the water to produce steam, which accumulates on the top of the shell side. For condenser, tubes transporting sea water are included within the upper side of the shell, where steam exists, whereas condensed water accumulates on the bottom. Therefore, EVA and COND are assimilated to drums with changing-phase fluids, hence mass storage in them is accounted for. The discretised energy equations for the fluid and solid domains used for EVA and COND

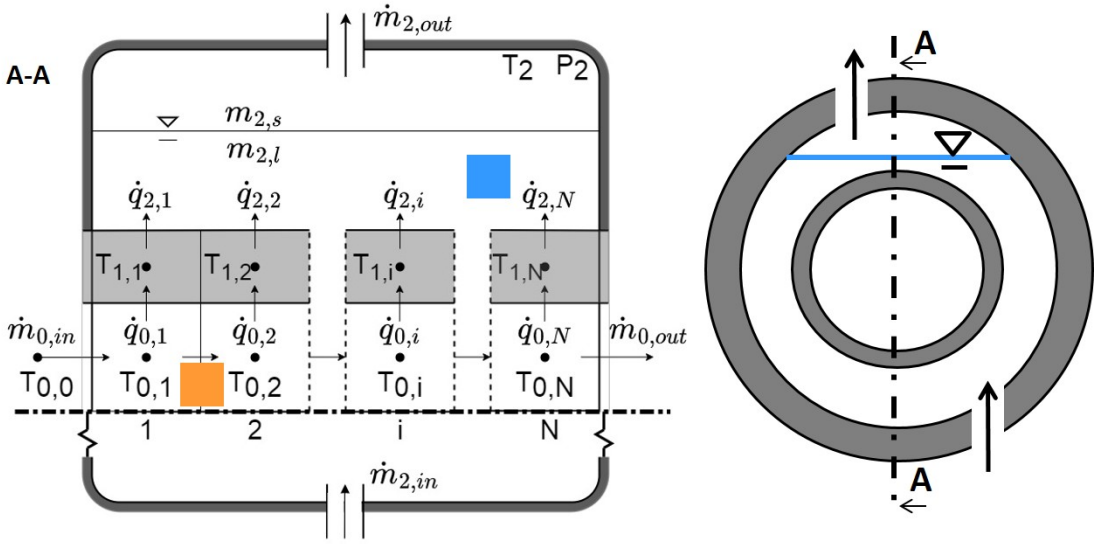

Fig. 6.24 Schematic view of discretized numerical model for phase-change heat exchangers.

are written as follows using the index notation:

$$\begin{aligned}
\rho_{0,i}c_{v,0}A_{0,i}\frac{T_{0,i}^{n+1}-T_{0,i}^{n}}{\Delta t} &= \dot{m}_0 c_{p,0}\frac{T_{0,i-1}^{n+1}-T_{0,i}^{n+1}}{\Delta x}-\frac{\dot{q}_0}{\Delta x}\\
\frac{(m_{2,l}^{n+1}u_{2,l}^{n+1}+m_{2,s}^{n+1}u_{2,s}^{n+1})-(m_{2,l}^{n}u_{2,l}^{n}+m_{2,s}^{n}u_{2,s}^{n})}{\Delta t} &= \dot{m}_{2,in}^{n+1}h_{2,in}^{n+1}-\dot{m}_{2,out}^{n+1}h_{2,out}^{n+1}+\sum_{i=1}^{N-1}\dot{q}_{2,i}-\dot{q}_{3,i}\\
m_{1,i}c_{v,1}\frac{T_{1,i}^{n+1}-T_{1,i}^{n}}{\Delta t} &= \frac{2\dot{q}_1+\dot{q}_0-\dot{q}_2}{\Delta x}\\
m_{3,i}c_{v,3}\frac{T_{3,i}^{n+1}-T_{3,i}^{n}}{\Delta t} &= \frac{2\dot{q}_4+\dot{q}_3-\dot{q}_a}{\Delta x}
\end{aligned} \tag{6.42}$$

where q indicates the conductive/convective heat flux for exchanged on the pipe or shell boundaries. In case heat fluxes are expressed as:

$$\begin{aligned}
\dot{q}_{0,i} &= \xi_0 S_{0,i}\left(\frac{T_{0,i+1}+T_{0,i}}{2}-T_{1,i}\right)\\
\dot{q}_{1,i} &= \lambda_1 A_1\frac{T_{1,i-1}-T_{1,i}}{\Delta x}+\lambda_1 A_1\frac{T_{1,i+1}-T_{1,i}}{\Delta x}\\
\dot{q}_{2,i} &= \xi_1 S_{1,i}(T_{1,i}-T_{2,all})\\
\dot{q}_{3,i} &= \xi_2 S_{2,i}(T_{2,all}-T_{3,i})\\
\dot{q}_{4,i} &= \lambda_3 A_3\frac{T_{3,i-1}-T_{3,i}}{\Delta x}+\lambda_3 A_3\frac{T_{3,i+1}-T_{3,i}}{\Delta x}\\
\dot{q}_{amb,i} &= \xi_4 S_{3,i}(T_{3,i}-T_{amb})
\end{aligned} \tag{6.43}$$

eqs. (6.44) for temperature grid are obtained:

$$
\begin{aligned}
&\rho_{0,i}c_{v,0}A_{0,i}\frac{T_{0,i}^{n+1}-T_{0,i}^{n}}{\Delta t}=\dot{m}_0 c_{p,0}\frac{T_{0,i-1}^{n+1}-T_{0,i}^{n+1}}{\Delta x}-\frac{\xi_0 S_{0,i}}{\Delta x}\left(\frac{T_{0,i-1}^{n+1}+T_{0,i}^{n+1}}{2}-T_{1,i-1}^{n+1}\right)\\
&\frac{(m_{2,l}^{n+1}u_{2,l}^{n+1}+m_{2,s}^{n+1}u_{2,s}^{n+1})-(m_{2,l}^{n}u_{2,l}^{n}+m_{2,s}^{n}u_{2,s}^{n})}{\Delta t}=\dot{m}_{2,in}^{n+1}h_{2,in}^{n+1}-\dot{m}_{2,out}^{n+1}h_{2,out}^{n+1}\\
&+\sum_{i=1}^{N-1}\xi_1 S_{1,i}/\Delta x(T_{1,i}^{n+1}-T_{2,all}^{n+1})-\xi_2 S_{2,i}/\Delta x(T_{2,all}^{n+1}-T_{3,i}^{n+1})\\
&m_{1,i}c_{v,1}\frac{T_{1,i}^{n+1}-T_{1,i}^{n}}{\Delta t}=\xi_0 S_{0,i}\left(\frac{T_{0,i+1}^{n+1}+T_{0,i}^{n+1}}{2}-T_{1,i}^{n+1}\right)-\xi_1 S_{1,i}(-T_{2,all}^{n+1}+T_{1,i}^{n+1})\\
&+\frac{\lambda_1 A_{1,i}\Delta t}{\Delta x}(T_{1,i-1}^{n+1}+2T_{1,i}^{n+1}+T_{1,i+1}^{n+1})\\
&m_{3,i}c_{v,3}\frac{T_{3,i}^{n+1}-T_{3,i}^{n}}{\Delta t}=\xi_2 S_{2,i}(T_{2,all}^{n+1}-T_{3,i}^{n+1})-\xi_3 S_{3,i}(T_{3,i}^{n+1}-T_{amb})\\
&+\frac{\lambda_3 A_{3,i}}{\Delta x}(T_{3,i-1}^{n+1}+2T_{3,i}^{n+1}+T_{3,i+1}^{n+1})
\end{aligned}
\tag{6.44}
$$

where $m_{2,s}$ and $m_{2,l}$ coincide with steam and water mass instantly contained within the shell, respectively. As can be seen from eq. (6.44), temperature level for the evaporating water is assumed uniform in space (i.e. $T_{2,all}$), hence a single node exchanging with exhaust gas is introduced in the cold domain. Variations of saturation pressure level induced by the charged/discharged mass within the shell are computed as [252]:

$$\dot{m}_{s,i,SH}-\dot{m}_{s,o,EVA}=C_f\cdot\frac{dp_{EVA}}{dt} \tag{6.45}$$

where $\dot{m}_{s,i,SH}$ and $\dot{m}_{s,o,EVA}$ are the steam mass flow rates supplied to SH and produced by EVA, respectively, whereas C_f represents the mass storage capacity of the heat exchanger. Analogous expression is used for condenser, with only differences in acronyms.

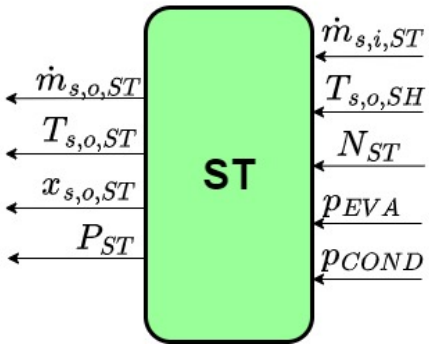

Fig. 6.25 Inputs/outputs for the steam turbine block.

Finally, schematic view of the condensing steam turbine model is reported in figure 6.25, together with characteristic map. The block receives as inputs the shaft rotational speed N_{ST}, the steam mass flow rate entering steam turbine $\dot{m}_{s,i,ST}$ and both the minimum and maximum pressure levels at outlet and inlet, respectively. The steam mass flow rate exiting steam turbine, together with its corresponding temperature and quality, are obtained as outputs in addition to the delivered power $P_{el,ST}$. Overall, the ST lumped volume model is divided into two numerically equivalent subsystems (not shown in figure 6.25), since steam extraction is performed at intermediate pressure to cover thermal power demand onboard. Similarly to the numerical scheme of turbines previously illustrated in figure 6.13, the mass flow exiting ST is obtained from the $(\varepsilon_{ST}, N_{ST}/\sqrt{T_{i,ST}}, \dot{m}_{s,i,ST}\sqrt{T_{i,ST}}/p_{i,ST})$ map reported in figure 6.25. At the exit of the HP steam turbine subsystem, the mass flow rate is subtracted from the extracted steam necessary to cover thermal power demand onboard and the result is provided as input to the LP subsystem. Power delivered by both HP and LP steam turbine modules is

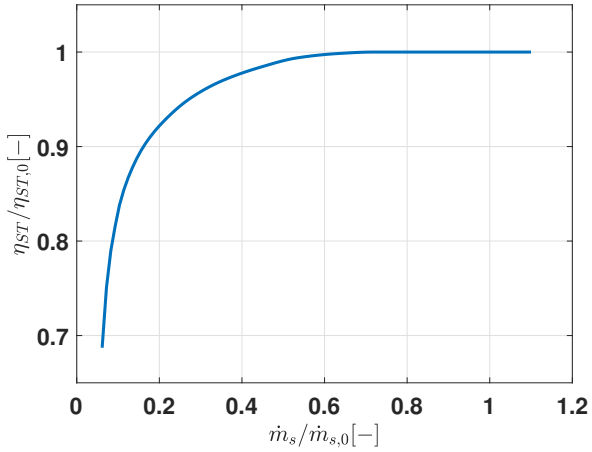

Fig. 6.26 Effect of partialization regulation on steam turbine efficiency.

computed by means of eq. (6.46):

$$P_{ST} = (h_{i,ST} - h_{o,ST,id})\dot{m}_s\eta_{ST} \tag{6.46}$$

Specifically, the adiabatic efficiency reduction occurring in off-design conditions is derived from figure 6.26, where the x-axis represents the partialization fraction [269]. Indeed, since partialization is able to regulate steam turbine operating conditions with reduced efficiency penalties in comparison with lamination, it is used to govern the bottoming steam power plant when GT works at part-loads [270, 271]. Specifically, the PAR block contains partialization control curves. The exhaust gas mass flow rate and temperature provided by the GT are entered as inputs in the PAR block, since waste thermal power available for heat recovery

in the HRSG is used to obtain in output the steam mass flow rate evolving within ST under partialization regulation [272, 273]. Therefore, the steam power plant follows the operating conditions of the topping GT cycle: partialization regulation is performed in function of the thermal power available from GT, whereas liquid level in both EVA and COND is maintained constant for safety reason. Overall, the interconnecting protocol as well as the control strategy adopted for the steam bottoming power plant appear in line with the work of Benato et al. [252]. Finally, it must be underlined that the Simulink code presented above can be applied to dynamically simulate COGES plants fed by methane as well as by other fuels.

6.2.4 Validation

In this section, as a final remarked on the MATLAB/Simulink codes, validation is performed for both gas turbine and steam power plant models.
Where validation of the GT code is concerned, the reliability of both nominal and part-load simulation is investigated, focusing on the main thermodynamic parameters. Dataset considered for validation consists in experimental results referring to a 32 MW LM2500+G4 GT fed by MDO which is currently installed onboard military ships of various Navies [274]. Furthermore, the main governing strategy actually implemented within the Turbine Control System (TCS) of this engine consists in regulating the fuel mass flow rate in function of the gas generator rotational speed. Power delivered by PT directly follows as a consequence. Other safety control strategies, aimed at avoiding over-temperature at the GG outlet and over-speed of power turbine shaft, are also included within the TCS. Since experimental dataset used for validation refers to mechanical propulsion architecture and the MATLAB/Simulink code applies to integrated electric scheme, few modifications have been inserted in the program to guarantee comparability. Specifically, the MATLAB/Simulink code has been modified to account for MDO feeding system, control strategies embedded with TCS and the presence of propeller on the PT shaft, instead of alternator. Comparison between experimental data available from the manufacturers and numerical results provided by the code is performed in table 6.2. Specifically, relative errors defined as $(V_{exp} - V_{num})/V_{exp}$, where V_{exp} and V_{num} represent the experimental and numerical values of each parameter, respectively, are reported. Comparison is carried out considering 25, 50, 75 and 100% load operating conditions. As can be seen, relative errors do not exceed 2% for all the parameters experimentally available from the manufacturer, over the entire load range from 25 to 100%. Therefore, the reliability and accuracy the MATLAB/Simulink code described in sections 6.1.1 and 6.2.1 appears well established.
Where validation of the bottoming steam power plant is concerned, data referring to the

Table 6.2 Relative errors obtained comparing experimental data and numerical results for LM2500+G4 gas turbine at 25%, 50%, 75% and 100% load operating conditions.

Parameters	**100 %**	**75 %**	**50 %**	**25 %**
P_{el}	0.06	0.07	0.06	0.05
η_{el}	0.52	1.84	1.47	0.70
N_{GG}	1.21	-0.03	-0.23	0.26
N_{PT}	0.00	0.00	0.00	0.00
$\dot{m}_f$	-0.53	-1.85	-1.48	-0.66
$P_{i,cc}$	0.15	0.55	1.03	1.62
$T_{i,cc}$	0.19	-0.26	-0.25	0.55
$P_{o,TGG}$	-1.46	-0.85	-0.08	1.03
$T_{o,TGG}$	1.40	-0.03	-0.21	0.25

natural gas fed combined cycle located at the Oseberg Field Center, in the North Sea [37], have been considered. The reference power plant includes two GE LM2500+ GTs, each driving a gas compressor and coupled with a one pressure level HRSG. Steam is produced at nearly 24 bar and feeds a condensing ST, which expands the flow up to 0.05 bar for electrical power generation purposes. Sea water at 8 °C ($T_{amb} = 9$ °C) is used as coolant in condenser, whereas both sliding pressure or partialization control modes are available for steam turbine. Comparison between the thermodynamic parameters reported by Nord and Montañés [37] and numerical results obtained by the model shown in figure 6.21 is carried out in table 6.3. Specifically, relative errors defined as $(V_R - V_{num})/V_R$ are shown for 20%, 40%, 60%, 80% and 100% load operating conditions of the LM2500+ GT. Validation accounts for data concerning the ST inlet pressure $p_{i,ST}$ and temperature $T_{i,ST}$, the rotational speed of ST N_{ST}, the steam mass flow rate $\dot{m}_s$ evolving within ST, the discharge pressure at condenser p_{COND}, the sea water mass flow rate $\dot{m}_{sea,COND}$ required for condensing purposes, the exhaust gas temperature T_{ex} and mass flow rate $\dot{m}_{ex}$ from the LM2500+ gas turbine and, finally, the electrical power delivered by steam turbine $P_{el,ST}$. Results obtained from the steam power plant model appear in good agreement with data reported by Nord and Montañés [37]. Specifically, relative errors do not exceed 2%, over the entire 20%-100% load range accounted for GT. Thus, the MATLAB/Simulink code shown in figure 3 is proved to reliably model the design and off-design performances of the bottoming steam power plant included within COGES. Finally, it must be underlined here that information on time dependent results is not available from the reference works considered for validation purposes, hence transient behaviour of both gas turbine and steam power plant is not reported here. Nevertheless, as shown in section 9.2.2, time dependent results obtained from the dynamical models well agree with both physics principles and scientific literature. Specifically, dead times, first order

Table 6.3 Relative errors obtained comparing reference datasets from the Oseberg Field Center combined cycle [37] with simulation results for the bottoming steam power plant shown in figure 6.21. Comparison has been carried out at 20%, 40%, 60%, 80% and 100% GT load operating conditions.

Parameters	**100 %**	**80 %**	**60 %**	**40 %**	**20 %**
$p_{i,ST}$	0.00	+0.06	+0.06	+0.15	+0.15
$T_{i,ST}$	+1.87	1.25	+1.05	+0.83	-0.26
$\dot{m}_{s,i,ST}$	-0.10	-0.53	-0.30	-0.31	-0.04
p_{COND}	-0.3	-0.64	-0.98	-1.32	-1.62
N_{ST}	0.00	0.00	0.00	0.00	0.00
P_{el}	-0.09	+0.52	+1.31	+0.88	+1.04
$\dot{m}_{sea,COND}$	-0.98	+0.13	-1.91	-0.08	+1.33
T_{ex}	-1.50	-1.30	-1.25	0.00	-0.01
$\dot{m}_{ex}$	-0.01	+0.07	-0.02	+0.07	+0.01

delays, thermo-mechanical inertia as well as transient response shape are proven practically reasonable for the machines considered in this work.

Chapter 7

Fortran code

In this section, a Fortran code for static simulation of ship power plants is described in details. Specifically, the code allows to identify which prime mover combination among those available within the engine room guarantees the highest power plant efficiency under various ship operating conditions. Steady state modeling for most of power plant components is implemented within the code. Two kinds of inputs need to be supplied:

- Performance data for prime movers included within the engine room, computed at variable load and ambient temperature. Specifically, loads ranging in 50-100% with step of 10% and ambient temperature grid dealing with 5 °C step, from 5 to 45 °C, are provided in tabular form together with the corresponding values achieved for net power P_{net}, electrical efficiency η_{el}, exhaust gas temperature T_{ex} and mass flow rate $\dot{m}_{ex}$. Prime movers that can be inserted in the engine room consist in GTs, successively coupled with steam bottoming power plants in COGES configuration, as well as reciprocating engines.

- Electrical and thermal power demands onboard the ship under study. Specifically, since only integrated propulsion systems can be analysed, electrical power comprehensive of both propulsion and hotel demands is provided as input. Instead, thermal power demands is divided into low and high temperature components, consisting in steam flows at $p = 7 - 9$ bar, $T \approx 100$ °C and steam/hot water supply at $p = 3$ bar, $T \approx$ 50-80 °C, respectively. Power demands onboard ships can be provided for each specific operating condition (maneuvering, navigation and port), vessel speed and weather condition.

Overall, the working principle of the Fortran code can be summarised into three main steps:

- Design of waste heat recovery systems downstream of prime movers: this point consists in performing design of waste heat recovery system (WHR) and Heat Recovery Steam Generator (HRSG) for reciprocating engines and gas turbines, respectively. All the prime movers considered within the engine room can deal with this design step, otherwise only a specific subset of them can be accounted for. Furthermore, the waste heat recovery system for reciprocating engines can be configured as the standard WHR system traditionally used onboard for reduced thermal power generation, or a complete steam bottoming power plant can be set up (see figure 7.1). Where the latter choice is

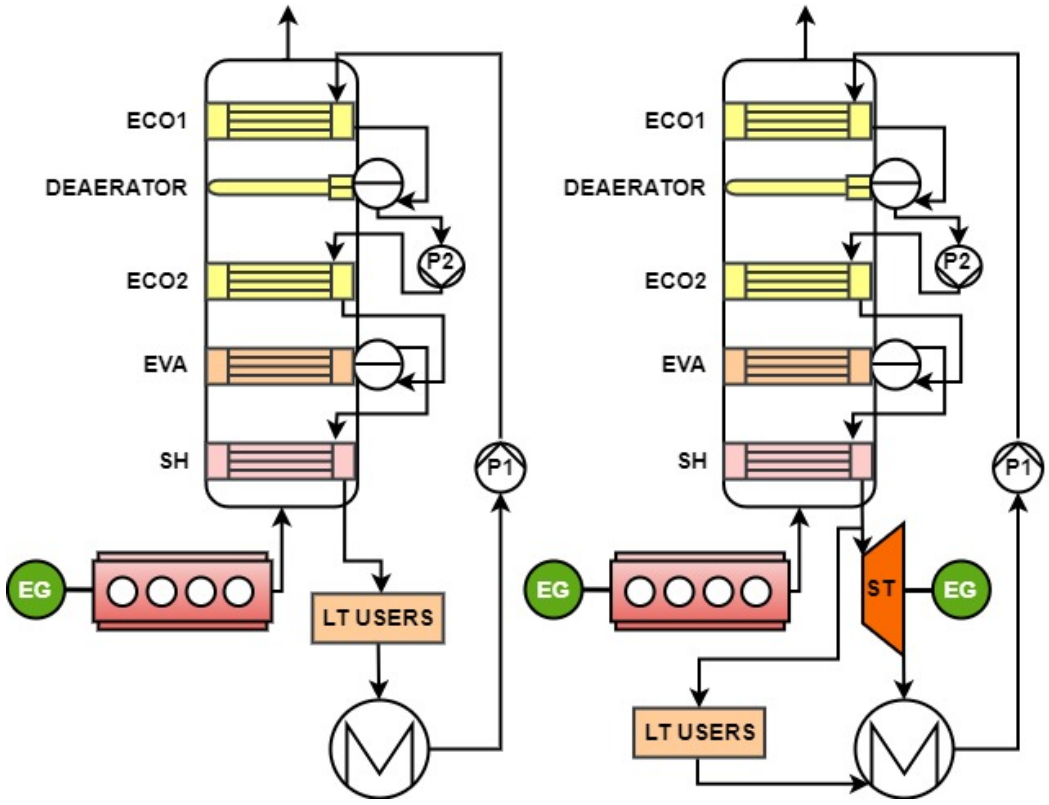

(a)

Fig. 7.1 Schematic view of the two layouts available for reciprocating engines in the Fortran code: without ST included (left side) or equipped with it (right side).

concerned, excessive steam generated by WHR systems evolves into small-size ST producing few additional MWs of electricity, with consequent benefits by an energy saving point of view, depending on power demands. On the other hand, since large amount of thermal power is available within the gas turbine exhaust gas (i.e. high temperature

and mass flow rates) in comparison to reciprocating engines, GTs are always coupled with HRSG and complete bottoming steam power cycle in COGES configuration. Thus, energy efficiency can be improved by producing significant amount of additional electrical power within steam turbine. It must be underlined that condensing steam turbine configuration is only available for reciprocating engines, whereas both back-pressure and condensing architectures are possible for ST installed within COGES plant. Indeed, the small amount of thermal power available in the exhaust gas from reciprocating engines drastically reduces the maximum steam pressure achievable within WHR systems ($\approx$7-9 bar). Therefore, not negligible P_{el} can only be addressed by a condensing steam turbine configuration, since too small pressure gap would be exploited in back-pressure scheme. This issue does not arise for COGES plants. Specifically, alternately back-pressure or condensing architectures can reveal more convenient, depending on thermal and electrical power demands onboard. Overall, high temperature (HT) thermal power demand onboard, which typically corresponds to steam demand at p =7-9 bar, can be covered by both steam generated within the WHR systems of reciprocating engines and steam extracted at proper pressure level from the ST being part of the COGES plant. Similarly, steam generated by WHR systems and exceeding the HT request as well as steam mass flow rate exiting back-pressure ST combined with GT can supply the low temperature (LT) thermal power demand onboard, which traditionally consists of steam at p =3 bar. When HT and LT demands are partially covered by heat recovery from prime movers, dedicated auxiliary boilers are accounted for in setting up the engine room. Nevertheless, the WHR system and HRSG are designed such to optimize the heat recovery from all the prime movers, hence ensuring high efficiency under flexible sailing conditions.

- Off-design performance computation: performances of all the prime movers coupled with their corresponding WHR or HRSG systems are assessed for variable load and ambient temperature. Specifically, the working conditions of prime movers in terms of P_{net}, η_{el}, T_{ex}, $\dot{m}_{ex}$ are found out by interpolation of the tabular data provided as inputs, as mentioned in the previous step. Successively, off-design for the waste heat recovery systems is addressed by thermodynamic relations, since geometrical characteristics of WHR and HRSG result fixed at this step. Evidently, off-design performance computation depends on the same configurations reported above for the design procedure (back-pressure/condensing steam turbine, traditional WHR/complete bottoming steam power plant,...).

- Power plant optimal working conditions: once off-design investigation is concluded, the engine room governing strategy allowing for maximization of the overall power plant performance with respect to demands is determined. Specifically, two objective functions are available, depending on the amount of thermal power requested onboard: electrical or cogeneration efficiency of the entire power plant, i.e. η_{el} or η_g, respectively. Then, the code determines which prime movers need to be turned on and at which corresponding load, with the aim of maximizing the chosen objective function. This procedure is repeated for every ship operating condition (ship speed and weather) included in the mission profile of the vessel provided as input. Finally, the overall objective function (i.e. η_{el} or η_g) achieved during the entire profile together with details on the operating conditions of prime movers are obtained as results.

7.1 Optimal design of waste heat recovery systems

As mentioned above, the design of WHR and HRSG systems for reciprocating engines and gas turbine is firstly performed. In the following, a schematic treatment is presented. For the sake of conciseness, the procedure is explained referring to the HRSG installed within COGES plants, since analogous procedure is assessed also for WHR systems downstream of reciprocating engines.

- As starting point, inputs concerning first-hypothesis values as well as range variation for both geometrical and fluid dynamics parameters are acquired. Specifically, where the geometrical parameters are concerned, the width W and length L of the HRSG section, pitch and external diameter of tubes, Pt and d_O respectively, pitch parallel to the flow direction Pt_p and the presence of fins on tubes to improve heat exchange are provided as inputs (see figure 7.2 for more details on the geometry considered). On the other hand, target velocity traditionally applied to both steam/water and exhaust gas flow in HRSG [275, 276, 271, 270] are provided as inputs, distinguishing for each heat exchanger. Further first-hypothesis values considered consist in pinch-point and subcooling temperature differences (i.e. ΔT_{pp} and ΔT_{sub}, respectively), steam turbine inlet pressure and temperature and recirculating ratio in the evaporator.

- Then, the entire bottoming steam power cycle is solved in non-definitive form using the first-hypothesis values previously acquired as inputs. A schematic view of the gas and water/steam transformations within the HRSG, with corresponding numbering points, is shown in figure 7.3 for a condensing ST arrangement. The subscript g is used for

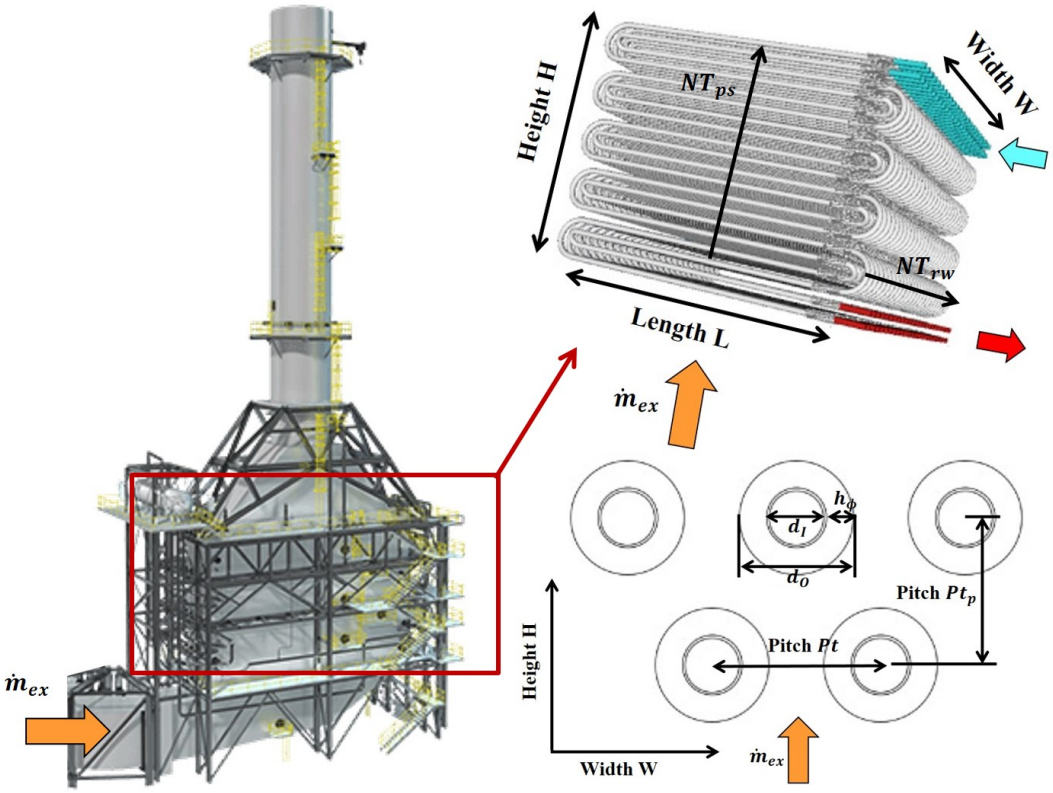

Fig. 7.2 Geometrical parameters of Heat Recovery Steam Generator (HRSG).

gas side for sake of clearness. Boiling-tubes configuration is assumed for deaerator, in order to remove dissolved gas from the boiler feedwater and limit energy penalties on the steam power plant efficiency. First, the thermal power to be exchanged in evaporator and superheater is found out from $h_{1g} = f(T_{1g})$ and $h_{3g} = f(\Delta T_{pp} + T(p_8, \tilde{x} = 1))$ and successively used to estimate the water mass flow rate $\dot{m}_w$:

$$\dot{q}_{SH+EVA} = \dot{m}_{ex}(h_{1g} - h_{3g}) \implies \dot{m}_w = \dot{q}_{SH+EVA}/(h_8 - h_6) \tag{7.1}$$

where $\dot{m}_{ex}$ is the GT exhaust mass flow rate, $h_6 = f(p_{EVA}, \tilde{x} = 0)$ and $h_8 = f(p_8, T_8)$. Then, preliminary steam cycle computation is performed by means of the following

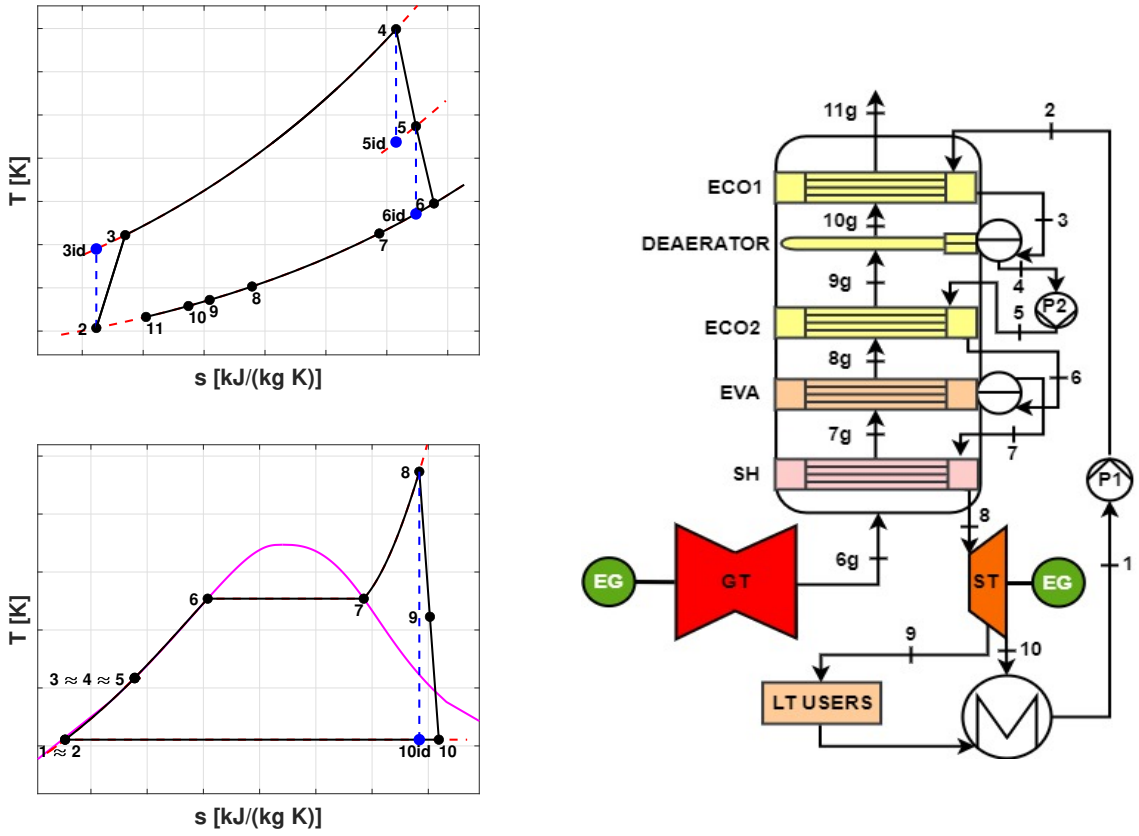

Fig. 7.3 Schematic view of the gas and water/steam transformations in a COGES plant. Where the plant scheme is concerned (right side), the subscript g is used for gas side for sake of clearness.

equations:

$$
\begin{aligned}
h_1, s_1 &= f(p_1, \tilde{x} = 0) \\
h_{2id} &= f(p_2, s_1) \\
h_2 &= f(h_{2id}, \eta_p, h_1) \\
h_3, s_3 &= f(p_3, T_3) \\
h_4, S_4 &= f(p_4, \tilde{x} = 0) \\
h_{se} &= f(T_{s,BT}, p_{s,BT}) \\
\dot{m}_{s,dea} &= \dot{m}_w (h_4 - h_3)/(h_{se} - h_4) \\
\dot{q}_{BT} &= \dot{m}_{s,dea}(h_{se} - h_4) \\
h_{5id} &= f(p_5, s_4) \\
h_5 &= f(h_{5id}, \eta_p, h_4) \\
s_6 &= f(p_{EVA}, \tilde{x} = 0) \\
h_7, s_7 &= f(p_{EVA}, \tilde{x} = 1) \\
s_8 &= f(p_8, T_8) \\
h_{9id} &= f(p_9, s_8) \\
h_9 &= f(h_{9id}, \eta_{ST}, h_8) \\
h_{10id} &= f(p_{10}, s_9) \\
h_{10} &= f(h_{10id}, \eta_{ST}, h_9)
\end{aligned}
\tag{7.2}
$$

Once the steam/water side is solved, thermodynamic points related to the exhaust gas cooling process are determined by means of analogous relations. Specifically, thermodynamics properties of air are evaluated by means of the NASA polynomial [277], corrected to reproduce recent correlations available in Refprop [278]. Since for a fixed mass flow rate variations in density provided by temperature levels directly influence the volume necessary for flow passage, the first-hypothesis value of L as well as density at the HRSG exit are used to compute the preliminary width W of HRSG:

$$W = \dot{m}_{ex}/V_{ex,max}/\rho_{4g})/L \tag{7.3}$$

In case back-pressure steam turbine is adopted, the numerical procedure changes, since the LP economizer (i.e. transformation 2-3), the deaerator (i.e. transformation 3-4) and the condenser are not included due to the single pressure level. Precisely, transformation 10-1 in figure 7.3 is directly carried out within the LT thermal users.

- Then, pressure and temperature levels obtained from the previous step are used to perform geometrical design of each HE included within HRSG. Specifically, the thermal power to be exchanged and minimum/maximum thermal capacities (i.e. C_{min}/C_{max})

are first computed in order to perform the NTU-$\tilde{\varepsilon}$ sizing method for heat exchangers:

$$\tilde{R} = C_{min}/C_{max} \tag{7.4}$$

$$\dot{q} = \dot{m}_{ex}(h_{1h} - h_{2h}) \tag{7.5}$$

$$\dot{q}_{max} = C_{min}(T_{1h} - T_{1c}) \tag{7.6}$$

$$\tilde{\varepsilon} = \dot{q}/\dot{q}_{max} \tag{7.7}$$

$$NTU = f(\tilde{R}, \tilde{\varepsilon}) \tag{7.8}$$

where the subscripts 1 and 2 indicate inlet and outlet sections, respectively, whereas h is used for exhaust gas (i.e. hot side) and c for water/steam (i.e. cold side). Successively, iterative procedure is applied to definitely determine both geometrical and fluid dynamics parameters, whose preliminary values were acquired as inputs. Specifically, starting values for pitch Pt, v and W/L are provided as inputs to compute both exchange surface area and HE geometry, whereas fluid dynamics parameters yield heat transfer coefficients for hot and cold sides. Where the exhaust gas side is concerned, the corresponding Reynolds number Re_h is obtained by:

$$Re_h = \dot{m}_{ex} d_O/(O\,L\,W\,\mu) \tag{7.9}$$

where d_O is the external diameter of tubes and $O = (P\,d_O - d_O - 2H_\phi)/(P\,d_O)$ is a parameter taking into account obstruction due to fins in case no brace tubes are installed. Then, Nusselt number concerning the hot side is computed from the ESCOA [279] or Grimson's [280] correlations, for finned-tubes and brace-tubes HEs, respectively. Finally, the overall heat transfer coefficient for the hot side (i.e. U_h) is found out by:

$$U_h = Nu_h\,\lambda/d_O \tag{7.10}$$

where λ indicates thermal conductivity. Focusing on the cold side, the overall heat transfer coefficient U_c is obtained in two different ways depending on possible phase-change for circulating H_2O. For single-phase HE, the definition of U_c is used together with the Dittus-Boelter correlation for turbulent flows:

$$U_c = Nu_c\lambda/d_I) \tag{7.11}$$

$$Nu_c = 0.023Pr^{0.333}Re_c^{0.8} \tag{7.12}$$

where λ represents the thermal conductivity of water/steam, d_I the internal diameter of tubes, Pr the Prandtl number and Re_c the Reynolds number of the cold side. Instead, where evaporator and deaerator are concerned, since heat transfer occurring in changing-phase flows is significantly improved in comparison to gas forced convection taking place on the hot side, an arbitrary high value for U_c has been assumed. Finally, the overall heat transfer coefficient involved between the cold and hot side is used to obtain the exchange surface area required for the component considered:

$$U = 1.0/((1.0+AR_\phi)/U_c + 1.0/(U_h \eta_\phi)) \tag{7.13}$$

$$S = NTUC_{min}/U \tag{7.14}$$

where the fin efficiency η_ϕ is 1 in case brace tubes are considered. The overall heat exchange surface and the tube surface $S_T = \pi d_O L(1+AR_\phi)$, where AR_ϕ represents increase in exchange area due to fins, are successively used to determine the number and disposition of tubes in the HE:

$$NT_{sf} = int(S/S_T) \tag{7.15}$$

$$NT_{rw} = int(W/(Ptd_O)) \tag{7.16}$$

$$n_{rw} = NT_{sf}/NT_{ps} \tag{7.17}$$

where NT_{sf} is the overall number of tubes in the HE guaranteeing the correct exchange surface area, NT_{rw} is the tube number on each HRSG cross-sectional plane (W,L) the HE is organised in, NT_{ps} represents the number of passages each tube deals with along H and n_{rw} consists in the number of distinct tube rows the HE develops along the vertical direction (see figure 7.2 for more details). Then, the definitive values for the height H of the HE within HRSG, the overall number of tubes NT_{all} and the corresponding heat exchange surface S are computed:

$$H = Pt_p \, d_O \, n_{rw} \tag{7.18}$$

$$NT_{all} = n_{rw} \, NT_{ps} \tag{7.19}$$

$$S = S_T \, n_{rw} \, NT \, p \tag{7.20}$$

The effective flow velocity in tubes $V_{c,eff}$ is successively obtained by $V_{c,eff} = \dot{m}_w/\rho_c/A_T/NT_{ps}$, where $A_T = \pi d_I^2/4$ is the cross-sectional area of the tube. If relative error between effective and reference flow velocity exceeds a certain threshold,

then iteration on geometry parameters is needed, moving within ranges supplied by input files. Specifically, the first parameter to be varied is length L while keeping constant WL, i.e. the cross-sectional area of HE. Overall, minimum and maximum values imposed for W/L are 0.5 and 2.5, respectively. In case requirements on $V_{c,eff}$ are not ensured yet, the pitch value is additionally changed between 2 and 4. When variations on new variable is introduced, all the geometric parameters involved within the optimization procedure are initialized with the first-hypothesis values. In this way, the solution space around initial point derived from the literature is accurately explored. It must be remarked that the design algorithm reported above overall consists in an optimization procedure, whose objective functions to be minimized coincide with gaps arising between actual geometrical and fluid dynamics parameters and the preliminary ones, i.e. those traditionally assumed in the literature. When convergence is reached, the heat exchanger deals with geometry and flow velocity constraints. Finally, the distributed and localised pressure losses in the heat exchanger considered are computed by eq. (6.38). The above procedure is sequentially applied to each heat exchanger included within the HRSG system. This implies that different optimal values for L may be obtained for distinct HEs. However, despite width W in HRSG can vary passing from a heat exchanger to an other, the length L must be kept fixed to guarantee simple and compact HRSG layout onboard ships. Thus, once geometrical parameters of each optimally designed HE have been found out, the maximum value of L among those obtained is imposed within the entire the HRSG. Indeed, due to the optimization algorithm reported above, the maximum L relates to the most demanding heat exchanger. Then, thermodynamic cycle computation for the bottoming steam power plant as well as HE geometrical sizing (NT_{all}, n_{rw}, ...) are iteratively performed with no changes on L allowed yet. Overall, convergence on geometrical and fluid dynamics parameters of HRSG as well as on thermodynamic cycle is reached within 10 iterations. The above procedure ends the HRSG design. On the other hand, from now on, the numerical algorithm adopted for condenser design is presented [281]. The main geometrical inputs required consist in baffle spacing $\tilde{B}$, baffle cut BC, baffle number n_β, external diameter of tubes d_O, tube pitch Pt, tube clearance $C_t = Pt - d_O$, number of tube passages NT_{ps} (see figure 7.4). On the other hand, thermal inputs consist of the sea water inlet temperature $T_{sea,i}$, its corresponding increase while passing through condenser ΔT_{sea} and the thermal power to be wasted $\dot{q}_{COND}$. As starting point, the logarithmic mean temperature difference for condenser is computed:

$$LMTD = \frac{T_{sea,o} - T_{sea,i}}{ln((T_{sat} - T_{sea,i})/(T_{sat} - T_{sea,o}))} \tag{7.21}$$

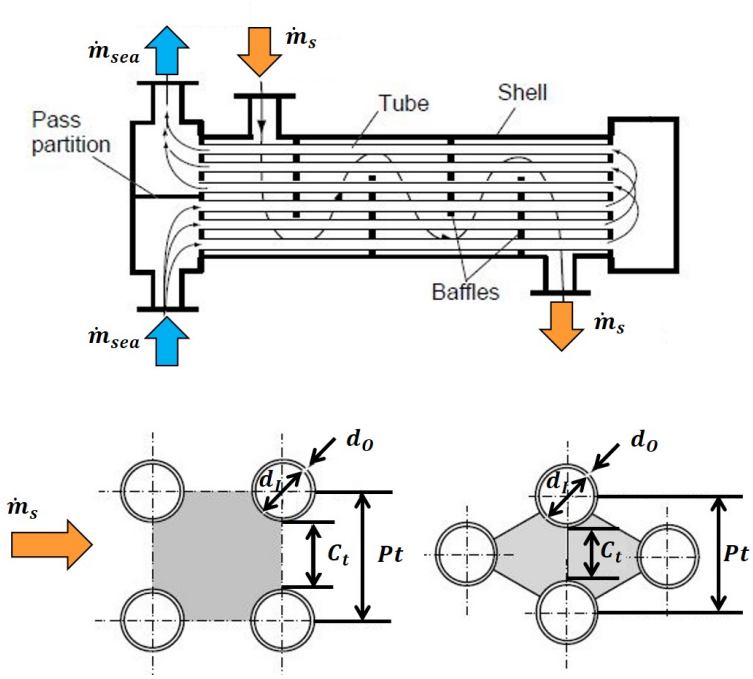

Fig. 7.4 Geometrical parameters of condenser.

where T_{sat} represents the saturation temperature at the condenser pressure (i.e. $T_{sat} = T(p_{COND}, \tilde{x} = 0)$). Then, Reynolds number traditionally imposed by the literature

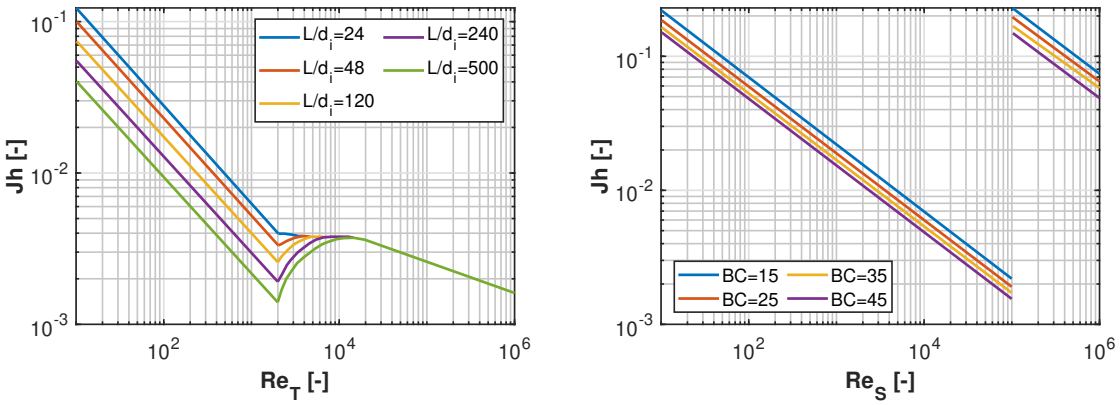

Fig. 7.5 Diagrams providing the heat transfer factor Jh for tube (a) and shell (b) sides.

for both shell and tube sides is assumed to find the heat transfer factor Jh from the experimental diagrams reported in figure 7.5. Typical values of the Reynolds number within the shell and tube side are 35000 and 11000, respectively. By using the definition of Jh, the convective heat transfer coefficient on the tube side (i.e. ξ_I) can be obtained

from:

$$JH = JhRe_T = \frac{\xi_I d_I}{\lambda_{sea}} \frac{c_{p,sea}\mu_{sea}}{\lambda_{sea}}^{-1/3} (\frac{\mu_{sea}}{\mu_{wall}})^{-0.14} = Nu_T Pr^{-1/3} (\frac{\mu_{sea}}{\mu_{wall}})^{-0.14} \quad (7.22)$$

where Re_T and Nu_T are the Reynolds and Nusselt number on the tube side, μ indicates the dynamic viscosity, λ the thermal conductivity, c_p the constant pressure heat coefficient and d_I the internal diameter of tubes. Furthermore, if the influence of temperature on viscosity is neglected, the viscosity correction factor μ_{sea}/μ_{wall} is imposed to 1. Successively, hypothesis on the convective heat transfer coefficient on the shell side (i.e. ξ_O) is made to compute preliminary values of the wall and film temperatures, i.e. T_{wall} and T_{film} respectively, where condensed water forms:

$$T_{wall} = T_{c,avg} + (\xi_O(T_{sat} - T_{c,avg}))/(\xi_I d_I/d_O + \xi_O) \quad (7.23)$$

$$T_{film} = (T_w + T_{sat})/2 \quad (7.24)$$

where $T_{c,avg}$ is the average temperature on the cold side. Depending on square or triangular pitch is assumed, the equivalent diameter d_{eq} of the shell is computed as:

$$d_{eq} = 4(Pt^2 - \pi d_O^2/4)/(\pi d_O) \quad (square\ pitch) \quad (7.25)$$

$$d_{eq} = 4(\sqrt{3}/4Pt^2 - \pi d_O^2/8)/(\pi d_O) \quad (triangular\ pitch) \quad (7.26)$$

and inserted into eq. (7.27) to obtain a calculated value of the external heat transfer coefficient ξ_O:

$$JH = (\xi_O d_{eq})/\lambda_s((c_{p,s}\mu_s)/\lambda_s)^{-1/3}(\mu_s/\mu_{wall})^{-0.14} \quad (7.27)$$

where the subscript s refers to steam. In case hypothesised and computed values for ξ_O are not coincident, iteration on ξ_O is performed starting loop at eq. (7.23). When convergence is reached, the overall heat transfer coefficient U of the condenser can be assessed by:

$$U = (1/\xi_O + RO + S_O/S_I(d_O - d_I)/(2\lambda_w) + S_O/S_I 1/\xi_I + S_O/S_I RI)^{-1} \quad (7.28)$$

where RO and RI are the dirt factor on the shell and tube sides, respectively, as S_O and S_I represents the surface area for the shell and tube side related to geometry. Once the global heat transfer coefficient is known, the overall exchange surface area S as well as

the exchange area of a single tube S_T are obtained:

$$S = \dot{q}_{COND}/(U\ LMTD) \tag{7.29}$$

$$S_T = \pi d_O L \tag{7.30}$$

where L is the tube length. Thus, the overall number of tubes $NT_{all} = int(S/S_T)$ can be found. Then, assuming a value for the number of tube passages NT_{ps}, the Reynolds number within tubes is obtained by $Re_c = \dot{m}_{sea}(4NT_{ps}/NT_{all})/(d_I \mu_{sea} \pi)$, where $\dot{m}_{sea}$ is the sea water mass flow rate. Where the geometrical parameters of the shell are concerned, the bundle diameter d_β and length L_β are estimated as:

$$d_\beta = d_O(NT_{all}/K_1)^{1/n} \tag{7.31}$$

$$L_\beta = L/NT_{ps} \tag{7.32}$$

where K_1 and n are parameters evaluated from the tables 7.6 below, depending on pitch, NT_{ps} and tube arrangement. Instead, the shell diameter d_S able to contain the overall number of tubes is chosen from the tube count tables for heat exchangers available in the literature [282]. The cross-sectional area A_S and Reynolds number Re_S of the shell

d_O [mm]	Pt [mm] (square)	Pt [mm] (triangular)
16	22	20
19	25	25
25	32	32
32	39	39
38	47	47

Pt=1.25 d_O (triangular)					
NT_{ps}	1	2	4	6	8
K_1	0.319	0.249	0.175	0.0743	0.0365
n	2.142	2.207	2.285	2.499	2.675
Pt=1.25 d_O (square)					
NT_{ps}	1	2	4	6	8
K_1	0.215	0.156	0.158	0.0402	0.0331
n	2.207	2.291	2.263	2.617	2.643

Fig. 7.6 Tables for computing K_1 and n parameters during condenser design.

are computed as:

$$A_S = (d_S C_t B)/P \tag{7.33}$$

$$Re_S = \dot{m}_s d_{eq}/(A_S \mu) \tag{7.34}$$

Finally, pressure losses of both shell and tube side (Δp_S and Δp_T, respectively) can be evaluated:

$$\Delta p_T = 4((fL)/d_I + 1)NT_{ps}/2\rho V^2 \tag{7.35}$$

$$\Delta p_S = (f d_S)/d_{eq}(n_\beta + 1)/2\rho V^2 \tag{7.36}$$

where V indicates velocity, $f = (1.58ln(Re_T) - 3.28)^{-2}$ (tube side), $f = e^{0.576-0.19ln(Re_S)}$ (shell side) and $V = Re_S\mu_s/(d_{eq}\rho_s)$. The above procedure, often referred to Kern's method, ends the condenser design.

As a final remark concerning the first step performed by the Fortran code, the design procedure repeats for WHR systems of reciprocating engines with few differences with respect to what has been shown above referring to HRSG in COGES plant. Indeed, differences mainly arise from the possibility of excluding steam turbine and condenser from the WHR system. Furthermore, since reduced thermal power is available from the exhaust gas of reciprocating engines, no further heat exchanger for hot water production is present downstream economizer.

7.2 Off-design of the steam power plant

At this step, geometry of all the HEs included within HRSG is known and their off-design performance in terms of mass flow rates, temperatures, pressure losses and thermal powers are now investigated in case variations on $\dot{m}_{ex}$ and T_{ex} occur. As starting point, the steam mass flow rate generated by SH is estimated assuming linear proportionality with exhaust gas flow rate of GT: $\dot{m}_s = \dot{m}_{s,0}\dot{m}_{ex}/\dot{m}_{ex,0}$, where subscript 0 refers to nominal values. Then, off-design performance of each HE is assessed in terms of inlet temperatures on hot and cold sides together with exhaust gas and water mass flow rates. It must be remarked that superior and inferior pressure levels under off-design conditions are assumed to remain fixed to those found out in the design analysis, except for pressure losses. This well agrees with actual operation of steam power plants, where the evaporator drum dampens the pressure variations induced by transient operation of pumps. Thus, the computation starts from the superheater, where $T_{1h} = T_{ex}$ and T_{1c} coincides with the saturation temperature at the evaporator pressure. Analogous procedure is successively applied to all the other HEs. In details, focusing on the hot side, Re_h, which is influenced by $\dot{m}_{ex}$ reduction occurring at GT part-loads, is computed from its definition (7.9) and successively used as input within the ESCOA [279] or Grimson's [280] correlation to find out the overall off-design heat transfer coefficient U_h in case of finned or braced tubes. Where the cold side is concerned, Nu_c is obtained from the Dittus-Boelter correlation reported in eq. (7.12) above. Specifically, reduction of the amount steam generated at part-loads is accounted for in Re_c. Analogously to what made under design conditions, the heat transfer coefficient U_c for the water/steam side is derived from Nu_c and successively inserted in eq. (7.37) to compute the overall heat

transfer coefficient U:

$$U = 1.0/((1.0+AR_{\phi})/U_c + 1.0/(U_h \eta_{\phi})) \tag{7.37}$$

Then, once minimum and maximum capacities are identified depending on the HE considered, $NTU = SU/C_{min}$ and $\tilde{R} = C_{min}/C_{max}$ are computed and used to found out the heat exchanger efficiency $\tilde{\varepsilon}$ by the $(NTU, \tilde{\varepsilon})$ method. Finally, the exchanged thermal power $\dot{q}$ is obtained from eq. (7.38) below:

$$\dot{q} = \tilde{\varepsilon}\dot{q}_{max} = \tilde{\varepsilon}C_{min}(T_{1h} - T_{1c}) \tag{7.38}$$

and successively used to compute enthalpy h_{2h} and corresponding temperature T_{2h}:

$$h_{2h} = h_{1h} - Q/\dot{m}_{ex} \implies T_{2h} = f(h_{2h}) \tag{7.39}$$

Analogous procedure is followed for h_{2c} and T_{2c}, depending on the specific heat exchanger considered. The main results of off-design computation concerning each single HE consist in the exhaust gas and water/steam outlet temperatures, the corresponding thermal power exchanged and pressure losses (derived from eq. (6.38)). The algorithm reported above is sequentially applied for all the heat exchangers installed within the HRSG as well as for all the off-design conditions considered (in terms of GT loads and ambient temperature). Once

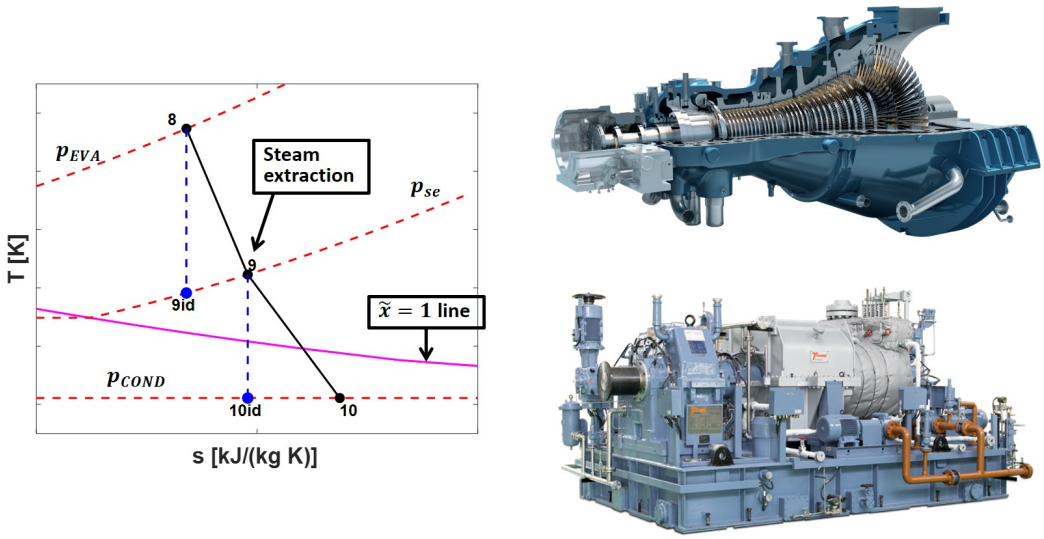

Fig. 7.7 Thermodynamic transformations concerning ST expansion (left side) together with schematic view of condensing steam turbines (right side) [29, 30].

the off-design performance of HRSG is known, the corresponding working conditions for steam turbine can be assessed. The turbine inlet pressure and temperature, together with both the overall steam mass flow rate and the ST exit pressure are provided as inputs. As mentioned

above, since steam extraction at intermediate pressure level is enabled for steam turbines coupled with GTs to cover the HT thermal power demand onboard, expansion in ST is split into two parts, each following analogous numerical approach. Focusing on the first expansion fraction (from p_8 to $p_9 \approx 7-9$ bar), point 9id in figure 7.7 needs to be firstly solved. In order to check if point 9id falls inside the two-phase region or superheated region, $s_{9id} = s_8$ is compared with $s = f(p_{HT}, \tilde{x} = 1)$. In case point 9id is inside the two-phase region, all its properties can be obtained from pressure and entropy. Conversely, hypotheses on T_{9id} are iteratively performed and checked by means of thermodynamic relation $s_{9id} = f(T_{9id}, p_{HT})$, where s_{9id} is known. Nevertheless, the enthalpy h_{9id} is obtained either as $f(s,p)$ or $f(T,p)$. Successively, adiabatic efficiency of the first expansion fraction in turbine is computed by means of polytropic efficiency η_{pol} and expansion ratio ε:

$$\eta_t = \frac{1-\varepsilon^{-(k-1)\eta_{pol,t}/k}}{1-\varepsilon^{-(k-1)/k}} \tag{7.40}$$

where $k = c_p/c_v$ for steam. From η_{ST} the enthalpy of the real state 9 can be derived. Again, in case the point 9r lays inside the two-phase region, then entropy $s_9 = f(h_9, p_{HT})$ is easily obtained. On the contrary, in case 9 is outside the bell, iterative loop on T_9 is performed until convergence on $h_9 = f(p_{HT}, T_9)$ is reached. The same approach is used for the second part of the expansion within ST (i.e. transformation 9-10). As a final step, for each off-design condition considered for the bottoming steam power plants, electrical power delivered by ST and thermal power covered by steam extraction at 7-9 bar are computed as:

$$P_{el} = \eta_{mecc}\eta_a(\dot{m}_{s,i,ST}(h_8 - h_{9id}) + \dot{m}_{s,o,ST}(h_9 - h_{10id})) \tag{7.41}$$

$$P_{th,HT} = (\dot{m}_{HT}(h_9 - h(p_{HT}, \tilde{x} = 0)) \tag{7.42}$$

Furthermore, off-design conditions in condenser are managed by adjusting the sea water mass flow rate in function of the thermal power to be wasted, by means of the following eq.:

$$P_{th,COND} = (\dot{m}_{w,o,COND}(h_{10} - h(p_{COND}, \tilde{x} = 0))) \tag{7.43}$$

$$\dot{m}_{sea} = \frac{P_{th,COND}}{c_{p,sea}\Delta T_{sea}} = \frac{\dot{m}_{w,o,COND}(h_{10} - h(p_{COND}, \tilde{x} = 0))}{c_{p,sea}\Delta T_{sea}} \tag{7.44}$$

where ΔT_{sea} is equal to 10 °C. It must be remarked that in case back-pressure steam turbine is considered, the second part of the expansion stops at 3 bar, i.e. pressure levels required from the LT thermal users installed onboard. Thus, the function of condenser is directly supplied by thermal users, from which condensed water is withdrawn. As underlined for

the design step, the off-design procedure introduced above for HRSG still applies with few differences for WHR systems of reciprocating engines. Specifically, since steam mass flow rate is generated at 7-9 bar by WHR systems, no steam extraction could be present within steam turbine and a single block expansion takes place.

7.3 Optimization of engine room operating condition

Once the off-design performances provided by each prime mover included within the engine room are obtained in terms of electrical and LT/HT thermal power generation, the Energy Management System (EMS) determines how to optimally match power demands onboard for each ship operating condition (weather, ship speed or phase). Specifically, a full-factorial optimization procedure has been implemented with the aim of identifying which prime movers need to be turned on and at which load, in order to maximize the objective function. As mentioned above, both electrical and cogeneration efficiencies are available objective functions. The implemented optimization procedure is reported in details in the following. First, electrical and thermal power demands onboard are acquired from input files and stored in specific data structures. Power data are coupled with their corresponding ship operating phase (port, maneuvering or navigation), weather condition (ambient temperature) and duration. Successively, settings for optimization algorithm are provided by the user. Specifically, choice concerning condensing/back-pressure steam turbine to be installed in COGES plant as well as the eventual installation of a unique ST also downstream all the reciprocating engine WHR systems is made. Analogously, the Engine Margin (EM) level desired for each different prime mover installed onboard is determined by the user. Finally, the main numerical settings concerning the multiple steps the optimization procedure consists in are fixed. Successively, from the off-design performances stored in tabular form from the previous step, a predefined grid is created for each prime mover referring to power delivered. Specifically, the 50-100% power interval analysed in the previous step concerning off-design conditions is discretised in n_{pt} points. For all the discretisation points considered, the corresponding electrical efficiency, LT/HT thermal power, exhaust gas temperature and mass flow rate are computed by interpolation of off-design tables. The same operation is made for all the n_{pm} prime movers assumed turned on within the engine room, hence n_{pm} vectors of size n_{pt} are finally obtained for each relevant parameter (P_{el}, $P_{th,LT}$, $P_{th,HT}$, load, η_{el}, ...). It must be remarked that increasingly high number of turned on prime movers is considered, in order to clearly identify which n_{pm} guarantees the objective function maximization. Linear algebra is successively used to organise these vectors in matrices containing all the possible

combinations concerning the prime movers operating conditions. As mentioned above, increasingly high number of turned on prime movers are iteratively considered, i.e. matrices of all the possible operating conditions are sequentially built for $n_{pm} \in [1, n_{er}]$, where n_{er} coincides with the overall number of prime movers included within the engine room. Focusing on the case a certain n_{pm} is imposed, all the combinations found out represent candidate solutions in terms of i-th prime mover parameters ($P_{el,i}$, $P_{th,LT,i}$, $P_{th,HT,i}$, $\eta_{el,i}$, ...) to cover power demands onboard. Therefore, all the candidate solutions are tested in maximizing the objective function while coping with power demand constraints. This is the well-known working principle of full-factorial optimization, where all the possible combinations are analysed to identify the best one. Figure 7.8 shows a schematic view of the optimization

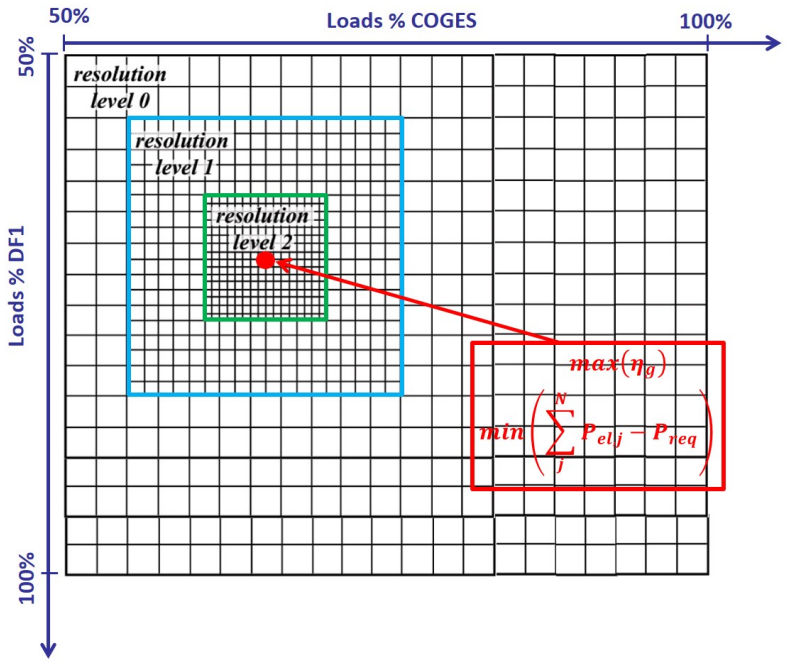

Fig. 7.8 Schematic view of the full-factorial optimization procedure performed by the Fortran code.

procedure performed in the code. Firstly, combinations of turned on prime movers providing electrical power excessively low or high are discarded, as they would generate electrical grid failures onboard. Specifically, the discarding condition is $\|P_{el,REQ} - P_{cand}\| > \Delta P_{el}$, where ΔP_{el} is the discretisation interval considered for electrical power, $P_{el,REQ}$ the electrical power demand and $P_{cand} = \sum_{i=1}^{n_{pm}} P_{el,i}$. A second discarding condition is represented by the maximum ship speed navigation condition as well as safety return to port, which must be guaranteed by turned on prime movers installed onboard. It must be remarked that discarding processes are performed neglecting LT/HT thermal power generated by prime movers. Indeed, auxiliary thermal boilers may be installed onboard, in case thermal power demands are not completely

supplied by waste heat recovered. On the other hand, electrical power can be exclusively delivered by prime movers, thus consisting in a more strict constraint to cope with. For all the combinations survived the discarding processes, the objective function (i.e. electrical or cogeneration efficiency) is computed and stored in memory. When objective functions related to all the non-discarded combinations have been computed, the best solution is identified. Though Fortran always reduces RAM requirements in comparison to interpreted programming languages, the full-factorial algorithm implemented result quite expensive, since it accounts for millions of candidates. Therefore, the number of point used to built prime mover grids cannot be infinitely high. Especially for large-size prime movers, this implies low accuracy in determining the optimal engine room operating condition. For this reason, the above full-factorial optimization algorithm is sequentially applied on prime mover grids dealing with finer discretisation. Specifically, as outlined in figure 7.8, after the best combination of turned on prime movers is identified using the first discretisation grid, a second, finer grid is defined around it, ranging from $P_{cand} - \Delta P_{el,p}$ to $P_{cand} + \Delta P_{el,p}$, where $\Delta P_{el,p}$ derives from the first discretisation. Then, the best combination of turned on prime movers is derived also from the second grid by comparing millions of candidates in terms of objective function. Therefore, the algorithm is repeatedly applied on more refined grids up to reach accurate results in terms of gap between $P_{el,REQ}$ and P_{cand} ($\approx 10W$). This optimization process is performed for each ship operating phase (navigation, port or maneuvering) and weather conditions included within the mission profile considered. The overall process takes few seconds to run, when nearly 1000 ship operating phases are analysed. As results of the optimization process, the main performance parameters (η_{el}, P_{el}, $P_{th,LT}$, $P_{th,HT}$, $\dot{m}_f$, ...) for each ship operating condition tested are obtained, distinguishing the contribution from each prime mover included within the engine room. Therefore, as a final step, the eventual inclusion of auxiliary boilers to cover LT/HT thermal power demands not supplied by waste heat recovery systems is assessed. Finally, the overall electrical and cogeneration efficiencies of power plant are computed over the entire mission profile.

Chapter 8

Mixed-Integer Linear Programming (MILP) code

Even more demanding environmental regulations concerning emissions from ship power plants have been recently introduced [283, 46]. To cope with them, various power generation technologies are currently installed within engine rooms, with the aim of improving efficiency, and even more complex governing strategies arise when thermal or electrical energy storage is considered. Thus, optimally design and operate power plants onboard ships is becoming a mandatory challenge to be faced in the early future, analogously to what happened within the polygeneration power production field [284–288]. In details, the short- and long-term optimal planning of distributed energy systems is traditionally faced with Mixed-Integer Linear programming (MILP) codes. In this way, only linear relations between thermodynamic parameters are used to reduce computational cost, while maintaining the reliability of results. Wu et al. [289] were one of the first to investigate the optimal layout and operation of Combined Heat and Power (CHP) plants by means of MILP code. Overall costs, including CAPital EXpenditure (CAPEX) and OPerational EXpenditure (OPEX), were considered as the objective function to be minimized. Mehleri et al. [290] studied analogous problem for micro-cogeneration units based on photovoltaic panels and boilers installed in limited urban areas or residential districts. Bracco et al. [291] developed a MILP code to investigate optimal design problem for polygeneration system in the Savona campus and both economic and environmental objective functions were considered. Similarly, eco-campus and eco-town problem were successively faced in the literature by Weber et al. [292] and Ren et al. [293]. However, some works in recent years coupled MILP problem with additional non-linear relations between parameters. Indeed, Gabrielli et al. [294] developed a Mixed Integer Non-Linear Programming (MINLP) code to assess the optimal operation strategy for the

ETH of Zurich power generation system, whereas Pruitt et al. [295] faced analogous problem for cogeneration plants dealing with non-linear constraints. Since the computational cost of MINLP codes is significantly increased in comparison to MILP, Coffrin et al. [296] proposed piecewise linear method to account for non-linearities often present in real problems, with reduced computational effort. Nowadays, despite various alternative numerical procedures were tested to optimally design and operate power plants by an energetic, environmental and economic point of view [297], MILP problem, eventually including piecewise linear relations, remain the preferred method. As mentioned above, analogous problems for the optimal design and operation of power plants arise for ships, despite few works in the literature focus on this topic. In the following, the MILP code developed in this thesis project is introduced. The procedure is based on both continuous and binary decision variables, as well as on piecewise linear relations between them. Specifically, the model is able to address the optimal design and operation of hybrid-electric power plants installed onboard ships. Optimizations of costs, environmental impact, energetic efficiency, weights and volumes are available computations. Furthermore, both short- and long-term studies can be performed by the MILP code developed, since only changes in the time horizon are required. Specifically, in this thesis work, both phase mean and hourly ship operating profiles are considered. Finally, no restrictions are imposed on the main fuel feeding prime movers, therefore the MILP code can be flexibly applied to alternative fuels analyses.

8.1 Inputs:

Inputs being necessary to the code consist in three main types of variables. Firstly, variables concerning general data, useful to identify which power plant configurations are considered, are required. Specifically, they relate to the choice on the type and number of prime movers to be installed onboard. Furthermore, fully general variables, as the time sampling adopted for computing the solution, are also included in this category of inputs. In the following, a brief item of the first input class is summarised:

- G: set of COGES plants available to be installed within the ship power plant
- R: set of reciprocating engines which can be included within the engine room onboard ship
- $B9$: set of MDO-fed boilers generating steam at 9 bar (i.e. suitable for HT demand) and eventually included within the ship power plant. Indeed, in case the HT thermal power

demand is not entirely covered by waste heat recovery from prime movers, auxiliary boilers are needed

- $B3$: set of MDO-fed boilers generating steam at 3 bar (i.e. suitable for LT demand) and eventually included within the ship power plant. Indeed, in case the LT thermal power demand is not entirely covered by waste heat recovery from prime movers, auxiliary boilers are needed

- $\tilde{T}$: set of time intervals t forming the time horizon of the mission profile considered for the vessel. Each interval may deal with potentially variable time duration Δt

Secondly, technical data referring to performances provided by each prime mover in terms of electrical and thermal power, electrical efficiency, fuel consumption, CO_2 and NO_x emissions, weights and volumes are necessarily acquired as inputs. Minimum and maximum boundaries for performances as well as parameters related to the sizing of components are included. Furthermore, the electrical and LT/HT thermal power demands required onboard ship belong to this input category:

- $\tilde{\pi}^{el,G}$, $\tilde{\Pi}^{el,G}$: minimum and maximum electrical power which can be covered by COGES. The maximum value considered directly derives from the Engine Margin (EM) accounted for. Since EM is not required by regulations for COGES due to its high reliability and low maintenance costs, only a 3% EM is cautiously considered [298, 74, 77, 299]. On the other hand, the minimum electrical power is mainly fixed considering the deep affection of GT performances to part-loads, despite the bottoming steam power plant dampens this phenomenon. Focusing on GTs, acceptable efficiencies are typically obtained up to 50% loads, whereas too low energy savings is achieved for further part-load conditions. Therefore, 50% is considered in the code, but this limit can be easily varied

- $\tilde{\pi}^{th3,G}$, $\tilde{\Pi}^{th3,G}$: minimum and maximum LT thermal power which can be supplied by COGES at 3 bar. LT power can be supplied by the discharged flow at the steam turbine exit section in case back-pressure configuration is considered.

- $\tilde{\pi}^{th9,G}$, $\tilde{\Pi}^{th9,G}$: minimum and maximum HT thermal power which can be supplied by COGES at 9 bar. This kind of thermal power can be supplied through steam extraction at 9 bar from the steam turbine included within COGES

- $\tilde{\pi}^{el,R}$, $\tilde{\Pi}^{el,R}$: minimum and maximum electrical power provided by reciprocating engines. In this case a 10% EM is accounted for, due to the high maintenance

costs and low reliability reciprocating engines can provide in comparison to COGES [298, 74, 77, 299]. On the other hand, the minimum power from reciprocating engines has been fixed at 50% load

- $\tilde{\pi}^{th3,R}$, $\tilde{\Pi}^{th3,R}$: minimum and maximum LT thermal power available from reciprocating engines at 3 bar. Thermal power sources for 3 bar steam production mainly consist in the excess HT power generated by the WHR systems. Indeed, since thermal power availalbe from reciprocating engine exhaust gas is quite low, steam production from WHR is firstly assessed at 9 bar by the code. In case excessive steam at 9 bar is produced, it is used to partially cover LT thermal demand

- $\tilde{\pi}^{th9,R}$, $\tilde{\Pi}^{th9,R}$: minimum and maximum HT thermal power provided by reciprocating engines at 9 bar. This source of thermal power consists in steam at 9 bar generated by the WHR system, as explained above

- $\tilde{\mu}^{G}_{g,\tau}$, $\tilde{\tau}^{G}_{g,\tau}$, $\tilde{\mu}^{R}_{r,\tau}$, $\tilde{\tau}^{R}_{r,\tau}$: linearization coefficients applied to the efficiency curves of GTs and reciprocating engines, respectively. Indeed, it is well established that electrical efficiency shows non-linear dependence with respect to load. It must be remarked here that the influence played by ambient temperature on electrical efficiency of GTs is accounted for in full non-linear way, using curves available from manufacturers (see figure 6.17 for analogous curves)

- $\sigma^{G}_{g,\tau}$, $\psi^{G}_{g,\tau}$, $\sigma^{R}_{r,\tau}$, $\psi^{R}_{r,\tau}$: linearization coefficients applied to the fuel consumption curves of GTs and reciprocating engines, respectively.

- $\tilde{\pi}^{th3,B}$, $\tilde{\Pi}^{th3,B}$: minimum and maximum thermal power provided by boilers generating steam at 3 bar

- $\tilde{\pi}^{th9,B}$, $\tilde{\Pi}^{th9,B}$: minimum and maximum thermal power provided by boilers generating steam at 9 bar

- η_B: boiler efficiency

- LHV: lower heating value of the fuel used within prime movers and boilers

- $\tilde{d}^{el,ES}$, $\tilde{D}^{el,ES}$: minimum and maximum discharge rate for the electrical energy storage, respectively

- $\tilde{c}^{el,ES}$, $\tilde{C}^{el,ES}$: minimum and maximum charge rate for the electrical energy storage, respectively

- NB_{max}: maximum number of Li-ion batteries installed within the electrical energy storage system
- NB: number of batteries which are currently installed within the electrical storage system. This value can be optimized in order to minimize objective function, i.e. optimally designed battery pack can be determined
- $C_{bat,max}$: maximum capacity of Li-ion batteries installed within the electrical energy storage system
- C_{bat}: currently installed capacity for battery pack
- $\eta_{\tilde{d},ES}$, $\eta_{\tilde{c},ES}$: discharge and charge efficiency of the energy storage system, respectively
- $\tilde{\pi}_{grid}$, $\tilde{\Pi}_{grid}$: minimum and maximum electrical power withdrawable from the harbour grid in case Cold Ironing (CI) is available at berth. If the aim is studying optimal design and operation of ship power plant in the absence of cold ironing, these parameters are excluded from computation
- $\gamma_{CO_2}^{fuel}$, $\gamma_{CO_2}^{MDO}$: CO_2 emission factor from the main fuel and MDO. In this thesis, LNG is considered as main fuel, but other choices (e.g. MDO) can be made
- $\tilde{\alpha}_{NO_x}^{G}$, $\tilde{\beta}_{NO_x}^{G}$: : correlation coefficients used for computing the NO_x emissions from GTs
- $\tilde{\alpha}_{NO_x}^{R}$, $\tilde{\beta}_{NO_x}^{R}$: correlation coefficients used for computing the NO_x emissions from reciprocating engines
- $\tilde{\alpha}_{NO_x}^{B3}$, $\tilde{\beta}_{NO_x}^{B3}$: correlation coefficients used for computing the NO_x emissions from boilers producing steam at 3 bar
- $\tilde{\alpha}_{NO_x}^{B9}$, $\tilde{\beta}_{NO_x}^{B9}$: correlation coefficients used for computing the NO_x emissions from boilers producing steam at 9 bar
- D_{τ}^{el}, D_{τ}^{th9}, D_{τ}^{th3}: electrical and thermal power demands at time τ. As mentioned above, the thermal power is distinguished in LT and HT demands depending on the steam pressure required, 3 or 9 bar, respectively. On the other hand, D_{τ}^{el} represents the summation of both propulsion and hotel electrical services

The third type of input data required by the MILP code consists in economical parameters. Specifically, power specific CAPital EXpenditure (CAPEX) cost for component as well as maintenance and fuel costs are needed to perform economic optimization:

- CC_G, CC_R, CC_{B9}, CC_{B3}: power specific CAPEX cost for purchasing COGES plants, reciprocating engines and auxiliary boilers. Specifically, CC_{B9} and CC_{B3} refer to boilers producing steam at 9 bar and 3 bar, respectively, and are non-zero in case waste heat recovery from prime movers does not succeed in covering the entire demands. For the sake of conciseness, CAPEX costs for all the power plant components which are included within engine rooms in this thesis are reported in table 8.1 [300–302]. It must be remarked that power specific cost of reciprocating engines is given in terms of range: the superior limit refers to small-size components, while inferior ones to those dealing with large-size. Furthermore, a 5% higher price in €/kW has been assumed for natural gas engines in comparison to DF engines dealing with similar size.

Table 8.1 Power specific CAPEX costs.

COMPONENT	CAPEX
DF engines [€/kW]	365-420
Gas Turbines [€/kW]	377
Li-ion batteries [€/kWh]	200
HRSG + ST [€/kW]	127
Tanks [€/kWh]	0.94
Electrical Generators [€/kW]	90
Electrical Motors [€/kW]	80
AC/DC-DC/AC converters [€/kW]	100
Propellers [€/kW]	30

- CF_{fuel},CF_{MDO}: fuel cost in €/tonn. Subscripts refer to the main fuel and MDO, respectively

- CM^G,CM^R,CM^B: maintenance costs for COGES plants, reciprocating engines and boilers, respectively

- $\tilde{p}_{el}$: purchasing price of electricity from the harbour grid in case Cold-Ironing is present. Specifically, the price currently available for middle-large users in the ports of Spain and Sweden is considered [303–305].

- CRF: capital recovery factor of prime movers, expressed as $\frac{\chi(1+\chi)^N}{(1+\chi)^N+1}$ where χ indicates the discount rate and N the number of years the useful life is made up. Since GTs, reciprocating engines and boilers have comparable useful life, equal CRF is assumed for them. Specifically, $N = 20$ years useful life and a χ=6% discount rate were adopted following the literature [306, 301].

- CRF_{ES}: capital recovery factor for the electrical energy storage (i.e. Li-ion batteries). A shorter useful life was assumed for batteries (15 years) to take into account performance reduction after certain amount of charge-discharge cycles [307]. Instead, the discount rate has been kept at 6%.
- CT: carbon tax eventually imposed on CO_2 emissions. Since nowadays no carbon tax for the maritime sector is globally present, it has been estimated from the early-future policies and intentions in EU, according to Perčić et al. [302].
- CC_{ES}: investment cost for the electrical energy storage system, assumed 200 €/kWh.

8.2 Decision variables:

Three main types of decision variables are available within the MILP program. Firstly, binary variables are necessary to model the presence or absence of components within the engine room onboard. Similar variables are used to account for turned-on or turned-off conditions for each prime mover installed within the engine room, at every time interval the mission profile grounds on:

- $\tilde{Y}_g^G, \tilde{Y}_r^R, \tilde{Y}_b^{B3}, \tilde{Y}_b^{B9}$: variables accounting for the eventual installation onboard of COGES g, reciprocating engine r and boilers b producing steam at 3-bar/9-bar. Specifically, they are equal to 1 in case installation is considered, 0 otherwise
- $\tilde{Y}^{ES}$: variable accounting for the eventual installation onboard of electrical energy storage systems. Specifically, it is equal to 1 if batteries are included within the engine room, 0 otherwise
- $\tilde{X}_{g,\tau}^G, \tilde{X}_{r,\tau}^R, \tilde{X}_{b,\tau}^{B3}, \tilde{X}_{b,\tau}^{B9}$: variables accounting for turned-on/turned-off working conditions for COGES g, reciprocating engine r and boilers b producing steam at 3-bar/9-bar. Specifically, they are equal to 1 in case the component is working, 0 if turned-off conditions occur. In case some of these components are not installed onboard, 0 values are imposed
- $\tilde{X}_\tau^{ES}$: variable accounting for working conditions of electrical energy storage systems, in both charge or discharge mode. Unitary value occurs in case batteries are working at time τ, 0 is imposed otherwise. In case batteries are not installed onboard, 0 value is used

The second type of decision variables used by the MILP code consists in operative variables representing electrical and thermal powers, efficiency, loads,... related to each component inserted within the engine room. All the operative variables are evaluated at each time τ comprised within the mission profile:

- $P^G_{el,g,\tau}$, $P^G_{th3,g,\tau}$, $P^G_{th9,g,\tau}$, $\eta^G_{g,\tau}$, $F^G_{g,\tau}$: electrical power and thermal power (at 3 or 9 bar), electrical efficiency and fuel consumption, delivered from the COGES plant g at time τ, respectively

- $P^R_{el,r,\tau}$, $P^R_{th3,r,\tau}$, $P^R_{th9,r,\tau}$, $\eta^R_{r,\tau}$, $F^R_{r,\tau}$,: electrical power and thermal power (at 3 or 9 bar), electrical efficiency and fuel consumption generated from the reciprocating engine r at time τ, respectively

- $P^{B3}_{b,\tau}$, $P^{B9}_{b,\tau}$: thermal power generated by boiler b at time τ, by means of 3-bar and 9-bar steam production, respectively

- $F^{B3}_{b,\tau}$, $F^{B9}_{b,\tau}$: fuel consumption required by the 3-bar and 9-bar boilers b at time τ, respectively. In case no auxiliary boilers are needed to cover thermal power demands onboard, zero values are imposed at each time instant t

- $P^{ES}_{in,\tau}$, $P^{ES}_{out,\tau}$: electrical power charged to and discharged from for the electrical energy storage system at time τ, respectively. Charging and discharging modes are mutually exclusive

- $P_{grid,\tau}$: electrical power withdrawn from the harbour grid at time τ due to cold ironing. In case cold ironing is avoided, $P_{grid,\tau}$ is imposed equal to zero

- $OPEX^G_{g,\tau}$, $OPEX^R_{r,\tau}$, $OPEX^{B3}_{b,\tau}$ and $OPEX^{B9}_{b,\tau}$: fuel consumption and maintenance costs concerning COGES plant g, reciprocating engine r and boilers b which are turned on at time τ. In case some component is turned-off, then null contribute to fuel consumption and maintenance costs is surveyed. If a LNG fed power plant is considered, fuel and maintenance costs are reported in table 8.2 [308, 302, 309, 310, 300].

- $Em^G_{g,\tau}$, $Em^R_{r,\tau}$, $Em^{B3}_{b,\tau}$ and $Em^{B9}_{b,\tau}$: carbon dioxide emissions generated by the COGES plant g, reciprocating engine r and boilers b which are turned on at time τ. Zero values are surveyed in turned-off conditions

- $CEM^G_{g,\tau}$, $CEM^R_{r,\tau}$, $CEM^{B3}_{b,\tau}$ and $CEM^{B9}_{b,\tau}$: costs due to the carbon pricing of CO_2 emissions generated by COGES plant g, reciprocating engine r and boilers b which are turned-on at time τ. Zero values are surveyed in turned-off conditions

Table 8.2 OPEX costs.

COMPONENT	OPEX
LNG fuel [€/tonn]	398
MDO fuel [€/tonn]	575
Reciprocating engine OM [€/kWh]	0.015
COGES OM [€/kWh]	0.002
Boiler OM [€/kWh]	0.006
CO_2 price [€/kg]	0.115

- CG_τ: cost related to electrical power purchased from the harbour grid at time τ due to cold ironing. Zero value is imposed in case cold ironing is excluded
- $Emno^G_{g,\tau}$, $Emno^R_{r,\tau}$, $Emno^{B3}_{b,\tau}$ and $Emno^{B9}_{b,\tau}$: nitrogen oxide (NO_x) emissions generated by COGES plant g, reciprocating engine r and boilers b which are turned-on at time τ. Zero values are surveyed in turned-off conditions

8.3 Objective functions:

As outlined above, the developed MILP code allows for many optimization studies. Specifically, optimal design and operation of power plants onboard can be addressed by energetic, environmental, economic, weight and volume requiring points of view. Examples of objective functions related to different optimization strategies are reported below:

- Energetic optimization: optimal design and operation are assessed by maximizing the overall efficiency delivered by the engine room in each ship working condition included within the mission profile. Both electrical and cogeneration efficiencies can be adopted as objective functions, in case thermal power demand onboard is relevant or negligible, respectively. Definition of cogenerative efficiency adopted in the code is reported below (analogous definition for η_{el} can be obtained by neglecting thermal power within the numerator N):

$$\eta_g = \frac{N}{D} \tag{8.1}$$

where

$$\begin{cases} N = \sum_{\tau=1}^{\tilde{T}} (D^{el}_\tau + D^{th9}_\tau + D^{th3}_\tau)\Delta t) \\ D = \sum_{\tau=1}^{\tilde{T}} \left[\sum_{i=1}^{n_{pm}} F_{fuel,i} LHV_{fuel} + \sum_{j=1}^{n_{DF}} F_{MDO,j} LHV_{MDO} + \sum_{k=1}^{n_B} F_k LHV_{MDO} \right] \Delta t \end{cases}$$

- Environmental optimization: optimal design and operation are investigated minimizing CO_2-equivalent emissions generated by the entire power plant. Specifically, the GHG effect deriving from both CO_2 and NO_x emissions is accounted for. In this case, definition of the objective function is reported below:

$$Total\ CO_2 = \sum_{\tau=1}^{\tilde{T}} \left[\sum_{i=1}^{n_{pm}} F_{fuel,i} \gamma_{CO_2}^{fuel} + \sum_{j=1}^{n_{DF}} F_{MDO,j} \gamma_{CO_2}^{MDO} + \sum_{k=1}^{n_B} F_k \gamma_{CO_2}^{MDO} \right]$$

$$+ \left[\sum_{i=1}^{n_{pm}} Emno_{fuel,i} + \sum_{j=1}^{n_{DF}} Emno_{MDO,j} + \sum_{k=1}^{n_B} Emno_{MDO,k} \right] \Delta t$$

  However, since specific regulations limiting NO_x emissions exist in the maritime sector, also the minimization of nitrogen oxides appears relevant. Thus, in order to assess differences between CO_2 and NO_x emission generated by engine rooms, NO_x minimization is also possible considering the following objective function:

$$Total\ NO_x = \sum_{\tau=1}^{\tilde{T}} + \left[\sum_{i=1}^{n_{pm}} Emno_{fuel,i} + \sum_{j=1}^{n_{DF}} Emno_{MDO,j} + \sum_{k=1}^{n_B} Emno_{MDO,k} \right] \Delta t \quad (8.2)$$

- Economic optimization: in this case, minimization of the overall costs (i.e. CAPEX+OPEX), aimed at the optimal design and operation of the ship power plant, is performed. However, multiple variants of objective functions are available to better appreciate the pros and cons provided by various configurations. For example, different scenarios arise including/excluding carbon tax or cold ironing from the harbour grid. Nevertheless, the most complete objective function for the economic optimization is

reported below:

$$
\begin{aligned}
Total\ Costs = {} & C_{bat} CC_{ES} CFR_{ES} + \sum_{i=1}^{n_{pm}} \left[CC_i P_{el,0,i} \right] + \\
& \sum_{\tau=1}^{\tilde{T}} \left[\sum_{i=1}^{n_{pm}} F_{fuel,i} CF_{fuel} + \sum_{j=1}^{n_{DF}} F_{MDO,j} CF_{MDO} + \sum_{k=1}^{n_B} F_k CF_{MDO} \right] \Delta t \\
& + \sum_{\tau=1}^{\tilde{T}} \left[\sum_{i=1}^{n_{pm}} P_{el,i} CM_i + \sum_{k=1}^{n_B} P_{th,k} CM_k \right] \Delta t \\
& + \sum_{\tau=1}^{\tilde{T}} \left[\sum_{i=1}^{n_{pm}} CEM_i + \sum_{k=1}^{n_B} CEM_k \right] \Delta t \\
& + \sum_{\tau=1}^{\tilde{T}} CG_\tau \Delta t
\end{aligned}
\tag{8.3}
$$

- Engine room weight optimization: in this case, minimization of the overall weight provided by engine room (i.e. prime movers and auxiliary boilers) is targeted:

$$
Total\ Weight = \sum_{i=1}^{n_{pm}} \left[\tilde{W}_i \right] + \sum_{j=1}^{n_B} \left[\tilde{W}_j \right] \tag{8.4}
$$

  where $\tilde{W}$ indicates weights, n_B represents the number of auxiliary boilers included within the engine room.

- Volume optimization: in this case, minimization of the overall volume occupied by the engine room (i.e. prime movers and auxiliary boilers) is targeted:

$$
Total\ Volume = \sum_{i=1}^{n_{pm}} \left[\tilde{V}_i \right] + \sum_{j=1}^{n_B} \left[\tilde{V}_j \right] \tag{8.5}
$$

  where $\tilde{V}$ indicates volumes.

8.4 Constraints:

Various types of constraints are defined in the MILP code. Firstly, constraints aimed at considering only the components (i.e. prime movers and boilers) effectively installed onboard as candidate for covering the D_{τ}^{el}, D_{τ}^{th9}, D_{τ}^{th3} demands are needed. These constraints are imposed on the binary variables, as reported below:

$$\begin{aligned}
\tilde{X}_{g,\tau}^{G} &\leq \tilde{Y}_{g,\tau}^{G} \\
\tilde{X}_{r,\tau}^{R} &\leq \tilde{Y}_{r,\tau}^{R} \\
\tilde{X}_{b,\tau}^{B3} &\leq \tilde{Y}_{b,\tau}^{B3} \\
\tilde{X}_{b,\tau}^{B9} &\leq \tilde{Y}_{b,\tau}^{B9}
\end{aligned} \tag{8.6}$$

Secondly, the electrical and thermal power delivered by each prime mover or auxiliary boiler needs to range between its corresponding minimum and maximum values provided by manufacturers. Therefore, the following constraints must be imposed to assure it:

$$\begin{aligned}
&\tilde{\pi}_{g,\tau}^{G} \geq P_{el,g,\tau}^{G} \leq \tilde{\Pi}_{g,\tau}^{G} \,||\, P_{el,g,\tau}^{G} = 0 \\
&\tilde{\pi}_{g,\tau}^{G} \geq P_{th3,g,\tau}^{G} \leq \tilde{\Pi}_{g,\tau}^{G} \,||\, P_{th3,g,\tau}^{G} = 0 \\
&\tilde{\pi}_{g,\tau}^{G} \geq P_{th9,g,\tau}^{G} \leq \tilde{\Pi}_{g,\tau}^{G} \,||\, P_{th9,g,\tau}^{G} = 0 \\
&\tilde{\pi}_{r,\tau}^{R} \geq P_{el,r,\tau}^{R} \leq \tilde{\Pi}_{r,\tau}^{R} \,||\, P_{el,r,\tau}^{R} = 0 \\
&\tilde{\pi}_{r,\tau}^{R} \geq P_{th3,r,\tau}^{R} \leq \tilde{\Pi}_{r,\tau}^{R} \,||\, P_{th3,r,\tau}^{R} = 0 \\
&\tilde{\pi}_{r,\tau}^{R} \geq P_{th9,r,\tau}^{R} \leq \tilde{\Pi}_{r,\tau}^{R} \,||\, P_{th9,r,\tau}^{R} = 0 \\
&\tilde{\pi}_{b,\tau}^{B3} \geq P_{b,\tau}^{B3} \leq \tilde{\Pi}_{b,\tau}^{B3} \,||\, P_{b,\tau}^{B3} = 0 \\
&\tilde{\pi}_{b,\tau}^{B9} \geq P_{b,\tau}^{B9} \leq \tilde{\Pi}_{b,\tau}^{B9} \,||\, P_{b,\tau}^{B9} = 0 \\
&0 \geq P_{in,g,\tau}^{ES} \leq \tilde{\Pi}_{in,g,\tau}^{ES} \\
&0 \geq P_{out,g,\tau}^{ES} \leq \tilde{\Pi}_{out,g,\tau}^{ES}
\end{aligned} \tag{8.7}$$

Similarly, further constraints are used to effectively perform piecewise linearization of non-linear relationships, as those concerning efficiency or fuel consumption from prime movers [311, 312]:

$$\begin{aligned}
\eta_{g,\tau}^{G} &= \tilde{\mu}_{g,\tau}^{G} P_{el,g,\tau}^{G} + \tilde{\tau}_{g,\tau}^{G} \\
\eta_{r,\tau}^{R} &= \tilde{\mu}_{r,\tau}^{R} P_{el,r,\tau}^{R} + \tilde{\tau}_{r,\tau}^{R} \\
F_{g,\tau}^{G} &= \sigma_{g,\tau}^{G} P_{el,g,\tau}^{G} + \psi_{g,\tau}^{G} \\
F_{r,\tau}^{R} &= \sigma_{r,\tau}^{R} P_{el,r,\tau}^{R} + \psi_{r,\tau}^{R}
\end{aligned} \tag{8.8}$$

where the carbon dioxide and nitrogen oxide emissions from gas turbines, reciprocating engines and boilers are concerned, they are computed by means of the following constraints:

$$\begin{aligned}
&Em^{G}_{g,\tau} = F^{G}_{g,\tau}\gamma^{fuel}_{CO_2}\\
&Em^{R}_{r,\tau} = F^{R}_{r,fuel,\tau}\gamma^{fuel}_{CO_2} + F^{R}_{r,MDO,\tau}\gamma^{MDO}_{CO_2}\\
&Em^{B3}_{b,\tau} = F^{B3}_{b,\tau}\gamma^{MDO}_{CO_2}\\
&Em^{B9}_{b,\tau} = F^{B9}_{b,\tau}\gamma^{MDO}_{CO_2}\\
&Emno^{G}_{g,\tau} = \tilde{\alpha}^{G}_{NO_x}P^{G}_{el,g,\tau} + \tilde{\beta}^{G}_{NO_x}\\
&Emno^{R}_{r,\tau} = \tilde{\alpha}^{R}_{NO_x}P^{R}_{el,r,\tau} + \tilde{\beta}^{R}_{NO_x}\\
&Emno^{B3}_{b,\tau} = \tilde{\alpha}^{B3}_{NO_x}P^{B3}_{b,\tau} + \tilde{\beta}^{B3}_{NO_x}\\
&Emno^{B9}_{b,\tau} = \tilde{\alpha}^{B9}_{NO_x}P^{B9}_{b,\tau} + \tilde{\beta}^{B9}_{NO_x}
\end{aligned} \tag{8.9}$$

Analogously, cost computation is numerically performed imposing the following constraints, which simply resemble CAPEX, fuel costs and maintenance cost definitions:

$$\begin{aligned}
&CAPEX^{G}_{g} = CC_{G}\tilde{\Pi}^{G}_{g}\\
&CAPEX^{R}_{r} = CC_{R}\tilde{\Pi}^{R}_{r}\\
&CAPEX^{B3}_{b} = CC_{B3}\tilde{\Pi}^{B3}_{b}\\
&CAPEX^{B9}_{b} = CC_{B9}\tilde{\Pi}^{B9}_{b}\\
&OPEX^{G}_{g} = CF^{fuel}F^{G}_{g,\tau}\Delta t + CM^{G}P^{G}_{el,g,\tau}\Delta t\\
&OPEX^{R}_{r} = CF^{fuel}F^{R}_{r,\tau}\Delta t + CF^{MDO}F^{R}_{r,\tau}\Delta t + CM^{R}P^{R}_{el,r,\tau}\Delta t\\
&OPEX^{B3}_{b} = CF^{MDO}F^{B3}_{b,\tau}\Delta t + CM^{B}P^{B3}_{b,\tau}\Delta t\\
&OPEX^{B9}_{b} = CF^{MDO}F^{B9}_{b,\tau}\Delta t + CM^{B}P^{B9}_{b,\tau}\Delta t\\
&CEM^{G}_{g,\tau} = CTEm^{G}_{g,\tau}\\
&CEM^{R}_{r,\tau} = CTEm^{R}_{r,\tau}\\
&CEM^{B3}_{b,\tau} = CTEm^{B3}_{b,\tau}\\
&CEM^{B9}_{b,\tau} = CTEm^{B9}_{b,\tau}\\
&CG_{t} = \tilde{p}_{el}P_{grid,\tau}
\end{aligned} \tag{8.10}$$

Chapter 9

Results

9.1 Feasibility study of integrated COGES-DF engine power plants in LNG propulsion for a cruise-ferry

In the following sections, integrated COmbined Gas Electric and Steam-reciprocating engine propulsion plants installed onboard a LNG powered cruise-ferry is investigated by energetic, environmental and economic point of views. The aim is to respond to Grandi Navi Veloci (GNV) shipowners' need to equip cruise-ferries sailing in future ECA zones with power plants preserving high efficiency under flexible operating conditions. Specifically, investigations were carried out in a repowering study for La Suprema ship. Firstly, a cogeneration efficiency optimization algorithm has been applied to many, highly efficient power plant configurations, whose performances were assessed over a wide ship speed range (16-26 knots), for both summer and winter seasons. As a main result, the propulsion plant configuration guaranteeing high cogeneration efficiency on flexible ship operating conditions is identified. Successively, environmental impact of all the power plant configurations considered is assessed by evaluating the Energy Efficiency Design Index (EEDI) and compliance with IMO regulations is shown. Finally, in order to investigate economic viability of integrated COGES-reciprocating engine power plants, comparison in terms of cost savings is performed over four different GNV routes and both investment and operational costs have been computed. Therefore, the power plant delivering the best performances by an energetic, environmental and economic point of view under flexible ship operating conditions is proposed to repower La Suprema.

9.1.1 Case study

In this section, electrical and thermal power demands onboard La Suprema as well as its current propulsion plant are presented.

Table 9.1 Main characteristics of the cruise-ferry La Suprema.

Dimension	Value
Overall length [m]	211.21
Length between perpendicular [m]	186.21
Beam [m]	30.4
Height [m]	10
Draft [m]	7.4
Gross Tonnage [TSL]	49257
Deadweight tonnage [t]	9720
Displacement [t]	26376
Volume [m^3]	25733
Passengers [-]	2920

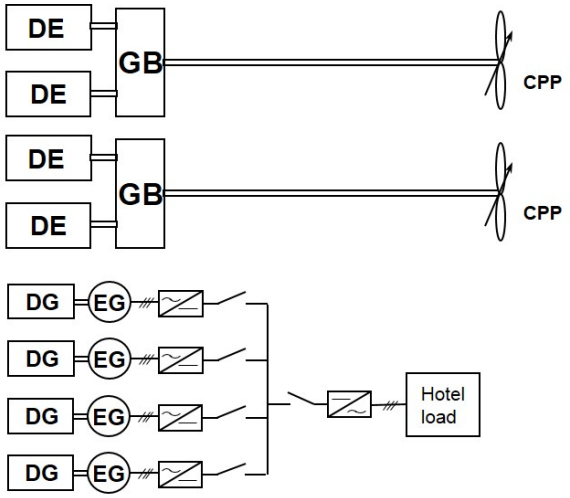

Fig. 9.1 Schematic view of the propulsion power plant currently installed onboard the cruise-ferry La Suprema.

The main characteristics of the vessel are reported in in table 9.1, whereas schematic view of the currently installed power plant onboard La Suprema is shown in figure 9.1. Propulsion power plant for La Suprema was designed to guarantee a 28 knots cruise speed and a 30 knots maximum ship speed. As can be seen from figure 9.1, it deals with a mechanical propulsion architecture based on 16.8 MW x 4 Wärtsilä 16V46C Diesel engines rotating at 500 rpm in

nominal condition and directly connected with changeable propellers. Four Wärtsilä-Vasa 6R32LNE Diesel generators, overall delivering 9.7 MW, are additionally installed onboard to cover electrical power demand during harbour and manoeuvring operating conditions. Therefore, the power plant accounts for 76.9 MW installed power. In order to reduce fuel consumption, La Suprema currently sails on the Genoa-Palermo route at approximately 22 knots ship speed. Specifically, power request from propulsion services is covered by only two Wärtsilä 16V46C, each driving a single propeller. Thus, the current operating conditions are evidently far distant from the designed ones. Furthermore, ship speeds currently adopted along Mediterranean sea routes for GNV cruise-ferries are summarised in table 9.2. Specifically, GP stands for Genoa-Palermo route, GB for Genoa-Barcelona, NP for

Table 9.2 GNV operating routes for Mediterranean sea.

Route	Speed [knots]	Distance [nm]	Duration [h]
GP	22	427	19
GB	20	352	18
NP	17	167	10
NC	25	223	9

Naples-Palermo and NC for Naples-Catania. As can be seen, all the current sailing conditions from GNV deal with lower ship speeds around 20 knots: a 25 knots maximum ship speed is obtained during the NC route. Therefore, in order to match the current operating conditions of GNV cruise-ferries, a new power plant to be installed onboard La Suprema appears necessary. With the aim of preserving high efficiency under different operating conditions for

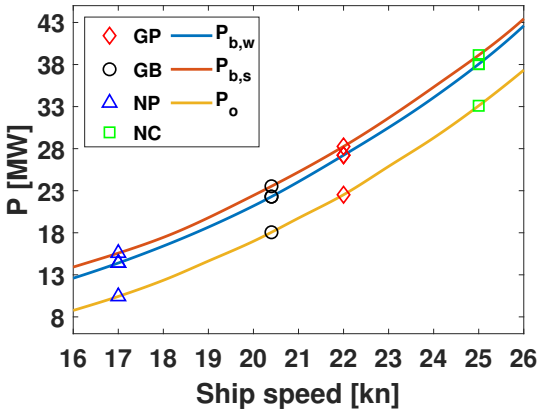

Fig. 9.2 Brake and propulsion power required onboard La Suprema, for summer and winter seasons.

La Suprema, performances have been assessed within a wide ship speed range. The electrical

power demand onboard La Suprema during navigation at different ship speeds is reported in figure 9.2, distinguishing winter and summer season. Specifically, Pb,s and Pb,w indicate the summer and winter brake power, respectively, whereas Po consists in the propulsion power evaluated at propeller. The power gap existing between Pb and Po curves represents the hotel load onboard, which is unaffected by ship speed. Values for hotel and propulsion

Table 9.3 Genoa-Palermo power requirements for the cruise-ferry La Suprema.

Operating condition	**Power [MW]**
hotel cruise-summer	4.35
hotel cruise-winter	3.37
maneuvering	5.32
harbour	3.21
propulsion	24.04

power demand onboard La Suprema are shown in table 9.3 focusing on the Genoa-Palermo route. On the other hand, the thermal power demand during navigation consists in 900 kg/h and 1050 kg/h steam mass flow rates at 7 bar, respectively for summer and winter seasons. A schematic view of the integrated COGES-reciprocating engine power plant investigated

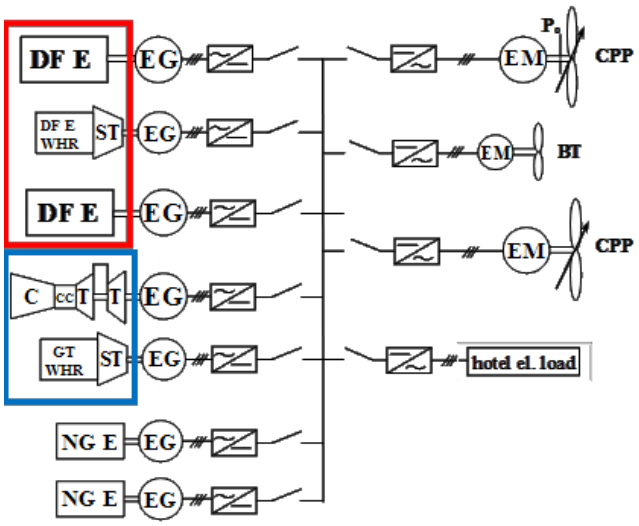

Fig. 9.3 Schematic view of the integrated COGES-reciprocating engine power plant investigated (DFE=dual-fuel engine, NGE=natural gas engine, WHR=waste heat recovery generator, C=compressor, CC=combustion chamber, T=turbine, ST=steam turbine, EG=electrical generator, EM=electrical motor).

is shown in figure 9.3. It must be underlined here that the arrangement in figure 9.3 can effectively exploit benefits from both COGES plant and small-size reciprocating engines.

Indeed, increased power density per unit volume or weight as well as higher cogeneration efficiencies around design ship operating conditions are provided by COGES plants. On the other hand, weak detrimental affection of electrical power and efficiency is guarantee by reciprocating engines in case of ambient temperature increase or at part-loads. Furthermore, adopting small-size reciprocating engines allows to cover power demand with higher working loads, i.e. higher efficiencies. As visible from figure 9.3, prime movers included within the power plant under study comprise COGES plant, two DF reciprocating engines and two natural gas (NG) generators. An emergency generating set not shown in figure 9.3 is also included within power plant to ensure safety sailing conditions in case of prime mover failures. Moving from prime movers to users, electrical power is generated by alternators in alternate current, then is transformed in direct current passing through AC/DC converters to change frequency. Finally, direct current is returned to alternate mode by means of DC/AC converters before distribution to the hotel and propulsion load is assessed. Electric bar connects turned on generation side with final users by means of electrical switches. Propulsion demand is represented by two controllable pitch propellers (CPPs) for navigation as well as bow thruster for maneuvering., whose rotational speed is controlled by means of electrical motors EM. Overall, the schematic view reported in figure 9.3 clearly shows how prime mover operating condition and power demand side are completely independent in integrated electric power plants, since the double step AC/DC and DC/AC conversion ensures frequency matching. Thus, energy savings can be achieved especially at part-loads, according to previous works in the literature [313]. Furthermore, as mentioned in previous sections, no distinction is made between main and auxiliary engines in electric propulsion architecture, hence all the prime movers included within figure 9.3 can work without any restriction imposed by ship operating conditions, with consequent efficiency benefits [313–315]. In details, approximately 10% efficiency improvement was surveyed by Nuchturee et al. [313] at part-loads in case harbour generating set is switched on during navigation. Referring to figure 9.3, the well-known chain rule has been used to move brake powers to hotel and propulsion users. Specifically, chain rule applied to propulsion power P_o is reported below:

$$\begin{aligned} P_b = \frac{P_{bar}}{\eta_{AC-DC}\eta_a} = \frac{P_{bar,p}+P_{bar,el}}{\eta_{AC-DC}\eta_a} = \\ = \frac{\frac{P_o}{\eta_r\eta_{mep}\eta_{DC-AC}} + \frac{P_{el}}{\eta_{DC-AC}}}{\eta_{AC-DC}\eta_a} \end{aligned} \tag{9.1}$$

where P_{bar}, $P_{bar,p}$, $P_{bar,el}$ are the overall generated power evaluated at the electric bar, the corresponding fraction transferred towards propulsion and hotel users, respectively. The

following values available from the literature have been imposed for converter η_{ACDC}, η_{DCAC}, alternator η_a electrical motor η_{EM} and rotative η_r efficiencies:

Table 9.4 Main characteristics of prime movers considered to be installed onboard the cruise-ferry La Suprema.

GT	P_{el} **[MW]**	η_{el} **[%]**	T_{ex} **[°C]**	**L [m]**	**W [m]**	**H [m]**	**Weight [t]**
GE25.1	24.31	36	566	13.94	2.64	3.98	90
TITAN250	21.75	39	465	10.3	3.4	3.9	49.9
12V MAN 51/60-DF	11.23	45.5	309	10.25	4.71	5.52	189
9L MAN 51/60-DF	8.42	45.5	309	11.16	3.28	5.34	148
R-R Bergen C26 L9	2.33	45	-	8.151	2.304	3.161	46.02

Table 9.5 Propulsion system configurations being selected for the cruise-ferry La Suprema.

PLANTS	**12VMAN**	**9LMAN**	**GE25.1**	**TITAN250**	**Inst. Power [MW]**
SOL1a	X X		X		56.5
SOL2a		X X	X		50.9
SOL3a	X	X	X		53.7
SOL1b	X X			X	50.5
SOL2b		X X		X	44.9
SOL3b	X	X		X	47.7

The main characteristics of prime movers considered within the analysis are reported in table 9.4 for both reciprocating engines and GTs. Dimensions reported in table 9.4 consists into the base-plate length L, width W and height H. As can be seen, gas turbines can deliver higher power with reduced occupied volume and weight in comparison to reciprocating engines. Focusing on GTs, TITAN250 deals with lower size and higher electrical efficiency in comparison to GE25.1. Thus, maximum cogeneration efficiency will be achieved at different ship speeds by the two corresponding COGES plants. Despite lower waste heat is available from the exhaust gas of reciprocating engines, steam turbine inclusion within WHR system of DF engines is eventually investigated. All the power plant configurations analysed in this work are reported in table 9.5 and were derived according to the design procedure proposed in [227]. As can be seen, installed power for all configurations is far lower than the current one available on La Suprema, despite the maximum ship speed of 30 knots and safety conditions during maneuvering are ensured. This clearly proves how energy savings benefits are provided by all the configurations reported in table 9.5. Since SOL2a and SOL2b resulted to cover power demands with higher cogeneration efficiencies over the entire ship speed range considered, only performances of power plants including two 9LMAN DF engines are reported in the following sections for sake of conciseness.

9.1.2 Results

In this section, performances of power plant configurations reported in table 9.5 are assessed by an energetic point of view. First, all prime movers are compared in terms of heat recovery potential Φ defined as:

$$\phi_i(\%LOAD) = \frac{\dot{m}_{ex,i}(h_{ex,i} - h_{air})}{P_{mecc,i}} \tag{9.2}$$

where P_mecc,i indicates mechanical power delivered by the i-th prime mover, $\dot{m}_{ex,i}$ and $h_{ex,i}$ consist in its corresponding exhaust gas mass flow rate and enthalpy, respectively, hair is the air enthalpy at ambient temperature. As can be seen from eq. (9.2), Φ compares the amount of thermal power available for recovery within the exhaust gas flow with the corresponding mechanical power delivered. Thus, the potential of each prime mover in increasing efficiency when coupled with a bottoming cycle driven by waste heat is assessed by Φ. Figure 9.4

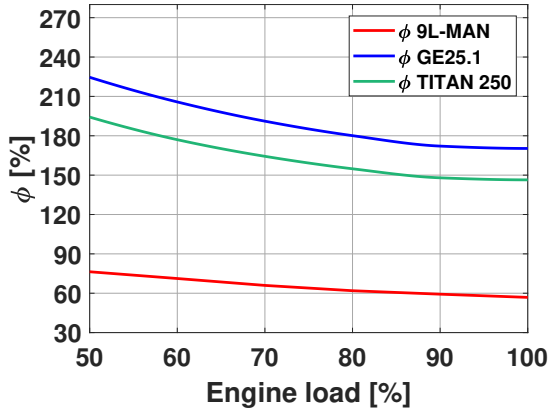

Fig. 9.4 Heat recovery potential of all prime movers considered for the cruise ferry La Suprema.

shows results obtained for prime movers dealing with heat recovery, i.e. GTs and DF engines. As can be seen, GTs present a far higher potential for thermal power recovery in comparison to reciprocating engines. This mainly derives from the large mass flow rate dealing with high temperature (in the range 450-600 °C) available from the exhaust gas from GTs. On the other hand, reduced values of Tex and Mex deal with DF engines. Definition of Φ is clearly related to electrical efficiency delivered by prime movers, i.e. the higher η_{el} the lower the thermal power available for exhaust gas heat recovery and consequently, Φ. Indeed, DF engines reported in table 9.4 are more efficient than GTs in converting fuel primary energy into electric power. Analogously, TITAN250 is presents higher electrical efficiency in comparison to GE25.1, hence it provides a lower Φ value. However, the large amount of thermal power available from GE25.1 exhaust gas can be recovered by an highly efficient bottoming steam power cycle to produce additional power. Hence, in combination with heat

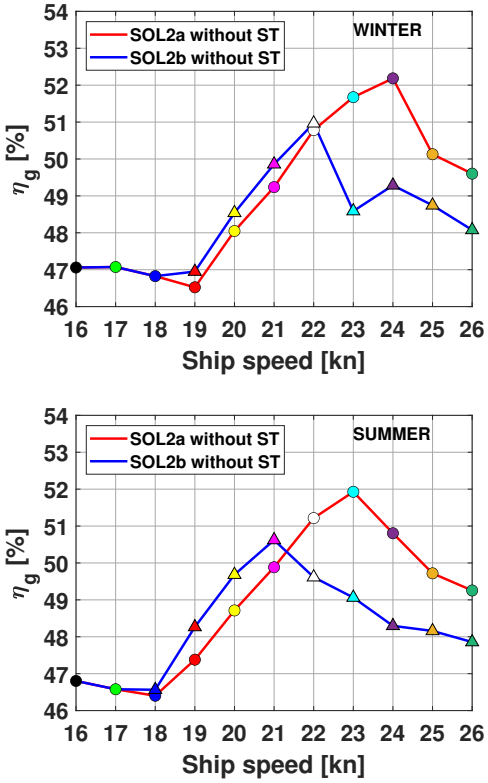

WINTER						SUMMER					
	% LOAD						% LOAD				
	C	DF2	DF2	NGE	NGE		C	DF2	DF2	NGE	NGE
●	-	73.7	73.7	-	-	●	-	78.8	78.8	-	-
●	-	85.6	85.6	-	-	●	-	79.7	79.7	79.7	-
●	-	85.6	85.6	85.6	-	●	-	80.3	80.3	80.4	80.4
●	53.2	-	-	-	-	●	57.5	-	-	-	-
●	60.9	-	-	-	-	●	65.6	-	-	-	-
●	68.8	-	-	-	-	●	73.7	-	-	-	-
○	79.8	-	-	-	-	○	85.1	-	-	-	-
●	89.2	-	-	-	-	●	94.2	-	-	-	-
●	96.7	-	-	-	-	●	90.3	-	-	89.8	89.8
●	87.1	86.7	-	-	-	●	86.6	86.3	-	86.3	-
●	87.3	86.8	-	86.9	86.9	●	86.9	86.5	-	86.5	86.5
▲	66.2	-	-	-	-	▲	64.5	-	-	-	-
▲	75.2	-	-	-	-	▲	74.2	-	-	-	-
▲	84.1	-	-	-	-	▲	83.8	-	-	-	-
△	96.0	-	-	-	-	▲	93.0	-	-	-	-
▲	82.7	82.0	-	-	-	△	90.6	-	-	89.9	89.9
▲	90.1	89.4	-	-	-	▲	89.6	88.9	-	-	-
▲	89.5	88.8	-	88.8	88.8	▲	86.2	85.5	-	85.6	85.6
▲	86.8	86.1	86.1	86.1	-	▲	87.9	87.2	87.2	-	-
						▲	88.0	87.3	87.3	87.4	87.4

Fig. 9.5 SOL2a and SOL2b cogeneration efficiency considering DF engines not equipped with ST: winter (top) and summer (bottom) seasons.

recovery technologies, GTs can guarantee higher efficiencies than reciprocating engines. In the following, comparison between power plant configurations is assessed in terms of cogeneration efficiency and fuel cost of SOL2a and SOL2b plants. First, configurations not equipped with ST downstream of the WHR system of reciprocating engines are considered, then possible improvements in terms of efficiency are assessed by installing a condensing steam turbine within the DF engines WHR circuit. Focusing on cogeneration efficiency results obtained avoiding installation of ST in the DF engine WHR systems are shown in figure 9.5 for the ship speed range 16-26 knots. Winter and summer seasons refer to the left and right column, respectively. The corresponding engine load information for each operating condition is summarised in the tabular legend below, where C, DF2 and NGE refer to COGES plant, 9LMAN engines and R-R Bergen C26 L9 engines, respectively. As can be seen from figure 9.5, cogeneration efficiency provided by SOL2a and SOL2b coincides at low ship speeds, independently from season. Indeed, in these ship operating conditions reciprocating engines are turned on to maximize η_g for both power plant configurations. On the contrary, the electrical power demand onboard is covered by COGES plants for

ship speeds ranging between 18 and 23 knots (see the tabular legend) or by COGES plants coupled with reciprocating engines for further high V_{ship}. The power distribution visible from figure 9.5 in function of ship speed clearly depends from prime mover performances. Indeed, reciprocating engines can provide energy benefits at reduced ship speeds, since their efficiency is weakly affected by part-loads and high-load conditions can derive from their small size. Instead, COGES supply power demand more efficiently than reciprocating engines for ship speeds around 22 knots. Finally, for very high ship speeds, power delivered by COGES does not cover the entire onboard request, hence few reciprocating engines need to be turned on to fill in the gap. Therefore, figure 9.5 clearly proves that COGES plants based on GE25.1 and TITAN250 provide higher energy savings with respect to reciprocating engines within the medium-high ship speed range, well centered around the current operating condition for La Suprema (i.e. 22 knots). Furthermore, power plant flexibility is enhanced by small-size reciprocating engines, which allow for fine power regulation coupled with COGES. Focusing on comparison between COGES plants grounding SOL2a and SOL2b, slightly higher η_g is obtained by SOL2b where only COGES is turned on, whereas SOL2a is

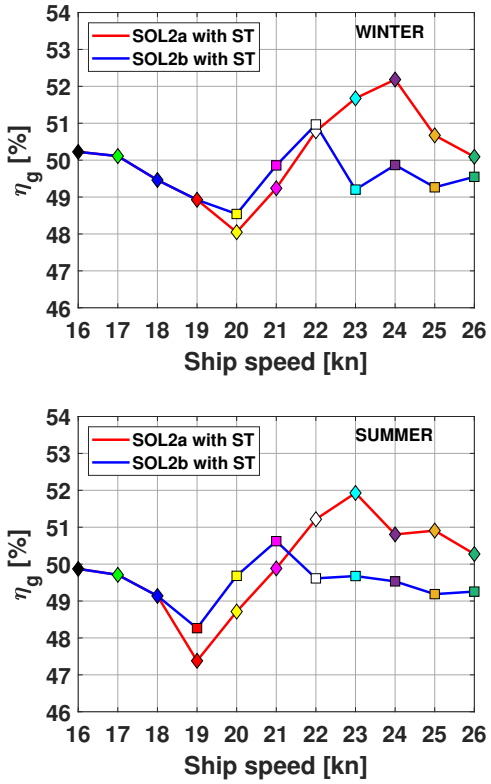

WINTER						SUMMER					
	% LOAD						% LOAD				
	C	DF2	DF2	NGE	NGE		C	DF2	DF2	NGE	NGE
◆	-	68.7	68.7	-	-	◆	-	73.7	73.7	-	-
◆	-	80.1	80.1	-	-	◆	-	85.1	85.1	-	-
◆	-	80.7	80.7	81.4	-	◆	-	85.2	85.2	85.7	-
◆	-	83.5	83.5	84.1	84.1	◆	57.5	-	-	-	-
◆	60.9	-	-	-	-	◆	65.6	-	-	-	-
◆	68.8	-	-	-	-	◆	73.7	-	-	-	-
◇	79.8	-	-	-	-	◇	85.1	-	-	-	-
◆	89.2	-	-	-	-	◆	94.2	-	-	-	-
◆	96.7	-	-	-	-	◆	90.3	-	-	89.8	89.8
◆	86.1	85.2	-	-	-	◆	90.6	89.7	-	-	-
◆	86.4	85.5	-	86.0	86.0	◆	90.4	89.5	-	89.9	89.9
■	75.2	-	-	-	-	■	74.2	-	-	-	-
■	84.1	-	-	-	-	■	83.8	-	-	-	-
□	96.0	-	-	-	-	■	93.0	-	-	-	-
■	81.6	80.3	-	-	-	□	90.6	-	-	89.9	89.9
■	88.9	87.8	-	-	-	■	88.3	87.2	-	-	-
■	88.4	87.3	-	87.7	87.7	■	90.4	89.3	-	89.7	-
■	89.3	88.2	88.2	-	-	■	85.9	84.7	84.7	-	-
						■	90.5	89.5	89.5	89.8	-

Fig. 9.6 SOL2a and SOL2b cogeneration efficiency considering DF engines equipped with ST: winter (top) and summer (bottom) seasons.

able to keep efficiency high in a broader operating range. Where the current ship operating conditions are concerned (i.e. 22 knots), cogeneration efficiency from SOL2b is slightly higher in winter in comparison to performances from SOL2a, but opposite results with larger gap arise for summer, where SOL2a clearly provides the highest energy savings. Thus, COGES based on GE25.1 appears to perform better under extremely flexible operating conditions, comprising the current ship speed adopted for navigation. In case ST is installed within the WHR systems of DF engines, results on cogeneration efficiency are shown in figure 9.6 for the ship speed range 16-26 knots. The same power distribution previously observed in figure 9.5 is visible. Specifically, COGES plants cover the entire power demand within the medium ship speed range, whereas some reciprocating engines are needed to be turned on at high V_{ship} to provide additional power. On the other hand, reciprocating engines maximize η_g in case low ship speeds are considered. Interestingly, since including ST within the WHR systems increases both power and electrical efficiency available from DF engines, reciprocating engines maximize η_g over a wider ship speed range. Specifically, a 2-3% higher cogeneration efficiency is recorded at 16, 17 and 18 knots, where COGES plants working conditions would require less than 60% load. Conversely, for high ship speeds, cogeneration efficiency appears slightly improved. Nevertheless, COGES still provides the maximum cogeneration efficiency around 22 knots and importantly contributes to cover demand at medium-high ship speeds. Furthermore, it must be underlined that significant increase in power plant complexity, volumes, weights and costs arise in case ST is installed within the WHR system of reciprocating engines. Thus, feasibility of these configurations needs to be carefully examined by the ownership, depending on the future operating conditions for La Suprema. In order to provide a direct feedback to ownerships in terms of costs arising from a certain ship operating condition, the fuel cost per unitary nautical mile is introduced, which is defined as:

$$Fuel\ cost = \frac{\sum_{i=1}^{n_{pm}} \dot{m}_{f,i} 3600}{V_{ship}} \tilde{p} \tag{9.3}$$

where V_{ship} is the ship speed in knots, $\dot{m}_{f,i}$ indicates the fuel mass flow rate of fuel [t/s] and $\tilde{p}$ consists in the fuel price [€/t]. It must be remarked that both LNG and MDO fuel consumption is accounted for DF engines. Furthermore, 398 €/t and 575 €/t have been assumed as LNG and MDO prices, respectively, according to the literature [316].

Results concerning fuel cost are shown in figure 9.7 for SOL2a and SOL2b configurations. Winter and summer seasons refer to the left and right column, respectively, whereas the top and bottom rows relate to steam turbine not installed or installed within the WHR systems of DF engines, respectively. Overall, figure 9.7 shows monothonically increasing curves with V_{ship}. Indeed, high ship speeds relates to high power delivered by prime movers and,

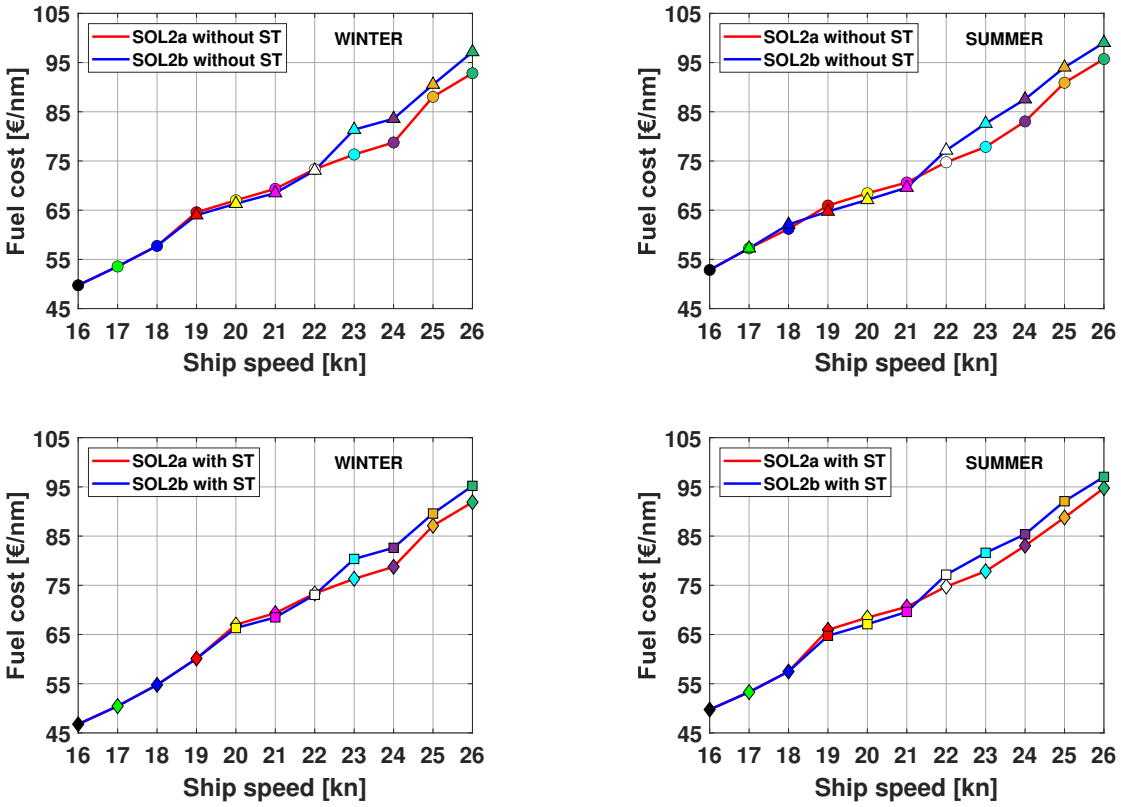

Fig. 9.7 Fuel cost results: DF engines not equipped (first row) or equipped (second row) with ST downstream of WHR systems.

consequently, to high fuel consumption. This should be taken into account carefully from shipowners when deciding operating condition for ships, since coupling curves in figure 9.7 with revenue data and demand for voyages determines break-even point. Secondly, reduced variations on fuel cost related to η_g fluctuations are locally surveyed, hence the same comments previously made for figure 9.5 remain valuable here. Specifically, fuel cost is locally minimized by COGES plants within the medium-high ship speed range, by reciprocating engines where low V_{ship} is required.

9.1.3 Environmental analysis

In this section, environmental impact provided by all power plant configurations of table 9.5 with/without ST installed within DF engine WHR systems is investigated through the Energy Efficiency Design Index (EEDI) $[gCO_2/t/nm]$, whose definition for a Ropax ship is reported

below [317]:

$$EEDI = \frac{\prod_{j=1}^{n} f_j \sum_{i=1}^{n_{ME}} P_{ME_i} CF_{ME_i} SFC_{ME_i}}{f_i f_c GT f_w V_R} + \\ - \frac{\sum_{i=1}^{n_{eff}} f_{eff_i} P_{eff_i} CF_{ME} SFC_{ME}}{f_i f_c GT f_w V_R} \tag{9.4}$$

where the numerator of the first and second term accounts for CO_2 emissions from main engines and CO_2 emission reduction obtained through enhancing efficiency technologies (i.e. bottoming steam power plants), respectively. As can be seen, negative sign is required by regulations for the second term. P indicates power, SFC is specific fuel consumption, CF consists in emission factor depending on fuel (2.75 $gCO_2/gfuel$ and 3.206 $gCO_2/gfuel$ for LNG and MDO, respectively), capacity for Ropax ferries is considered equal to Gross Tonnage and n is the number of engines. The subscripts ME and eff indicate main engines and enhancing efficiency technologies, respectively, whereas power and specific fuel consumption are evaluated at 75% load for each prime mover. Finally, the factors f_{eff}, f_i, f_c and f_w can be assessed by consulting regulations [80]. In order to comply with regulations, attained EEDI must be lower than the required one, yielded by:

$$Required\ EEDI = (1 - \frac{X}{100}) ab^{-c} \tag{9.5}$$

where a and c are coefficients depending on ship type, while b relates to ship dimensions. X is a reduction factor which can be derived from the ship construction year. Results obtained from EEDI computation performed for all the power plant configurations up to 2025 are shown in figure 9.8. Despite best configurations consist in SOL2a and SOL2b, EEDI index is presented also in case larger DF engines (i.e. 12 V MAN 51/60-DF) are included within power plant layout, for the sake of completeness. Different types of line in figure 9.8 distinguish progressive EEDI requirements in time. Comparing different COGES plants, figure 9.8 shows how COGES based on GE25.1 provides the lowest carbon impact, mainly due to the larger amount of thermal power available from exhaust gas of GE25.1. Furthermore, steam turbine installation within DF engine WHR systems guarantees further EEDI reduction. Interestingly, all configurations reported in figure 9.8 comply with EEDI requirements in a long term perspective (i.e. up to 2025), except for SOL2b not equipped with ST downstream of the DF engines. On the contrary, SOL1 configurations do not cope with EEDI requirements at 2025, whereas only SOL3a equipped with DF engine steam turbine complies with the same requirements. This appears to mainly derive from the increase in

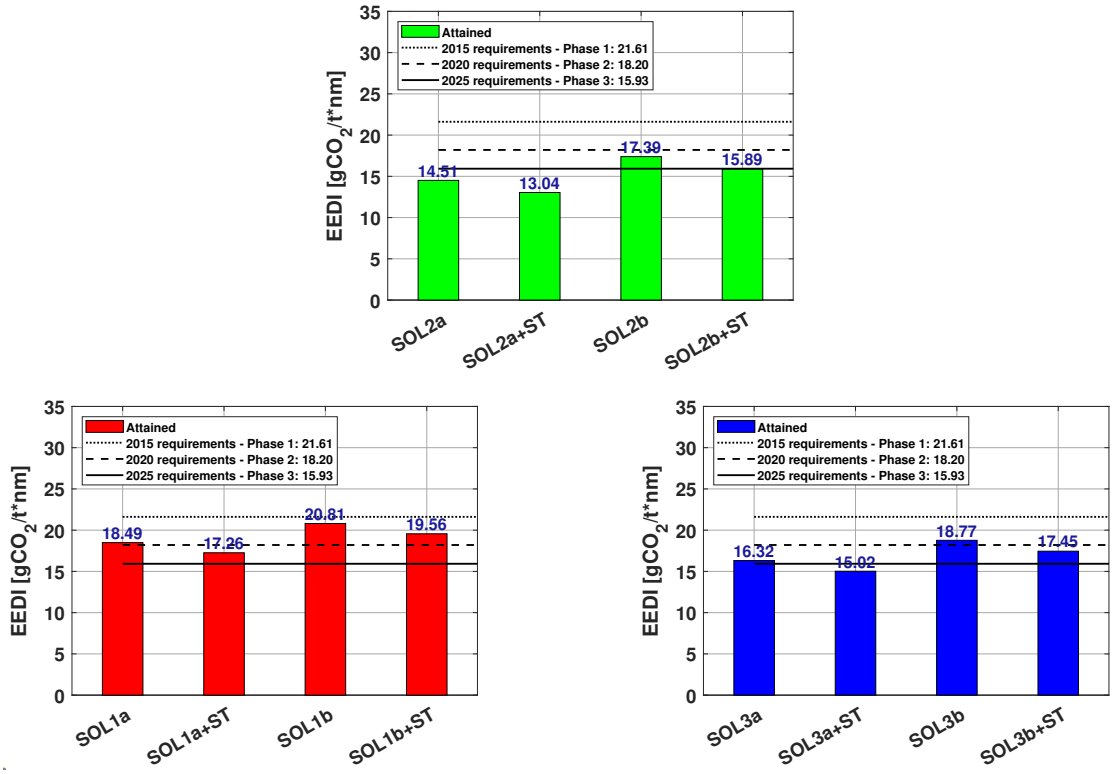

Fig. 9.8 Energy Efficiency Design Index (EEDI) for SOL2a-SOL2b (top row), SOL1a-SOL1b (bottom row, left side) and for SOL3a-SOL3b (bottom row, right side) configurations.

installed power achieved in case one or two 12 V MAN 51/60-DF engines are present within engine room.

9.1.4 Economic analysis

In this section, the economic viability of SOL2a and SOL2b configurations is assessed considering the four operating conditions provided by GNV for Mediterranean routes and reported in table 9.2 above. Steam turbine installation within DF engine WHR systems is also investigated. First, CAPital EXpenditure costs have been computed using power specific costs of each component, according to the literature and manufacturers' indications [318, 319, 300, 306]. The corresponding values in €/kW considered for the analysis are summarised in table 9.6. In case ranges of €/kW are provided, superior and inferior limits relate to smaller and larger size components, respectively. On the other hand, OPerational EXpenditure costs have been evaluated taking into account fuel consumption AFC and

Table 9.6 Capital costs for main power plant components.

COMPONENT	**[€/kW]**
Reciprocating Engines	365-400
Gas Turbines	368-385
LNG tanks and auxiliary plants	200
WHR systems + ST	103-150
Electrical Generators	90-100
Electrical Motors	70-100
AC/DC and DC/AC converters	95-120
Propellers	30-35

maintenance AMC costs, as shown by eq. (9.6):

$$OPEX = AFC + AMC \tag{9.6}$$

where maintenance costs for waste heat recovery systems (i.e. HRSG and WHR) have been assumed equal to 0.6 mln€/year in case they are used, 0.3 mln€/year for vice versa. LNG and MDO prices have been assumed equal to 398 €/t and 575 €/t. It must be underlined that LNG price can be significantly affected by both fluctuations on demand and economic crisis. Furthermore, an operating mode consisting in 7 trips a week during summer period (half May - half September) and 6 during winter one (rest of the year) has been considered, based on the current working conditions of La Suprema. Figure 9.9 shows results obtained from the economic analysis performed over 25 years horizon. Specifically, cost savings in relative form with respect to SOL2a are reported, to improve readness. Diagrams on top refer to Genoa-Palermo (left) and Naples-Palermo (right) routes, whereas in the bottom of the figure results for Naples-Catania (left) and Genoa-Barcelona (right) routes are depicted. Furthermore, the influence of LNG and MDO price volatility on cost savings has been accounted for by performing economic analysis also for a $\pm 10\%$ variation on the reference fuel prices commented out above. Corresponding results are shown in figure 9.9 by means of dotted lines positioned around reference cost savings, dealing with continuous line. In this way, the reliability of economic results is clearly addressed for fuel price volatility available in normal market conditions, i.e. without energy or economic crisis. When the same prime movers are turned with respect to the reference configuration (i.e. SOL2a without ST in DF engine WHR systems) no dotted lines are visible. Indeed, an eventual increase or reduction in cost savings caused by a fuel price volatility are equally surveyed in the reference power plant, hence no relative differences arise. As can be seen from figure 9.9, since no

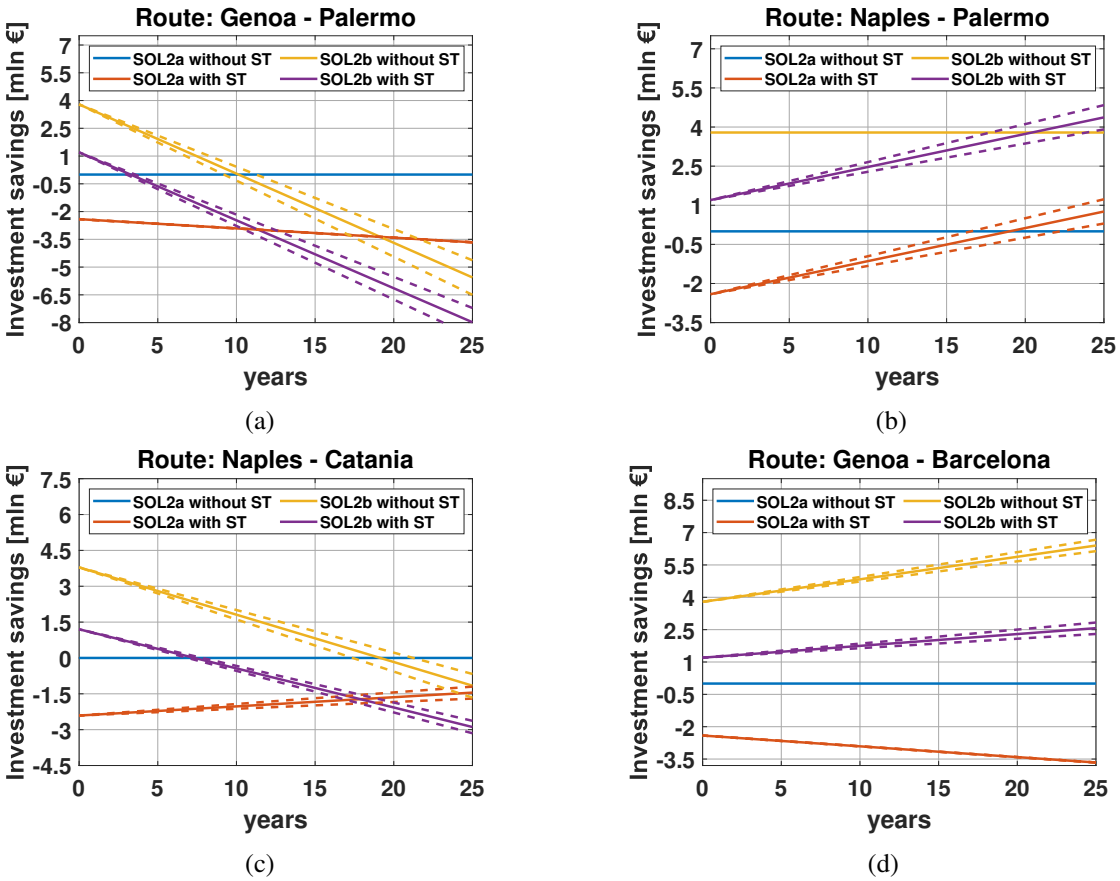

Fig. 9.9 Cost savings over 25 years for four GNV Mediterranean sailing routes.

fuel consumption or maintenance costs are still occurring at the 0-th year, cost savings on CAPEX can be assessed by the starting point of each curve. Namely, positive and negative starting point denotes CAPEX savings and penalties, respectively. Similarly, OPEX cost information can be derived from the curve slope: positive rates of change consist in higher maintenance and fuel consumption costs, negative vice versa. In figure 9.9, ST installation in DF engine WHR systems generates CAPEX penalties, independently from the sailing route. Furthermore, navigation conditions where the entire power demand is covered by COGES plants (22 knots Genoa-Palermo and 20 knots Genoa- Barcelona routes) including steam turbine downstream DF engines provides economical drawbacks also on OPEX, since non-zero maintenance cost is required. Comparison between power plant configurations on the same two routes shows CAPEX benefits for COGES based on TITAN250, due to the lower SOL2b size. Additionally, SOL2b ensures higher η_g at 20 knots, hence lower OPEX are gained in this condition. The opposite scenario occurs at 22 knots, where SOL2b provides significantly lower η_g. In this operating condition, benefits on CAPEX are extinguished within 10 years. Overall, within these two operating conditions, SOL2a not equipped with

DF engine ST provides cost savings over the entire time horizon considered, amounting at 5.5 mln€ at 25-th year. Furthermore, only ±1 mln€ variations are caused by fuel price volatility at 25-th year for SOL2b, therefore intersections between curves are moved by 1.5-2 years. Within navigation condition where reciprocating engines cover the entire power demands (i.e. 17 knots Naples-Palermo route), including steam turbine downstream of DF engines reduces OPEX cost, due to the increase in η_g obtained. On the other hand, penalties on investment costs directly following from the major complexity of power plant architecture are entirely compensated by OPEX benefits after a long-time period (approximately 19 years). Therefore, cost savings obtained by including ST within the WHR systems of DF engines appear too low to motivate the corresponding investment. Furthermore, analogously to what commented out above for medium ship speeds, volatility of fuel price only provides weak variations in economic performances gained from SOL2a and SOL2b configurations, both equipped with DF engine ST. Finally, for high ship speeds, where both COGES and reciprocating engines are turned on (i.e. 25 knots Naples-Catania route), installing DF engine steam turbine guarantees lower OPEX and higher CAPEX costs, for both SOL2a and SOL2b. However, OPEX benefits result too low to recover CAPEX penalties within the time horizon considered. Comparing the two COGES plant configurations, figure 9.9 shows how CAPEX savings and OPEX penalties arise for SOL2b, mainly deriving from the lower nominal size of TITAN250 and reduced η_g on 25 knots, respectively. 18 years last to completely balance minor investment costs, hence SOL2b appears inadequate for a long term perspective. Furthermore, fuel price volatility produces reduced variations on costs (0.5 mln€ at most) and temporal intersections (±1.5 years at most), similarly to what underlined above for other sailing speeds. In conclusion, SOL2a configuration not including ST in DF engine WHR systems was found to provide economic benefits over all the four routes considered. From the previous sections, high energetic and environmental performances were obtained from SOL2a without DF engine ST, therefore it is identified as the best power plant configuration within a repowering perspective for La Suprema. On the other hand, possible inclusion of DF engine ST in SOL2a can guarantee benefits in terms of η_g and EEDI index against penalties in terms of costs. Thus, it can become feasible in future in case more strict regulations will enter to force.

9.1.5 Main findings

In the previous sections, the feasibility of an integrated COGES-reciprocating engine power plant for Mediterranean cruise-ferry powered by LNG has been investigated by energetic, environmental and economic point of views. Specifically, highly efficient propulsion plants

for cruise-ferries have been assessed over a wide ship speed range (16-26 knots), according to GNV shipowners' requests. La Suprema has been taken as reference ship for electrical and thermal power demands onboard, within a cogeneration efficiency maximization study. Where energetic analysis is concerned, results confirmed the potential of integrating COGES with small-size reciprocating engines for marine propulsion applications. In details, COGES plants guarantee the highest cogeneration efficiency within the medium-high ship speed range centered around the current sailing condition for La Suprema (i.e. 22 knots). Comparison between combined gas-steam configurations considered in this study showed that TITAN250-based COGES plant provides slightly higher energy savings in short ship speed range, whereas including GE25.1 maintains high performances under extremely flexible operating conditions. Furthermore, few and weak improvements on η_g were achieved by installing ST in DF engine WHR systems between 16 and 18 knots. Where the environmental impact investigation is concerned, long-term compliance with regulations resulted to be guaranteed by most of power plants including small DF engines. Equipping DF engine WHR systems with steam turbine further reduced CO_2 emissions, since more heat is recovered and used to produce electrical power. Comparison between COGES plants tested identified improved environmental benefits for COGES based on GE25.1 gas turbine. Finally, economic viability was investigated for four different GNV routes within the Mediterranean sea. ST inclusion in DF engine WHR systems revealed to be economically inadequate for most of ship sailing conditions since CAPEX penalties need at least 19 years to be recovered in case OPEX benefits exist. It must be remarked here that economical feasibility of DF engine steam turbine may change in future in case more restrictive regulations are imposed. Overall, cost savings were maximized by COGES plant based on GE25.1 over most of the routes considered. Therefore, the power plant configuration based on the GE25.1 gas turbine and not equipped with DF engine steam turbine resulted to perform better under energetic, environmental and economic point of views, for extremely flexible ship operating conditions.

9.2 Dynamic performance simulation of COGES power plants for cruise-ferry ships

In the following sections, the dynamic simulation of COmbined Gas Electric and Steam (COGES) power plants onboard Liquefied Natural Gas (LNG) powered ships is assessed by means of the Matlab/Simulink code presented in sections 6.2.1 and 6.2.3. Three successive steps have been sequentially faced. Firstly, the two-step optimization procedure introduced in section 6.1.1 and based on both Multi-Objective Genetic Algorithm (MOGA) and gradient descent optimization is used to accurately reconstruct the nominal operating conditions of 6 commercially available gas turbines. Secondly, dynamic performances provided by these GTs is investigated by means of the Matlab/Simulink code previously described in section 6.2.1. In order to assess the influence of the governing strategy of GTs on performances, both the turbine inlet temperature (TITc) and the turbine outlet temperature (TOTc) controls have been considered within the analysis. Equilibrium results gained from dynamic simulation of the 6 GTs for various load conditions are successively introduced as input into the Fortran code described in section 7, in order to optimally assembly integrated COGES-reciprocating engine power plants. Then, all the generated layouts are tested in a cogeneration efficiency optimization study aimed to repowering the cruise-ferry GNV La Suprema. Overall, optimization is carried out for 264 ship operating conditions, accounting for variable ship speed, season and GT control strategy, and the best power plant is identified by an energetic point of view. Finally, the time-dependent performance provided by the best COGES plant during actual navigation conditions for La Suprema is investigated.

9.2.1 Case study

As mentioned above, the dynamic simulation and repowering study performed in this work concern the cruise-ferry La Suprema, whose main characteristics have been previously introduced in section 9.1.1 together with its electrical and thermal power demands. Specifically, La Suprema currently operates along the Genoa-Palermo route at 22 knots with reduced energy savings, since power plant installed onboard was designed for 28 knots of cruise speed, hence it now results oversized. Therefore, a repowering study appears necessary to guarantee high efficiency over extremely flexible operating conditions. Previous work in sections 9.1.2, 9.1.3 and 9.1.4 showed how integrating the COGES plant with reciprocating engines can effectively provide benefits under energetic, environmental and economic point of view. Thus, many integrated COGES-reciprocating engine plants are here investigated in order to find out

optimal gas turbine to be combined with the bottoming steam power plants and then installed onboard La Suprema. Where the repowering study is concerned, time-mean electrical power required by propulsion and hotel services are reported in figure 9.2 above, whereas 900 kg/h and 1050 kg/h steam mass flow rates at 7 bar have been considered as thermal demands for summer and winter seasons. Performances of each power plant are assessed over a wide ship speed range (16-26 knots), with the aim of identifying highly-efficient configurations under flexible operating conditions. On the other hand, time-dependent demands for La Suprema have been derived from data available from the literature concerning cruise-ferries of comparable size [31]. Specifically, the profiles available from the literature have been scaled such to guarantee the same electrical energy exchange obtained by time-mean data. The time-dependent demand considered for electrical power over navigation is shown in figure 9.10 for both summer and winter seasons. On the other hand, small variations in terms

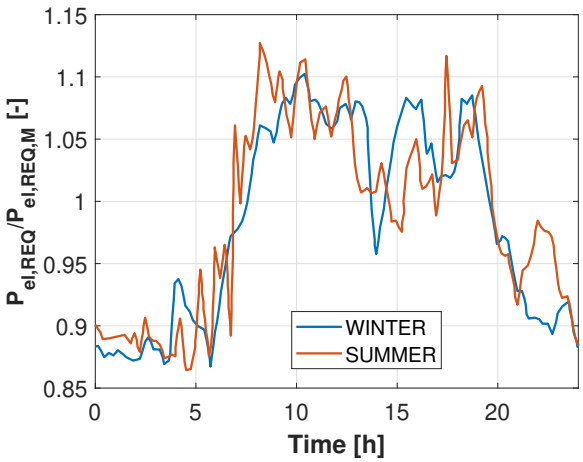

Fig. 9.10 Time-dependent electrical power demand from hotel services onboard a medium-size cruise ship during winter and summer days [31].

of thermal power demand are present onboard cruise-ferries sailing on daily routes, thus a the time-mean data are maintained also for transient simulations. It must be remarked that time-dependent analysis has been carried out only during navigation, since time-mean power demand during maneuvering and port were not provided by shipowners. A schematic view of the power plant configuration considered in this work is depicted in figure 9.11, where reciprocating engines dealing with large/small size are indiscriminately depicted and dots in correspondence of the electric bar indicate variable number of prime movers/users. In this way, generality of the schematic view reported in figure 9.11 is preserved over all the six power plant configurations considered. Overall, the prime movers installed within engine room account for a COGES plant, two DF engines of variable size and three harbour reciprocating engines fed by natural gas. The harbour generating set is allowed to run also

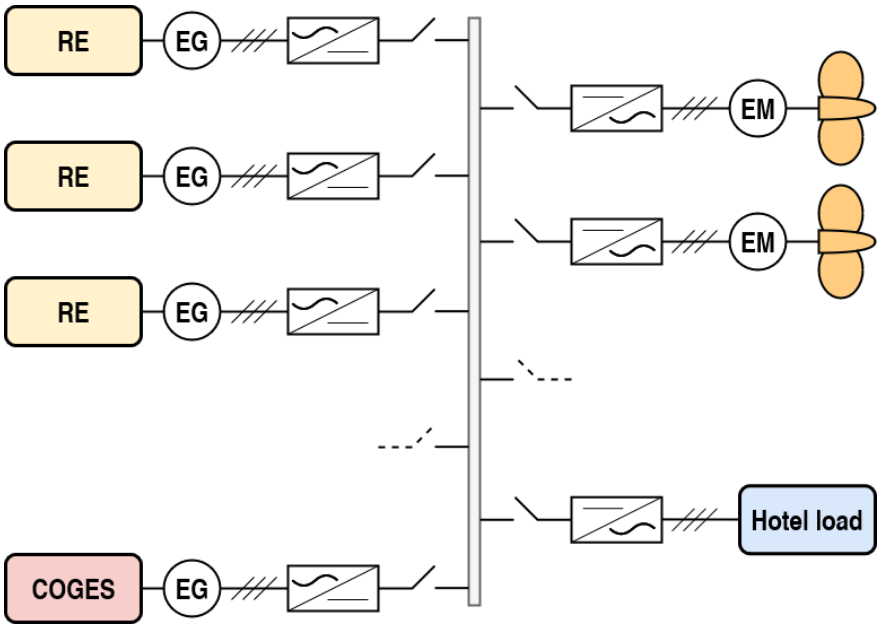

Fig. 9.11 Schematic view of the integrated COGES-reciprocating engine power plant investigated. RE indicates reciprocating engines (both dual-fuel and natural gas engines), EG stands for electrical generator, EM means electrical motor.

on navigation in case it may provide benefits in terms of power plant efficiency, according to [313]. All the possible prime movers included within the engine room are summarised in table 9.7. Specifically, six different GTs from General Electric, Rolls-Royce, Siemens and Solar dealing with 21-30 MW size are investigated, together with two different DF engines from MAN and a natural gas Rolls-Royce engine. As can be seen, LM2500+ and LM2500+G4 are characterized by major size, whereas SGT600 and RB211 deal with intermediate η_{el} together with lower T_{ex} and $\dot{m}_{ex}$ in comparison to LM2500 or TITAN250. Since waste heat available for recovery from exhaust gas is particularly low for small-size reciprocating engines, no WHR system is installed downstream R-R Bergen C26 L9, thus no exhaust gas temperature is inserted in table 9.7. A 90% and 97% engine margin was adopted for reciprocating engines and COGES plant, respectively. On the other hand, power plant configurations considered for the repowering study have been designed following well-established procedures [227] and are summarised in table 9.8. DF engines dealing with higher nominal power (i.e. 12VMAN) have been coupled with large-size GTs to satisfy power demand in the intermediate ship speed range (18-21 knots), where GTs would work at significantly reduced load ($\leq$ 50%) and efficiency. Indeed, too low power would be delivered by 9LMAN engines to cover electrical demand within these sailing conditions.

Table 9.7 Main characteristics of prime movers considered to be installed onboard the cruise-ferry La Suprema.

GT	P_{net} [MW]	η_{el} [%]	T_{ex} [°C]
LM2500	24.31	36	566
TITAN250	21.75	39	465
SGT600	24.58	33.6	543
RB211	25.25	34.7	488
LM2500+	29.26	38	518
LM2500+G4	36	38.4	549
12V MAN 51/60	11.23	45.5	309
9L MAN 51/60	8.42	45.5	309
R-R Bergen C26 L9	2.33	45	-

Table 9.8 Propulsion system configurations being selected for the cruise-ferry La Suprema.

GT	12VMAN51/60	9LMAN51/60	R-R Bergen C26 L9
LM2500		XX	XXX
Titan 250		XX	XXX
RB211		XX	XXX
SGT600		XX	XXX
LM2500+	X	X	XXX
LM2500+G4	XX		XXX

9.2.2 Results

In this section, the dynamic behaviour of GTs is investigated in details, focusing on the time-dependent response concerning the most relevant operating parameters. Since 6 different GTs have been simulated, only results from the LM2500 gas turbines are presented to preserve conciseness. Nevertheless, qualitatively analogous results can be obtained for other GTs due to the flexibility of the Matlab/Simulink code. Furthermore, 3 different governing strategies for GTs have been accounted for in the following. Indeed, transient results gained from disabling IGV control are assessed as reference condition, other than the TITc and TOTc strategies introduced in section 6.2.2 above. The corresponding acronyms used in the following for the reference control is Fc. First, equilibrium running lines referring to all the three control strategies considered are reported on the compressor map in figure 9.12a together with analogous data available within the literature (see dashed black line) [260]. In details, equilibrium states for the aeroderivative gas turbines are obtained by imposing as input power request ranging from 20% to 100%. Operational points corresponding to 20%, 40%, 60%, 80% and 100% loads are reported with different shapes and colors. Surge limit is

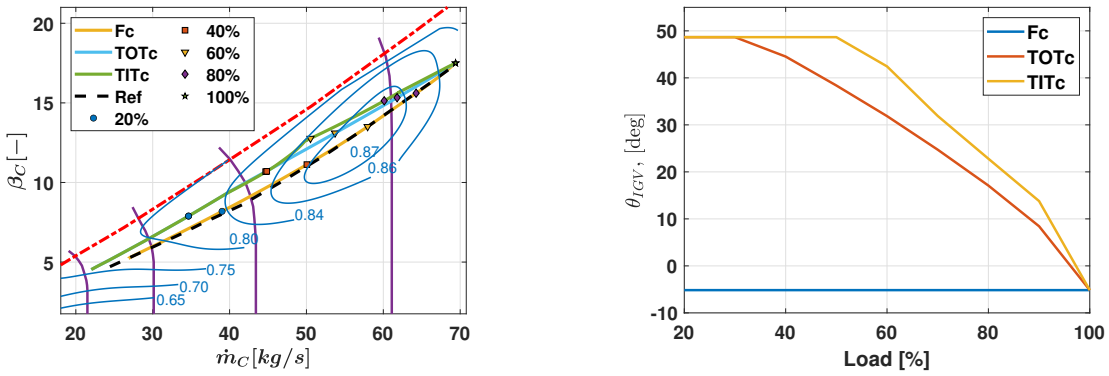

(a) (b)

Fig. 9.12 Equilibrium running lines for TITc, TOTc and Fc control strategies on compressor map (a) together with the corresponding IGV actuation laws (b).

depicted in dash-dot line, whereas contour levels for N_{GG} and η_c are reported in purple and blue, respectively. As can be seen, all the three equilibrium running lines are positioned far away from the surge limit (SL $\geq$ 0.22), hence safety operation for compressor is ensured. Furthermore, distinct starting points, all dealing with 20% load are obtained in case IGV is enabled or not. Specifically, starting point for the blue curve, related to no IGV control, deals with higher mass flow rates in comparison to those obtained enabling IGV. This mainly derives from the influence played by IGV closing angle on the compressor characteristic map in terms of β_c, $\dot{m}_a$ and η_c as described in previous sections [262, 77, 261]. On the other hand, differences existing for the TITC and TOTc control strategies mainly depend on the IGV actuation laws reported in figure 9.12b. Indeed, maximum opening angle is imposed at full load, whereas IGV is gradually closed up to achieve full-closed condition when gas turbine works at 30-50% load. For further reduced loads the intake air mass flow rate cannot be lowered to maintain TIT or TOT constant and equilibrium lines from TITc and TOTc coincide (see figure 9.12a for $\dot{m}_a \leq 40 kg/s$. Minimum loads where TIT and TOT are controlled mainly depends on the closing rate adopted for IGV to implement regulation. As can be seen, higher slope in magnitude is imposed to keep turbine inlet temperature constant, hence the minimum IGV angle is firstly achieved by TITc. Overall, good agreement arises within the comparison between the dashed black curve from Klapproth et al. [260] and equilibrium lines numerically computed. Focusing on detailed thermodynamic operating conditions involved with Fc, TITc and TOTc governing strategies, time-dependent results concerning P_{net}, TIT, T_{ex} and N_{GG} are reported in figure 9.13. Results are obtained by imposing as input a start-up/switch-off load ramp ranging from 0% to 100% and vice versa, while extending on 50 s in time (see the black dashed line in figure 9.13). As can be seen, the dynamical response to accelerating and

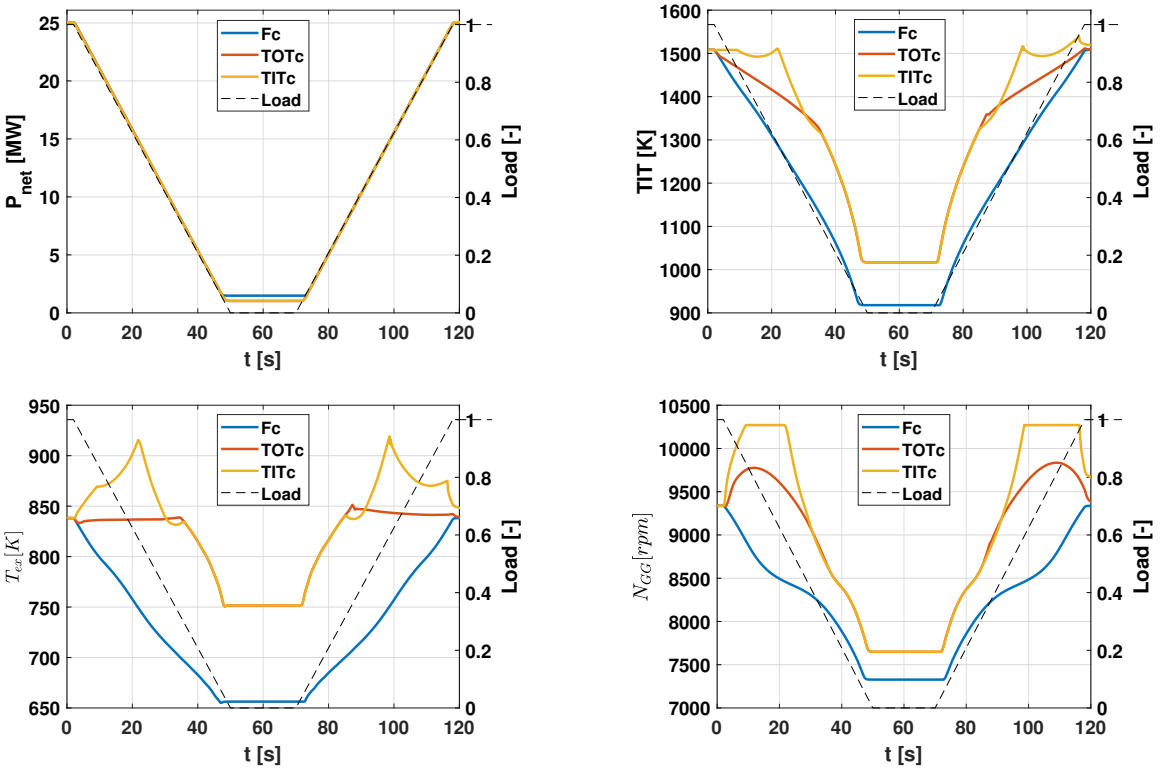

Fig. 9.13 Time-dependent behaviour concerning the main GT thermodynamic parameters for TITc, TOTc and Fc control strategies: net power (a), TIT (b), T_{ex} (c) and N_{GG} (d).

decelerating ramps is nearly characterized by symmetric behaviour, independently from the thermodynamic parameters considered. Focusing on the N_{GG} response to switch-off ramp, a plateaux induced by the over-speed PID controller is clearly visible around t= 10 - 23 s (GT load $\approx$ 60-70%), only for the TITc strategy. Indeed, moving from full-load to part-load operating conditions, the fuel flow rate needs to be reduced in order to lower power delivered. This, in case IGV control is disabled, corresponds to a reduction in both turbine inlet and outlet temperatures (see the blue curve for Fc). On the contrary, closing IGV within the TITc and TOTc control strategies allows for maintaining TIT and TOT constant, respectively, with a consequent acceleration of the gas generator shaft [320]. However, the closing rate of IGV previously shown in figure 9.12b directly determines the possible exceeding of over-speed limit. Indeed, since IGV is more rapidly closed within the TITc strategy with respect to TOTc, keeping constant the turbine inlet temperature generates a stronger increase for N_{GG}, which exceeds the over-speed limit assumed equal to 110% of nominal value (see the yellow curve in figure 9.13). On the contrary, the weaker closing rate for IGV adopted by TOTc governing strategy avoids over-speed exceeding conditions. Nevertheless, when the GT working load further reduces, simultaneous decrease of $\dot{m}_f$ and IGV opening angle

implies a reduction in N_{GG}. Thus, the over-speed control stops working for TITc. Analogous comments can be made for the switch-on ramp. Furthermore, a clear visualization of the

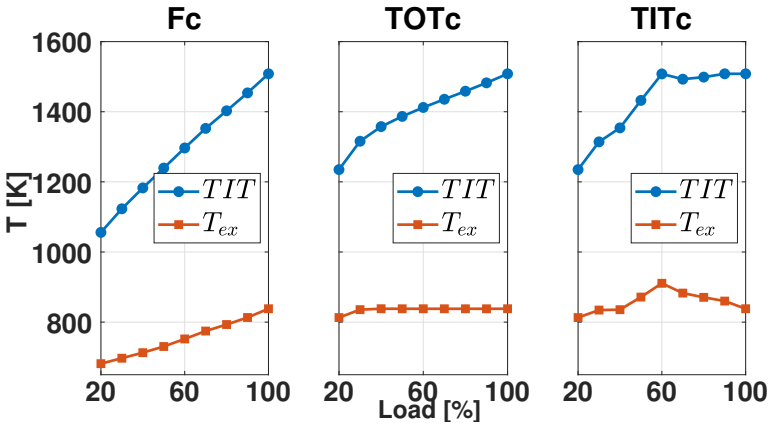

Fig. 9.14 Dependency of T_{ex} and TIT on GT load for Fc, TOTc and TITc control strategies, from left to right.

load range where TITc and TOTc succeeds in keeping TIT and TOT constant, respectively, is shown in figure 9.14. Interestingly, T_{ex} is kept constant up to approximately 30% of the load, hence reduced off-design operating conditions for the bottoming steam power plant are reached, with consequent benefits on efficiency. On the other hand, the turbine inlet temperature is maintained constant by TITc up to 70% of the load, where weak deviations from TIT occur due to enabling of the over-speed control, as previously commented out. Specifically, deviations from the nominal TIT are within 2% of relative error up to 60% load conditions. Overall, results concerning load ranges where TIT and TOT are kept constant appear to fairly agree with the literature [77]. Finally, qualitatively analogous results are obtained from transient simulation of all the gas turbines reported in table 9.7, despite are not reported here for sake of conciseness.

9.2.3 Repowering study

In this section, performances provided by all the power plant configurations reported in table 9.8 above are are assessed by an energetic point of view. Specifically, comparison in terms of cogeneration efficiency η_g is carried out over a wide ship speed range (16-26 knots), for both summer and winter seasons. Furthermore, in order to identify the best governing mode for COGES plant installed onboard ships, both TITc and TOTc control strategies are considered

in the analysis. Definition for η_g adopted here is reported below:

$$\eta_g = \frac{\sum_{i=1}^{n_{pm}} P_{el,i} + P_{th,i}}{\sum_{i=1}^{n_{pm}} \dot{m}_{f,i} LHV_{NG} + \sum_{j=1}^{n_{DF}} \dot{m}_{f,j} LHV_{MDO}} \tag{9.7}$$

where n_{pm} is the number of turned on engines, n_{DF} the number of DF engines, LHV the lower heating value of fuel, $P_{el,i}$ and $P_{th,i}$ the portion of electrical and thermal demands covered by the i-th engine, $\dot{m}_{f,i}$ the LNG mass flow rate burned within the i-th engine, $\dot{m}_{f,j}$ the MDO mass flow rate used by the j-th DF engine. Where the TOTc strategy is assumed, cogeneration

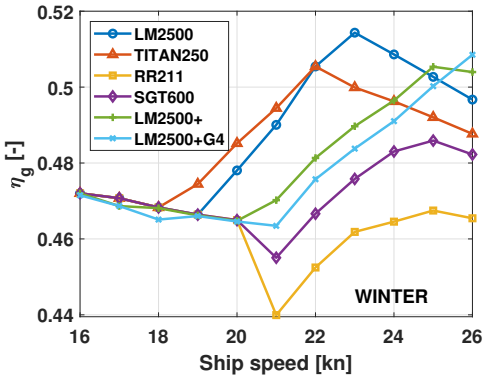

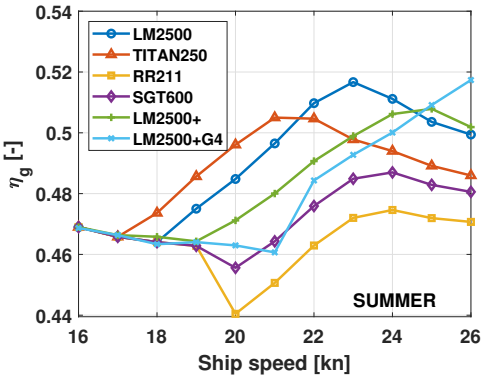

TOTc, WINTER												
Ship Speed [kn]		16	17	18	19	20	21	22	23	24	25	26
LM2500	C	0,0	0,0	0,0	0,0	61,4	69,3	80,4	89,8	93,2	97,0	97,0
	DF1	79,8	85,6	85,0	87,5	0,0	0,0	0,0	0,0	0,0	0,0	74,6
	DF2	0,0	85,6	85,0	87,5	0,0	0,0	0,0	0,0	0,0	0,0	0,0
	B1	81,4	0,0	89,6	89,4	0,0	0,0	0,0	0,0	62,9	86,1	79,7
	B2	81,4	0,0	0,0	89,4	0,0	0,0	0,0	0,0	0,0	86,1	0,0
	B3	81,4	0,0	0,0	0,0	0,0	0,0	0,0	0,0	0,0	0,0	0,0
LM2500+	C	0,0	0,0	0,0	0,0	0,0	56,2	66,3	75,1	83,0	94,4	97,0
	DF1	0,0	78,1	79,8	89,6	90,0	0,0	0,0	0,0	0,0	0,0	0,0
	DF2	79,8	0,0	88,4	81,5	85,1	0,0	0,0	0,0	0,0	0,0	0,0
	B1	81,4	80,6	0,0	85,5	88,7	0,0	0,0	0,0	0,0	0,0	69,4
	B2	81,4	80,6	0,0	0,0	88,7	0,0	0,0	0,0	0,0	0,0	69,4
	B3	81,4	80,6	0,0	0,0	0,0	0,0	0,0	0,0	0,0	0,0	0,0
LM2500+G4	C	0,0	0,0	0,0	0,0	0,0	0,0	51,1	58,0	64,2	73,3	82,9
	DF1	76,3	78,1	73,1	84,2	86,0	88,4	0,0	0,0	0,0	0,0	0,0
	DF2	0,0	0,0	73,1	84,2	86,0	88,4	0,0	0,0	0,0	0,0	0,0
	B1	82,3	80,6	0,0	0,0	89,8	87,0	0,0	0,0	0,0	0,0	0,0
	B2	82,3	80,6	0,0	0,0	0,0	87,0	0,0	0,0	0,0	0,0	0,0
	B3	0,0	80,6	0,0	0,0	0,0	0,0	0,0	0,0	0,0	0,0	0,0
RB211	C	0,0	0,0	0,0	0,0	0,0	65,9	77,8	88,2	93,2	97,0	97,0
	DF1	79,8	85,6	85,0	87,5	90,0	0,0	0,0	0,0	0,0	0,0	74,0
	DF2	0,0	85,6	85,0	87,5	90,0	0,0	0,0	0,0	0,0	0,0	0,0
	B1	81,4	0,0	89,6	89,4	89,5	0,0	0,0	0,0	53,1	58,0	83,9
	B2	81,4	0,0	0,0	89,4	89,5	0,0	0,0	0,0	0,0	58,0	0,0
	B3	81,4	0,0	0,0	0,0	89,5	0,0	0,0	0,0	0,0	58,0	0,0
SGT600	C	0,0	0,0	0,0	0,0	0,0	61,9	73,6	83,6	92,7	97,0	97,0
	DF1	79,8	85,6	85,0	87,5	90,0	0,0	0,0	0,0	0,0	0,0	80,2
	DF2	0,0	85,6	85,0	87,5	90,0	0,0	0,0	0,0	0,0	0,0	0,0
	B1	81,4	0,0	89,6	89,4	89,5	0,0	0,0	0,0	0,0	56,4	0,0
	B2	81,4	0,0	0,0	89,4	89,5	0,0	0,0	0,0	0,0	56,4	0,0
	B3	81,4	0,0	0,0	0,0	89,5	0,0	0,0	0,0	0,0	0,0	0,0
TITAN 250	C	0,0	0,0	0,0	63,7	73,7	83,6	92,3	97,0	97,0	97,0	97,0
	DF1	79,8	85,6	85,0	0,0	0,0	0,0	0,0	0,0	0,0	70,0	82,7
	DF2	0,0	85,6	85,0	0,0	0,0	0,0	0,0	0,0	0,0	0,0	82,7
	B1	81,4	0,0	89,6	0,0	0,0	0,0	57,8	68,2	84,3	83,9	0,0
	B2	81,4	0,0	0,0	0,0	0,0	0,0	0,0	68,2	84,3	83,9	0,0
	B3	81,4	0,0	0,0	0,0	0,0	0,0	0,0	0,0	84,3	0,0	0,0

TOTc, SUMMER												
Ship Speed [kn]		16	17	18	19	20	21	22	23	24	25	26
LM2500	C	0,0	0,0	0,0	57,9	66,0	74,2	85,6	94,7	97,0	97,0	97,0
	DF1	83,3	79,5	80,1	0,0	0,0	0,0	0,0	0,0	0,0	0,0	73,3
	DF2	0,0	79,5	80,1	0,0	0,0	0,0	0,0	0,0	0,0	0,0	0,0
	B1	89,5	81,0	81,3	0,0	0,0	0,0	0,0	0,0	86,6	85,1	83,9
	B2	89,5	0,0	81,3	0,0	0,0	0,0	0,0	0,0	0,0	85,1	83,9
	B3	89,5	0,0	0,0	0,0	0,0	0,0	0,0	0,0	0,0	85,1	0,0
LM2500+	C	0,0	0,0	0,0	0,0	51,4	58,6	68,8	77,5	85,1	95,4	97,0
	DF1	0,0	80,8	90,0	90,0	0,0	0,0	0,0	0,0	0,0	0,0	0,0
	DF2	83,3	0,0	85,2	90,0	0,0	0,0	0,0	0,0	0,0	0,0	0,0
	B1	89,5	88,7	0,0	89,9	0,0	0,0	0,0	0,0	0,0	0,0	75,6
	B2	89,5	88,7	0,0	0,0	0,0	0,0	0,0	0,0	0,0	0,0	75,6
	B3	89,5	88,7	0,0	0,0	0,0	0,0	0,0	0,0	0,0	0,0	0,0
LM2500+G4	C	0,0	0,0	0,0	0,0	0,0	0,0	53,0	59,9	66,4	75,6	84,7
	DF1	81,7	80,8	76,9	88,1	89,9	83,4	0,0	0,0	0,0	0,0	0,0
	DF2	0,0	0,0	76,9	88,1	89,9	83,4	0,0	0,0	0,0	0,0	0,0
	B1	87,9	88,7	0,0	0,0	89,6	86,3	0,0	0,0	0,0	0,0	0,0
	B2	87,9	88,7	0,0	0,0	0,0	86,3	0,0	0,0	0,0	0,0	0,0
	B3	0,0	88,7	0,0	0,0	0,0	86,3	0,0	0,0	0,0	0,0	0,0
RB211	C	0,0	0,0	0,0	0,0	60,2	68,7	80,2	89,4	94,2	97,0	97,0
	DF1	83,3	79,5	80,1	80,9	0,0	0,0	0,0	0,0	0,0	50,7	77,8
	DF2	0,0	79,5	80,1	80,9	0,0	0,0	0,0	0,0	0,0	0,0	0,0
	B1	89,5	81,0	81,3	87,9	0,0	0,0	0,0	0,0	54,6	0,0	79,8
	B2	89,5	0,0	81,3	87,9	0,0	0,0	0,0	0,0	0,0	0,0	0,0
	B3	89,5	0,0	0,0	87,9	0,0	0,0	0,0	0,0	0,0	0,0	0,0
SGT600	C	0,0	0,0	0,0	0,0	56,4	64,7	76,4	85,8	94,3	97,0	97,0
	DF1	83,3	79,5	80,1	80,9	0,0	0,0	0,0	0,0	0,0	0,0	84,7
	DF2	0,0	79,5	80,1	80,9	0,0	0,0	0,0	0,0	0,0	0,0	0,0
	B1	89,5	81,0	81,3	87,9	0,0	0,0	0,0	0,0	0,0	64,2	0,0
	B2	89,5	0,0	81,3	87,9	0,0	0,0	0,0	0,0	0,0	64,2	0,0
	B3	89,5	0,0	0,0	87,9	0,0	0,0	0,0	0,0	0,0	0,0	0,0
TITAN 250	C	0,0	0,0	57,2	67,1	76,9	86,1	94,2	97,0	97,0	97,0	97,0
	DF1	83,3	79,5	0,0	0,0	0,0	0,0	0,0	0,0	75,4	76,5	85,6
	DF2	0,0	79,5	0,0	0,0	0,0	0,0	0,0	0,0	0,0	0,0	85,6
	B1	89,5	81,0	0,0	0,0	0,0	0,0	55,3	75,7	0,0	82,3	0,0
	B2	89,5	0,0	0,0	0,0	0,0	0,0	0,0	75,7	0,0	82,3	0,0
	B3	89,5	0,0	0,0	0,0	0,0	0,0	0,0	0,0	0,0	0,0	0,0

Fig. 9.15 On the top of the figure, cogeneration efficiency considering TOTc control strategy: winter (left) and summer (right) seasons. On the bottom: engine loads in terms of percentage of maximum continuous rating.

efficiency results obtained from all the 6 different configurations tested are shown in figure 9.15 for winter (left column) and summer (right column) season. The corresponding working conditions for each prime mover are summarised within the tabular legend in terms of % loads, where the GT module identifies COGES plants, DF1 and DF2 refer to 12VMAN and 9LMAN engines, and B1, B2 and B3 relates to R-R Bergen C26 L9 engines. Three distinct operating regions can be identified in figure 9.15, independently from power plant and season. Firstly, slight variations on cogeneration efficiency provided by all the 6 configurations are surveyed in the low ship speed range (i.e. $\approx$ 16-19 knots). Specifically, some curves exactly coincide at certain ship speed conditions (e.g. see the purple and red curves for 16-18 knots), whereas few differences locally arise among other configurations (e.g. see the purple and light blue curves at 17-18 knots). Indeed, power demand at low V_{ship} is mainly covered by reciprocating engines (DF or NG), since they guarantee higher η_g at part-loads than COGES plants. In case reciprocating engines of the same type are installed and turned on in two distinct machine rooms, the η_g-curves corresponding to these two power plant configurations collapse at the corresponding ship speed. On the contrary, weak variations on η_g are surveyed if the turned on reciprocating engines are different. In this case, all the reciprocating engines considered present similar level of η_{el}, though those dealing with small-size often operate at higher loads, with consequent benefits in terms of energy savings (e.g., see the light blue and purple curves at 17-18 knots). Secondly, power demand is covered by COGES within the intermediate ship speed range (i.e. $\approx$ 19-23 knots), as shown in the tabular legend. Indeed, cogeneration efficiency benefits are provided by COGES plants in comparison with reciprocating engines for power request $\geq$ 16MW. Finally, at high ship speed sailing conditions COGES plants work almost at 97% loads and few extra power is eventually delivered by reciprocating engines, depending on gas turbine size. Overall, significant effect is played by the prime mover performances in determining the power distribution over the entire ship speed range visible in figure 9.15. Indeed, reciprocating engines summarised in table 9.7 are all characterized by reduced power size in comparison to COGES plants, hence they can operate at higher loads (i.e. efficiency) when low power demand occurs, as within 16-19 knots. Furthermore, they weakly suffer from efficiency reduction at part-loads, with positive effect on operational flexibility. On the other hand, COGES plants can cover the entire power demand with maximum efficiencies for ship speeds around 22 knots. Finally, in case COGES plants do not manage to supply the entire power demand at high ship speeds, few reciprocating engines are turned. However, the amount of the energy savings depends on COGES plant. Indeed, COGES plants based on LM2500 and TITAN250 are shown to provide the highest η_g within the middle-high ship speed range. On the contrary, since SGT-600 and RB211 deliver nearly the same P_{net} of LM2500 and

TITAN250 but with lower electrical efficiency, installing them onboard generates energy penalties (i.e. 1-2% lower η_g for ship speeds $\geq$ 20 knots). Furthermore, SGT-600 and RB211 deal with lower exhaust gas temperature and mass flow rates in comparison to LM2500 and TITAN250, hence compensation of GT energy penalties can not be assessed by the bottoming steam power plant. Finally, benefits in terms of η_g values are obtained including LM2500+ and LM2500+G4 within COGES plant at few, high ship speeds (25-26 knots) in comparison to performances provided by LM2500 and TITAN250. Specifically, looking at figure 9.15, η_g curves from LM2500+ and LM2500+G4 based COGES plants appear shifted towards high ship speeds, hence higher efficiencies would be probably achieved beyond 26 knots. Thus, their large size seems to not match well power demands onboard La Suprema. On the other hand, analogous results obtained from all the 6 power plant configurations are reported in figure 9.16 in case TITc control strategy is implemented. Plots concerning winter and summer seasons are positioned on the left and right side, respectively, whereas tabular legend summarises load data for each operating conditions dealing with ship speed within the range 16-26 knots. Again, three main distinct regions can be identified, depending on the ship speed range, in both winter and summer seasons. As can be seen from the tabular legend, power demand is covered by reciprocating engines in the low ship speed range, whereas in the middle-high ship speed range COGES plants provide the highest cogeneration efficiency. Few small-size reciprocating engines can eventually help COGES plants to cover the entire power request onboard at 25-26 knots. Where comparison between different COGES plants is concerned, SGT-600 and RB211 are proved to deliver the worst performances when combined with bottoming steam power plant, as well as LM2500+ and LM2500+G4 appear oversized for La Suprema, hence their potential remains unused. Finally, including LM2500 GT within engine room offers high performance over a wider ship speed range (19-24 knots), despite COGES based on TITAN250 guarantees energy savings within limited ship speed range (19-21 knots), independently from the control strategy adopted. Comparing figures obtained from TITc and TOTc governing strategies reveals comparable values of η_g for ship speeds where COGES plants are turned on, where cogeneration efficiency appears unaffected by GT control at reduced V_{ship}. However, TITc governing strategy appears to provide lower energy savings within the middle-high ship speed range (see η_g delivered by the LM2500-based COGES plant at 24 knots). Indeed, since TITc targets to maximize electrical efficiency of GT, it guarantees lower exhaust gas temperature and mass flow rate, with consequent reduction of performances delivered by the bottoming steam power plant. On the contrary, TOTc strategy is specifically aimed at maximizing efficiency of the overall COGES plant, as traditionally done within the power generation sector. In details, off-design conditions for bottoming steam power plants are dampened. Nevertheless, weak gap ($\approx$

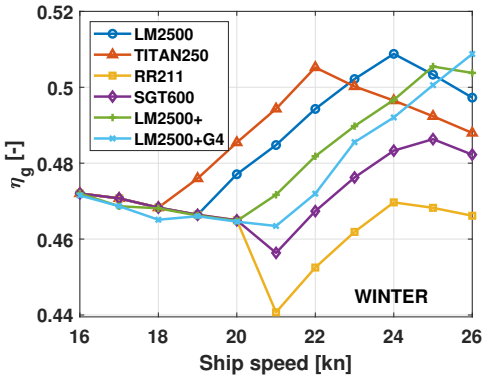

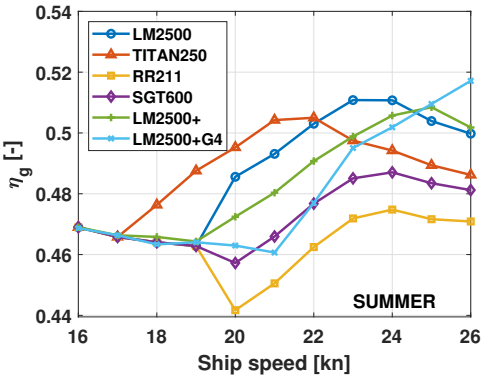

TITc, WINTER												
Ship Speed [kn]		16	17	18	19	20	21	22	23	24	25	26
LM2500	C	0,0	0,0	0,0	0,0	52,4	61,3	75,0	85,7	95,6	97,0	97,0
	DF1	79,8	85,6	85,0	87,5	0,0	0,0	0,0	0,0	0,0	0,0	69,7
	DF2	0,0	85,6	85,0	87,5	0,0	0,0	0,0	0,0	0,0	0,0	0,0
	B1	81,4	0,0	89,6	89,4	0,0	0,0	0,0	0,0	0,0	76,0	77,2
	B2	81,4	0,0	0,0	89,4	0,0	0,0	0,0	0,0	0,0	76,0	0,0
	B3	81,4	0,0	0,0	0,0	0,0	0,0	0,0	0,0	0,0	0,0	0,0
LM2500+	C	0,0	0,0	0,0	0,0	0,0	52,3	62,9	73,0	81,4	93,1	97,0
	DF1	0,0	78,1	79,8	89,6	90,0	0,0	0,0	0,0	0,0	0,0	0,0
	DF2	79,8	0,0	88,4	81,5	85,1	0,0	0,0	0,0	0,0	0,0	0,0
	B1	81,4	80,6	0,0	85,5	88,7	0,0	0,0	0,0	0,0	0,0	62,7
	B2	81,4	80,6	0,0	0,0	88,7	0,0	0,0	0,0	0,0	0,0	62,7
	B3	81,4	80,6	0,0	0,0	0,0	0,0	0,0	0,0	0,0	0,0	0,0
LM2500+G4	C	0,0	0,0	0,0	0,0	0,0	0,0	50,2	54,3	60,4	71,1	81,4
	DF1	76,3	78,1	73,1	84,2	86,0	88,4	0,0	0,0	0,0	0,0	0,0
	DF2	0,0	0,0	73,1	84,2	86,0	88,4	0,0	0,0	0,0	0,0	0,0
	B1	82,3	80,6	0,0	0,0	89,8	87,0	0,0	0,0	0,0	0,0	0,0
	B2	82,3	80,6	0,0	0,0	0,0	87,0	0,0	0,0	0,0	0,0	0,0
	B3	0,0	80,6	0,0	0,0	0,0	0,0	0,0	0,0	0,0	0,0	0,0
RB211	C	0,0	0,0	0,0	0,0	0,0	61,3	75,1	86,0	91,4	97,0	97,0
	DF1	79,8	85,6	85,0	87,5	90,0	0,0	0,0	0,0	0,0	0,0	69,9
	DF2	0,0	85,6	85,0	87,5	90,0	0,0	0,0	0,0	0,0	0,0	0,0
	B1	81,4	0,0	89,6	89,4	89,5	0,0	0,0	0,0	53,8	79,6	83,9
	B2	81,4	0,0	0,0	89,4	89,5	0,0	0,0	0,0	0,0	79,6	0,0
	B3	81,4	0,0	0,0	0,0	89,5	0,0	0,0	0,0	0,0	0,0	0,0
SGT600	C	0,0	0,0	0,0	0,0	0,0	58,1	67,2	82,0	91,3	97,0	97,0
	DF1	79,8	85,6	85,0	87,5	90,0	0,0	0,0	0,0	0,0	0,0	77,3
	DF2	0,0	85,6	85,0	87,5	90,0	0,0	0,0	0,0	0,0	0,0	0,0
	B1	81,4	0,0	89,6	89,4	89,5	0,0	50,1	0,0	0,0	51,2	0,0
	B2	81,4	0,0	0,0	89,4	89,5	0,0	0,0	0,0	0,0	51,2	0,0
	B3	81,4	0,0	0,0	0,0	89,5	0,0	0,0	0,0	0,0	0,0	0,0
TITAN 250	C	0,0	0,0	0,0	59,5	71,1	81,9	91,3	97,0	97,0	97,0	97,0
	DF1	79,8	85,6	85,0	0,0	0,0	0,0	0,0	0,0	0,0	70,3	88,3
	DF2	0,0	85,6	85,0	0,0	0,0	0,0	0,0	0,0	0,0	0,0	0,0
	B1	81,4	0,0	89,6	0,0	0,0	0,0	52,0	63,0	80,8	78,1	89,5
	B2	81,4	0,0	0,0	0,0	0,0	0,0	0,0	63,0	80,8	78,1	89,5
	B3	81,4	0,0	0,0	0,0	0,0	0,0	0,0	0,0	80,8	0,0	89,5

TITc, SUMMER												
Ship Speed [kn]		16	17	18	19	20	21	22	23	24	25	26
LM2500	C	0,0	0,0	0,0	0,0	54,3	63,4	76,7	88,5	93,2	96,8	97,0
	DF1	83,3	79,5	80,1	80,9	0,0	0,0	0,0	0,0	0,0	50,1	75,5
	DF2	0,0	79,5	80,1	80,9	0,0	0,0	0,0	0,0	0,0	0,0	0,0
	B1	89,5	81,0	81,3	87,9	0,0	0,0	0,0	0,0	61,1	0,0	82,4
	B2	89,5	0,0	81,3	87,9	0,0	0,0	0,0	0,0	0,0	0,0	0,0
	B3	89,5	0,0	0,0	87,9	0,0	0,0	0,0	0,0	0,0	0,0	0,0
LM2500+	C	0,0	0,0	0,0	0,0	0,0	53,7	64,4	74,0	83,3	95,2	97,0
	DF1	0,0	80,8	90,0	90,0	80,0	0,0	0,0	0,0	0,0	0,0	0,0
	DF2	83,3	0,0	85,2	90,0	83,0	0,0	0,0	0,0	0,0	0,0	0,0
	B1	89,5	88,7	0,0	89,9	90,0	0,0	0,0	0,0	0,0	0,0	74,8
	B2	89,5	88,7	0,0	0,0	90,0	0,0	0,0	0,0	0,0	0,0	74,8
	B3	89,5	88,7	0,0	0,0	90,0	0,0	0,0	0,0	0,0	0,0	0,0
LM2500+G4	C	0,0	0,0	0,0	0,0	0,0	0,0	50,4	55,2	61,9	72,1	82,9
	DF1	81,7	80,8	76,9	88,1	89,9	83,4	0,0	0,0	0,0	0,0	0,0
	DF2	0,0	0,0	76,9	88,1	89,9	83,4	0,0	0,0	0,0	0,0	0,0
	B1	87,9	88,7	0,0	0,0	89,6	86,3	0,0	0,0	0,0	0,0	0,0
	B2	87,9	88,7	0,0	0,0	0,0	86,3	0,0	0,0	0,0	0,0	0,0
	B3	0,0	88,7	0,0	0,0	0,0	86,3	0,0	0,0	0,0	0,0	0,0
RB211	C	0,0	0,0	0,0	0,0	53,6	63,3	76,9	88,6	94,2	97,0	97,0
	DF1	83,3	79,5	80,1	80,9	0,0	0,0	0,0	0,0	0,0	0,0	77,1
	DF2	0,0	79,5	80,1	80,9	0,0	0,0	0,0	0,0	0,0	0,0	0,0
	B1	89,5	81,0	81,3	87,9	0,0	0,0	0,0	0,0	50,4	60,5	79,9
	B2	89,5	0,0	81,3	87,9	0,0	0,0	0,0	0,0	0,0	60,5	0,0
	B3	89,5	0,0	0,0	87,9	0,0	0,0	0,0	0,0	0,0	60,5	0,0
SGT600	C	0,0	0,0	0,0	0,0	50,3	59,3	72,4	83,9	93,9	97,0	97,0
	DF1	83,3	79,5	80,1	80,9	0,0	0,0	0,0	0,0	0,0	0,0	84,0
	DF2	0,0	79,5	80,1	80,9	0,0	0,0	0,0	0,0	0,0	0,0	0,0
	B1	89,5	81,0	81,3	87,9	0,0	0,0	0,0	0,0	0,0	63,0	0,0
	B2	89,5	0,0	81,3	87,9	0,0	0,0	0,0	0,0	0,0	63,0	0,0
	B3	89,5	0,0	0,0	87,9	0,0	0,0	0,0	0,0	0,0	0,0	0,0
TITAN 250	C	0,0	0,0	51,7	61,4	73,2	84,7	94,2	97,0	97,0	97,0	97,0
	DF1	83,3	79,5	0,0	0,0	0,0	0,0	0,0	0,0	75,2	77,7	85,5
	DF2	0,0	79,5	0,0	0,0	0,0	0,0	0,0	0,0	0,0	0,0	85,5
	B1	89,5	81,0	0,0	0,0	0,0	0,0	53,7	75,2	0,0	79,7	0,0
	B2	89,5	0,0	0,0	0,0	0,0	0,0	0,0	75,2	0,0	79,7	0,0
	B3	89,5	0,0	0,0	0,0	0,0	0,0	0,0	0,0	0,0	0,0	0,0

Fig. 9.16 On the top of the figure, cogeneration efficiency considering TITc control strategy: winter (left) and summer (right) seasons. On the bottom: engine loads in terms of percentage of maximum continuous rating.

1%) arise on η_g between TITc and TOTc control strategies in figures 9.15 and 9.16 due to the HRSG optimization performed by the Fortran code in both cases. Overall, power plant configuration based on LM2500 gas turbine appears the optimal one for a repowering purpose of La Suprema, since it provides high cogeneration efficiency under flexible sailing conditions. In order to better visualize cogeneration efficiency provided by LM2500-based COGES plant for the current sailing conditions of La Suprema, Table 5 reports corresponding time-mean performances achieved at 22 knots.

9.2.4 Dynamical simulations

In this section, the dynamic simulation of the best power plant previously identified is assessed focusing on the current navigation condition La Suprema is operated on, for both winter and summer seasons. As mentioned above, the profiles for time-dependent electrical demand were obtained from previous works available in the literature and concerning cruise-ferries dealing with comparable size [31]. On the other hand, thermal power demand is assumed constant in time. From the previous section, cogeneration efficiency at 22 knots was found to be maximized by turning on only COGES plant, hence no dynamic simulation is required for reciprocating engines. Furthermore, comparison between TITc and TOTc governing strategies showed that the turbine outlet temperature control provides the highest energy saving benefits. Therefore, TOTc regulation is considered in this section. Results

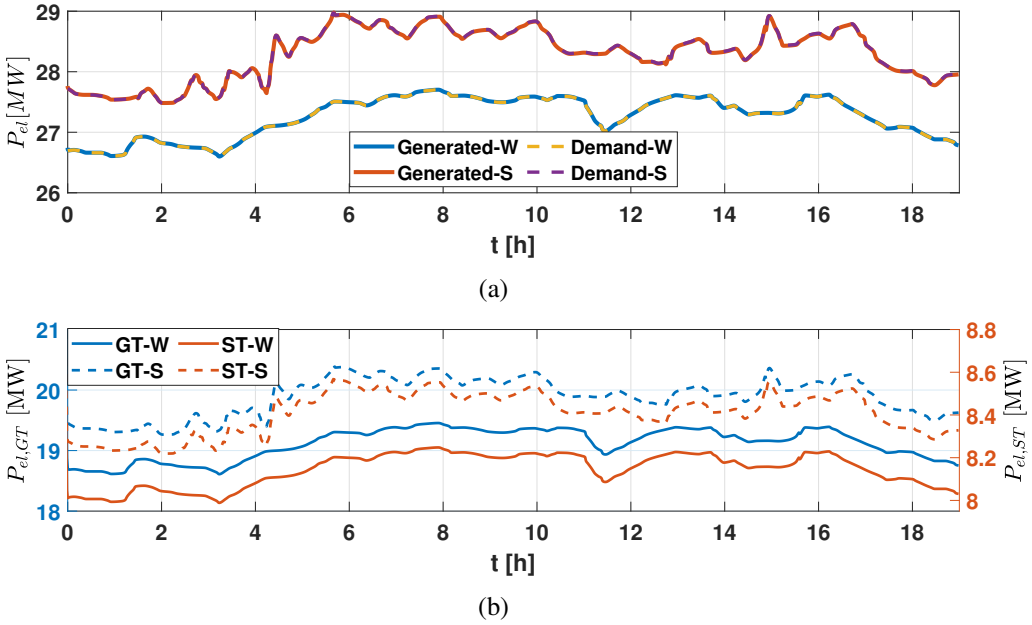

Fig. 9.17 Time-dependent performances of repowering plant under current operating conditions for the cruise-ferry La Suprema, during winter and summer seasons.

obtained by dynamical simulation of LM2500-based COGES plant regulated by means of TOTc strategy are shown in figure 9.17. Specifically, net power output from engine room and the corresponding electrical demand are reported in continuous and dashed lines, respectively. Winter and summer curves are shown in yellow and purple for the power request, whereas blue and red colors for generated power, respectively. Since time domain covers the overall duration of 19 hours for the current navigation condition between Genoa and Palermo, a real-time simulation is performed. Figure 9.17 clearly shows how electrical demand is

closely followed by power delivered by COGES plant over the entire navigation phase. This well agrees with the load following ability traditionally recognized to gas turbines and combined cycles within the power generation sector, where I, II and III frequency reservoir are performed by these configurations. Details concerning the contribution of both gas turbine and steam turbine to the net power output are outlined in figure 9.17b. Specifically, red and blue curves are related to GT and ST power and refer to the right-side and left-side ordinate axis, respectively. Furthermore, continuous and dashed lines indicate winter and summer seasons, respectively. Interestingly, similar transient behaviour is surveyed for power delivered by both gas turbine and steam turbine, despite GT covers 2/3 of the electrical demand. Indeed, due to the small size of marine gas turbines, lower thermal power is available for the bottoming steam power plant in comparison to what occur in power generation sector [321–323, 267]. Nevertheless, electrical power delivered by bottoming steam power plant fairly agrees with data concerning ST currently installed onboard ships [324–326]. Detailed view of time-dependent analysis concerning the main thermodynamic parameters is reported in figure 9.18, where winter and summer seasons are related to blue and red colors, respectively. Focusing on figure 9.18a, the exhaust gas temperature of the LM2500 gas turbine is shown. As can be seen, T_{ex} is approximately constant according to the TOTc regulation, despite the PID controller time response generates weak, local fluctuations. Instead, the exhaust mass flow rate shown in figure 9.18b appears directly proportional to power request. Thus, an increase in exhaust mass flow rate occurs in case power demand rises. Therefore, combining the effect of the exhaust gas temperature and mass flow rate, thermal power available for recovery within the bottoming steam power plant grows,with consequent increase in electrical output from steam turbine. Focusing on the rotational speed of gas generator shaft (see figure 9.18c), closing angles imposed to IGV to maintain T_{ex} constant trigger an increase in N_{GG} up to 104% with respect to the nominal value, independently from season. Indeed, as visible from the tabular legends reported above, COGES plant based on LM2500 under TOTc control does not work at 100% load during navigation at 22 knots, hence closing angle for IGV is needed to keep T_{ex} constant at part-loads. Interestingly, rotational speed of GG shaft strictly follows the transient power demand during winter (i.e. N_{GG} increases in case power request grows and vice versa), whereas opposite trend occurs for summer in correspondence of power demand around 19-20 MW. This change in dependency mainly derives from the relation $N_{GG} = f(load)$, previously shown in figure 9.13. Indeed, where the TOTc governing strategy is concerned, N_{GG} locally increases, without exceeding the over-speed limit, and then decreases during a decelerating load ramp. Specifically, the maximum of the rotational speed for GG is achieved when the power demand is around 19-20 MW (see the red curve in figure 9.13). Thus, the change in proportionality observed in

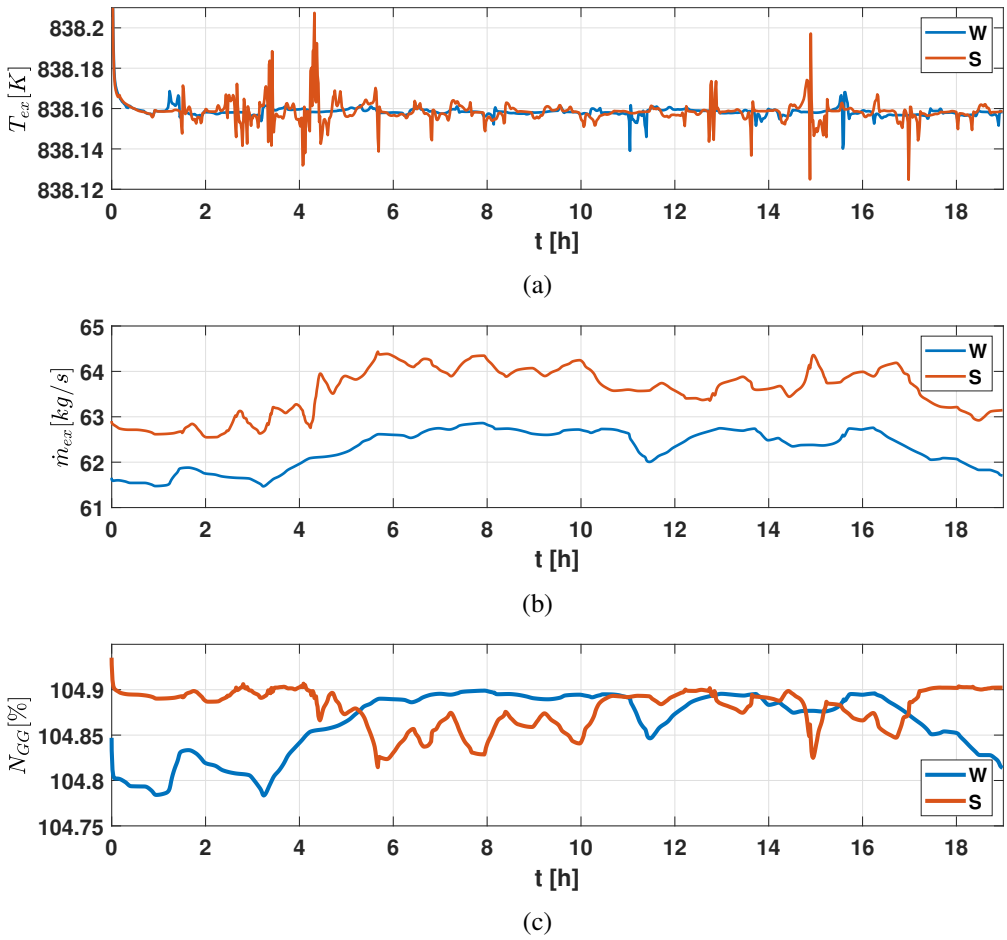

Fig. 9.18 T_{ex} (a), $\dot{m}_{ex}$ (b) and N_{GG} (c) time-dependent results for the cruise operating condition of the ship GNV La Suprema, for winter (W) and summer (S) seasons.

figure 9.18c for comparable power demands appears definitely due to the maximum trend experienced by N_{GG} for decreasing loads.

9.2.5 Main findings

In the previous sections, dynamic simulation of COmbined Gas Electric and Steam (COGES) power plants for LNG powered cruise-ferries was assessed. Specifically, a flexible and modular code was used to simulate thermodynamic performances of 6 different gas turbine, whose nominal operating conditions were reconstructed completely by a mixed MOGA-gradient descent algorithm within 1% relative error for global parameters (i.e. P_{net}, η_{el}, T_{ex} and η_{mecc}). In order to assess the sensitivity of gas turbine performances to the governing strategy, both turbine inlet temperature (TITc) and turbine outlet temperature (TOTc) controls

were investigated.

Overall, the transient response surveyed for the main thermodynamic parameters appeared physical-based and in fairly agreement with previous literature works. Specifically, keeping TIT or TOT constant during a decelerating ramp ranging from 100% to 20% load was shown to require closing angles for IGV, which in turns provoked transient acceleration for the GG rotational speed. Since TITc strategy relates to higher closing rates for IGV, stronger acceleration occurs and over-speed control is temporarily enabled around 65% gas turbine load. For further reduced power demand, decrease in the fuel mass flow rate imposes GG shaft to decelerate. Overall, TITc and TOTc control strategies manage to keep constant their corresponding temperatures up to 70% and 30% loads, respectively. Then, equilibrium points obtained from dynamic simulation of all the six gas turbines, were used to optimally assembly various COGES plants within a repowering study for the cruise-ferry GNV La Suprema. Specifically, 6 integrated COGES-reciprocating engines power plants were investigated as candidate configurations in a cogeneration efficiency optimization study performed over wide ship speed range (16-26 knots), for both winter and summer seasons. Overall, the potential of combining COGES plants with small-size reciprocating engines was proved by an energetic point of view. For sailing conditions where low ship speeds are required, η_g is maximized by reciprocating engines due to their weak affection to part-loads. On the other hand, COGES plants provide energy savings benefits in the middle-high ship speed range (19-26 knots), where the entire power demand is covered by them and only few navigation conditions require extra power from reciprocating engines. Specifically, 1-5% higher η_g in comparison to reciprocating engines is provided by COGES, depending on the GT installed onboard. COGES plants grounding on large-size gas turbines (i.e. LM2500+ and LM2500+G4) showed maximum cogeneration efficiencies shifted towards ship speeds $\geq$25-26 knots, hence their potential remains unexploited for application on the La Suprema. On the other hand, SGT-600 and RB211 are characterized by lower electrical efficiencies and comparable size with respect to LM2500 and TITAN250, as well as lower thermal power is available for recovery within their exhaust gas (i.e. reduced $\dot{m}_{ex}$ and T_{ex}). Therefore, they cover electrical demand onboard with the worst performances in terms of cogeneration efficiency. Overall, the highest η_g within the middle-high ship speed range were achieved by COGES plants including LM2500 and TITAN250 gas turbines. Specifically, installing LM2500 ensured high cogeneration efficiency in a broad operating range, whereas TITAN250-based COGES plant guaranteed energy savings within a short ship speed range, especially under TITc governing strategy. Since shipowners aim at repowering La Suprema with power plant able to provide high efficiency over extremely flexible operating conditions, COGES based on LM2500 resulted the best combined gas-steam plant to be installed onboard cruise-ferries. Where

control strategies are concerned, TOTc guaranteed energy savings over most of the middle-high ship speed range, due to the reduced off-design conditions the bottoming steam power plant works at. Finally, the transient performances of the best power plant configuration identified by the previous study were assessed considering the time-dependent electrical and thermal demands occurring onboard the current navigation conditions for La Suprema. Furthermore, the turbine outlet temperature control was adopted due to its major energy savings. Overall, results obtained from dynamic simulation confirmed high performances available from COGES plant in terms of efficiency and load following ability and proved the reliability of the model in reproducing physical-based dynamics.

9.3 Alternative fuels applied onboard large-size cruise ships

To stop climate change, caused by the continuous growth of GHG emissions, energy transition is gaining much attention from governments and international associations to reach more sustainable pathways. Since the 90% of the world trade is performed by ships, the maritime sector consists in an important field where energy transition is mandatory. With even more stringent regulations on pollutant and GHG emissions, two main different strategies appear the most promising [327]: installing highly-efficient power plants to improve energy savings [328] and employing more sustainable alternative fuels [329]. Recently, hydrogen (H_2), ammonia (NH_3) and methanol (CH_3OH) are currently receiving most of the attention fro ship propulsion, since they can effectively reduce GHG emissions in a short- or long-term perspective. In the following sections, the feasibility of these alternative fuels applied to large cruise ships is assessed by energetic, environmental and economic point of views. Firstly, electrical and thermal power profiles required onboard a modern 114000 Gross Tonnage cruise ship have been constructed. Specifically, 5 different routes, three different operating conditions (maneuvering, port and navigation) and summer-winter seasons have been accounted for. Fuel flexibility for gas turbines is well established, since commercially available gas turbines (GT) are currently able to operate on NH_3, $CH_3OH$and CH_4- H_2 blends containing up to 85% of H_2 in volume. Therefore, GTs appear to significantly contribute to the energy transition scenario. On the other hand, fuel flexibility for reciprocating engines appears less advanced, since research from the major companies is still to be developed for NH_3 and CH_4-H_2 blends dealing with high hydrogen contents. Therefore, integrating COmbined Gas Electric and Steam (COGES) plants with reciprocating engines appears a possible choice in a energy transition scenario. Specifically, three candidate power plants based on large, middle and low COGES sizes have been applied to cruise ships. First, the numerical procedure previously introduced in section 6.1.2 was used to solve for static and dynamic performance of COGES plants fed by alternative fuels. Secondly, in section 9.3.2, power plant performances in terms of cogeneration efficiency are assessed when working on CH_3OH, NH_3 and CH_4-H_2 blends, for all the 5 cruise routes, operating conditions and seasons. Then, in order to compare power plant and fuel solutions under an environmental point of view, CO_2 emissions over different routes together with both the Energy Efficiency Design Index (EEDI) and Carbon Intensity Indicator (CII) are computed in section 9.3.3. Since the CII index directly relates to the current operating condition of ship while EEDI takes into account only design procedure for new power plants, ability of each fuel and power configuration in providing short- or long-term compliance with regulations is investigated. Finally, in section 9.3.4, the economic feasibility underlined possible issues which eventually

may arise for certain fuel feeding systems as well as where major benefits can be obtained. Furthermore, attention has been paid to the influence of the fuel production chain currently have on cost and environmental issues.

9.3.1 Case study

In this section, electrical and thermal power profiles for a large cruise ship characterized by 114000 Gross Tonnage (GT) and transporting about 3700 passengers are defined. The

Table 9.9 Main characteristics for the large-size cruise ship considered.

Dimension	Value
Gross tonnage	114000 t
Displacement	57000 t
Length	290 m
Draft	8.3 m
Passengers	3700

main features of the vessel are reported in table 9.9 and refer to a typical MSC, Carnival or Costa cruise ship built in recent years. The ship under study deals with 62-76 MW installed powers and is currently equipped by a Diesel-electric propulsion plant, where both main and auxiliary engines may indiscriminately cover hotel and propulsion loads. On the other hand, the integrated electric propulsion plant reported in figure 9.19 is proposed here. As can be seen, power plant configuration in figure 9.19 resembles a Diesel electric engine room, despite a COmbined Gas Electric and Steam (COGES) plant is additionally installed onboard. Specifically, in order to minimize space occupied onboard, a back-pressure steam turbine is inserted within the bottoming steam power plant. Since waste heat available from reciprocating engines is significantly low, WHR systems are installed only downstream large-size engines. Overall, as underlined in previous section, this propulsion plant configuration can provide high efficiency over wide operating range. Focusing on the construction of operating profiles under navigation, port and maneuvering conditions, experimental data from cruise ships characterized by comparable Gross Tonnage and passenger number have been derived from the literature. Specifically, where the propulsion demand is concerned, the cubic curve (V_{ship}, P_o) reported by [32] for the Costa Serena cruise ship and obtained by actual operating data from shipboard measurements is used. Figure 9.20 shows the corresponding polynomial curve $P = AS^3 + BS^2 + CS + D$. It well established within the maritime field that negligible influence on the propulsion power is played by season, since

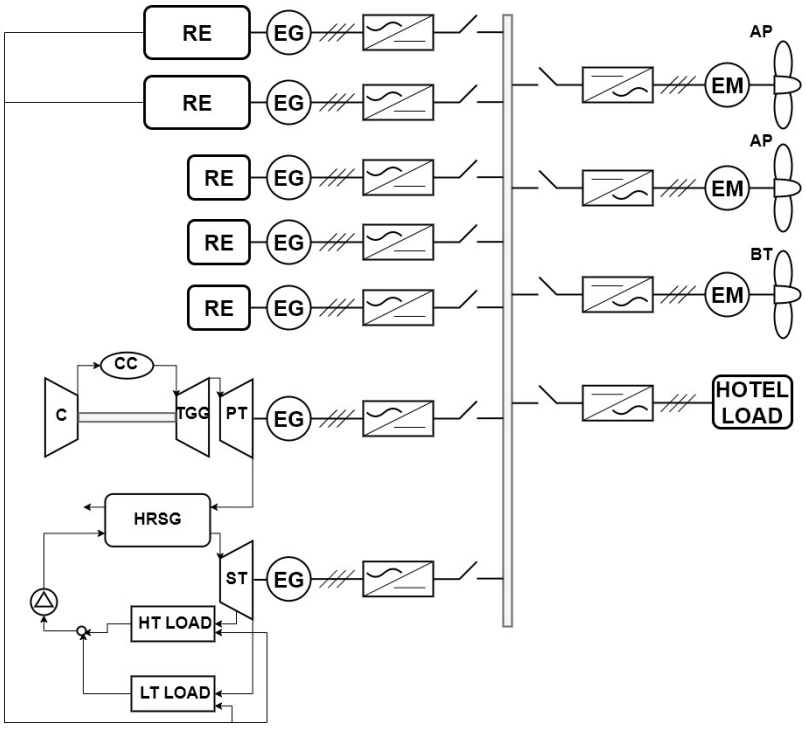

Fig. 9.19 Schematic view of the power plant under study (RE=reciprocating engine, C=compressor, CC=combustion chamber, TGG=gas generator turbine, PT=power turbine, ST=steam turbine, HRSG=heat recovery steam generator, EG=electrical generator, EM=electrical motor, AP=azipod, BT=bow thruster).

cubic curve in figure 9.20 mainly depends on ship speed and weather condition. Entering with ship speed required by navigation into the cubic curve, the corresponding propulsion power can be found out. It must be remarked that a 15% sea margin is considered, to account for increase in ship resistance due to hull fouling, wind and wave drag. This facilitates to strictly respect arrival/departure timetables, which is a particularly relevant target for cruise ships. Furthermore, power demand for propulsion usually accounts for thrust delivered by azipods in sailing conditions, while power required by both azipods and bow thrusters during maneuvering is differently evaluated. Thus, the cubic curve reported in figure 9.20 can not be applied during port activities during departure/arrival conditions. Furthermore, it must be underlined that accurately estimating power demand during maneuvering currently typically deals with unavoidable uncertainties, due to its dependency from local climatic conditions, port layouts and master's expertise. Nevertheless, where maneuvering conditions are concerned, power request from bow thrusters and azipods is traditionally considered coupled with that from hotel services in a simplified approach [330–332]. Here, the method proposed by Meyer et al. [330] and Tzannatos [331], which derives from experimental data of cruise ships operating in the Piraeus port, is adopted. In details, a 20% and 75% load

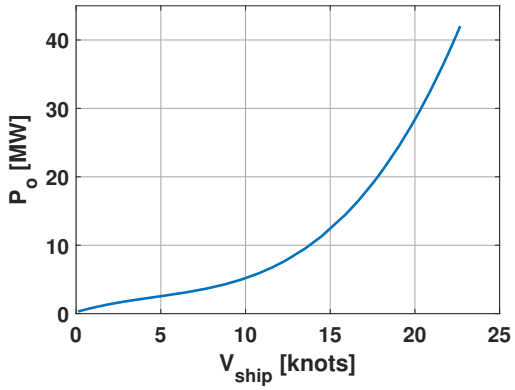

Fig. 9.20 Propulsion power request for the large-size cruise ship considered [32].

operating conditions is considered for main (ME) and auxiliary (AE) engines, respectively. However, as visible from schematic view reported in figure 9.19, no clear distinction is made between ME and AE in integrated electric propulsion. Therefore, manufacturers' information concerning the overall installed power and the power demand for propulsion referring to modern Costa and MSC cruise ships has been used [333]. Furthermore, it must be remarked that one or two extra diesel generators are cautiously turned on during maneuvering for Diesel-electric propulsion architecture, in order to comply with safety regulations. On the contrary, this measure is not necessary when COGES plant are installed within the engine room, due to the high reliability and fast load cycling provided by gas turbines. Focusing on the electrical and thermal power demands from hotel services during port and navigation conditions, data concerning large cruise ships from the Costa company are reported in table 9.10, distinguishing summer and winter season [299]. As can be seen

Table 9.10 Electrical (P_{el}=electrical power for hotel services) and thermal (LT=low temperature thermal power, and HT=high temperature thermal power) power demands onboard large-size cruise ship.

Power demands	Phase	Summer	Winter
LT	**Navigation**	21.262	24.822
	Port	10.937	14.327
HT	**Navigation**	1.784	1.784
	Port	1.784	1.784
P_{el}	**Navigation**	9.962	9.090
	Port	8.704	7.504

from table 9.10, power demand required by hotel services is negligibly affected by ship operating condition, while higher variations are surveyed changing season. This mainly derives from the power requested by air conditioning in cabins, which significantly increases during summer. Furthermore, it must be observed that hotel power during port is slightly lower than in navigation, independently from season. Indeed, since the propulsion chain

is enabled, the power demand from auxiliary systems installed onboard gets higher during sailing conditions [32]. Finally, the chain rule has been applied on each single component of the electrical power demand reported above. Specifically, the following values have been assumed: alternator efficiency $\eta_{alt} = 0.97$, DC-AC converter efficiency $\eta_{AC-DC} = 0.99$, propeller rotative efficiency $\eta_r = 0.99$. Where thermal power demand is concerned, requests from two main users are traditionally distinguished for cruise ships. Specifically, the Low Temperature (LT) demand is typically supplied through steam or hot water at 3 bar and represents requirements from both accomodation and fresh water (FW) production by multi-stage evaporators. On the contrary, the High Temperature (HT) demand aims to cover 9 bar steam requests from accomodation (sanitary water, swimming pool water, galley and laundry services), engine room service and tank heating. Table 9.10 summarises the values for LT and HT thermal power demands considered for the analysis. In details, according to Amaya-Vias et al. [334], a 1000 m^3/day fresh water need has been assumed for large cruise ships. Then, from the literature concerning multi-stage flash evaporators, a fresh water capacity of 130 kWh_{th}/h has been derived [335]. Furthermore, it is well established that generation of fresh water can not occur during maneuvering or at berth for hygienic and biological reasons. Thus, the daily request of fresh water onboard has been spread over only the navigation conditions. In this way, multi-stage evaporators are correctly sized. Looking at the schematic view of propulsion plant reported in figure 9.19, both steam exiting back-pressure ST and 3 bar hot water production in specific heat exchangers within HRSG can be effectively used to supply LT demand. Where the HT thermal power demand is concerned, a 1.784 MW constant level including requirements from accomodation has been estimated, independently from season [336, 31]. Within the integrated electric propulsion plant shown in figure 9.19, both steam extracted from ST or steam produced by WHR system downstream reciprocating engines can be used to cover the HT demand. Specifically, the WHR systems downstream reciprocating engines is able to generate steam at 9 bar, which can be laminated up to reach 3 bar in case excess power is recovered. However, due to the reduced thermal power available from the exhaust gas of small-size reciprocating engines, WHR system is considered only for engines delivering ≥ 8 MW power at nominal condition. As mentioned above, power plant performances are investigated under flexible ship operating conditions, which include 5 different operating profiles. Specifically, Mediterranean (C1, C2), North Sea (C3), Caribbean Sea (C4) and Red Sea (C5) routes from the MSC and Costa companies have been considered. For illustrative purposes, table 9.11 summarises main information regarding the C2 cruise route operating profile. Analogous tables for all the other routes are reported in the appendix A, for sake of conciseness. Phase duration and nautical miles between two distinct locations have been used to obtain navigation ship speeds reported in table 9.11 [32].

Table 9.11 C1 cruise route in the Mediterranean sea.

LOCATION	PHASE	t [h]	V_{ship} [knots]
Genoa	M	0.5	0
Genoa-Civitavecchia	N1	13	15
Civitavecchia	M	0.5	0
Civitavecchia	P	10	0
Civitavecchia	M	0.5	0
Civitavecchia-Palermo	N2	15	17
Palermo	M	0.5	0
Palermo	P	7	0
Palermo	M	0.5	0
Palermo-Malta	N3	16	18
Malta	M	0.5	0
Malta	P	8	0
Malta	M	0.5	0
Malta-Barcelona	N4	38	18
Barcelona	M	0.5	0
Barcelona	P	10	0
Barcelona	M	0.5	0
Barcelona-Marseille	N5	13	15
Marseille	M	0.5	0
Marseille	P	8	0
Marseille	M	0.5	0
Marseille-Genoa	N6	14	16
Genoa	M	0.5	0

In order to perform power plant design, the distribution of cumulative energy in function of electrical power demand occurring over all the five operating profiles is shown in figure 9.21, together with the best Gaussian fitting pattern (see the red curve). Power demands during both summer and winter seasons are accounted for. As visible from figure 9.21, the red pattern is well centered around 25-30MW, despite some energy peaks out of statistics occur at low (6-10 MW) and high (40 MW and 50 MW) power demands. Since propulsion power represents the highest contribute to power demand, the meaning of these energy peaks can be found looking at ship speeds reported in table 9.11 and appendix A. In particular, the lowest ship speeds arise from Norwegian fjords sailing conditions in profile C3, precisely during the Bergen-Olden and Olden-Alesund navigation. Slightly higher ship speeds are surveyed in Profile 4 and 5 during Dubai-Abu Dabi and Ocean Cay MSC-Miami navigation, respectively. Furthermore, table 9.10 shows how the power request from hotel services is around 8-10 MW, for both summer and winter. Thus, other than low ship speed conditions,

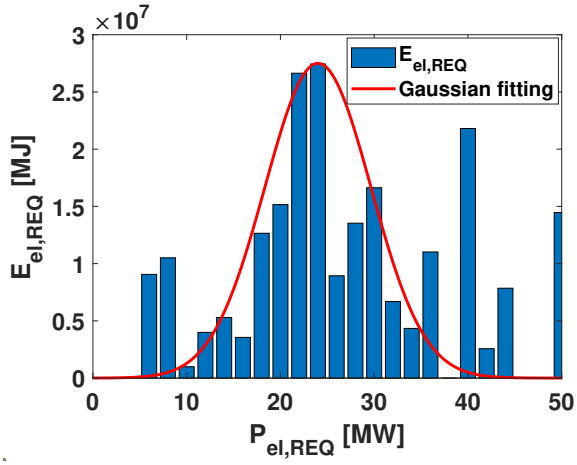

Fig. 9.21 Cumulative energy distribution for large-size cruise ships.

also port operating phase contribute to the high energy peak at 9 MW reported in figure 9.21. Similarly, high speeds required in C4 and C5 for navigation during Charlotte-Nassau and Eraklion-Civitavecchia, respectively, mainly correspond to high energy peaks positioned around 40 MW and 50 MW. Finally, the high energy peak occurring around 30 MW appears to derive from both maneuvering and some navigation conditions. Indeed, electrical power request during in port activities coincides with 31-33 MW in all the five profiles analysed, but short time is traditionally spent in maneuvering, hence low energy is exchanged.

Table 9.12 Main characteristics of prime movers to be installed onboard large-size cruise ship, under nominal fuel feeding conditions.

GT	P_{net} **[MW]**	η_{el} **[%]**	T_{ex} **[°C]**
LM2500	24.31	36	566
LM2500+	29.26	38	518
TITAN250	21.75	39	465
12V MAN 51/60	11.23	45.5	309
R-R Bergen C26 L9	2.33	45	-

Table 9.13 Selected power plant configurations to be installed onboard large-size cruise ship.

Configuration	**GT**	**12VMAN51/60**	**Bergen**
S1	LM2500	XX	XXX
S2	LM2500+	XX	XXX
S3	Titan 250	XXX	XX

Overall, since the main pattern, statistically referring to the most frequent operating condition, is well centered around 25-30 MW, this size is adopted as reference for gas turbine selection. The main characteristics of both gas turbines and reciprocating engines considered in this study are reported in table 9.12. As can be seen, three different GTs, all dealing with size around 25-30 MW, have been considered to be coupled with bottoming steam power plant forming COGES configuration. However, TITAN250 provides the lowest nominal power, whereas LM2500+ delivers the highest one. Since all the power plants tested need to deal with comparable installed power such to comply with safety regulations and ensure comparability, a distinct power plant configuration is designed for each GT, as shown in table 9.13. Specifically, large-size reciprocating engines are coupled with small-size COGES plants and vice versa. Thus, installed power characterizing each power plant reported in table 9.13 guarantees safety return to port ability in case of failure experienced by one prime mover [337]. In the following, the effect of fuel flexible operating conditions on thermodynamics performances of all the prime movers reported in table 9.12 has been accounted for as described in section 6.1.2. Where CH_4-H_2 blends are concerned, 85% volumic concentration of hydrogen has been considered for the LM2500 and LM2500+ GTs, whereas 50% has been accounted for the TITAN250 gas turbine, according to the fuel flexibility level claimed by manufacturers. Analogously, reciprocating engines are considered fed by CH_4-H_2 blends based on 30% volumic concentration of hydrogen. According to standard propulsion plant design procedures, a 90% engine margin (EM) is considered for reciprocating engines, aimed at minimizing maintenance costs and avoiding failures [338]. On the other hand, EM is traditionally neglected for COGES plants, due to their higher reliability and lower maintenance costs in comparison to reciprocating engines. However, a 97% engine margine is cautiously accounted for COGES in this study.

Since the EEDI and CII indexes will be used in the following to assess environmental impact of various power plants and fuels, these parameters are defined in the following for a cruise ship with non-conventional power plant installed onboard. Focusing on EEDI, it limits GHG impact of newly designed power plant. Indeed, EEDI $[gCO_2/t/nm]$ compares the CO_2 emissions from engine rooms considering all the prime movers operating at 75% load with

the useful work provided by the ship transport, as shown in eq. (9.8):

$$EEDI = \frac{\prod_{j=1}^{n} f_j \sum_{i=1}^{n_{ME}} P_{ME_i} CF_{ME_i} SFC_{ME_i}}{f_i f_c Capacity f_w V_R} + \\ + \frac{\prod_{j=1}^{n} f_j \sum_{i=1}^{n_{AE}} P_{AE_i} CF_{AE_i} SFC_{AE_i}}{f_i f_c Capacity f_w V_R} + \\ - \frac{\sum_{i=1}^{n_{eff}} f_{eff_i} P_{eff_i} CF_{ME} SFC_{ME}}{f_i f_c Capacity f_w V_R} \tag{9.8}$$

where SFC indicates specific fuel consumption, P is the delivered power, CF consists in the CO_2 emission factor depending on fuel molecules and n is number of engines installed onboard. The subscripts ME, AE and eff refer to main engines, auxiliary engines and innovative energy technologies (i.e. bottoming steam power cycle), respectively. As underlined above, main and auxiliary engines are not distinctly identified, thus only terms concerning ME are traditionally considered. Finally, the factors f_{eff}, f_i, f_j, f_c, and f_w can be assessed by consulting IMO regulations [339]. Where the CII index is concerned, it measures CO_2 emissions during annual, effective operation. Thus, it is mainly affected by power plant working condition, i.e. how the ship operates. Definition for the attained CII index is reported in eq. (9.9):

$$CII = \frac{\sum_{j=1}^{n_{pm}} m_j CF_j}{Capacity L_s} \tag{9.9}$$

where CF represents the CO_2 emission factor depending on fuels, n_{pm} the number of turned-on prime movers, m consists in the burned fuel mass, $Capacity$ indicates the Gross Tonnage and L_s are the nautical miles annually covered. In order to verify regulation compliance, the attained CII must be compared each year with the requested CII, defined as:

$$CII_{REQ} = (1 - Z/100)\, CII_R \tag{9.10}$$

where Z is a reduction emission factor related to 2019 reference data, whereas CII_R represents a reference value depending on ship size and computed as: $CII_R = aCapacity^{-c}$, where $Capacity$ indicates the Gross Tonnage, $a = 930$, $c = 0.383$ for a cruise ship. IMO provides reference values fro the Z factor up to 2026 [81], in order to correct regulation in case issues arise: the z factor starts from 5% in 2023 (with respect to 2019) and 2% additional reduction is yearly summed up to reach 2026. Since measurements of NO_x production from

prime movers is particularly difficult, both EEDI and CII do not account for equivalent carbon dioxide emissions. Nevertheless, in this study, NO_x emissions from each prime mover fed by alternative fuels are estimated from previous works available in the literature [187, 340, 341, 174] as well as manufacturers' indication [28, 125, 131]. Furthermore, Selective Catalytic Reduction (SCR) dealing with a 85% abatement capacity [342, 343] has been obligatorily included in power plants when NH_3 and CH_4-H_2 blends feeding conditions are considered. Indeed, SCR can abate NO_x emissions of both GTs and reciprocating engines up to comply with the IMO Tier III limits. SCR needs to be included for analogous reasons downstream reciprocating engines in case methanol is used as fuel [125]. Finally, CAPital EXpenditure (CAPEX) and OPerational EXpenditure (OPEX) are taken into account in order to investigate the economic viability of power plants fed by alternative fuels. Specifically, power specific price for components installed onboard (prime movers, propellers, storage tanks,...) are used to quantify CAPEX costs. The values adopted in this work, deriving from previous works as well as from manufacturers' indications, are summarised in table 9.14. On the other hand, fuel consumption cost (AFC), maintenance cost (AMC) and costs due

Table 9.14 Power specific CAPEX costs.

COMPONENT	**[€/kW]**	**Ref.**
RE CH_4-H_2 [€/kW]	470 [344, 308]	
RE CH_3OH [€/kW]	265	[344, 308]
RE NH_3 [€/kW]	370	[344, 308]
Gas Turbines [€/kW]	368	[300, 301]
HRSG + ST [€/kW]	150	[300, 301]
SCR [€/kW]	126	[345]
Reformer-Evaporator [€/kW]	360	[345]
H_2 tanks [€/kWh]	1.71	[344, 308]
CH_3OH tanks [€/kWh]	0.14	[344, 308]
NH_3 tanks [€/kWh]	0.29	[344, 308]
Electrical Generators [€/kW]	90	[301]
Electrical Motors [€/kW]	80	[301]
AC/DC-DC/AC converters [€/kW]	100	[301]
Propellers [€/kW]	30	[301]

to carbon pricing CEM have been all considered to quantify OPEX costs, as shown in eq. (9.11):

$$OPEX = AFC + AMC + CEM \tag{9.11}$$

where fuel prices in €/kg have been considered to obtain AFC. On the other hand, AMC and CEM have been evaluated by means of component maintenance costs in €/kWh and carbon

pricing in €/kg, respectively. Corresponding values assumed from the literature are reported in table 9.15. It must be remarked that carbon pricing is not existing yet in the maritime

Table 9.15 OPEX costs.

COMPONENT	**[€/kW]**	**Ref.**
LNG fuel [€/kg]	0.398	[308]
H_2 fuel [€/kg]	5.35	[308, 346]
CH_3OH fuel [€/kg]	0.4	[347]
NH_3 fuel [€/kg]	0.7	[308]
ICE OM [€/kWh]	0.014	[308]
COGES OM [€/kWh]	0.002	[310, 300]
SCR OM [€/kWh]	0.006	[83]
CO_2 price [€/kg]	0.115	[302]

sector, despite regulations introducing it will be available in the early future [57, 56, 55]. Furthermore, the price of green H_2 generated from renewables in EU has been considered. This explains its far higher value in comparison to methanol or ammonia. Finally, a 398 €/kg is assumed as relevant LNG price in time of no economic crisis [316].

9.3.2 Results

In this section, comparison between power plant configurations reported in table 9.13 is assessed in terms of cogeneration efficiency. Phase-mean electrical and thermal power demands over 5 different sailing routes, for both winter and summer season, and for variable fuel have been accounted for. The electrical power distribution over prime movers obtained maximizing η_g during the C2 profile is reported in figure 9.22 in function of ship operating conditions (port P, navigation N and no symbol for maneuvering). In the legend, E and e subscripts followed by numbering refer to the large and small size reciprocating engines, i.e. 12V MAN 51/60 and R-R Bergen C26 L9, respectively. Results concerning winter and summer seasons are depicted on the left and right column, respectively, whereas S1, S2 and S3 configurations refer to the top, mid and bottom row, respectively. In the legend, E and e subscripts followed by numbering refer to the large and small size reciprocating engines, i.e. 12V MAN 51/60 and R-R Bergen C26 L9, respectively. Where fuel is concerned, only results for power plants fed by CH_4-H_2 blends are are shown for the sake of conciseness. Focusing on results on the first row (i.e. S1 power plant), higher power is requested during summer season since demand for air conditioning significantly increases. Where port conditions are concerned, the energy management strategy only turns on a 12V MAN 51/60 engine,

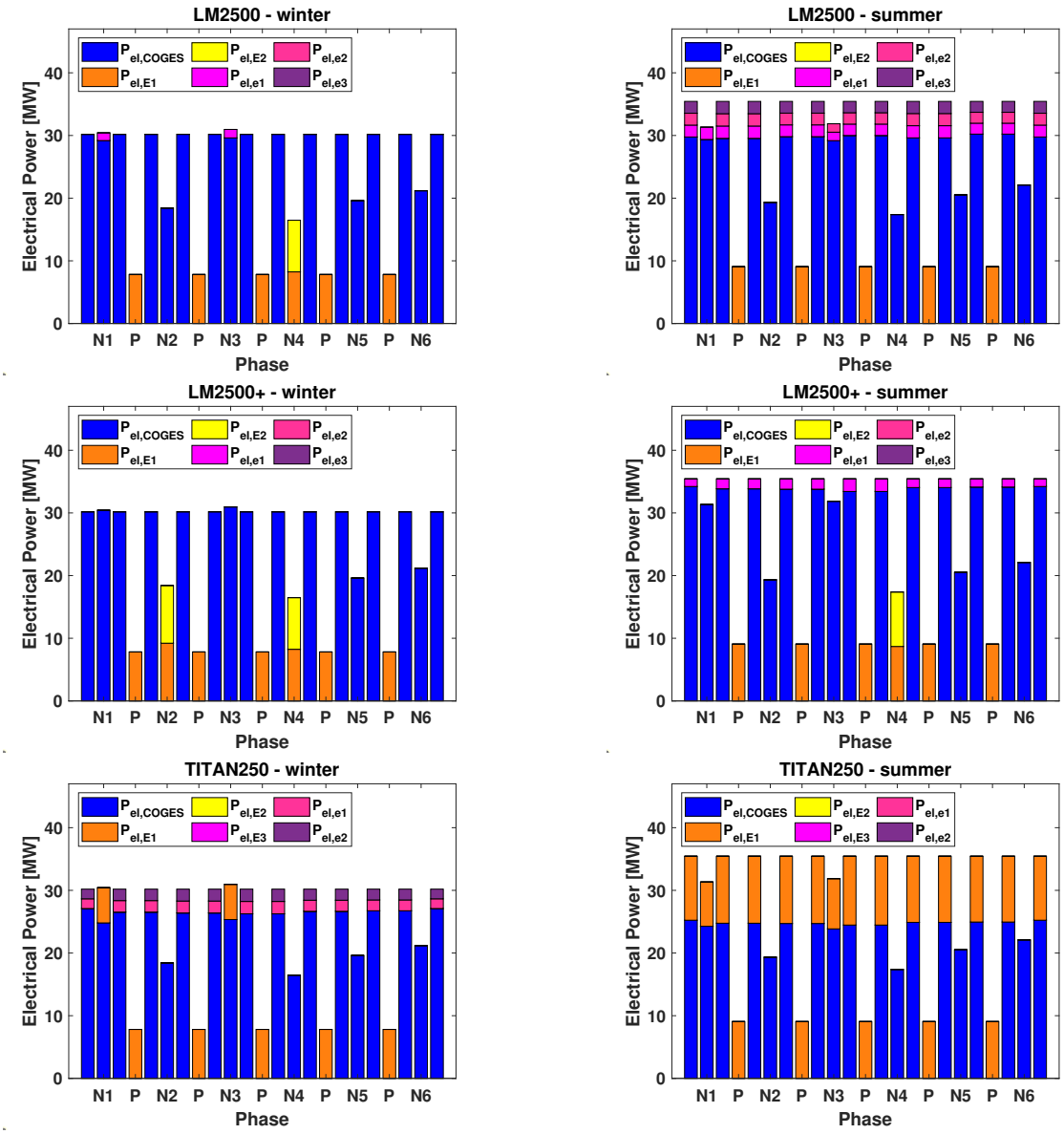

Fig. 9.22 Electrical power generated by prime movers during each operating condition for the route C2. Left and right columns refer to winter and summer seasons, respectively. Top, mid and bottom rows are related to the S1, S2 and S3 power plant configurations fed by CH_4-H_2 blends.

independently from the season. On the other hand, COGES alone supplies power demand during winter maneuvering, while three R-R Bergen C26 L9 are additionally turned on to cover the increase in power. This appears to mainly derive from the negative effect ambient temperature plays on GT performances, reducing both net power and efficiency. Indeed, despite COGES plant still works at its maximum load (i.e. 97%) to improve cogeneration efficiency, power delivered is reduced due to ambient temperature, thus further engines are required to be turned on. Specifically, all the three R-R Bergen C26 L9 engines are turned on

instead of a single 12V MAN 51/60 since their smaller size guarantees higher operating loads, i.e. higher efficiencies. Finally, where navigation is concerned, power demand in almost all the sailing modes is covered by COGES plant, since it provides the highest benefits in terms of η_g in comparison to reciprocating engines. Since COGES plant works at 97% load, further power is additionally provided by R-R Bergen C26 L9 engines only during highly demanding navigation conditions (i.e. 1.5MW on the Genoa-Naples route, 2.5MW on the Messina-Tunis one). Increase in power demand for navigation services along these routes derives from higher ship speed adopted. Analogously, power demand drops during Tunis-Barcelona navigation ($P_{el,REQ} \approx 16MW$), where lower ship speeds are required. Thus, since this ship operating condition would required COGES plant to work at part-load with negative effect on efficiency, especially for winter season, demand is supplied by 12V MAN 51/60 engines to optimize η_g. Differently from winter season, COGES plant still provides the highest efficiency during summer. Moving the attention on the S2 configuration (i.e. mid-row diagrams), COGES plant continues to cover most of power demand during navigation and maneuvering, delivering the highest efficiency among all the prime movers. However, since S2 deals with major size in comparison to S1, reduced and null extra power is required from R-R Bergen C26 L9 engines during maneuvering in summer and winter seasons, respectively. Indeed, 97% load conditions for COGES are exceeded only during summer maneuvering, where 1.5 MW are provided by a R-R Bergen C26 L9 engine. However, since efficiency reduction for part-loads occurs at higher power demands due to the major size of S2, power demand is supply by 12V MAN 51/60 engines in two additional navigation conditions (i.e. Naples-Messina for winter, Tunis-Barcelona for summer). Finally, where the S3 configuration is concerned, COGES plant remains the prime mover providing the highest efficiency during maneuvering and navigation, despite more power is supplied by reciprocating engines due to the low size of TITAN250. Specifically, nearly 3.5MW are covered by R-R Bergen C26 L9 engines during winter maneuvering, whereas 12V MAN 51/60 engines are turned on at 85-90% load in summer for the same conditions. For the same reason, a 12V MAN 51/60 engine is turned on during the Genoa-Naples and Messina-Tunis navigation conditions, for both winter and summer season. On the other hand, power demand at berth continues to be covered by 12V MAN 51/60 engines, similarly to what happened for the S1 and S2 configurations. Overall, figure 5 clearly shows how COGES plants provide the highest cogeneration efficiency within power range around 19-24 MW, hence they cover most of the power demand during navigation and maneuvering. Results concerning other cruise routes or fuel feeding systems are qualitatively analogous to figure 5 and are not shown here for sake of conciseness. Where the LT and HT power are concerned, figure 9.23 reports in cumulative form contribution of each prime mover to the overall amount of thermal demand. All the three power plant

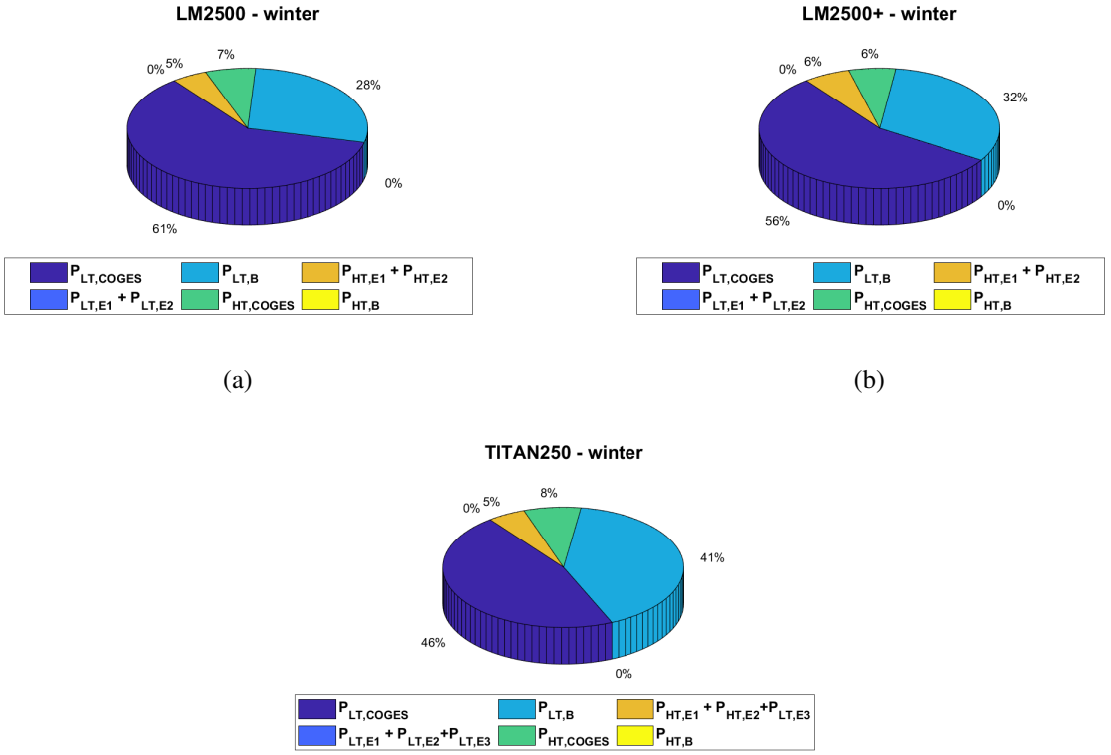

Fig. 9.23 Cumulative plots of thermal power supplied by prime movers and boilers during winter season, along the route C2. Figures (a), (b) and (c) correspond to the S1, S2 and S3 power plant configurations, respectively.

configurations summarised in table 9.13 have been considered, together with CH_4-H_2 blends fed system. Only results concerning winter season are shown, for the sake of conciseness. Focusing on the cumulative pie for LT power, comparable fraction of the overall demand is covered by COGES plants based on LM2500 (61%) and LM2500+ (56%). Few differences appear due to the variations in working load of GTs, since LM2500 and LM2500+ provide comparable values of waste heat (i.e. exhaust mass flow rates and temperatures). Instead, COGES plant based on TITAN250 ensures a 53% covering of LT demand, due to lower exhaust mass flow rate and temperature available from gas turbine. Since negligible LT power is delivered by 12V MAN 51/60 engines, the remaining portion of LT demand not covered by COGES plants is provided by auxiliary boilers producing steam at 3 bar, independently from the power plant configuration. On the other hand, focusing on the HT power, COGES plant appears to cover most of the demand within the S1 and S3 configurations, whereas nearly half of the required level is provided in case COGES plant based on the LM2500+ is

considered. Differences occurring for the S2 configuration appear due to the reduced number of navigation conditions where the LM2500+ based COGES is turned on, as observed in figure 9.22. Interestingly, due to the low amount of HT demand, the remaining part of it can be covered by reciprocating engines, hence auxiliary boilers producing steam at 9 bar are not necessary. Furthermore, cogeneration efficiencies delivered by the S1, S2 and S3 power plants during each ship operating condition (navigation, port, maneuvering) are investigated in figure 9.24. Specifically, information concerning all the five cruise routes is distinguished. Top, mid and bottom row refers to navigation, maneuvering and port operating conditions, whereas columns identify season. Focusing on winter navigation, the highest η_g on C1, C3 and C5 routes is delivered by S1, whereas S3 ensures energy benefits only along C2. During C4 cruise, nearly the same η_g is achieved by all the power plant configurations. On summer, power plant configuration based on TITAN250 provides the energy benefits on the C1, C3, C4 and C5 cruises, whereas S1 is advantageous only during C2. Comparing different routes at fixed power plant during navigation, a $\pm 4\%$ maximum variation on η_g is surveyed. Interestingly, navigation condition for the C4 cruise is characterized by the lowest η_g, in both winter and summer seasons. Indeed, as shown in tables reported within appendix A, both very high and low ship speed sailing conditions are present within the Caribbean route, making it the most demanding cruise among those tested. On the other hand, the highest η_g is reached during the C1 navigation condition due to particularly regular ship speed profile. Focusing on maneuvering, weaker differences arise between power plant configurations. Specifically, figures 9.24c and 9.24d show that S3 guarantees highest efficiency over all the routes, whereas S1 and S2 provides the worst performance in summer and winter, respectively. Comparing different cruises at fixed power plant, a maximum 1% gap on η_g is obtained. Finally, where port conditions are concerned, the same η_g is provided by all the power plants, since 12V MAN 51/60 engines covers demand independently from configurations. Overall, the S3 configuration appears to maximize cogeneration efficiency over the majority of the ship operating conditions, for both winter and summer. This seems to derive from a better fitting achieved between COGES plant size and electrical power demand. Indeed, as shown in figure 5, 97% load working conditions for COGES plant based on TITAN250 occur during nearly all the maneuvering and navigation conditions, whereas COGES plants ins S1 and S2 configuration often work on loads around 90%. Finally, comparison in terms of cogeneration efficiency among all the fuel feeding systems is reported in figure 9.25. Specifically, the time mean values of η_g computed over each cruise profile are shown, focusing on winter season for sake of conciseness. As can be seen, CH_4-H_2 blends provide the highest cogeneration efficiency, independently from power configuration. On the contrary, a 2-3% lower η_g is obtained when prime movers are fed by methanol or

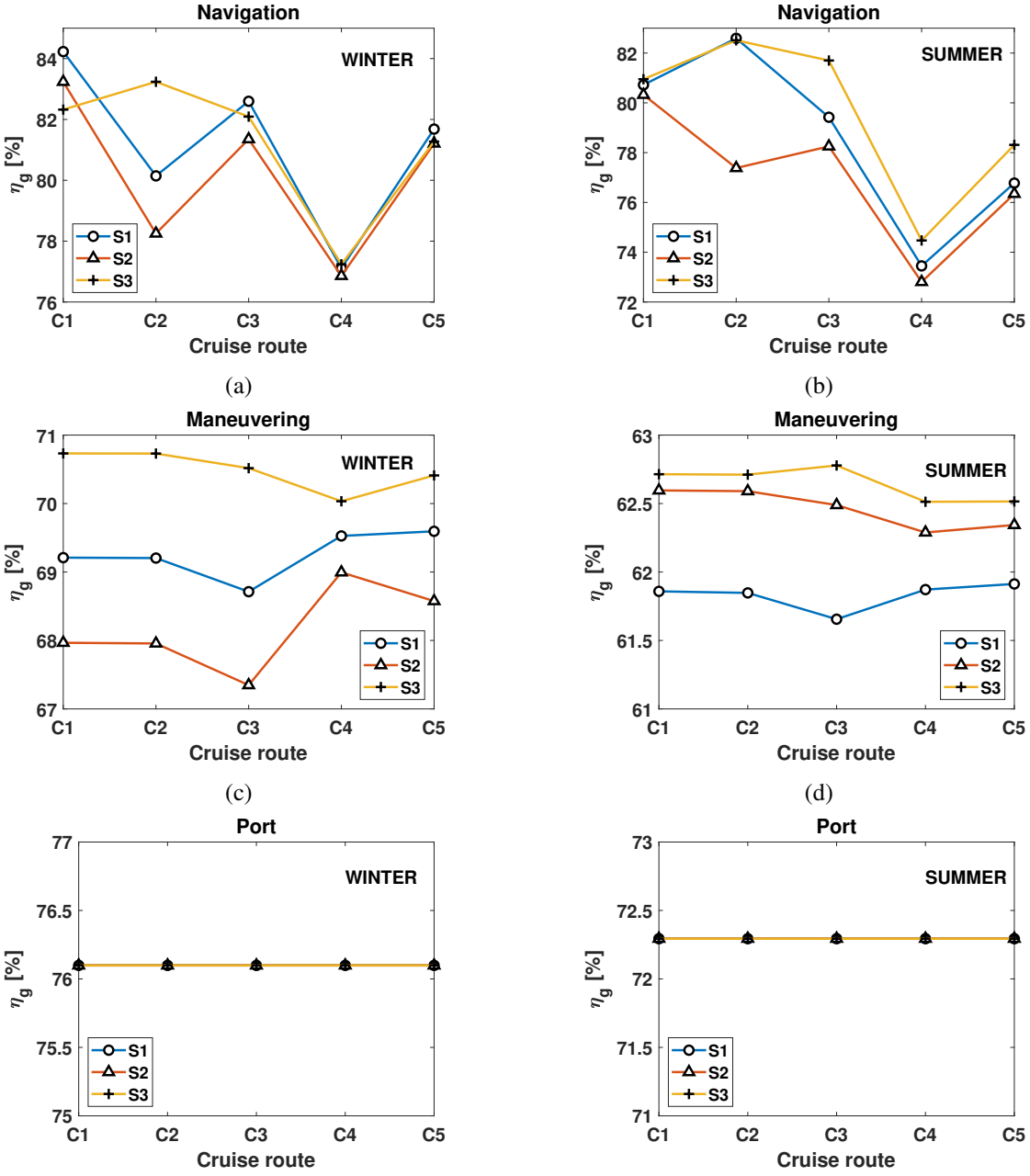

Fig. 9.24 Effect of cruise route on cogeneration efficiency obtained by S1, S2 and S3 configurations, under CH_4-H_2 blend feeding conditions. The left and right columns refer to winter and summer season, respectively, whereas results from navigation, maneuvering and port conditions are reported in the top, mid and bottom rows, respectively.

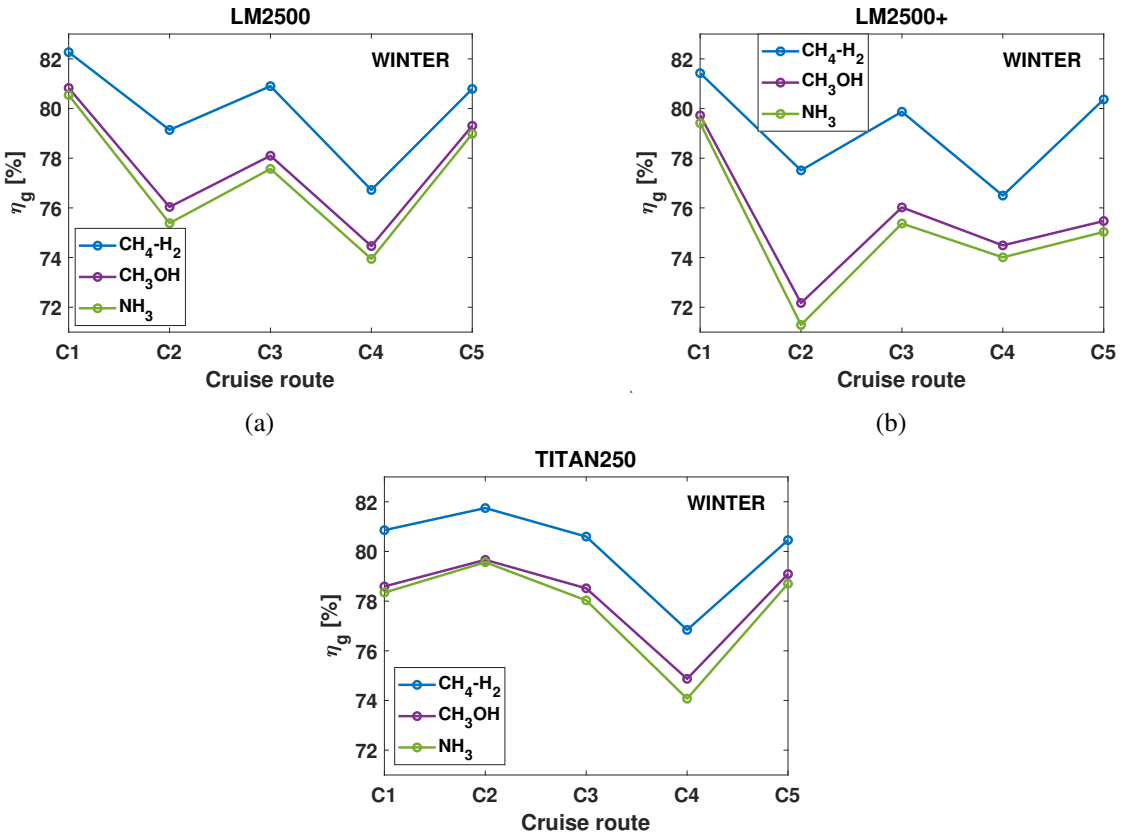

Fig. 9.25 Comparison in terms of cogeneration efficiency levels provided by NH_3, CH_3OH and $CH_4 - H_2$ blends, over all the five routes at winter. Figures (a), (b) and (c) refer to the S1, S2 and S3 power plant configurations, respectively.

ammonia within the S1 and S3 configurations. Even worse cogeneration efficiency levels are surveyed for S2. Changing route provides η_g variations analogous to those previously observed in figure 9.24. Overall, η_g variations shown in figure 9.25 for different fuel feeding system appear to mainly descend from the influence played by alternative fuels on prime mover performances. Specifically, as previously commented out, NH_3 and CH_3OHprovide drawbacks on electrical efficiency delivered by reciprocating engines, opposite to what occurs for η_{el} and P_{net} of GTs. On the other hand, tendencies for GTs and reciprocating engines are reversed in case CH_4-H_2 blends are considered. Nevertheless, to understand the effect of alternative fuels on power plant cogeneration efficiency it is necessary to couple demands with modified performance parameters. For this reason, increase in power achieved by feeding GTs with NH_3 and CH_3OH appears to overall constitute a drawback on η_g. Indeed, the fitting between generated and requested power get worse. The opposite occurs feeding

power plants with CH_4-H_2 blends, which result to deliver the highest η_g over all the routes, independently from plant configuration.

9.3.3 Environmental analysis

In this section, comparison between the S1, S2 and S3 power plant configurations fed by alternative fuels is carried out on environmental point of view. Where the equivalent

Table 9.16 Comparison on equivalent CO_2 emissions in tonns between different fuels.

CONFIGURATION	FUEL	WINTER					SUMMER				
		C1	C2	C3	C4	C5	C1	C2	C3	C4	C5
S1	CH_4-H_2	696.1	737.4	928.5	2001.3	1731.3	746.7	667.8	988.4	2093.2	1833.1
	CH_3OH	1995	1796.4	2430	4917.5	4839.5	2075.5	1908.6	2540.5	5130.8	5017.2
	NH_3	10.6	24.7	25.9	63.8	31.2	13.6	10.4	29.1	71	37.5
S2	CH_4-H_2	689.9	772	940.6	1942.1	1668.7	719.7	771.8	991.5	2067.3	1783.3
	CH_3OH	2025.5	1797.5	2456.3	4907.1	4828.7	2087.5	1891.9	2569.5	5124.5	5022.9
	NH_3	10.6	36.6	31.5	55.5	51.9	12	26.7	28.7	63.9	32.1
S3	CH_4-H_2	814.3	511.9	907	2195.1	1984.9	924.1	617.3	996.6	2317.2	2162.5
	CH_3OH	1959	1779.7	2341.5	4844.1	4716.8	2046.3	1851.8	2459.2	5079.4	4937.2
	NH_3	15.3	11.3	22.6	73.2	40.7	21.6	15.7	27.6	78.6	52.5

carbon dioxide emissions are concerned, results are summarised in table 9.16 distinguishing both route and season. As previously outlined, also the GHG effect of NO_x emissions is included while estimating $CO_{2,eq}$ in addition to carbon dioxide [348]. On the other hand, it must be remarked that unburned CH_4 emissions due to the methane slip factor occurring in reciprocating engines are drastically abated when hydrogen is added within the fuel, hence their impact is neglected [165]. Table 9.16 firstly shows that the lowest equivalent CO_2 emissions are provided by NH_3 feeding system. This mainly derives from both the null carbon content in NH_3 chemical formula and the higher amount of NO_x generated by ammonia. Overall, $CO_{2,eq}$ from NH_3 appears 1-2 orders of magnitude lower than that surveyed from methanol or CH_4-H_2 blends. Specifically, since H_2 addition to CH_4 significantly lowers carbon impact, CH_3OH results to provide the highest amount of equivalent carbon dioxide, independently from route, season and power plant configuration. Comparing S1, S2 and S3 in case of methanol feeding system, power plants based on LM2500 and LM2500+ are shown to deal with comparable $CO_{2,eq}$ emissions over all the ship profiles considered (+0.2% tonn of carbon dioxide are produced annually by S2). Instead, -2.2% CO_2 emissions in comparison to S1 is achieved by configuration including TITAN250. These trends appear to be related to variations in η_g levels each power plant configuration manage to deliver. Indeed, as was observed in the previous section, power plant based on TITAN250 overall guarantees the highest cogeneration efficiencies, whereas S2 the lowest one. Finally, focusing on the CH_4-H_2 blend feeding case, S1 reaches a 0.6% lower carbon intensity in comparison to S2,

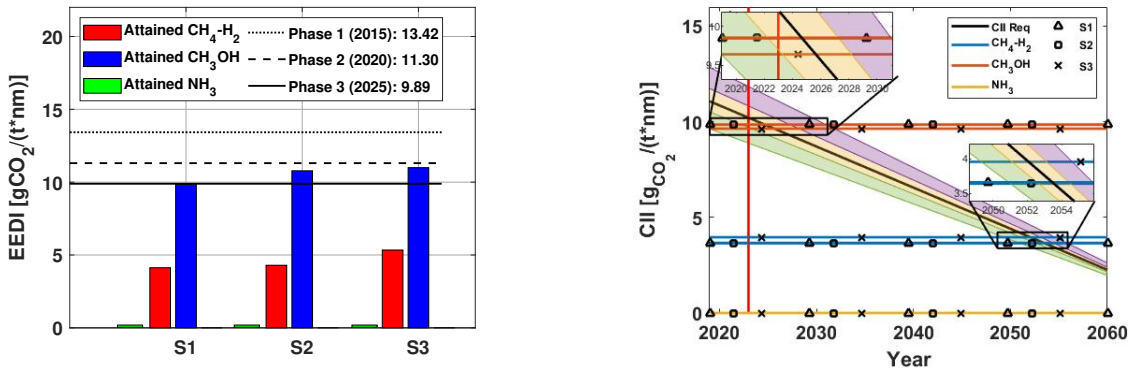

(a) (b)

Fig. 9.26 Results concerning Energy Efficiency Design Index (EEDI) and Carbon Intensity Indicator (CII) for S1, S2 and S3 configurations, powered by CH_4-H_2, CH_3OH and NH_3.

whereas S3 achieves 2-30% higher CO_2 emission level with respect to S1. Since the same H_2 volumic fraction is accounted for LM2500 and LM2500+, differences arising between S1 and S2 appear due to cogeneration efficiency. On the other hand, the far higher carbon intensity provided by S3 mainly derives from the lower H_2 content available for TITAN250. Further drawbacks for S3 are provided by reciprocating engines, which works with only 30% volumic concentration of H_2 and are more frequently turned on in case TITAN250 is included within COGES plant. Then, the Energy Efficiency Design Index (EEDI) and Carbon Intensity Indicator (CII) for all the three power plant configurations are reported in figure 9.26 with the aim of assessing compliance with regulations, in case alternative fuels are used onboard cruise ships. As outlined above, EEDI limits carbon intensity of propulsion plants installed on new ships, whereas CO_2 emissions during effective yearly operating conditions are assessed by CII. Focusing on figure 9.26a, null CO_2 emissions are surveyed fro NH_3 fed power plants, due to the chemical formula of ammonia. It must be remembered here that both EEDI and CII only account for CO2, not $CO_{2,eq}$, emissions. Thus, the high NO_x emissions generated by NH_3 fed power plants are not included, despite their GHG contribution is non-null. Interestingly, feeding power plants with CH_4-H_2 blends guarantees compliance with EEDI regulation also beyond 2025. This proves that adding H_2 to CH_4 consists in an effective middle- long-term strategy to lower carbon impact of the maritime sector. However, it must be remarked that results in figure 9.26a can be obtained only including carbon capture system onboard in case grey H_2 is produced by LNG steam reforming. Furthermore, increasing H_2 content will eventually provide further reduced CO_2 emissions, hence compliance with more restrict future regulations is ensured. Finally, where methanol feeding systems are concerned, only S1 complies with EEDI limit for new ships up to 2025, despite low gap arises with

requirement from the third phase. This mainly derives from the high carbon content existing within the methanol chemical molecule. Therefore, only a short term strategy towards energy transition can take into account CH_3OH as viable. Focusing the attention on CII index, figure

Table 9.17 Attained CII values for the S1, S2 and S3 configurations, powered by alternative fuels. Values correspond to horizontal lines depicted in figure 9.26b.

FUEL	S1	S2	S3
CH_4-H_2	3.66	3.64	3.96
CH_3OH	9.85	9.86	9.64
NH_3	0	0	0

9.26b reports results for all the power configurations and fuel feeding system considered in this work. For sake of clearness, table 9.17 summarises the corresponding attained CII values. Since the analysis is carried out up to 2060, zooms around intersection between attained CII and ratings defined by IMO are also added to the plot, to improve visualization. Specifically, B, C and D rating boundaries are depicted as shaded purple, yellow and green areas, respectively, whereas the A and E rating zones are positioned under B and over D categories. Black line indicates the required CII for a 114000 Gross Tonnage cruise ship. It must be underlined here that the required CII as well as rating boundaries shown in figure 9.26b have been extrapolated beyond limits available from MEPC.339(76) IMO resolution, which extends up to 2026 [81]. In order to continuously improve energy efficiency onboard, reaching ratings above or equal to C is required from annually surveyed ship operating conditions. Due to chemical composition of fuel, S1, S2 and S3 fed by NH_3 always remain position in A rating. Differently, feeding prime movers with methanol causes B (for S3) and C (for S1 and S2) ratings since approximately 2023. Successively, C and D ratings are maintained up to 2028 and 2031, respectively, independently from the power configuration considered. Indeed, as commented out for table 9.16, the S3 configuration provides the lowest CO_2 emissions among power plants, due to its energy saving benefits. Analogously, slightly reduced attained CII is provided by S1 in comparison to S2. On the other hand, far lower CII indexes are attained feeding power plants with CH_4-H_2 blends. Specifically, the S1 and S2 configurations remains within A ratings up to 2051, whereas the same condition last up to 2050 for S3. Furthermore, rating C is kept up to 2053 (for S3) and 2055 (for S1 and S2). Differences in ratings achieved by S1, S2 and S3 mainly derives from the hydrogen content available within prime movers. Indeed, TITAN250 included within S3 can burn blends containing to 50% H_2, while only 30% concentrations are allowed by reciprocating engines. Overall, figure 9.26b confirms how mid-, long-term compliance with regulations is achieved by feeding power plants with CH_4-H_2 blends or NH_3, as well as methanol is shown

to represent only a short term solution for energy transition. Where comparison between power plants is concerned, COGES based on LM2500 provides the lowest environmental impact under fuel flexible operating conditions.

9.3.4 Economic analysis

In this section, economic viability of all the three power plant configurations reported in table 9.13, fed by alternative fuels, is investigated. Cost savings obtained over 25 years ship

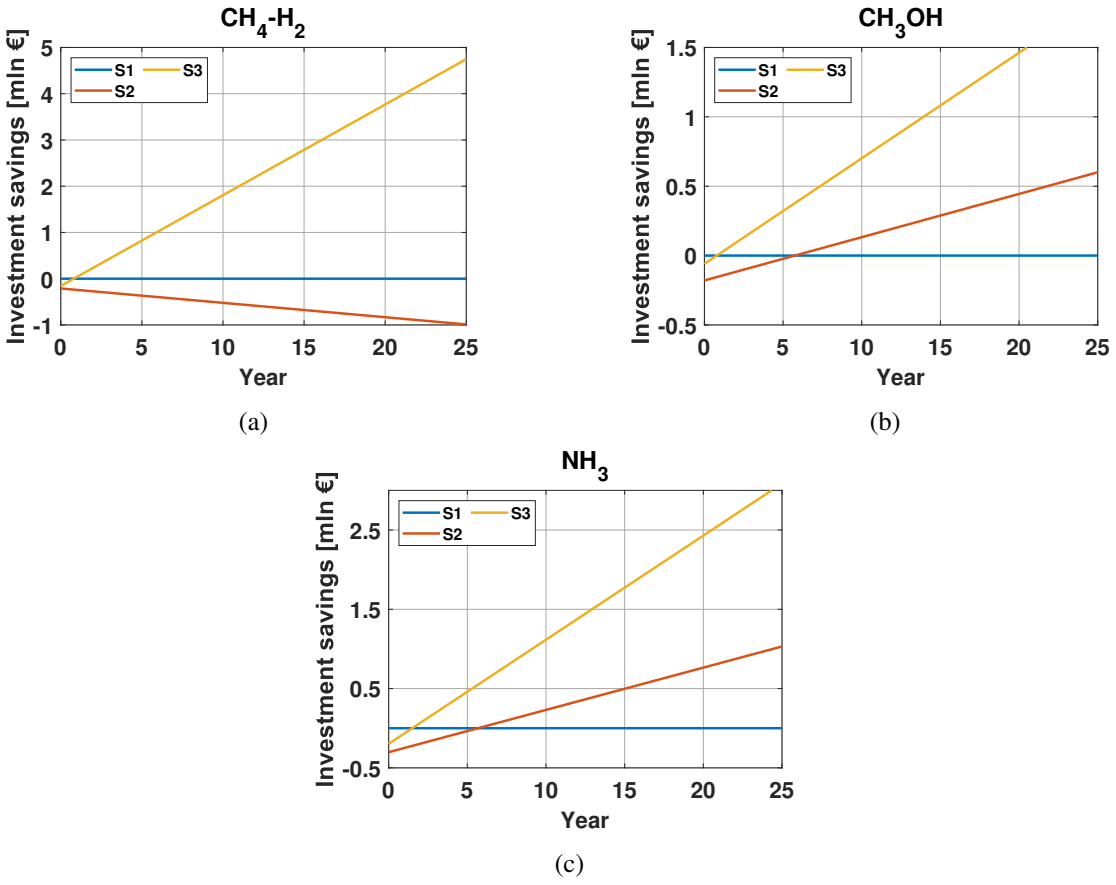

Fig. 9.27 Investment savings for CH_4-H_2 (a), CH_3OH (b) and NH_3 (c) fed power plants over 25 years.

useful life are reported in figure 9.27 for power plants operating on CH_4-H_2 blends (top left), CH_3OH (top right) and NH_3 (bottom). In details, cost savings are shown in relative form with respect to the S1 configuration, with the aim of improve clearness in comparison. For this reason, cost savings for S1 are null over all the 25 years. The first point of each curve occurs at the 0-th year, hence it identifies the cost savings related to CAPEX, since no OPEX cost still exists. Specifically, in case savings on CAPEX arise in comparison to S1,

positive cost savings occur at the 0-th year, vice versa for penalties. Furthermore, in case cost savings on OPEX arise with respect to S1, a positive slope is obtained. Where higher fuel or maintenance costs occur, decreasing line is surveyed. Focusing the attention on economic viability of CH_4-H_2 blends fed power plants, both S2 and S3 deal with higher investment costs in comparison to the S1, since negative starting point is visible. These drawbacks mainly depend on the slightly higher installed power of S2 and S3 configurations, as visible from table 9.13 above. Indeed, S2 configuration is based on the LM2500+, which deals with the highest nominal power among GTs, whereas three large-size reciprocating engines are installed within S3. Focusing on OPEX costs, negative and positive slopes are provided by S2 and S3, respectively. Furthermore, benefits on OPEX characterizing S3 manage to entirely compensate penalties on investment costs within 1 year. Differences arising among power plants in terms of OPEX cost appear to reflect the η_g levels guaranteed by each configuration. Indeed, since yearly maintenance costs are nearly one-tenth fuel consumption ones, AFC dominates OPEX cost computation. As previously shown, configuration based on TITAN250 ensures the highest cogeneration efficiency over most of operating conditions and mission profiles, whereas S2 was shown to provide slightly lower η_g when compared to S1. Focusing on results concerning methanol and ammonia, the same considerations made on investment costs for CH_4-H_2 blends repeat here, hence S2 and S3 provide CAPEX penalties with respect to S1. On the contrary, OPEX savings (i.e. positive slopes) occur for both S2 and S3 and compensate CAPEX penalties in 1.5 and 7.5 years for S3 and S2 fed by methanol. On the other hand, 2 and 6.5 years are needed in case ammonia fed power plants are considered. Again, differences in terms of η_g provided by power plants yield variations on OPEX costs. Overall, by an economic point of view, S3 deals with major cost savings (approximately 1-4 mln€ at the 25-th year). With the aim of clearly visualize comparison between different

Table 9.18 Variations on CAPEX and OPEX costs related to different fuels.

FUEL	COST	S1	S2	S3
CH_4-H_2	**CAPEX [mln €]**	0	-0.21	-0.16
	OPEX [mln €]	0	-0.99	4.75
CH_3OH	**CAPEX [mln €]**	1.8	1.62	1.69
	OPEX [mln €]	62.12	62.72	63.97
NH_3	**CAPEX [mln €]**	0.57	0.27	0.38
	OPEX [mln €]	37.16	38.19	40.25

fuels, table 9.18 reports CAPEX and OPEX savings in relative form with respect to S1 configuration fed by CH_4-H_2 blends. Comparison on OPEX costs have been carried out at the 25-th year. Where investment costs are concerned, approximately 2 mln€ CAPEX savings are provided by methanol in comparison to the corresponding CH_4-H_2 power plant

configurations. On the other hand, benefits reduce at 0.3-0.6 mln€ for NH_3. The penalties on investment costs related to CH_4-H_2 blends are mainly due to the major cost of reciprocating engines and tanks (see table 9.14 above). Focusing on fuel and maintenance costs, hydrogen addition to CH_4 strongly increases OPEX, since fuel cost for hydrogen is approximately 10 times that of methanol or ammonia. In details, 62-63 mln€ and 37-40 mln€ of OPEX savings are obtained feeding power plants with CH_3OH and NH_3, respectively. Interestingly, economic penalties generated by hydrogen fuel cost are not compensated by benefits in terms of cogeneration efficiency in comparison to $CH_3OH$and NH_3 fed systems. Thus, economic penalties provided by CH_4-H_2 blends at the 25-th year overall amount to current investment cost for traditional power plant, i.e. CAPEX costs are nearly doubled [349]. Therefore, a strong reduction in green hydrogen cost is necessary to burn it on cruise ships. Furthermore, fuel cost for ammonia is sightly higher than that of methanol, hence feeding power plants with NH_3 causes OPEX penalties. Overall, by an economic point of view, cost savings are maximized by CH_3OH power plants and, secondly, by NH_3. Indeed, mature know-how exists for methanol and ammonia, hence lower costs from production to distribution are available. On the other hand, excessive fuel cost descending from green H_2 production by electrolysis and logistics/transportation currently relates to CH_4-H_2 blends. Economic viability may be further improved in case gray H_2 (i.e. H_2 produced from CH_4 through steam reforming) is available. However, carbon capture systems must be installed onboard to mitigate negative effects on environment. In future, with wider production of renewables and green H_2 production, costs for CH_4-H_2 fed power plants may be economically viable. For these reasons, as previously shown in figure 9.9, if fuel price volatility normally surveyed on the market (i.e., $\pm 10\%$) had been considered here, weak variations on cost savings would have been obtained, since non-negligible differences can arise only in a long term perspective, in case green H_2 price settles on much lower levels.

9.3.5 Main findings

In sections above, energetic, environmental and economic performances provided by three different integrated COGES-reciprocating engines power plants fed by alternative fuels are investigated within an energy transition scenario for the maritime sector. The analysis has been carried out considering electrical and thermal power demands onboard modern large cruise ships and relies on cogeneration efficiency optimization study. Specifically, three different ship operating conditions (maneuvering,port and navigation) and 5 different routes have been taken into account, together with seasonality. Overall, due to the energy savings benefits provided by COGES plants in comparison to reciprocating engines for $\geq$ 16MW

power, most of the electrical and thermal power demands required during navigation and maneuvering was supplied by GT-ST combined power plants. On the other hand, only the low power demand required onboard when the ship is at berth was covered by reciprocating engines, since COGES would work at part-loads with significant reduction in efficiency. Comparison in terms of configuration revealed how the highest cogeneration efficiency is obtained considering COGES plant based on TITAN250 gas turbine, over most of the routes and seasons. Only few, localised energy savings benefits are provided by the LM2500-based plant. Indeed, better fitting was achieved between electrical demand and the size of COGES based on TITAN250. On the other hand, comparison on performances in case different alternative fuels are fed within prime movers showed how the highest cogeneration efficiency can be achieved by CH_4-H_2 blends. Overall, the role played by fuel on thermodynamic performances of prime movers can deeply influence matching between power requested and delivered, with positive/negative effects on η_g levels provided by the overall power plant. Where environmental viability is concerned, $CO_{2,eq}$ emissions over different routes together with the Energy Efficiency Design Index (EEDI) and Carbon Intensity Indicator (CII) were adopted as relevant parameters. Overall, the lowest environmental impact was shown to be achieved by NH_3 fed power plants, since null carbon content is present in ammonia. Nevertheless, power plants fed by CH_4-H_2 blends coped with EEDI and CII regulations up to 2025 and 2050, respectively. Therefore, CH_4-H_2 blends appear to be suitable for a long-term strategy aimed at energy transition, since they remain effective with even more restrictive regulations. On the contrary, methanol appeared only useful in a short-term strategy, since it fails in coping with EEDI and CII regulations since 2025 and 2031, respectively. Finally, by an economic point of view, comparable costs from NH_3 and CH_3OH fed plants were shown, whereas fuel price for green H_2 is proved to represent the major challenge for CH_4-H_2 blends. Specifically, CH_4-H_2 blends provide ≈40-60 mln € penalties at the 25-th year, which nearly equalize the investment usually borne for traditional power plants onboard cruise ships [349]. However, more strict regulations on CO_2 emissions together with renewables spreading can strongly reduce penalties of power plant fed by green H_2. Similar improvements in the economic viability of CH_4-H_2 fed power plants can be obtained by gray H_2 produced through steam reforming of LNG. However, carbon capture systems must be installed onboard to preserve low carbon emissions. Overall, including TITAN250 within the engine room resulted to provide the best economic viability, independently from the fuel considered. Indeed, despite CAPEX penalties deriving from slightly higher installed power occurring for S3 configuration, they are entirely compensated in few years by benefits on fuel consumption costs. Therefore, this work overall shows how including COGES plants within the engine

room of large-size cruise ships can represent an effective and just commercially available choice for both short- and long-term strategies within energy transition scenario.

9.4 Hybrid-electric power plants onboard large-size cruise ships

In the last few decades, regulations limiting pollutant and greenhouse gas (GHG) emissions from ships have been entered to force within the maritime sector. Recently, the short- and long-term purposes identified by the European Commission to ground the road map towards energy transition focused attention on the need for more environmentally friendly maritime transport sector. In this scenario, hybrid-electric ship power plants are currently receiving great attention due to their benefits in terms of efficiency and emission reduction. Indeed, installing batteries onboard ships can provide more flexible usage of engine room with energy savings achieved, with consequent reduction of CO_2 emissions. Furthermore, in case electricity from renewables is used during the charging process, thus even lower environmental issues are reached. However, including electrical energy storage system onboard ships can significantly increase complexity for optimal design and operation of power plants, since many different technologies are coupled together with possibility of moving electrical power in time, depending on engine room performances. From the distributed power generation sector, it is well known that optimal design and operation of polygeneration power plants are mandatory to guarantee high performances of grids in terms of costs, emissions and efficiency as well as to avoid failures. A traditional strategy to face these two challenges consists in developing Mixed-Integer Linear Programming (MILP) tools able to work on both short and long time horizons. Despite analogous problems arise for the optimal design and operation of cruise ships, mandatory to comply with new regulations [56, 57, 55], few works exists in the literature focusing on these issues [350]. Therefore, in this section performances provided by hybrid-electric power plants installed onboard large-size cruise ships are assessed under energetic, environmental and economic point of view. Since Li-ion batteries are currently receiving major attention for the maritime sector due to their high useful life, efficiency and less-volume required, energy storage system of this type is considered. Similarly to the previous section, the ship investigated here consists in a large-size cruise ship powered by Liquefied Natural Gas (LNG) and operating within the Mediterranean Sea. The MILP code described in section 8 has been applied implementing cogeneration efficiency η_g, equivalent carbon dioxide emissions $CO_{2,eq}$, nitrogen oxide emissions and cost optimization. Firstly, the case study of the cruise ship together with candidate power plants are introduced in section 9.4.1. Secondly, in section 9.4.2, optimization has been performed considering as inputs the phase-mean electrical and thermal power demands and the sizing of the energy storage system is determined. Since carbon pricing will be imposed in EU in the early future, its importance in improving economic feasibility of Li-ion battery is also investigated.

Thirdly, energetic, environmental and economic optimization is performed in section 9.4.3 on hourly electrical and thermal power demand profiles, for an overall time extension of 2 days. In this case, the optimally sized Li-ion battery pack is considered installed onboard, thus its capacity is assumed fixed. Thanks to the high temporal resolution this second study is based on, detailed insight into the best operating strategies of power plant are gained. Finally, the influence played by cold ironing on the energy management system is assessed. Overall, batteries appeared to provide benefits by an energetic, environmental and economic point of view and to improve energy management flexibility onboard.

Table 9.19 C2 cruise route in the Mediterranean sea.

LOCATION	**PHASE**	**t [h]**	V_{ship} **[knots]**
Genoa	M	0.5	0
Genoa-Civitavecchia	N	13	15
Civitavecchia	M	0.5	0
Civitavecchia	P	10	0
Civitavecchia	M	0.5	0
Civitavecchia-Palermo	N	15	17
Palermo	M	0.5	0
Palermo	P	7	0
Palermo	M	0.5	0
Palermo-Malta	N	16	18
Malta	M	0.5	0
Malta	P	8	0
Malta	M	0.5	0
Malta-Barcelona	N	38	18
Barcelona	M	0.5	0
Barcelona	P	10	0
Barcelona	M	0.5	0
Barcelona-Marseille	N	13	15
Marseille	M	0.5	0
Marseille	P	8	0
Marseille	M	0.5	0
Marseille-Genoa	N	14	16
Genoa	M	0.5	0

9.4.1 Case study

Power plant performances of the large cruise ship considered in section 9.3.1 have been investigated focusing on the Mediterranean route reported in table 9.19, typically occurring

for large MSC and Costa cruise ships. Details on the journey are reported in table 9.19, where ship speeds were computed by means of arrival/departure times and nautical miles covered, as explained in section 9.3.1. Where the first study is concerned, power plant performance on the entire route is assessed by considering mean values for power demands during port, maneuvering and navigation conditions. In this case, variable time step reproducing phase duration is provided as input to the MILP code. For this analysis, data introduced in section

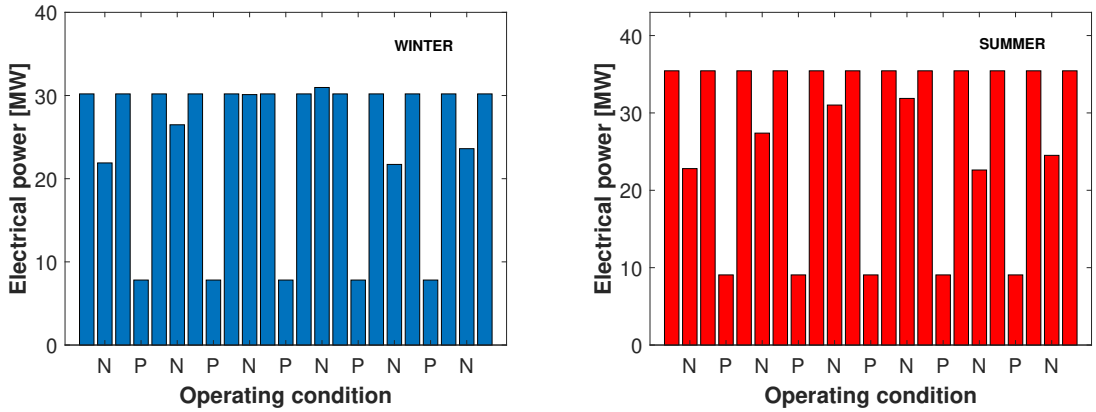

Fig. 9.28 Phase-mean electrical power demands during winter and summer season, for a large-size cruise ship on Mediterranean route.

9.3.1 have been used to build power demands and the corresponding mission profile obtained for both electrical and thermal power is shown in figure 9.28, distinguishing winter and summer season, for the 8-days journey. From figure 9.28 it can be seen how the highest P_{el} are required during maneuvering conditions, whereas the lowest ones occur at berth. Instead, during navigation intermediate power demands exist. Focusing on the LT thermal power demand, a regular profile is shown, with reduced variations for changing phases. Specifically, the maximum power request at 3 bar occurs during navigation, since fresh water must be produced while sailing to avoid sanitary issues. Where the second study is concerned, hourly power demands were built using daily profiles available from the literature [351]. It must be underlined that large cruise ship dealing with comparable Gross Tonnage was investigated Baldi et al. [351], hence reliability of the analysis is assured. In details, the first 48 hours, centered around the Genoa-Civitavecchia and Civitacchia-Palermo navigation conditions, have been considered for the analysis. Hourly fluctuations of the propulsion power demand onboard have been obtained entering the cubic curve reported in figure 3 with the actual ship speed profile, which was derived from marine traffic online platforms for the Genoa-Civitavecchia-Palermo route. Then, with the aim of conserving the electrical and thermal energy demand during each ship operating condition, all the shapes of the experimentally surveyed profiles from Baldi et al. [351] have been scaled with the time mean values reported

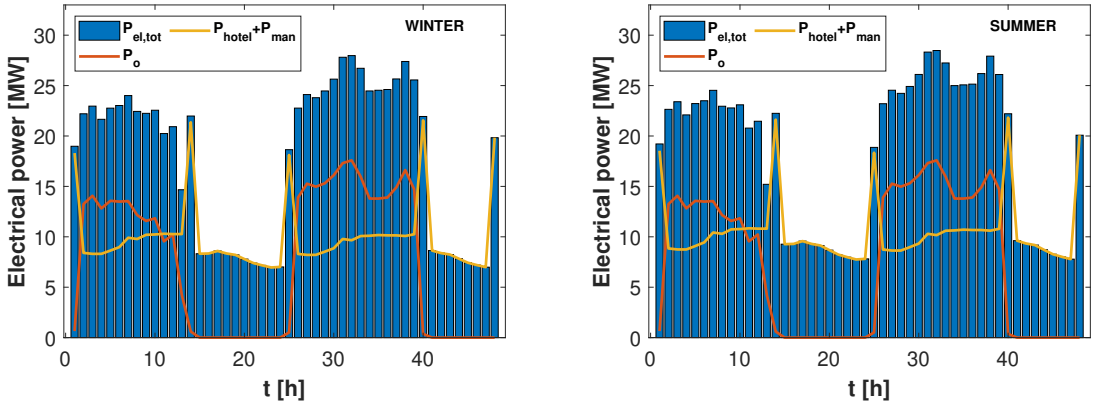

Fig. 9.29 Hourly-mean electrical power demands during winter and summer seasons, for a large-size cruise ship along the C1 Mediterranean route.

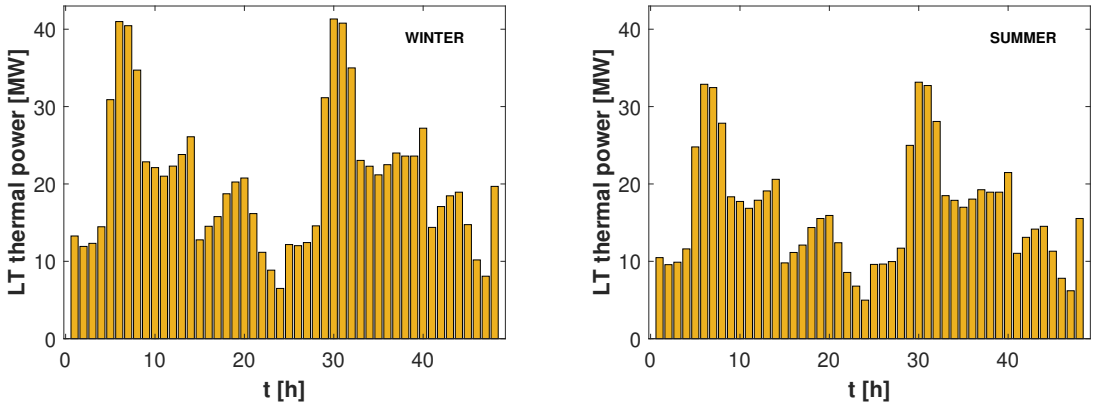

Fig. 9.30 Hourly-mean LT power demands during winter and summer seasons, for a large-size cruise ship along the C1 Mediterranean route.

in section 9.3.1. For analogous reasons, energetic level of the electrical energy storage system provided by the phase-mean study has be used as initial conditions to correctly account for energy availability. Since reduced variations are often surveyed for the HT power demand, a fixed level of it is considered under all the 48 hours simulated. Cumulative plots of electrical and LT thermal power demands obtained for hourly profiles are shown in figures 9.29 and 9.30 together with composition details. The time extension considered is fixed equal to the 48 hours accounted for and both winter and summer data are reported. HT demand is not shown since its value is retained constant. The cumulative plot for electrical power demand is shown in blue bars, whereas the hotel and propulsion power components are reported separately in yellow and orange curve, respectively. Instead, the LT thermal power demand is reported in yellow bars. As can be seen from figure 9.29, 4-5 MW amplitude fluctuations are surveyed for propulsion power demand. This appears to mainly derived from

both ship speed modulations during navigation and time-dependent differences in weather conditions. On the other hand, the shape of LT thermal power profile appears characterized by three peaks. These peaks occur around 8 am, 12 am and 20 pm, respectively, hence they are generated by fresh water, accomodation, laundry and galley users. Interestingly, high deviation from the mean (+250% variation) is provided by peaks, hence extremely flexible thermal power suppliers are needed to entirely cover them. Figure 9.31 shows the power

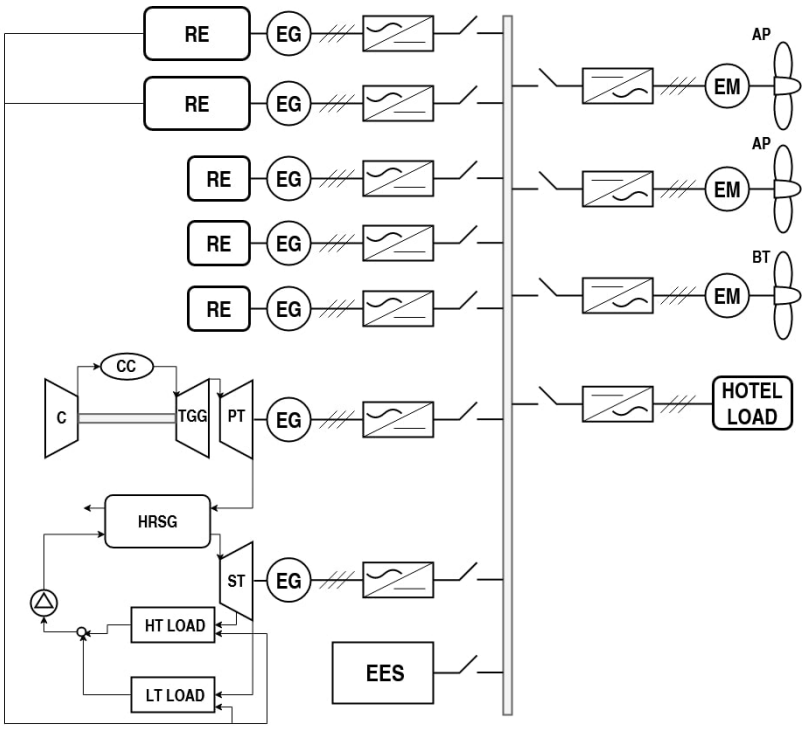

Fig. 9.31 Schematic view of the power plant under study (RE=reciprocating engine, C=compressor, CC=combustion chamber, TGG=gas generator turbine, PT=power turbine, ST=steam turbine, HRSG=heat recovery steam generator, EG=electrical generator, EM=electrical motor, AP=azipod, BT=bow thruster, EES=electrical energy storage).

plant configuration considered to be installed onboard the cruise ship under study. As can be seen, the traditional integrated electric layout is adopted, since prime overs are connected with propellers through electrical lines consisting in AC/DC and DC/AC converters, electrical motors, switch and bars. Differently from the Diesel-electric configuration currently installed onboard most of cruise ships, reciprocating engines are integrated with COmbined Gas Electric and Steam (COGES) plant. It must be remarked that back-pressure configuration is considered here, to reduce volume occupied by engine room onboard. Two azipods driven by 21 MW electrical motors cover propulsion demand, whereas one bow thruster is inserted to facilitate maneuvering during port activities. Figure 9.31 also shows how the HT thermal power demand can be indiscriminately supplied by steam extraction at 9 bar from the ST

included within COGES or from the WHR systems downstream of reciprocating engines. On the other hand, the LT power demand may be covered by steam exiting the back-pressure ST or by fraction of the steam produced by reciprocating engine WHR systems. Since steam at 9 bar is generated within WHR systems, lamination is performed up to reach 3 bar before supplying steam at the LT users. In any case, precedence is given to the HT power production within the WHR of reciprocating engines.

Table 9.20 Main characteristics of prime movers installed within the hybrid-electric power plant.

GT	P_{net} **[MW]**	η_{el} **[%]**	T_{ex} **[°C]**
LM2500	24.31	36	566
9L MAN 51/60	8.42	45.5	309
R-R Bergen C26 L9	2.33	45	-

Table 9.21 Propulsion system configuration being selected for the hybrid-electric power plant.

Prime mover	
LM2500	X
9L MAN 51/60	XX
R-R Bergen C26 L9	XXX

Table 9.20 reports the main characteristics of prime movers used for power plant. Specifically, the LM2500 gas turbine from General Electric is considered coupled with a bottoming steam power plant in a COGES configuration. On the other hand, two 9L MAN 51/60 dual-fuel reciprocating engines available from MAN and delivering 8.42 MW each are used. In addition, three R-R Bergen C26 L9 natural gas reciprocating engines from Rolls-Royce are introduced as small-size electrical generators able to cover small power gaps with increased loads and, consequently, efficiencies. The overall installed power of prime mover excluding battery pack achieves 50.9 MW. This allows to comply with regulations concerning the safely return to port, in he eventuality of possible failure of one prime mover [337]. According to traditional propulsion plant design onboard ships, a 10% Engine Margin (EM) has been assumed for all the reciprocating engines [338], whereas a 3% EM is considered for COGES plants. It must be remarked that no EM is required by regulations for COGES plants due to their reliability and low maintenance costs in comparison with reciprocating engines, thus 3% engine margin is cautiously adopted.

9.4.2 Results

In this section, the optimization of the hybrid-electric power plant is performed by an energetic, environmental and economic point of view considering phase-mean power requests. All the four different optimization procedures relying on the objective functions previously defined in section 9.4.1 have been set up. Specifically, cogeneration efficiency maximization and CO_2 equivalent, NO_x emission and overall cost optimizations have been performed. Each optimization is carried out for both summer and winter season. As results, thermal and electrical powers delivered by each prime mover to optimally cover corresponding demands at each ship operating condition are computed together with the overall value assumed by the objective function on the entire route. Finally, the size of the Li-ion battery pack is optimally identified, for capacity ranging between 0 and 40000 kWh. Figure 9.32 reports

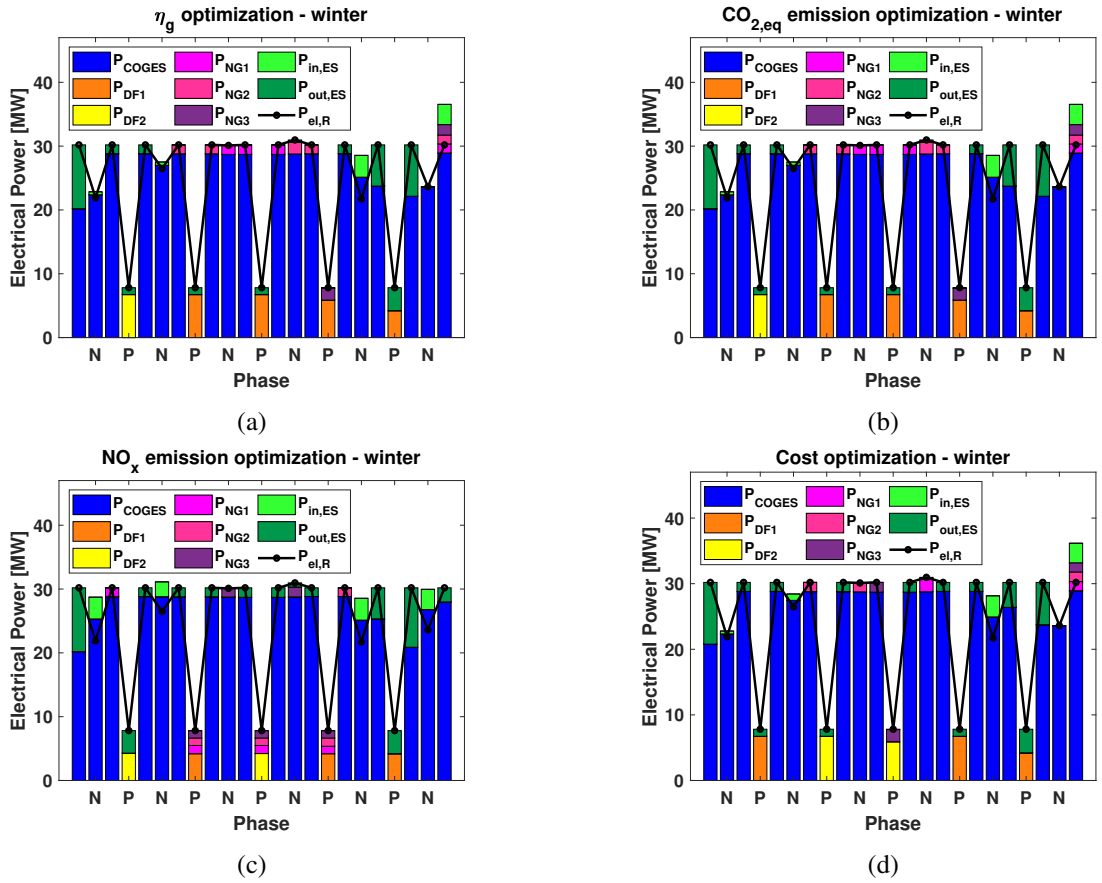

Fig. 9.32 Electrical power distribution for phase-mean analysis. Results are optimized for η_g (a), $CO_{2,eq}$ (b), NO_x (c) and costs (d).

the electrical power delivered by each prime mover in case of η_g (top left), $CO_{2,eq}$ (top right), NO_x (bottom left) and cost (bottom right) optimizations, during winter conditions.

Power demand required onboard cruise ship is depicted in black, dotted line, as reference, whereas operating phase is indicated on the x-axis (port P, navigation N, maneuvering no symbol for sake of conciseness). Specifically, the ship operating conditions are ordered following the same order used in table 9.19 above. Results from summer season are not reported in figure 9.32 for sake of conciseness. Focusing the attention on figure 9.32a, electrical power is withdrawn from batteries in almost all port and maneuvering operating phases. E.g. see maneuvering during departure from Genoa or arrival to Civitavecchia and conditions at berth in Civitavecchia and Palermo ports. Specifically, power discharged by batteries during maneuvering is around 3-10 MW and covers power gap COGES plant does not succeed to supply. Thus, during maneuvering COGES plant coupled with batteries appear to provide the highest η_g among all the available prime movers included within the power plant. On the other hand, energy benefits are obtained at berth from discharging batteries coupled with DF engines. In this condition, nearly 2 MW are supplied by the energy storage system. Interestingly, negative drawbacks are surveyed on the efficiency delivered by prime movers in both maneuvering and port conditions since they work at reduced load with respect to the EM limit. However, drawbacks are entirely compensated by nearly 90% efficiency provided batteries during discharge mode. For this reason, the optimization algorithm enables energy storage system in a cogeneration efficiency maximization purpose. On the other hand, energy is charged into batteries during few navigation conditions (e.g. see Genoa-Civitavecchia, Civitavecchia-Palermo and Barcelona-Marseille routes). Specifically, since COGES covers almost the the entire power demand during navigation, small amount of excessive power is required by COGES to charge batteries, with benefits in terms of loads and electrical efficiency it is working at. Furthermore, the amount of excessive power required to COGES appears small due to the long duration of navigation condition, which increases energy exchanged. Excess power from NG engines is used to charge batteries only in correspondence of the last maneuvering, since the corresponding working conditions of COGES consist in 97% load (i.e. maximum load due to EM). Overall, the energy management system decides for charging mode of batteries at ship operating conditions where high η_g values would be obtained also in the absence of electrical energy storage. On the contrary, discharging mode of batteries is positioned where low efficiencies from prime movers are gained. Therefore, batteries resulted in significant energy savings, since they increase η_g both during charging and discharging phase. Moving the attention on figure 9.32b, results obtained optimizing equivalent carbon dioxide emission coincides with those reported in figure 9.32a. Indeed, maximizing η_g under certain electrical and thermal power demands consists in minimizing the fuel consumption from prime movers. On the other hand, the only differences which may arise between the two optimization procedures follow from

different emission factor of MDO and LNG burned by prime movers and from different amount of NO_x production within engines. However, small amount of MDO is used by DF engines (nearly 2% of the overall fuel consumption) and NO_x emissions are further lower than CO_2 ones. Therefore, maximizing η_g nearly coincides with minimizing $CO_{2,eq}$. Focusing on the NO_x minimization, 9.32c shows power distribution among prime movers provided by the optimization algorithm. As can be seen, results obtained from the minimization of NO_x production locally differ from those previously commented out for η_g and $CO_{2,eq}$ optimizations. Indeed, more dark green bars are reported in figure 9.32c during maneuvering condition, thus power is more frequently withdrawn from batteries with the aim of help COGES in these operating conditions. Consequently, more power is supplied by COGES to charge batteries during navigation ($\approx$ 3 MW). Where port conditions are concerned, no power is withdrawn from batteries and the entire electrical demand is covered by NG engines working at reduced loads. Instead, minimizing NO_x production avoids to discharge batteries in some port operating conditions in favour of NG engines. Indeed, comparing purple, pink and magenta areas from figures 9.32c and 9.32a, 9.32b it can be clearly seen how higher number of NG engines is turned on at berth, each one working at lower load. This mainly derives from the dependency of NO_x emissions from load in reciprocating engines, which shows maximum values at high fraction of MCR. Overall, to minimize NO_x production, energy management system replaces high load operating conditions for reciprocating engines with power withdrawn from batteries or reciprocating engines working at part-loads. The first strategy is applied during few maneuvering conditions, whereas the second one is pursued when the ship is at berth. Focusing the attention figure 9.32d, electrical power distribution over all the ship operating conditions is reported for cost optimization study. It must be underlined that carbon pricing is here included within OPEX cost computation. Comparing figure 9.32d with figures 9.32a and 9.32b, results from cost minimization appear quite similar to those obtained maximizing η_g and minimizing $CO_{2,eq}$. Indeed, charging mode for batteries is enabled while sailing on the routes Genoa-Civitavecchia, Civitavechia-Palermo and Barcelona-Genoa, as well as during arrival maneuvering to Genoa port. On the other hand, discharging mode for batteries is mainly performed during maneuvering and few port conditions. However, discharging phase occurring during port conditions at Palermo and La Valletta in figures 9.32a and 9.32b is replaced by power withdrawn from batteries during navigation on the Palermo-La Valletta route. This main difference appears to derive from quantitative comparison between OPEX cost generated by DF and NG engines with the actualized investment cost of batteries. Indeed, detailed insight can be gained focusing on the optimal sizing of battery pack achieved by all the four optimization procedures. Specifically, optimizing η_g, $CO_{2,eq}$ and NO_x identifies 40000 kWh capacity, i.e. 2000 batteries each

dealing with 20 kWh capacity, as the optimal size. Instead, cost minimization is reached by installing LI-ion batteries which overall provide slightly lower capacity (i.e. 37640 kWh). This different sizing appears to motivate variations shown in figure 9.32d in comparison to figures 9.32a and 9.32b. Interestingly, the larger the battery pack the higher the performance of power plant by an energetic and environmental point of views, since reduced emission and fuel consumption may be achieved. Therefore, η_g, $CO_{2,eq}$ and NO_x optimization all identify maximum capacity available from constraints as the optimal one. On the contrary, the price currently assumed by Li-ion batteries (i.e. 200 €/kWh) generates a minimum for costs at capacities slightly reduced with respect to the maximum size available in the problem. If further reduction of battery price is achieved in future as foreseen by major companies in the power generation sector, larger electrical energy storage systems will be economically feasible. Interestingly, results concerning EES sizing based on cost optimization appear well fitted with current projects financed by major shipowners to construct hybrid-electric cruise ships in the last few years [229]. Figure 9.33 reports results concerning LT and HT

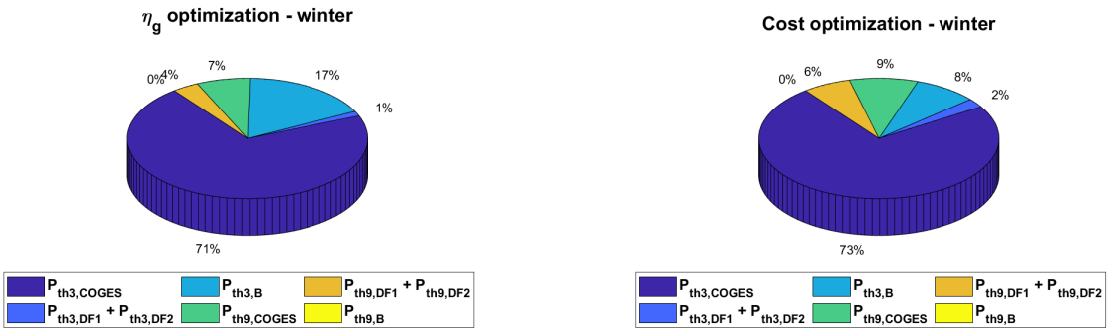

(a) (b)

Fig. 9.33 Cumulative LT and HT thermal power distribution for phase-mean analysis obtained from η_g (a) and cost (b) optimization studies, during winter season.

thermal powers delivered by prime movers to cover respective demands during winter season. Results are reported in cumulative form, i.e. summing LT and HT power delivered, and only η_g and cost optimizations are considered, for the sake of conciseness. For both the optimization processes considered, the LT power supplied by COGES nearly consists in 71-73% of the overall demand, whereas 8-17% is covered by auxiliary boilers producing steam at 3 bar. Instead, LT power provided by DF engines is around 1-2% due to the lower waste heat available within their exhaust gas in comparison to that from COGES (i.e. lower T_{ex} and $\dot{m}_{ex}$). Furthermore, as mentioned above, HT power production has priority against the LT one for DF engines, since WHR systems considered in this study generate steam

at 9 bar, whose excessive fraction is eventually laminated up to reach 3 bar. Focusing on figure 9.33, most of the HT demand is covered by the steam extraction from the ST included in COGES. On the other hand, DF engines approximately supply one-half of the request and no auxiliary boilers generating steam at 9 bar are required. Indeed, due to the small amount of the HT power request for laundry, galley and propulsion auxiliary, waste heat from prime movers succeeds in covering demand during all the ship operating conditions. Then,

Table 9.22 Objective function values obtained from all the optimization procedures considered, during the 8-days phase-mean profile. Analogous results computed for a reference power plant (Ref) without batteries installed are also reported for comparison.

CONFIGURATION		η_g	$CO_{2,eq}$ [t]	NO_x [t]	**Cost [k€]**	**Ref**
η_g **optimization**	**W**	**83.05**	**1792.8**	**3.090**	**549.22**	η_g **=81.8**
	S	**78.35**	**1760.8**	**1.991**	**534.72**	η_g **=77.2**
$CO_{2,eq}$ **optimization**	**W**	**83.05**	**1792.8**	**3.090**	**549.22**	$CO_{2,eq}$ **=1822.0**
	S	**78.35**	**1760.8**	**1.991**	**534.72**	$CO_{2,eq}$ **=1809.8**
NO_x **optimization**	**W**	**82.05**	**1808.6**	**2.920**	**552.32**	NO_x **=3.272**
	S	**78.04**	**1766.4**	**1.952**	**535.84**	NO_x **=2.762**
Cost optimization	**W**	**83.03**	**1793.1**	**3.082**	**549.12**	**Costs=549.22**
	S	**78.34**	**1761.0**	**1.966**	**534.41**	**Costs=538.71**

in order to assess differences in terms of cost functions, values assumed by the objective function in each optimization algorithm are reported in table 9.22. In details, values of η_g, $CO_{2,eq}$, NO_x and overall costs are computed for the Mediterranean cruise route reported in table 9.19, for both summer and winter seasons. Corresponding results obtained by the same optimization processes applied to candidate power plant dealing with no energy storage systems are additionally shown with the aim of identify pros and cons of batteries. It is well visible from table 9.22 how the maximum value for η_g and the minimum values for $CO_{2,eq}$, NO_x and costs are provided by the corresponding optimization procedures. Furthermore, as underlined above for power distribution, results from cogeneration efficiency optimization coincide with those obtained by minimizing $CO_{2,eq}$, since negligible variations are introduced by NO_x production and CO_2 emission factor of LNG and MDO. Overall, focusing on the η_g and $CO_{2,eq}$ values, results from all the optimization procedures differ for $\approx$ 1-2%, for fixed season. Indeed, similar size of battery pack is identified by all the analyses. On the other hand, stronger variations between the four optimization processes arise in terms of NO_x emissions, where nearly 6% maximum deviation is surveyed. Finally, where costs are concerned, a $\leq 2\%$ variation is achieved. Comparing results from the hybrid-electric power plants with those obtained not including batteries, drawbacks on all the four objective functions are provided in case energy storage system is avoided. Thus, benefits offered by

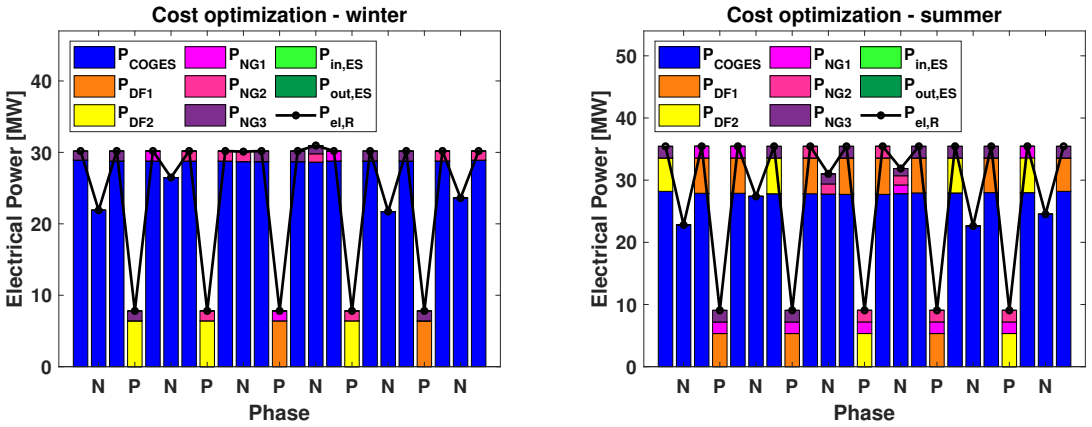

(a) (b)

Fig. 9.34 Electrical power distribution for phase-mean analysis obtained from cost optimization without carbon tax, for winter (a) and summer (b) seasons.

installing onboard Li-ion batteries are proved. Specifically, lower emissions and higher η_g are achieved since the energy management system can move power from/to batteries in a flexible and efficient way in all the ship operating conditions. Also benefits in terms of costs can be offered by hybrid-electric propulsion plant when carbon pricing exists. The role played by carbon pricing in improving the economic feasibility of battery inclusion onboard has been investigated by applying cost optimization algorithm without CO_2 taxation, in both summer and winter seasons. The corresponding results in terms of power distribution over prime movers are summarised in figure 9.34, where no charging/discharging power to/from batteries is visible. Indeed, comparison between figure 9.34 with figure 9.32d clearly shows that COGES plant, DF and NG engines are working at higher loads with the aim of covering the entire electrical demand with no contribute played by batteries. Thus, minimization of costs is achieved by not installing batteries onboard cruise ship. Therefore, with the current Li-ion battery price, carbon taxation appears necessary to improve their economical competitiveness with respect to the low costs provided by more mature technologies (i.e. COGES and reciprocating engines). For this reason, policies on carbon pricing for the maritime sector will be enacted in the early future in EU [56, 57, 55]. Overall, analysis carried out considering phase-mean power demand profiles shows benefits provided by Li-ion batteries by an energetic and environmental point of view, when installed on large cruise ships. Furthermore, the corresponding optimal capacity is identified at maximum limit considered in this work, i.e. 40000 kWh. Instead, slightly lower capacity (37640 kWh) is found to optimize costs. Since energy transition will introduce even more restrictive regulations in terms of emissions and energy savings, 40000 kWh is chosen as installed battery capacity onboard for the successive hourly-mean analyses. Furthermore, according to available battery price

reduction forecasts for 2020-2030 [302, 352, 353], economic feasibility of Li-ion batteries will be improved in this decade, hence increasingly higher sizes could be installed on cruise ships. Finally, the environmental impact of the newly proposed hybrid-electric power plant

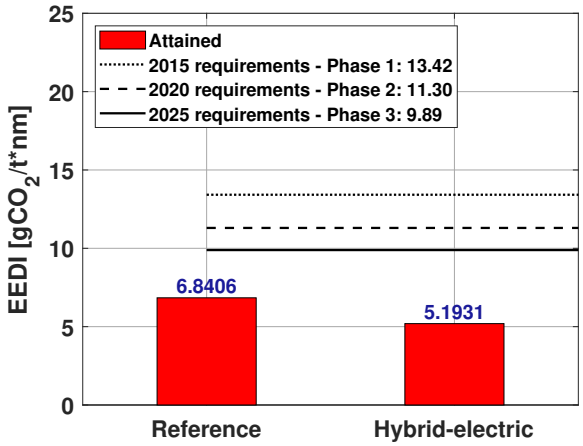

Fig. 9.35 Energy Efficiency Design Index (EEDI) computed for both reference power plant without any battery installed and hybrid-electric plant.

is investigated in figure 9.35 in terms of Energy Efficiency Design Index (EEDI). Results obtained from the power plant not including electrical energy storage systems are reported for comparison. EEDI required values for new cruise ships dealing with non conventional power plants are shown in black lines, for the three successive regulamentary phases introduced by IMO. As can be seen, both power plants comply with IMO regulations at 2025. Nevertheless, since hybrid-electric power plant offers further reduced EEDI, it appears more preferable in view of more restrictive regulations. Furthermore, EEDI value for power plant not without any battery pack installed onboard appears in agreement with previous works concerning highly efficient cruise ships [354].

9.4.3 Analysis on hourly power request profiles

In this section, the hourly mean power demand profiles shown in figures 9.29 and 9.30 above are considered in an optimization purpose. Specifically, the energetic, environmental and economic optimization algorithm previously used for phase-mean data are performed for a hybrid-electric power plant with 40000kWh Li-ion battery capacity installed. Optimization has been applied to an overall time extension of 48 hours to limit computational costs. Due to the reduced time interval considered within profiles, detailed insight on the energy management system governing strategy is possible. Figure 9.36 reports the electrical power

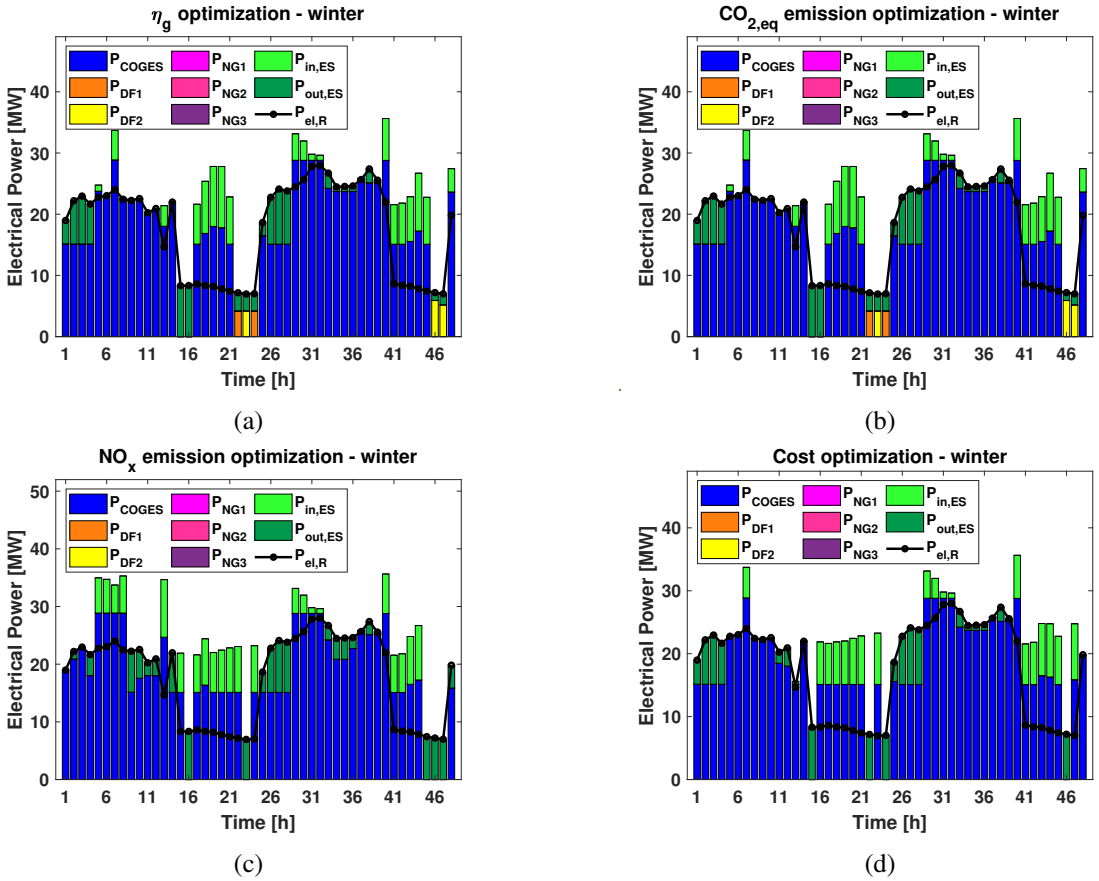

Fig. 9.36 Electrical power distribution for hourly demand analysis during winter season. Results are optimized for η_g (a), $CO_{2,eq}$ (b), NO_x (c) and costs (d).

distribution achieved in case of η_g (top left), $CO_{2,eq}$ (top right), NO_x (bottom left) and cost (bottom right) optimizations. Since results referring to summer are analogous, only winter season is shown for the sake of conciseness. Black, dotted line indicates electrical power demand, whereas the x-axis indicates time in hours. Focusing on results from the cogeneration efficiency optimization, nearly 8 MW of electrical power are discharged from batteries in the departure maneuvering from both Genoa and Civitavecchia ports. Analogous electrical power levels are required during the first stages of navigation on the Genoa-Civitavecchia and Civitavecchia-Palermo routes. Since COGES plant guarantees the highest efficiency among prime movers for $\geq$ 17MW power requests, it covers the rest of electrical power demand during maneuvering and navigation conditions. Interestingly, where cruise ship is at berth, energy management system turns on COGES plant for 50-65% of the time, differently from what observed in figure 9.36a. Since power request in port conditions is far lower than the minimum load available from COGES (i.e. 50%, corresponding to 16.51 MW), a portion of the power delivered by COGES at berth is used to charge batteries. The same

procedure is not performed through reciprocating engines, since lower efficiency would be gained during the charging process. The remaining part of electrical power demand at berth conditions is covered by batteries, coupled or not with DF engines. Overall, figure 9.36a shows how the energy management system decides for a mixed spinning-reserve and peak-shaving strategy to operate batteries, mainly coupled with COGES plant. Indeed, when the power demand is low, excess power is delivered by COGES to charge batteries and increase η_g. On the other hand, when the power demand is high or requires low values of energy exchanged, discharging mode for batteries is imposed. As result, peaks in power demand are locally shaved (see red circles in figure 10a), while COGES load is levelized moving energy from navigation to port operating conditions. Overall, comparing figure 9.36a with figure 9.32a, COGES plant is more frequently turned on in the hourly mean analysis. Indeed, COGES plant appears almost the only prime mover working over the 48 hours considered, within a η_g optimization strategy. On the contrary, energy management system turns on reciprocating engines only during port conditions, for less than 30% of the time spent at berth. This mainly derives from benefits provided by COGES in terms of efficiency when compared to reciprocating engines, which are further improved in case batteries are installed onboard. Moving to figure 9.36b, results from $CO_{2,eq}$ optimization coincide with those obtained maximizing η_g. Thus, also considering hourly mean power demand profiles, carbon dioxide emission minimization collapses on maximizing cogeneration efficiency. On the other hand, where only NO_x emissions are aimed to be minimized (see figure 9.36c), power distribution over prime movers locally differ from results reported in figures 9.36a and 9.36b, despite the mixed peak-shaving and spinning-reserve strategy is still implemented combining batteries with COGES plant. Energy management system keeps reciprocating engines turned off on over the entire 48 hours considered. Indeed, short time interval considered allows for a more flexible energy management, which prefers turning on COGES due to its far lower NO_x power specific emission in comparison to DF or NG engines (i.e. approximately 0.22 against 3.4 g/kWh). Specifically, COGES plant works coupled with batteries in charging or discharging mode over the entire port conditions. Focusing the attention on figure 9.36d, electrical power distribution obtained from cost optimization are reported. Similarly to what find out for NO_x minimization, energy management system avoids to turn on reciprocating engines during all the 48 hours considered. Indeed, mixed spinning-reserve and peak-shaving strategy is implemented to govern COGES coupled with charging/discharging batteries, over the entire time horizon considered. It must be underlined that carbon pricing is accounted for in this section and power plant configuration is fixed. Therefore, this result appears to mainly derive from detailed power demand profiles, which improve flexible decision making by the energy management system to minimize OPEX costs. In details, when low power

demands arise, excessive power delivered by COGES is moved to charge batteries, with benefits in terms of load and, consequently, efficiency. On the other hand, discharging mode for batteries is imposed when high or particularly low power demands are required. Thus, peak-shaving and spinning-reserve continue to constitute the main governing strategy.

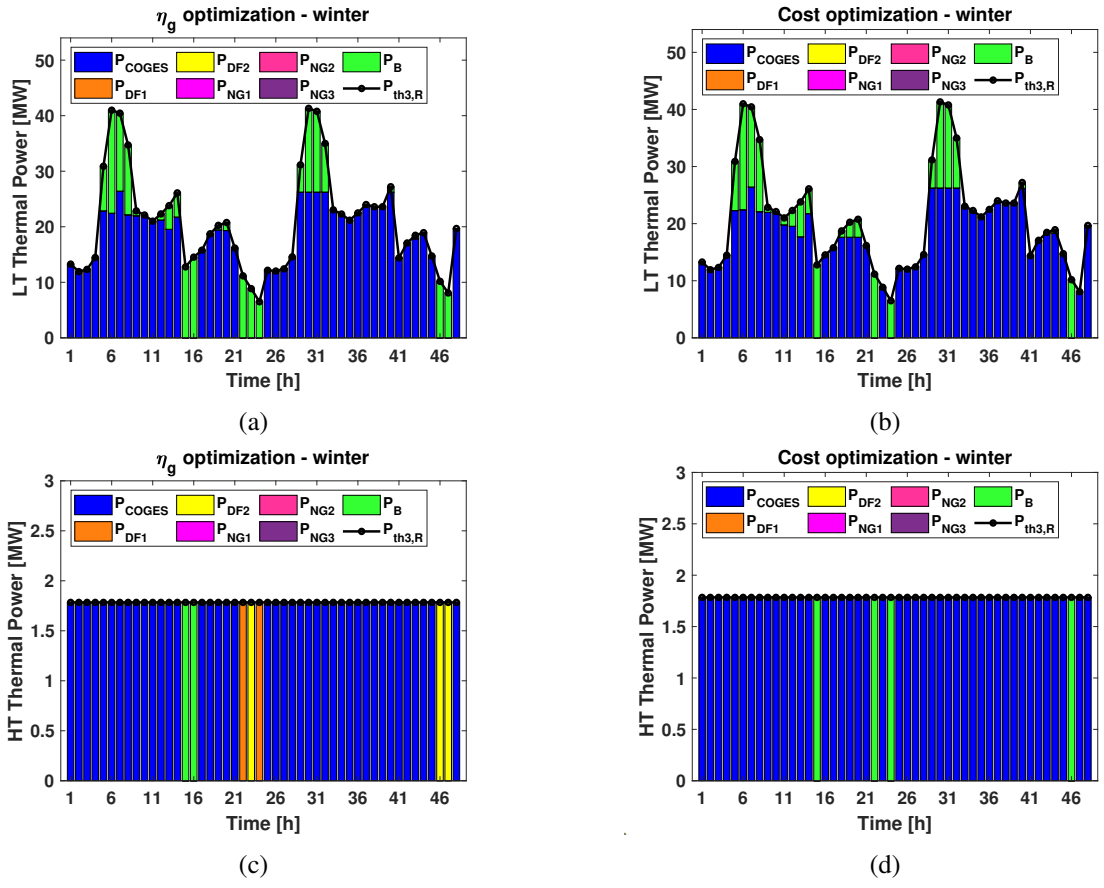

Fig. 9.37 LT (top row) and HT (bottom row) thermal power distributions for hourly demand analysis, obtained from η_g (a,c) and cost (b,d) optimization, for winter season.

Time-dependent results concerning LT and HT thermal power delivered by each prime mover to cover corresponding demands are reported in figure 9.37. Since analogous results can be achieved for summer, only winter season is considered for the sake of conciseness. As was for the phase-mean results, only cogeneration efficiency and cost optimization algorithm are considered. Focusing the attention on the LT thermal power, almost the 75-80% of the demand is supplied by COGES plant, whereas the remaining part is covered by auxiliary boilers producing steam at 3 bar. Looking at the peaks in power demand, waste heat recovery from COGES ensures base load, i.e. fraction of the profile dealing with low-amplitude fluctuations. On the other hand, working conditions for auxiliary boilers only occur in correspondence of the highest peaks at morning and evening, not covered by COGES. Where

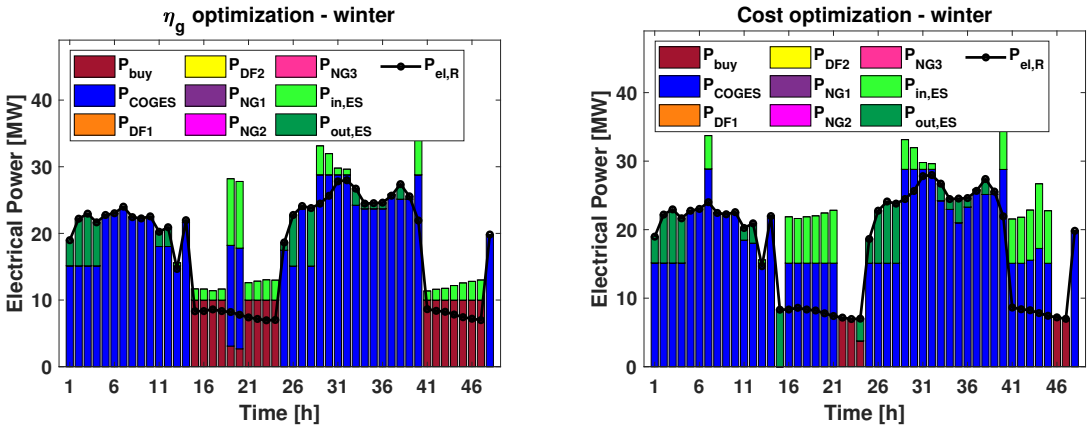

(a) (b)

Fig. 9.38 Electrical power distribution for hourly demand analysis considering cold ironing at berth, for winter season. Results are optimized for η_g (a) and costs (b).

DF engines are concerned, only few MWs of LT power are delivered during port condition, within the η_g optimization. Where the HT power is concerned (bottom row), constant demand has been assumed, as highlighted in section 9.4.1. Analogously to what observed for LT power, figures 9.37c and 9.37d clearly show how COGES plant covers almost the entire demand, independently from the optimization process considered. For reduced number of hours when DF engines are turned on at berth within η_g optimization, they succeed in covering the entire HT power demand. Instead, auxiliary boilers producing steam at 9 bar are needed to work in port conditions where only electric batteries are operating. Overall, the hourly mean analysis reported above further strengthens benefits of installing Li-ion batteries onboard cruise ships in terms of energetic, environmental and economic optimization. Specifically, coupling COGES with batteries in peak-shaving and spinning-reserve mode has been proved to represent the optimal governing strategy independently from the algorithm considered. Since cold ironing currently represents one of the most promising alternatives considered by port authorities to abate emissions while ships are stationing at berth. In case large penetration of renewables into the electric grid is available, further environmental benefits are gained. From now on, the feasibility of cold ironing and its effect on the hourly mean governing strategy for power plant onboard is investigated. Figure 9.38 shows electrical power distribution obtained by only the η_g and cost optimization algorithms, for winter season. As mentioned above, electricity price from harbour grid has been fixed to 0.065 €/kWh, according to Sweden and Spanish ports [355, 303–305]. Similarly to figure 9.36a, discharging mode for batteries occurs during the departure maneuvering at Genoa and Civitavecchia ports, as well as during the first stages of navigation over the Genoa-Civitavecchia and Civitavecchia-Palermo routes. However, reduced power is withdrawn from

the energy storage system during the Civitavecchia-Palermo route. Since cold ironing is used over the entire period at berth, energy management system keeps DF engines turned off during both port conditions. Interestingly, major part of the charging mode for batteries is supplied by electrical grid in harbour. Indeed, only reduced power is locally delivered by COGES plant to speed up charging of batteries, as well as to cover part of power demand at the Civitavecchia port. Consequently, the mixed peak-shaving and spinning-reserve strategy previously observed appears strongly influenced in case cold ironing is available at berth. Indeed, it only works during maneuvering and navigation conditions, since buying electricity from the grid avoids direct fuel consumption onboard, with cogeneration efficiency benefits for cruise ship. Analogous results can be obtained from the minimization of $CO_{2,eq}$ and NO_x emissions, hence thermodynamic and environmental benefits of cold ironing appear well established. Where the cost optimization is concerned, figure 9.38b shows how lower power from cold ironing is used when the ship is at berth. Indeed, similarly to what observed in figure 9.36d above, COGES plant covers again most of the power requested during port conditions as well as the charging mode of batteries, with energy efficiency benefits. This mainly derives from comparison between maintenance and fuel consumption costs arising in high load operating conditions from COGES and current cost of electricity for cold ironing. Specifically, electricity price for cold ironing still appears quite high to improve a widespread use of this technology. Instead, during highly demanding operating conditions, peak-shaving and spinning-reserve strategy continues to be adopted. Specifically, electrical power is withdrawn from batteries during the maneuvering and first stage of navigation departing from Genoa. When particularly low power demands are required, only batteries are working (see dark green areas in the Civitavecchia port). Overall, cold ironing for cruise ships is proved to provide benefits by an energetic and environmental point of view. Furthermore, the current electricity price available from the grid makes cold ironing competitive with low OPEX costs provided by COGES plant, despite its economical feasibility needs to be improved to spread it. Finally, peak-shaving and spinning-reserve continue to constitute the optimal energy management strategy independently from the objective function considered.

9.4.4 Main findings

In the sections above, the performances provided by a hybrid-electric power plant installed onboard large-size cruise ships have been investigated under an energetic, environmental and economic point of view through a Mixed-Integer Linear Programming code. Specifically, maximization of η_g and minimization of $CO_{2,eq}$, NO_x and costs are assessed. Firstly, the phase-mean electrical and thermal power requests have been considered, for both summer

and winter seasons. Most of both electrical and thermal power demands onboard during navigation and maneuvering was shown to be covered by COGES, independently from the objective function considered. On the other hand, reciprocating engines were turned on to cover reduced power request during port activities. In this framework, discharging mode from Li-ion batteries mainly occurred at maneuvering and port, where 3-10 MW and 2 MW are delivered, respectively. On the other hand, energy is stored into batteries during navigation. Since negligible effect is played by differences on fuel and NO_x emissions, results from the $CO_{2,eq}$ optimization procedure coincided with those from η_g maximization. Overall, for both η_g and $CO_{2,eq}$ algorithm, charging and discharging modes for the energy storage system are positioned in correspondence of ship operating conditions dealing with high and low loads (i.e. efficiencies) from prime movers, respectively. Therefore, batteries are shown to increase cogeneration efficiency both during charging and discharging phase. Similar strategy arise for the NO_x and cost optimizations, with only few differences. Specifically, minimization of nitrogen oxide emissions imposed load working conditions characterized by part-loads for reciprocating engines, whereas comparison between OPEX costs and battery investment costs drove the costs minimization. Benefits provided by energy storage in terms of η_g, $CO_{2,eq}$, NO_x emissions and costs were underlined, despite economical feasibility of Li-ion batteries currently needs carbon pricing. Overall, optimal sizing of battery pack at 40000 kWh capacity was found within η_g, $CO_{2,eq}$ and NO_x optimization, whereas slightly lower value was identified by economic analysis. This result appear well in agreement with battery capacities recently installed onboard new cruise ships. Secondly, the same optimization algorithms have been applied to hourly mean demand profiles, on an 48 hours horizon, in order to assess energy management strategy in details. Overall, the potential of combining COGES with batteries has been shown. Indeed, independently from the optimization algorithm, almost the entire amount of power demands over the 48 hours was covered by COGES coupled with charging/discharging batteries. Specifically, in case power demand is low (i.e. at berth), COGES delivers excess power to charge batteries, with benefits in terms of working loads and efficiencies. On the other hand, when the power demand is high (i.e. maneuvering and navigation) or particularly low (i.e. rest of port conditions) batteries operate in discharging mode. Thus, batteries are operated with a mixed spinning-reserve and peak-shaving strategy in combination with COGES. Instead, reciprocating engine are turned on for 30% of time spent at berth, where the η_g and $CO_{2,eq}$ optimization processes are considered. When cold ironing is available from the port, significant portion of the power demand at berth is covered by electricity withdrawn from the grid, especially in case energetic or environmental optimization is performed. However, the mixed peak-shaving and spinning-reserve operating mode for COGES and batteries continues to remain the main

energy management strategy, despite few differences. Overall, installing batteries onboard cruise ships is proved to enable more flexible energy management strategy, with significant benefits on energetic, environmental and economic point of views. Thus, it can effectively contribute to energy transition within the maritime sector.

Chapter 10

Conclusion

In this thesis, innovative ship power plant configurations enabling the energy transition in the maritime sector have been investigated. The studies have been focused on the two main pathways which are currently receiving major attention by the scientific community to limit the climate change. First, in a short-term perspective, a more efficient energy utilisation onboard ships is to be implemented by either waste heat recovery technologies and engine room operating condition optimization. Second, innovative and greener solutions able to drastically abate GHG and pollutant emissions from the maritime sector appear necessary in a long-term energy transition scenario. Analyses have been carried out by means of various codes and optimization tools developed in Fortran and MATLAB/Simulink languages. Specifically, quasi-static, dynamical and Mixed-Integer Linear Programming (MILP) models have been implemented to simulate design, off-design and transient performances of ship power plants. Furthermore, gradient-descent, Multi-Objective Genetic Algorithms (MOGA), full-factorial and linear programming optimization tools have been set up to assess optimal power plant design and operating conditions. The viability of innovative ship power plants has been investigated under energetic, economic and environmental point of views, in order to provide complete insight on the major solutions available in a short-, mid- and long-term energy transition scenario. Computations have been performed focusing on modern cruise-ferries and large-size cruise ships.

In section 9.1, the feasibility of a LNG-fuelled, integrated COGES-reciprocating engine repowering plant for the cruise-ferry GNV La Suprema has been investigated by energetic, environmental and economic point of views. According to GNV shipowner requests, the goal was to define highly efficient propulsion plants for Mediterranean cruise-ferries operating under extremely flexible ship speed conditions (16-26 knots). Focusing on the energy optimization analysis, results proved the potential of integrating COGES with small-size

reciprocating engines for marine propulsion applications. In details, all the analysed COGES plants revealed to guarantee maximum cogeneration efficiency within the medium-high ship speed range centered around the current sailing condition for La Suprema. Among all the COGES plants tested, the highest energy savings were obtained including the GE25.1 gas turbine within the engine room. On the other hand, utilising steam generated by the WHR systems of DF engines to produce additional electrical power showed reduced gains, due to the low-quality of thermal power recovered. By an environmental point of view, substituting large-size DF engines with COGES plants was shown to guarantee long-term compliance with EEDI requirements for new-built ships. In details, the minimum CO_2 emissions resulted from the power plant including the GE25.1-based COGES plant, with further benefits equipping DF engine WHR systems with steam turbine. Finally, including COGES plants within the engine room onboard La Suprema resulted economically competitive with respect to pure DF engine configurations, with maximum cost savings obtained by the GE25.1-based architecture. On the other hand, energy production from the WHR system of DF engines appears economically inadequate within a short-term horizon. Thus, combining GE25.1-based COGES plant with small-size 9LMAN reciprocating engines resulted the optimal repowering configuration under energetic, environmental and economic perspectives for La Suprema.

Then, in section 9.2, the repowering study for the cruise-ferry GNV La Suprema was deepened. Specifically, a wider range of GT size available in COGES architectures and dynamical performances of 6 different COGES plants under actual time-dependent sailing conditions have been analysed. In order to assess the sensitivity of GT performances to the governing strategy, both turbine inlet temperature (TITc) and turbine outlet temperature (TOTc) controls have been investigated. Overall, nominal values provided by the MOGA-gradient descent optimizer appeared accurate (within 1% error with respect to reference data) and physically-based transient response has been surveyed for the main thermodynamic parameters. Specifically, TITc and TOTc control strategies managed to keep constant their target temperatures up to 70% and 30% GT loads, respectively, with consequent benefits by an energetic point of view for the ship power plant. Similarly to what found in section 9.1 for static performances, the cogeneration efficiency optimization procedure proved that energy savings were maximized by turning on COGES plants in the medium to high ship speed range (19-26 knots). Particularly, a 1-5% higher cogeneration efficiency was guaranteed by COGES plants with respect to DF engines. Among the gas-steam combined plants tested, those based on the SGT600 and RB211 GTs revealed 2-3% lower cogeneration efficiency, owing to reduced η_{el} and exhaust thermal power related to gas turbines. On the other hand, COGES plants based on large-size GTs (LM2500+ and LM2500+G4) efficiently covered propulsion

and hotel loads within the high ship speed range for La Suprema, whereas energy penalties arise for low-medium V_{ship} due to part-loads. Overall, optimal energetic performances have been obtained by engine rooms coupling LM2500-/TITAN250-based COGES plants with small size reciprocating engines, with a 51% maximum cogeneration efficiency. In details, combining small-size reciprocating engines with LM2500-based COGES plant appeared to provide higher efficiencies on a wide ship speed range, hence resulting more suitable for a flexible operation of La Suprema. Furthermore, a more efficient energy utilisation was achieved by the TOTc governing strategy, which also limited off-design working conditions for the bottoming steam power plant. In this way, the optimally designed HRSG resulted to efficiently recovered waste heat also at GT part-loads. Specifically, the TOTc controller ensured a ± 0.5 °C on the exhaust temperature from GT during actual navigation conditions for La Suprema. Overall, the dynamic simulation of the current ship operating conditions confirmed high performances reliably provided by COGES plants.

Successively, the potential and challenges offered by alternative fuels for the energy transition in the maritime sector have been investigated in section 9.3, referring to modern large-size cruise ships. Specifically, energetic, environmental and economic performances provided by three different integrated COGES-reciprocating engines power plants have been sequentially analysed under CH_3OH, NH_3 and $CH_4 - H_2$ blend feeding conditions. Independently from the fuel and route considered, power plant cogeneration efficiency was optimized by COGES plants during most of the maneuvering and navigation conditions, while reduced additional power was eventually provided by reciprocating engines. Only when the vessel was at berth or sailing at reduced ship speed within Norwegian fjords, small-size reciprocating engines played relevant role in covering power demands. Overall, the configuration including TITAN250-based COGES plant guaranteed the highest energy savings over most of the routes and seasons, while few benefits were achieved the LM2500-based solution. On the other hand, where the energetic performance obtained by alternative fuels is concerned, the highest cogeneration efficiencies have been obtained by $CH_4 - H_2$ blends. This appears to mainly derive from the effect played by the fuel on thermodynamic performances of prime movers together with positive/negative influence on power demand matching. Then, the environmental analysis have been carried out in terms of $CO_{2,eq}$ emissions, EEDI and CII. Owing to its chemical composition, the minimum GHG emissions have been obtained by NH_3-fed power plants, despite higher NO_x concentrations imposed SCR utilisation. Thus, long-term compliance with EEDI and CII limits was guaranteed. On the other hand, $CH_4 - H_2$ fed power plants resulted able to cope with EEDI regulations, while C rating for CII resulted maintained up to 2050. Instead, where CH_3OH-fed configurations are concerned, compliance with EEDI and CII regulations vanishes at 2025 and 2031, respectively. Therefore, either NH_3

and $CH_4 - H_2$ blends appear suitable for energy transition in a long-term perspective with further benefits for higher H_2 contents, whereas methanol results relevant only for a short-term strategy. Where economic viability is concerned, combining TITAN250-based COGES plant with small-size reciprocating engines resulted to provide the highest cost savings over 25 years time horizon, thanks to its benefits on cogeneration efficiency. Comparable costs from NH_3- and CH_3OH-fed configurations have been shown, whereas fuel price for green H_2 is proved to significantly increase OPEX costs. However, renewables spreading aimed at energy transition in the power generation field is expected to improve economic viability of $CH_4 - H_2$ blends. Overall, power configurations based on combining small-size reciprocating engines with COGES plants appeared promising technology for GHGs abatement and efficient energy utilisation in large-size cruise ships, both in short- and long-term perspectives.

Finally, section 9.4 investigated LNG-fuelled hydrid-electric power plants installed onboard large-size cruise ships, implementing energetic, environmental and economic optimization under various energy management strategies. Phase-mean as well as hourly electrical and thermal power demands have been successively analysed to investigate the effect of schedule discretization on performances. First, when phase-mean profiles were accounted for, the COGES plant was shown to optimize objective functions during navigation and maneuvering, while reciprocating engines supplied power for port activities. Overall, optimal sizing of battery pack at 40000 kWh capacity was found, in agreement with recent installation onboard new cruise ships. Additional 3-10 MW and 2 MW electrical power was shown to be withdrawn from batteries during maneuvering and port conditions, whereas charging mode mainly occurred during navigation. Specifically, where η_g and $CO_{2,eq}$ optimization are concerned, charging and discharging modes for the energy storage system were optimally positioned in correspondence of ship operating conditions dealing with high and low loads (i.e. efficiencies) from prime movers, respectively. Thus, batteries helped to increase cogeneration efficiency both during charging and discharging phases. Instead, NO_x minimization imposed part-load working conditions to reciprocating engines, whereas economical viability of batteries was shown to deeply depend on carbon pricing to recover their investment costs. Second, optimization algorithms applied to hourly power demand profiles revealed the potential of combining COGES plants with batteries. Indeed, almost the entire amount of power demands was covered by COGES coupled with batteries operating on a mixed spinning-reserve and peak-shaving strategy, independently from the objective function considered. Specifically, in case power demand is low (i.e. at berth), COGES delivers excess power to charge batteries, with benefits in terms of working loads and efficiencies. On the other hand, when the power demand is high (i.e. maneuvering and navigation) or particularly low (i.e.

rest of port conditions) batteries operate in discharging mode. Reciprocating engine are rarely turned on at berth. When cold ironing availability is considered, the mixed peak-shaving and spinning-reserve operating mode for COGES and batteries continues to remain the main energy management strategy, despite significant portion of the power demand at berth is covered by electricity withdrawn from the grid. Overall, installing batteries onboard cruise ships has been proved to currently enable more flexible energy management strategy, with significant benefits on energetic, environmental and economic point of views. Thus, it can effectively contribute to energy transition within the maritime sector.

References

[1] Bjørn Louis Stranden. The aftermath: sulphur emission control areas impact on ship owners. Master's thesis, Høgskolen i Molde-Vitenskapelig høgskole i logistikk, 2016.

[2] https://www.dnv.com/maritime/insights/topics/CII-carbon-intensity-indicator/index.html.

[3] https://www.napa.fi/how-to-navigate-cii-what-it-is-and-how-you-can-stay-compliant/.

[4] https://www.shipsnostalgia.com/media/city-of-oporto.99862/.

[5] https://skipshistorie.net/Bergen/BRG522Rekstenrederiene/Tekster/.

[6] Renato Della Volpe. *Impianti motori per la propulsione navale*. Liguori Editore Srl, 2007.

[7] https://www.ferries.gr/it/ferry-companies/seajets/fleet/championjet2/.

[8] https://www.geaerospace.com/propulsion/marine/lm2500.

[9] A. Eykerman. Optimize flng powering solution. In *Wartsila Corporation*, 2011.

[10] https://www.analisidifesa.it/2021/03/.

[11] https://www.marina.difesa.it/noi-siamo-la-marina/mezzi/forze-navali/Pagine/Garibaldi.aspx.

[12] Monique B Vermeire. Everything you need to know about marine fuels. *Published by Chevron Global Marine Products*, 2012.

[13] https://www.iso.org/standard/64247.html.

[14] Salvatore Marrone, Andrea Colagrossi, J. S. Park, and Emilio Fortunato Campana. Challenges on the numerical prediction of slamming loads on lng tank insulation panels. *Ocean Engineering*, 141:512–530, 2017.

[15] https://valve-world-americas.com/.

[16] https://safety4sea.com/wp-content/uploads/2014/09/4.1_Raffaele_Piciocchi_ABS.pdf.

[17] https://safety4sea.com/dnv-gl-approves-khis-new-non-spherical-lng-tank/.

[18] https://www.maritimeprofessional.com/news/.

[19] Young-Gyu Lee, Jong-Kwan Kim, and Chang-Hee Lee. Analytic hierarchy process analysis for industrial application of lng bunkering: A comparison of japan and south korea. *Energies*, 14(10):2965, 2021.

[20] https://www.rivieramm.com/news-content-hub/news-content-hub/.

[21] Laurens Van Hoecke, Ludovic Laffineur, Roy Campe, Patrice Perreault, Sammy W Verbruggen, and Silvia Lenaerts. Challenges in the use of hydrogen for maritime applications. *Energy & Environmental Science*, 14(2):815–843, 2021.

[22] https://www.energy.gov/eere/fuelcells/hydrogen-storage.

[23] Byongug Jeong, Hayoung Jang, Wookjae Lee, Chybyung Park, Seungman Ha, Nak-Kyun Cho, et al. Is electric battery propulsion for ships truly the lifecycle energy solution for marine environmental protection as a whole? *Journal of Cleaner Production*, 355:131756, 2022.

[24] Xing Luo, Jihong Wang, Mark Dooner, and Jonathan Clarke. Overview of current development in electrical energy storage technologies and the application potential in power system operation. *Applied energy*, 137:511–536, 2015.

[25] Shengsheng Yin, Leping Zhou, Xiaoze Du, and Yongping Yang. Influence of temperature on performance of all vanadium redox flow battery: analysis of ionic mass transfer. *Ionics*, 25:593–606, 2018.

[26] Alberto Traverso. Transeo code for the dynamic performance simulation of micro gas turbine cycles. 2005.

[27] Jeongseog Oh, Minki Kim, and Y. Yoon. The tuning methodology of a ge 7fa + e dln-2.6 gas turbine combustor. *Applied Thermal Engineering*, 36:14–20, 2012.

[28] L.B. Davis and S.H. Black. Dry low nox combustion systems for ge heavy-duty gas turbines. *GE Power Systems Schenectady, NY, GER-3568G*.

[29] https://www.ge.com/steam-power/products/steam-turbines/.

[30] https://www.triveniturbines.com/.

[31] Francesco Baldi, Fredrik Ahlgren, Tuong-Van Nguyen, Marcus Thern, and Karin Andersson. Energy and exergy analysis of a cruise ship. *Energies*, 11:2508, 2018.

[32] Paola Gualeni, Alessandro Boveri, Federico Silvestro, and Aida Margarita. Decision support system for power generation management for an 110000+ grt cruise ship. *International Journal of Maritime Engineering*, 2016.

[33] Saeid Mokhatab, John Y Mak, Jaleel Valappil, and David A Wood. *Handbook of liquefied natural gas*. Gulf Professional Publishing, 2013.

[34] Kaveh Mazloomi and Chandima Gomes. Hydrogen as an energy carrier: Prospects and challenges. *Renewable & Sustainable Energy Reviews*, 16:3024–3033, 2012.

[35] https://www.rina.org/en/alternative-fuels.

[36] George Mallouppas and Elias Ar. Yfantis. Decarbonization in shipping industry: A review of research, technology development, and innovation proposals. *Journal of Marine Science and Engineering*, 2021.

[37] Lars O Nord and Rubén M Montañés. Compact steam bottoming cycles: Model validation with plant data and evaluation of control strategies for fast load changes. *Applied Thermal Engineering*, 142:334–345, 2018.

[38] TWP Smith, JP Jalkanen, BA Anderson, JJ Corbett, J Faber, S Hanayama, E O'keeffe, S Parker, L Johansson, L Aldous, et al. Third imo greenhouse gas study 2014. 2015.

[39] James J Corbett, James J Winebrake, Erin H Green, Prasad Kasibhatla, Veronika Eyring, and Axel Lauer. Mortality from ship emissions: a global assessment. *Environmental science & technology*, 41(24):8512–8518, 2007.

[40] M Goedkoop, R Heijungs, M Huijbregts, A De Schryver, JVZR Struijs, and R Van Zelm. A life cycle impact assessment method which comprises harmonized category indicators at the midpoint and the endpoint level. *The Hague, Ministry of VROM. ReCiPe.,*, 2009.

[41] Equasis Statistics. The world merchant fleet-statistics from equasis. *Report. URL https://www.emsa.europa.eu/equasis-statistics.html*, 2015.

[42] Michael D Kass, Zia Abdullah, Mary J Biddy, Corinne Drennan, Zia Haq, Troy Hawkins, Susanne Jones, Jonathan Holliday, Douglas E Longman, Seth Menter, et al. Understanding the opportunities of biofuels for marine shipping. Technical report, Oak Ridge National Lab.(ORNL), Oak Ridge, TN (United States), 2018.

[43] Sulaman Muhammad and Xingle Long. China's seaborne oil import and shipping emissions: The prospect of belt and road initiative. *Marine pollution bulletin*, 158:111422, 2020.

[44] Paul Balcombe, James Alan Brierley, C. Lewis, Line Skatvedt, Jamie F Speirs, Adam D. Hawkes, and Iain Staffell. How to decarbonise international shipping: Options for fuels, technologies and policies. *Energy Conversion and Management*, 2019.

[45] Hui Xing, Stephen Spence, and Hua Chen. A comprehensive review on countermeasures for co2 emissions from ships. *Renewable and Sustainable Energy Reviews*, 134:110222, 2020.

[46] IMO. International convention for the prevention of pollution from ships (marpol) annex VI. 2011.

[47] https://www.imo.org/en/OurWork/Environment/Pages/AirPollution-Default.aspx.

[48] Gerasimos Theotokatos and George Livanos. Techno-economical analysis of single pressure exhaust gas waste heat recovery systems in marine propulsion plants. *Proceedings of the Institution of Mechanical Engineers, Part M: Journal of Engineering for the Maritime Environment*, 227(2):83–97, 2013.

[49] Ulrik Larsen, Oskar Sigthorsson, and Fredrik Haglind. A comparison of advanced heat recovery power cycles in a combined cycle for large ships. *Energy*, 74:260–268, 2014.

[50] https://wwwcdn.imo.org/localresources/en/OurWork/Environment/Documents/Resolution%20MEPC.304%2872%29_E.pdf.

[51] Conor Walsh, Sarah Mander, and Alice Larkin. Charting a low carbon future for shipping: A uk perspective. *Marine Policy*, 82:32–40, 2017.

[52] Espen Skjong, Tor Arne Johansen, Marta Molinas, and Asgeir J Sørensen. Approaches to economic energy management in diesel–electric marine vessels. *IEEE Transactions on Transportation Electrification*, 3(1):22–35, 2017.

[53] https://www.lr.org/en/carbon-intensity-indicator/.

[54] CE Delft and Directorate-General for Climate Action (European Commission). Study on methods and considerations for the determination of greenhouse gas emission reduction targets for international shipping, 2019.

[55] https://ec.europa.eu/clima/eu-action/eu-emissions-trading-system-eu-ets_it?wt-search=yes.

[56] https://ec.europa.eu/clima/eu-action/eu-emissions-trading-system-eu-ets_it.

[57] https://ec.europa.eu/commission/presscorner/detail/en/qanda_21_3662.

[58] https://ec.europa.eu/info/strategy/priorities-2019-2024/european-green-deal/climate-action-and-green-deal_en.

[59] https://sustainableworldports.org/wp-content/uploads/DNV-GL_2019_Comparison-of-alternative-marine-fuelsreport.pdf.

[60] L. Smith, H. Karim, S. Etemad, and William C. Pfefferle. The gas turbine handbook. 2006.

[61] https://energy.ec.europa.eu/topics/oil-gas-and-coal/liquefied-natural-gas_en.

[62] S. Horvath, M. Fasihi, and C. Breyer. Techno-economic analysis of a decarbonized shipping sector: Technology suggestions for a fleet in 2030 and 2040. *Energy Conversion and Management*, 164:230–241, 2018.

[63] Levent Bilgili. Comparative assessment of alternative marine fuels in life cycle perspective. *Renewable and Sustainable Energy Reviews*, 144:110985, 2021.

[64] Omer Berkehan Inal, Burak Zincir, and Cengiz Deniz. Hydrogen and ammonia for the decarbonization of shipping. In *5th international hydrogen technologies congress (IHTEC-2021)*, pages 26–28, 2021.

[65] Meng-Choung Chiong, Hooi-Siang Kang, Nik Mohd Ridzuan Shaharuddin, Shabudin Mat, Lee Kee Quen, Ki-Hong Ten, and Muk Chen Ong. Challenges and opportunities of marine propulsion with alternative fuels. *Renewable and Sustainable Energy Reviews*, 149:111397, 2021.

[66] Nacera Bennabi, JF Charpentier, H Menana, Jean-Yves Billard, and P Genet. Hybrid propulsion systems for small ships: Context and challenges. In *2016 XXII International Conference on Electrical Machines (ICEM)*, pages 2948–2954, 2016.

[67] Valerio Ruggiero. Impact of hybrid propulsion on the project of small passenger ferries for italian scenario. In *Nautical and Maritime Culture, from the Past to the Future*, pages 191–201. IOS Press, 2019.

[68] F Mauro, U la Monaca, C Nasso, and V Bucci. An hybrid-electric solution for station-keeping and propulsion of a small coastal research vessel. In *2018 International Symposium on Power Electronics, Electrical Drives, Automation and Motion (SPEEDAM)*, pages 607–612. IEEE, 2018.

[69] Alba Martínez-López, Alejandro Romero-Filgueira, and Manuel Chica. Specific environmental charges to boost cold ironing use in the european short sea shipping. *Transportation Research Part D: Transport and Environment*, 94:102775, 2021.

[70] https://eur-lex.europa.eu/legal-content/EN/TXT/PDF/?uri=CELEX:32014L0094&from=EN.

[71] M. Altosole, M. Figari, M. Viviani, S. Michetti, and A. Trapani. Simulation of the dynamic behaviour of a codlag propulsion plant. pages 109–115, 2010.

[72] M. Altosole, G. Benvenuto, M. Figari, U. Campora, A. Bagnasco, S. D'Arco, M. Giuliano, V. Giuffra, A. Spadoni, A. Zanichelli, S. Michetti, and M. Ratto. Real time simulation of the propulsion plant dynamic behaviour of the aircraft carrier "cavour". 2008.

[73] Tony Giampaolo. *Gas turbine handbook: principles and practice*. River Publishers, 2020.

[74] C. A. Merz and T. J. Pakula. The design and operational characteristics of a combined cycle marine powerplant. volume ASME 1972 International Gas Turbine and Fluids Engineering Conference and Products Show of *Turbo Expo: Power for Land, Sea, and Air*, 1972.

[75] D. Barsi, C. Costa, F. Satta, P. Zunino, Adriano Busi, R. Ghio, C. Raffaeli, and A. Sabattini. Design of a mini combined heat and power cycle for naval applications. *Journal of Sustainable Development of Energy, Water and Environment Systems*, 8:281–292, 2020.

[76] D. Barsi, M. Luzzi, F. Satta, and P. Zunino. On the possible introduction of mini gas turbine cycles onboard ships for heat and power generation. *Energies*, 14(3), 568:1–12, 2021.

[77] Fredrik Haglind. Variable geometry gas turbines for improving the part-load performance of marine combined cycles - gas turbine performance. *Energy*, 35:562–570, 2010.

[78] https://www.fincantieri.com/it/prodotti-servizi/sistemi-componenti/turbine/.

[79] https://www.gard.no/web/updates/content/20736191/marine-diesel-engines-a-bluffers-guide.

[80] IMO. Resolution mepc.212(63) guidelines on the method of calculation of the attained energy efficiency design index (eedi) for new ships. *MEPC 63/23, London: International Maritime Organization*, 2012.

[81] https://imorules.com/MEPCRES_339.76.html.

[82] Fabio Burel, Rodolfo Taccani, and Nicola Zuliani. Improving sustainability of maritime transport through utilization of liquefied natural gas (lng) for propulsion. *Energy*, 57:412–420, 2013.

[83] Nikoletta L. Trivyza, Athanasios Rentizelas, and Gerasimos Theotokatos. A novel multi-objective decision support method for ship energy systems synthesis to enhance sustainability. *Energy Conversion and Management*, 168:128–149, 2018.

[84] D.F. Woodyard. Gas-diesel and dual-fuel engines. In *Pounder's marine diesel engines and gas turbines. 8th ed.*, pages 48–63, June 2004.

[85] M. Altosole, U. Campora, and S. Savio. Improvements of the ship energy efficiency by a steam powered turbogenerator in lng propulsion applications. *IEEE*, pages 449–455, 2018.

[86] Cheng Huang, Qingyao Hu, Hanyu Wang, Liping Qiao, Hongli Wang, Min Zhou, Shuhui Zhu, Yingge Ma, Shengrong Lou, Li Li, et al. Emission factors of particulate and gaseous compounds from a large cargo vessel operated under real-world conditions. *Environmental Pollution*, 242:667–674, 2018.

[87] Fan Zhang, Yingjun Chen, Chongguo Tian, Diming Lou, Jun Li, Gan Zhang, and Volker Matthias. Emission factors for gaseous and particulate pollutants from offshore diesel engine vessels in china. *Atmospheric Chemistry and Physics*, 16(10):6319–6334, 2016.

[88] Minjiang Zhao, Yan Zhang, Weichun Ma, Qingyan Fu, Xin Yang, Chunlei Li, Bin Zhou, Qi Yu, and Limin Chen. Characteristics and ship traffic source identification of air pollutants in china's largest port. *Atmospheric environment*, 64:277–286, 2013.

[89] O Sippula, B Stengel, M Sklorz, T Streibel, R Rabe, J Orasche, J Lintelmann, B Michalke, G Abbaszade, C Radischat, et al. Particle emissions from a marine engine: chemical composition and aromatic emission profiles under various operating conditions. *Environmental science & technology*, 48(19):11721–11729, 2014.

[90] Thorsten Streibel, Jürgen Schnelle-Kreis, Hendryk Czech, Horst Harndorf, Gert Jakobi, Jorma Jokiniemi, Erwin Karg, Jutta Lintelmann, Georg Matuschek, Bernhard Michalke, et al. Aerosol emissions of a ship diesel engine operated with diesel fuel or heavy fuel oil. *Environmental Science and Pollution Research*, 24(12):10976–10991, 2017.

[91] Michelle Michot Foss, F Delano, G Gulen, and R Makaryan. Lng safety and security. *Center for Energy Economics (CEE)*, 2003.

[92] Chen Dong, Qulan Zhou, Xiaoguang Zhang, Qinxin Zhao, Tongmo Xu, and Shi'en Hui. Experimental study on the laminar flame speed of hydrogen/natural gas/air mixtures. *Frontiers of Chemical Engineering in China*, 4(4):417–422, 2010.

[93] F.J. Lukman. The application of dual-fuel technology in inland waterway tankers. 2012.

[94] https://sweden.man-es.com/products/cryo.

[95] Gerd-Michael Wursig. Lng fuel tank, benefits and challenges. In *Tekna presentation, DNV*, June 2013.

[96] Pierre Sames. Costs and benefits of lng as a ship fuel for container vessels. In *Technical report, Germanischer Lloyd*, 2011.

[97] Miltiadis Kalikatzarakis, Gerasimos Theotokatos, Andrea Coraddu, Paul Sayan, and Seng Yew Wong. Model based analysis of the boil-off gas management and control for lng fuelled vessels. *Energy*, 251:123872, 2022.

[98] Mario Miana, Rafael Del Hoyo, Vega Rodrigálvarez, José Ramón Valdés, and Raúl Llorens. Calculation models for prediction of liquefied natural gas (lng) ageing during ship transportation. *Applied Energy*, 87(5):1687–1700, 2010.

[99] PerMagne Einang. The norwegian lng ferry. In *Natural Gas Vehicle*, 2000.

[100] Aesoy V., Einang P., Stenersen D., Hennie E., and Valberg I. Lng-fuelled engines and fuel systems for medium-speed engines in maritime applications. *JSAE*, 2011.

[101] Burel F., Taccani R., and Zulian N. Improving sustainability of maritime transport through utilization of liquefied natural gas (lng) for propulsion. *Energy*, 57:412–420, 2013.

[102] George Teriakidis. Lng as fuel - recent development. In *Technical report, DNVGL*, February 2014.

[103] https://sea-lng.org/why-lng/global-fleet/.

[104] https://ec.europa.eu/commission/presscorner/detail/en/ip_20_1833.

[105] https://www.bioenergy-news.com/news/.

[106] https://www.gasum.com/en/About-gasum/for-the-media/News/2020/ssab-raahes-steel-plant-is-testing-biogas-from-gasum-as-a-maritime-transport-fuel/.

[107] M. Tuner. Methanol as an engine fuel and as an energy storage. In *MOT-2030 Workshop. Lund University*, 2015.

[108] Selma Brynolf, Erik Fridell, and Karin Andersson. Environmental assessment of marine fuels: liquefied natural gas, liquefied biogas, methanol and bio-methanol. *Journal of Cleaner Production*, 74:86–95, 2014.

[109] https://www.methanol.org/.

[110] Antti Posti and Jani Häkkinen. Survey of transportation of liquid bulk chemicals in the baltic sea. In *Turku: Centre for Maritime Studies, University of Turku*, 2012.

[111] R. McGill, W. B. Remley, and K. Winther. Alternative fuels for marine applications. In *Paris: IEA*, 2013.

[112] J. Ellis and K. Tanneberger. Study on the use of ethyl and methyl alcohol as alternative fuels in shipping. In *Göteborg: European Maritime Safety Agency (EMSA), SSPA Sweden*, 2015.

[113] Sebastian Verhelst, James WG Turner, Louis Sileghem, and Jeroen Vancoillie. Methanol as a fuel for internal combustion engines. *Progress in Energy and Combustion Science*, 70:43–88, 2019.

[114] Andy Yates, Arthur Bell, and Andre Swarts. Insights relating to the autoignition characteristics of alcohol fuels. *Fuel*, 89(1):83–93, 2010.

[115] KC Waugh. Methanol synthesis. *Catalysis Today*, 15(1):51–75, 1992.

[116] Angelo Basile and Francesco Dalena. Methanol: Science and engineering. 2017.

[117] Ibram Ganesh. Conversion of carbon dioxide into methanol–a potential liquid fuel: Fundamental challenges and opportunities (a review). *Renewable and Sustainable Energy Reviews*, 31:221–257, 2014.

[118] P Galindo Cifre and Ossama Badr. Renewable hydrogen utilisation for the production of methanol. *Energy conversion and management*, 48(2):519–527, 2007.

[119] Marquez Salazar C. Andersson K. Methanol as a marine fuel report. *FCBI Energy*, 2015.

[120] J Bøgild Hansen. Methanol production technology: todays and future renewable solutions. In *Methanol Workshop, Lund University*, 2015.

[121] Rodrigo Rivera-Tinoco, M Farran, Chakib Bouallou, F Auprêtre, Solène Valentin, Pierre Millet, and JR Ngameni. Investigation of power-to-methanol processes coupling electrolytic hydrogen production and catalytic co2 reduction. *International journal of hydrogen energy*, 41(8):4546–4559, 2016.

[122] Suhas G Jadhav, Prakash D Vaidya, Bhalchandra M Bhanage, and Jyeshtharaj B Joshi. Catalytic carbon dioxide hydrogenation to methanol: A review of recent studies. *Chemical Engineering Research and Design*, 92(11):2557–2567, 2014.

[123] Éverton Simões Van-Dal and Chakib Bouallou. Design and simulation of a methanol production plant from co2 hydrogenation. *Journal of Cleaner Production*, 57:38–45, 2013.

[124] Laura A Pellegrini, Giorgio Soave, Simone Gamba, and Stefano Langè. Economic analysis of a combined energy–methanol production plant. *Applied energy*, 88(12):4891–4897, 2011.

[125] DNV-GL. Methanol as a marine fuel: Environmental benefits, technology readiness, and economic feasibility. 20-01-2016.

[126] The methanol-fuelled man b&w lgim engine. https://www.man-es.com/5510-0172_online.

[127] Talal Yusaf, Ihsan Hamawand, Paul J. Baker, and Gholamhassan Najafi. The effect of methanol-diesel blended ratio on ci engine performance. *International Journal of Automotive and Mechanical Engineering*, 8:1385–1395, 2013.

[128] A special report: Burning tomorrow's fuels, February 1979.

[129] A. Weir, W. Vonkleinsmid, and E. A. Danko. Test and evaluation of methanol in a gas turbine system. final report. 1981.

[130] W. H. von KleinSmid, H. Schreiber, and R. D. Klapatch. Methanol combustion in a 26-mw gas turbine. *ASME*, Volume 3: Heat Transfer; Electric Power, 1981.

[131] GE General Electric. Feasibility of methanol as gas turbine fuel.

[132] California Energy Commission. Methanol. clean coal stationary engine demonstration project. executive summary, February 1986.

[133] Japanese High-Technology Monitor. Methanol power generation - demonstration test starts for a power source at peak demand, 5 April 1993.

[134] J. Sepideh and I. Schjølberg. Emission reduction in shipping using hydrogen and fuel cells. In *V010T09A011*, 2017.

[135] Fahad Suleman, Ibrahim Dincer, and Martin Agelin-Chaab. Environmental impact assessment and comparison of some hydrogen production options. *International Journal of Hydrogen Energy*, 40:6976–6987, 2015.

[136] Andrew E Lutz, Robert W Bradshaw, Jay O Keller, and Dennis E Witmer. Thermodynamic analysis of hydrogen production by steam reforming. *International Journal of Hydrogen Energy*, 28(2):159–167, 2003.

[137] Chi Cheng Chong, Yoke Wang Cheng, Kim Hoong Ng, Dai-Viet N Vo, Man Kee Lam, and Jun Wei Lim. Bio-hydrogen production from steam reforming of liquid biomass wastes and biomass-derived oxygenates: A review. *Fuel*, page 122623, 2021.

[138] Adnan Midilli, Haydar Kucuk, Muhammed Emin Topal, Ugur Akbulut, and Ibrahim Dincer. A comprehensive review on hydrogen production from coal gasification: Challenges and opportunities. *International Journal of Hydrogen Energy*, 46(50):25385–25412, 2021.

[139] O. Veneri. Hydrogen as future energy carrier. pages 33–70, 2011.

[140] Arturo Goodwin and Katrine Hildre Storaker. Hydrogen in the maritime sector : a feasibility study on hydrogen as fuel in norwegian ferries. 2015.

[141] Adolfo Iulianelli, Paulo Ribeirinha, Adélio Mendes, and Angelo Basile. Methanol steam reforming for hydrogen generation via conventional and membrane reactors: a review. *Renewable and Sustainable Energy Reviews*, 29:355–368, 2014.

[142] Andreas Züttel. Materials for hydrogen storage. *Materials Today*, 6(9):24–33, 2003.

[143] F. Vogler and G. Sattler. Hydrogen-fueled marine transportation. In *Compendium of Hydrogen Energy. Woodhead Publishing Series in Energy. Oxford: Woodhead Publishing*, pages 35–65, 2016.

[144] Norman L Newhouse. Development of improved composite pressure vessels for hydrogen storage. Technical report, Hexagon Lincoln, Lincoln, NE (United States), 2016.

[145] Trine Nerem. Assessment of marine fuels in a fuel cell on a cruise vessel. 2018.

[146] Dale Simbeck and Elaine Chang. Hydrogen supply: cost estimate for hydrogen pathways–scoping analysis. *National Renewable Energy Laboratory*, 71, 2002.

[147] https://www.offshore-energy.biz/lr-clears-torghatten-nords-hydrogen-ferry-project/.

[148] Lindert van Biert, Milinko Godjevac, Klaas Visser, and P. V. Aravind. A review of fuel cell systems for maritime applications. *Journal of Power Sources*, 327:345–364, 2016.

[149] T. Q. Hua, Rajesh K. Ahluwalia, J. K. Peng, Matthew A. Kromer, Stephen Lasher, Kurtis Mckenney, Karen H. Law, and Jayanti Sinha. Technical assessment of compressed hydrogen storage tank systems for automotive applications. *International Journal of Hydrogen Energy*, 36:3037–3049, 2010.

[150] M. T. Syed, Sayed A. Sherif, T. Nejat Veziroglu, and John W. Sheffield. An economic analysis of three hydrogen liquefaction systems. *International Journal of Hydrogen Energy*, 23:565–576, 1998.

[151] https://www.ship-technology.com/news/fincantieri-hydrogen-cruise-ships-msc/.

[152] Hailian Li, Mohamed Eddaoudi, Michael O'Keeffe, and Omar M Yaghi. Design and synthesis of an exceptionally stable and highly porous metal-organic framework. *nature*, 402(6759):276–279, 1999.

[153] Matthias Thommes, Katsumi Kaneko, Alexander V Neimark, James P Olivier, Francisco Rodriguez-Reinoso, Jean Rouquerol, and Kenneth SW Sing. Physisorption of gases, with special reference to the evaluation of surface area and pore size distribution (iupac technical report). *Pure and applied chemistry*, 87(9-10):1051–1069, 2015.

[154] Michael Hirscher, Volodymyr A Yartys, Marcello Baricco, Jose Bellosta von Colbe, Didier Blanchard, Robert C Bowman Jr, Darren P Broom, Craig E Buckley, Fei Chang, Ping Chen, et al. Materials for hydrogen-based energy storage–past, recent progress and future outlook. *Journal of Alloys and Compounds*, 827:153548, 2020.

[155] Mykhaylo V Lototskyy, Ivan Tolj, Lydia Pickering, Cordellia Sita, Frano Barbir, and Volodymyr Yartys. The use of metal hydrides in fuel cell applications. *Progress in Natural Science: Materials International*, 27(1):3–20, 2017.

[156] C EG Padro and Victoria Putsche. Survey of the economics of hydrogen technologies. Technical report, National Renewable Energy Lab.(NREL), Golden, CO (United States), 1999.

[157] https://www.ge.com/gas-power/future-of-energy.

[158] https://www.siemens-energy.com/global/en/priorities/future-technologies/hydrogen/zehtc.html.

[159] A. Ciani, L. Tay-Wo-Chong, A. Amato, E. Bertolotto, and G. Spataro. Hydrogen blending into ansaldo energia ae94.3a gas turbine: High pressure tests, field experience and modelling considerations. Volume 3A: Combustion, Fuels, and Emissions, 2021.

[160] Mirko R. Bothien, Andrea Ciani, John P. Wood, and Gerhard Fruechtel. Sequential combustion in gas turbines: The key technology for burning high hydrogen contents with low emissions. Volume 4A: Combustion, Fuels, and Emissions, 2019.

[161] https://www.google.com/url?sa=t&rct=j&q=&esrc=s&source=web&cd=&ved=2ahUKEwiPw-magt_4AhVCXRoKHQFXBEUQFnoECAoQAQ&url=https%3A%2F%2Fwww.mhi.co.jp%2Ftechnology%2Freview%2Fpdf%2Fe583%2Fe583030.pdf&usg=AOvVaw2BcZ1MxOFTglw38VQMrz5_.

[162] Paolo Chiesa, Giovanni Gustavo Lozza, and Luigi Mazzocchi. Using hydrogen as gas turbine fuel. *Journal of Engineering for Gas Turbines and Power-transactions of The Asme*, 127:73–80, 2005.

[163] https://www.wartsila.com/media/news/.

[164] https://www.man-es.com/discover/designing-the-engines-of-the-future.

[165] Wartsila private communication.

[166] Jinbo Qu, Yongming Feng, Guodong Xu, Ming Zhang, Yuanqing Zhu, and Song Zhou. Design and thermodynamics analysis of marine dual fuel low speed engine with methane reforming integrated high pressure exhaust gas recirculation system. *Fuel*, 2022.

[167] Ilker Turgut Yilmaz. The effect of hydrogen on the thermal efficiency and combustion process of the low compression ratio ci engine. *Applied Thermal Engineering*, 197:117381, 2021.

[168] Hayder Abdullah Luaibi Alrazen and Kamarul Arifin Ahmad. Hcng fueled spark-ignition (si) engine with its effects on performance and emissions. *Renewable & Sustainable Energy Reviews*, 82:324–342, 2018.

[169] Manfred Klell, Helmut Eichlseder, and Markus Sartory. Mixtures of hydrogen and methane in the internal combustion engine - synergies, potential and regulations. *International Journal of Hydrogen Energy*, 37:11531–11540, 2012.

[170] Tarkan Sandalcı, Övün Işın, Serkan Galata, Yasin Karagöz, and İlker Güler. Effect of hythane enrichment on performance, emission and combustion characteristics of an ci engine. *International Journal of Hydrogen Energy*, 2019.

[171] Yasin Karagöz, Tarkan Sandalcı, Levent Yüksek, Ahmet Selim Dalkılıç, and Somchai Wongwises. Effect of hydrogen-diesel dual-fuel usage on performance, emissions and diesel combustion in diesel engines. *Advances in Mechanical Engineering*, 8, 2016.

[172] Zhengqing Chen, Boya Xu, Fan Zhang, and Jingping Liu. Quantitative research on thermodynamic process and efficiency of a lng heavy-duty engine with high compression ratio and hydrogen enrichment. *Applied Thermal Engineering*, 125:1103–1113, 2017.

[173] Antonio Mariani, Andrea Unich, and Mario Minale. Methane/hydrogen blends in controlled auto ignition engines with egr: Evaluation of nox emissions. *CHEMICAL ENGINEERING TRANSACTIONS*, 74, 2019.

[174] Pavlos Dimitriou and Taku Tsujimura. A review of hydrogen as a compression ignition engine fuel. *International Journal of Hydrogen Energy*, 42:24470–24486, 2017.

[175] Fridtjof Rohde, Björn Pape, and Claus Nikolajsen. Zero-emission ferry concept for scandlines. In *Proceedings of the International Conference on Ship Efficiency, Hamburg*, 2013.

[176] GL group. Costs and benefits of lng as ship fuel for container vessels. 2013.

[177] Norsk Hydrogenforum. Her finner du hydrogenstatsjonene i norge. 2018.

[178] Anne Sophie Sagbakken Ness. Conceptual design of ammonia-fueled vessels for deep-sea shipping. Master's thesis, NTNU, 2021.

[179] Hadi Nozari and Arif M. Karabeyoglu. Numerical study of combustion characteristics of ammonia as a renewable fuel and establishment of reduced reaction mechanisms. *Fuel*, 159:223–233, 2015.

[180] Sarbjit Giddey, Sukhvinder P.S. Badwal, Christopher Munnings, and Michael David. Dolan. Ammonia as a renewable energy transportation media. *ACS Sustainable Chemistry & Engineering*, 5:10231–10239, 2017.

[181] Calin Zamfirescu and Ibrahim Dincer. Ammonia as a green fuel and hydrogen source for vehicular applications. *Fuel Processing Technology*, 90:729–737, 2009.

[182] Rana Prathap Padappayil and Judith Borger. Ammonia toxicity. In *StatPearls*. StatPearls Publishing, 2021.

[183] Srinivasan Dasarathy, Rajeshwar P Mookerjee, Veronika Rackayova, Vinita Rangroo Thrane, Balasubramaniyan Vairappan, Peter Ott, and Christopher F Rose. Ammonia toxicity: from head to toe? *Metabolic brain disease*, 32(2):529–538, 2017.

[184] DNV-GL. Ammonia as a marine fuel safety handbook. 2020.

[185] Aaron J. Reiter and Song-Charng Kong. Combustion and emissions characteristics of compression-ignition engine using dual ammonia-diesel fuel. *Fuel*, 90:87–97, 2011.

[186] https://energypost.eu/hard-to-abate-sectors-need-hydrogen-but-only-4-is-green/.

[187] Hideaki Kobayashi, Akihiro Hayakawa, Kapuruge Don Kunkuma Amila Somarathne, and Ekenechukwu Chijioke Okafor. Science and technology of ammonia combustion. *Proceedings of the Combustion Institute*, 2019.

[188] https://royalsociety.org/-/media/policy/projects/green-ammonia/green-ammonia-policy-briefing.pdf.

[189] F. J. Verkamp, Mary C. Hardin, and J. R. Williams. Ammonia combustion properties and performance in gas-turbine burners. 1967.

[190] David T. Pratt. Performance of ammonia-fired gas-turbine combustors. 1967.

[191] Newhall H. and Starkman E.S. Theoretical performance of ammonia as a gas turbine fue. *SAE*, (Technical paper 660768), 1966.

[192] Jun Li, Hongyu Huang, Noriyuki Kobayashi, Zhaohong He, and Y. Nagai. Study on using hydrogen and ammonia as fuels: Combustion characteristics and nox formation. *International Journal of Energy Research*, 38:1214 – 1223, 2014.

[193] Brian E. Karabeyoglu A. Fuel conditioning system for ammonia fired power plants. *NH3 Fuel Association*, Available online https://nh3fuel.files.wordpress.com/2012/10/evans-brian.pdf, 2012.

[194] M. Balestri, D. Cecchini, and V. Cinti. Unconventional Fuels Experimental Campaigns in Gas Turbine Combustor at ENEL Sesta Facility. Volume 1: Turbo Expo 2004:121–128, 2004.

[195] MAN. Man ammonia engine update.

[196] Wartsila. Wartsila advances future fuel capabilities with frst ammonia tests.

[197] Carlos Gervasio Rodríguez, María Isabel Lamas, Juan de dios Rodriguez, and Amry Amin Abbas. Possibilities of ammonia as both fuel and nox reductant in marine engines: A numerical study. *Journal of Marine Science and Engineering*, 2022.

[198] Caneon Kurien and Mayank K. Mittal. Review on the production and utilization of green ammonia as an alternate fuel in dual-fuel compression ignition engines. *Energy Conversion and Management*, 2022.

[199] Aaron J. Reiter and Song-Charng Kong. Demonstration of compression-ignition engine combustion using ammonia in reducing greenhouse gas emissions. *Energy & Fuels*, 22:2963–2971, 2008.

[200] Bruno Scrosati, Jurgen Garche, and Werner Tillmetz. *Advances in battery technologies for electric vehicles*. Woodhead Publishing, 2015.

[201] Jakub Lach, Kamil Wróbel, Justyna Wróbel, Piotr Podsadni, and Andrzej Czerwiński. Applications of carbon in lead-acid batteries: a review. *Journal of Solid State Electrochemistry*, 23(3):693–705, 2019.

[202] Geoffrey J May, Alistair Davidson, and Boris Monahov. Lead batteries for utility energy storage: A review. *Journal of energy storage*, 15:145–157, 2018.

[203] Denise Crocce Romano Espinosa and Jorge Alberto Soares Tenório. Recycling of nickel–cadmium batteries using coal as reducing agent. *Journal of power sources*, 157(1):600–604, 2006.

[204] Kirby W Beard. *Linden's handbook of batteries*. McGraw-Hill Education, 2019.

[205] Xiayue Fan, Bin Liu, Jie Liu, Jia Ding, Xiaopeng Han, Yida Deng, Xiaojun Lv, Ying Xie, Bing Chen, Wenbin Hu, et al. Battery technologies for grid-level large-scale electrical energy storage. *Transactions of Tianjin University*, 26(2):92–103, 2020.

[206] Wenhua H Zhu, Ying Zhu, Zenda Davis, and Bruce J Tatarchuk. Energy efficiency and capacity retention of ni–mh batteries for storage applications. *Applied Energy*, 106:307–313, 2013.

[207] Álvaro Cunha, Jorge Martins, Nuno Rodrigues, and FP Brito. Vanadium redox flow batteries: a technology review. *International Journal of Energy Research*, 39(7):889–918, 2015.

[208] Eduardo Sánchez-Díez, Edgar Ventosa, Massimo Guarnieri, Andrea Trovò, Cristina Flox, Rebeca Marcilla, Francesca Soavi, Petr Mazur, Estibaliz Aranzabe, and Raquel Ferret. Redox flow batteries: Status and perspective towards sustainable stationary energy storage. *Journal of Power Sources*, 481:228804, 2021.

[209] Robert M Darling. Techno-economic analyses of several redox flow batteries using levelized cost of energy storage. *Current Opinion in Chemical Engineering*, 37:100855, 2022.

[210] Ruijie Ye, Dirk Henkensmeier, Sang Jun Yoon, Zhifeng Huang, Dong Kyu Kim, Zhenjun Chang, Sangwon Kim, and Ruiyong Chen. Redox flow batteries for energy storage: a technology review. *Journal of Electrochemical Energy Conversion and Storage*, 15(1), 2018.

[211] Michael Dieterle, Peter Fischer, Marie-Noëlle Pons, Nick Blume, Christine Minke, and Aldo Bischi. Life cycle assessment (lca) for flow batteries: A review of methodological decisions. *Sustainable Energy Technologies and Assessments*, 53:102457, 2022.

[212] Haisheng Chen, Thang Ngoc Cong, Wei Yang, Chunqing Tan, Yongliang Li, and Yulong Ding. Progress in electrical energy storage system: A critical review. *Progress in natural science*, 19(3):291–312, 2009.

[213] Ghassan Zubi, Rodolfo Dufo-López, Monica Carvalho, and Guzay Pasaoglu. The lithium-ion battery: State of the art and future perspectives. *Renewable and Sustainable Energy Reviews*, 89:292–308, 2018.

[214] Jürgen Janek and Wolfgang G Zeier. A solid future for battery development. *Nature Energy*, 1(9):1–4, 2016.

[215] Elena Mossali, Nicoletta Picone, Luca Gentilini, Olga Rodrìguez, Juan Manuel Pérez, and Marcello Colledani. Lithium-ion batteries towards circular economy: A literature review of opportunities and issues of recycling treatments. *Journal of environmental management*, 264:110500, 2020.

[216] Alain Mauger and CM Julien. Critical review on lithium-ion batteries: are they safe? sustainable? *Ionics*, 23(8):1933–1947, 2017.

[217] Omer Berkehan Inal, Jean Frédéric Charpentier, and Cengiz Deniz. Hybrid power and propulsion systems for ships: Current status and future challenges. *Renewable and Sustainable Energy Reviews*, 2022.

[218] Maria Alessandra Ancona, Francesco Baldi, Michele Bianchi, Lisa Branchini, Francesco Melino, Antonio Peretto, and James. Rosati. Efficiency improvement on a cruise ship: Load allocation optimization. *Energy Conversion and Management*, 164:42–58, 2018.

[219] Hai Lan, Shuli Wen, Ying-Yi Hong, David C. Yu, and Li jun Zhang. Optimal sizing of hybrid pv/diesel/battery in ship power system. *Applied Energy*, 158:26–34, 2015.

[220] George S. Misyris, Antonios Marinopoulos, Dimitrios I. Doukas, Tomas Tengnér, and Dimitris P. Labridis. On battery state estimation algorithms for electric ship applications. *Electric Power Systems Research*, 151:115–124, 2017.

[221] E Dedes, Dominic A. Hudson, and Stephen R. Turnock. Assessing the potential of hybrid energy technology to reduce exhaust emissions from global shipping. *Energy Policy*, 40:204–218, 2012.

[222] Giovani T. T. Vieira, C. O. Peralta, Maurício B. C. Salles, and Bruno Souza Carmo. Reduction of co2 emissions in ships with advanced energy storage systems. *2017 6th International Conference on Clean Electrical Power (ICCEP)*, pages 564–571, 2017.

[223] Rinze Geertsma, Rudy R. Negenborn, Klaas Visser, and J. J. Hopman. Design and control of hybrid power and propulsion systems for smart ships: A review of developments. *Applied Energy*, 194:30–54, 2017.

[224] Bijan Zahedi, Lars E. Norum, and Kristine B. Ludvigsen. Optimized efficiency of all-electric ships by dc hybrid power systems. *Journal of Power Sources*, 255:341–354, 2014.

[225] Li Wang, Dong Jing Lee, Weijen Lee, and Zhe Chen. Analysis of a novel autonomous marine hybrid power generation/energy storage system with a high-voltage direct current link. *Journal of Power Sources*, 185:1284–1292, 2008.

[226] Elif Bal Besikçi, Özcan Arslan, Osman Turan, and Aykut I. Ölçer. An artificial neural network based decision support system for energy efficient ship operations. *Comput. Oper. Res.*, 66:393–401, 2016.

[227] MAN. Man 51/60df IMO tier ii, IMO tier iii project guide-marine. pages 411–414, 2015.

[228] https://www.dfly.no/tag/mf-ampere/.

[229] https://www.carnivalcorporation.com/news-releases/news-release-details/aidaperla-will-receive-largest-battery-storage-system-passenger/.

[230] Gunter Sattler. Fuel cells going on-board. *Journal of Power Sources*, 86:61–67, 2000.

[231] Angela Psoma and Gunter Sattler. Fuel cell systems for submarines: from the first idea to serial production. *Journal of Power Sources*, 106(1-2):381–383, 2002.

[232] A. J. Fawke, H. I. H. Saravanamuttoo, and M. Holmes. Abstract of c.a.d. literature: Experimental verification of a digital computer simulation method for predicting gas turbine dynamic behaviour. *Computer-aided Design*, 6:52, 1972.

[233] Meinhard T. Schobeiri, Magdy S. Attia, and C. Lippke. Getran: A generic, modularly structured computer code for simulation of dynamic behavior of aero- and power generation gas turbine engines. *Journal of Engineering for Gas Turbines and Power-transactions of The Asme*, 116:483–494, 1994.

[234] Pericles Pilidis and N. R. L. Maccallum. A general program for the prediction of the transient performance of gas turbines. 1985.

[235] Doug Garrard. Atec: The aerodynamic turbine engine code for the analysis of transient and dynamic gas turbine engine system operations: Part 1 - model development. 1996.

[236] Sangjo Kim, Kui soon Kim, and Changmin Son. A new transient performance adaptation method for an aero gas turbine engine. *Energy*, 193:116752, 2020.

[237] Elias Tsoutsanis, Nader Meskin, Mohieddine A. Benammar, and Khashayar Khorasani. A component map tuning method for performance prediction and diagnostics of gas turbine compressors. *Applied Energy*, 135:572–585, 2014.

[238] Nadji Hadroug, Ahmed Hafaifa, Abdellah Kouzou, and Ahmed Chaibet. Dynamic model linearization of two shafts gas turbine via their input/output data around the equilibrium points. *Energy*, 120:488–497, 2017.

[239] Chen Wang, Yiguang Li, and B. Y. Yang. Transient performance simulation of aircraft engine integrated with fuel and control systems. *Applied Thermal Engineering*, 114:1029–1037, 2017.

[240] Guolian Hou, Linjuan Gong, Congzhi Huang, and Jian hang Zhang. Fuzzy modeling and fast model predictive control of gas turbine system. *Energy*, 200:117465, 2020.

[241] Jairo Rúa and Lars Olof Nord. Optimal control of flexible natural gas combined cycles with stress monitoring: Linear vs nonlinear model predictive control. *Applied Energy*, 265:114820, 2020.

[242] Abdollah Mehrpanahi, Gholamhasan Payganeh, and Mohammadreza Arbabtafti. Dynamic modeling of an industrial gas turbine in loading and unloading conditions using a gray box method. *Energy*, 120:1012–1024, 2017.

[243] Hamid Asgari, Xiaoqi Chen, Mirko Morini, Michele Pinelli, Raazesh Sainudiin, Pier Ruggero Spina, and Mauro Venturini. Narx models for simulation of the start-up operation of a single-shaft gas turbine. *Applied Thermal Engineering*, 93:368–376, 2016.

[244] Ugo Campora, Mark A. Capelli, Carlo Cravero, and Raphael Zaccone. Metamodels of a gas turbine powered marine propulsion system for simulation and diagnostic purposes. *Journal of Naval Architecture and Marine Engineering*, 12:1–14, 2015.

[245] David H. Cooke. On prediction of off-design multistage turbine pressures by stodola's ellipse. *Journal of Engineering for Gas Turbines and Power-transactions of The Asme*, 107:596–606, 1985.

[246] Asok Ray. Dynamic modelling of power plant turbines for controller design. *Applied Mathematical Modelling*, 4:109–112, 1980.

[247] Haihua Zhao, Hongbin Zhang, Ling Zou, and Richard C. Martineau. A strongly coupled reactor core isolation cooling system model for extended station black-out analyses. 2015.

[248] Ali Chaibakhsh and Ali Ghaffari. Steam turbine model. *Simul. Model. Pract. Theory*, 16:1145–1162, 2008.

[249] Falah Alobaid, Ralf Postler, Jochen Ströhle, Bernd Epple, and Hyun-Gee Kim. Modeling and investigation start-up procedures of a combined cycle power plant. *Applied Energy*, 85:1173–1189, 2008.

[250] Giampaolo Crosa, G. Ferrari, and Andrea Trucco. Modelling and recoupling the control loops in a heavy-duty gas turbine plant. 1995.

[251] Giampaolo Crosa, Ferruccio Pittaluga, Andrea Trucco, Francesco Beltrami, A. Torelli, and Federico Traverso. Heavy-duty gas turbine plant aerothermodynamic simulation using simulink. *Journal of Engineering for Gas Turbines and Power-transactions of The Asme*, 120:550–556, 1998.

[252] Alberto Benato, Anna Stoppato, and Stefano Bracco. Combined cycle power plants: A comparison between two different dynamic models to evaluate transient behaviour and residual life. *Energy Conversion and Management*, 87:1269–1280, 2014.

[253] Maddalena Pondini, Valentina Colla, and Annamaria Signorini. Models of control valve and actuation system for dynamics analysis of steam turbines. *Applied Energy*, 207:208–217, 2017.

[254] Johanna Beiron, Rubén M. Montañés, Fredrik Normann, and Filip Johnsson. Flexible operation of a combined cycle cogeneration plant - a techno-economic assessment. *Applied Energy*, 278:115630, 2020.

[255] Zhixin Sun, Lin Gao, Jiangfeng Wang, and Yiping Dai. Dynamic optimal design of a power generation system utilizing industrial waste heat considering parameter fluctuations of exhaust gas. *Energy*, 44:1035–1043, 2012.

[256] Nicolas Mertens, Falah Alobaid, Ralf Starkloff, Bernd Epple, and Hyun-Gee Kim. Comparative investigation of drum-type and once-through heat recovery steam generator during start-up. *Applied Energy*, 144:250–260, 2015.

[257] S. L. Dixon. Fluid mechanics and thermodynamics of turbomachinery seventh edition. 2013.

[258] John David Anderson. *Modern compressible flow: with historical perspective*, volume 12. McGraw-Hill New York, 1990.

[259] Henry E. Cohen, G. F. C. Rogers, and H. I. H. Saravanamuttoo. Gas turbine theory. volume Pearson, 1973.

[260] J. Klapproth, M. Miller, and D. Parker. *Aerodynamic development and performance of the CF6-6/LM2500 compressor*.

[261] GasTurb GmbH. *GasTurb 14 User Manual*, 2022.

[262] Muhammad Baqir Hashmi, Tamiru Alemu Lemma, and Zainal A. Abdul Karim. Investigation of the combined effect of variable inlet guide vane drift, fouling, and inlet air cooling on gas turbine performance. *Entropy*, 21, 2019.

[263] Nils A. Røkke, Johan Einar Hustad, and S. Berg. Pollutant emissions from gas fired turbine engines in offshore practice: Measurements and scaling. volume 3A, 1993.

[264] Marco Altosole, Giovanni Benvenuto, Ugo Campora, Michele Martelli, and Luca Bruga. Marine gas turbines pollutant emissions assessment. *NAV International Conference on Ship and Shipping Research*, (216369), 2012.

[265] N. K. Rizk and H. C. Mongia. Semianalytical correlations for NOx, CO, and UHC emissions. *ASME 1992 International Gas Turbine and Aeroengine Congress and Exposition, GT 1992*, 3(July 1993), 1992.

[266] S. Can Gülen. *Gas turbines for electric power generation*. 2019.

[267] Meherwan P. Boyce. Handbook for cogeneration and combined cycle power plants. 2010.

[268] Power plant instrumentation and control handbook. 2019.

[269] *Comparison of Partial vs Full Admission for Small Turbines at Low Specific Speeds*, volume Volume 1: Aircraft Engine; Marine; Turbomachinery; Microturbines and Small Turbomachinery of *Turbo Expo: Power for Land, Sea, and Air*, 1985.

[270] Dipak Sarkar. *Thermal power plant: design and operation*. Elsevier, 2015.

[271] Everett B Woodruff, Herbert B Lammers, and Thomas F Lammers. *Steam plant operation*. McGraw-Hill Education, 2017.

[272] Ankur Geete and A. I. Khandwawala. Thermodynamic analysis of 120 mw thermal power plant with combined effect of constant inlet pressure (124.61 bar) and different inlet temperatures. *Case Studies in Thermal Engineering*, 1:17–25, 2013.

[273] Asim Sinan Karakurt. Performance analysis of a steam turbine power plant at part load conditions. *Journal of Thermal Engineering*, 3:1121–1128, 2017.

[274] Giovanni Benvenuto and Ugo Campora. Numerical modelling of the engines governors of a codlag propulsion plant. pages 173–178, 7-9th October 2010.

[275] Han Deng, Geir Skaugen, Erling Næss, Mingjie Zhang, and Ole A Øiseth. A novel methodology for design optimization of heat recovery steam generators with flow-induced vibration analysis. *Energy*, 226:120325, 2021.

[276] Yanfeng Li, Jingru Liu, and Guohe Huang. Pressure drop optimization of the main steam and reheat steam system of a 1000 mw secondary reheat unit. *Energies*, 15(9):3279, 2022.

[277] Bonnie J McBride. *NASA Glenn coefficients for calculating thermodynamic properties of individual species*. National Aeronautics and Space Administration, John H. Glenn Research Center, 2002.

[278] https://www.nist.gov/srd/refprop.

[279] ESCOA, 1979, ESCOA Turb-X HF Rating Instructions, Pryor, Oklahoma.

[280] ED Grimson. Correlation and utilization of new data on flow resistance and heat transfer cross-flow of gases over tube banks. *Trans. ASME*, 59:583–594, 1937.

[281] Raymond K Sinnott, John Metcalfe Coulson, and John Francis Richardson. *Chemical engineering design*, volume 6. Elsevier Butterworth-Heinemann Oxford, 2005.

[282] Eduardo Cao. *Heat transfer in process engineering*. McGraw-Hill Education, 2010.

[283] IMO. Report of the marine environment protection committee (mepc) on its fifty-seventh session. 57th session, 2008.

[284] C. Weber, François Maréchal, and Daniel Favrat. Design and optimization of district energy systems. *Computer-aided chemical engineering*, 24:1127–1132, 2007.

[285] Adam D. Hawkes and Matthew Leach. Modelling high level system design and unit commitment for a microgrid. *Applied Energy*, 86:1253–1265, 2009.

[286] Giuseppe Genon, Marco Filippo Torchio, Alberto Poggio, and M A Poggio. Energy and environmental assessment of small district heating systems: Global and local effects in two case-studies. *Energy Conversion and Management*, 50:522–529, 2009.

[287] Shengwei Wang and Zhenjun Ma. Supervisory and optimal control of building hvac systems: A review. *HVAC&R Research*, 14:3 – 32, 2008.

[288] Fernando Domínguez-Muñoz, José M Cejudo-López, Antonio Carrillo-Andrés, and Manuel Gallardo-Salazar. Selection of typical demand days for chp optimization. *Energy and Buildings*, 43(11):3036–3043, 2011.

[289] Jing Yi Wu, Jia long Wang, and Sheng Li. Multi-objective optimal operation strategy study of micro-cchp system. *Energy*, 48:472–483, 2012.

[290] E. D. Mehleri, Haralambos Sarimveis, Nikolaos C. Markatos, and Lazaros G. Papageorgiou. A mathematical programming approach for optimal design of distributed energy systems at the neighbourhood level. *Energy*, 44:96–104, 2012.

[291] Stefano Bracco, Federico Delfino, Fabio Pampararo, Michela Robba, and Mansueto Rossi. Economic and environmental performances quantification of the university of genoa smart polygeneration microgrid. *2012 IEEE International Energy Conference and Exhibition (ENERGYCON)*, pages 593–598, 2012.

[292] C. Weber and N. Shah. Optimisation based design of a district energy system for an eco-town in the united kingdom. *Energy*, 36(2):1292–1308, 2011.

[293] Hongbo Ren and Weijun Gao. A milp model for integrated plan and evaluation of distributed energy systems. *Applied Energy*, 87:1001–1014, 2010.

[294] Paolo Gabrielli, Alberto Acquilino, Silvia Siri, Stefano Bracco, Giovanni Sansavini, and Marco Mazzotti. Optimization of low-carbon multi-energy systems with seasonal geothermal energy storage: The anergy grid of eth zurich. *Energy Conversion and Management*, 8:100052, 2020.

[295] Kristopher A Pruitt, Robert J. Braun, and Alexandra M. Newman. Evaluating shortfalls in mixed-integer programming approaches for the optimal design and dispatch of distributed generation systems. *Applied Energy*, 102:386–398, 2013.

[296] Carleton Coffrin and Pascal Van Hentenryck. A linear-programming approximation of ac power flows. *INFORMS J. Comput.*, 26:718–734, 2014.

[297] Jiangjiang Wang, Youyin Jing, and Chunfa Zhang. Optimization of capacity and operation for cchp system by genetic algorithm. *Applied Energy*, 87:1325–1335, 2010.

[298] Abdullah NFNR. Alkhaledi, Suresh Sampath, and Pericles Pilidis. Propulsion of a hydrogen-fuelled lh2 tanker ship. *International Journal of Hydrogen Energy*, 2022.

[299] Andrea Armellini, S. Daniotti, and Piero Pinamonti. Gas turbines for power generation on board of cruise ships: A possible solution to meet the new imo regulations? *Energy Procedia*, 81:540–547, 2015.

[300] Pequot Editor.

[301] A. Dotto, U. Campora, and F. Satta. Feasibility study of an integrated COGES-DF engine power plant in lng propulsion for a cruise-ferry. *Energy Conversion and Management*, 245:114602, 2021.

[302] Maja Perčić, Nikola Vladimir, and Ailong Fan. Life-cycle cost assessment of alternative marine fuels to reduce the carbon footprint in short-sea shipping: A case study of croatia. *Applied Energy*, 279:115848, 2020.

[303] Alba Martínez-López, Alejandro Romero-Filgueira, and Manuel Chica. Specific environmental charges to boost cold ironing use in the european short sea shipping. *Transportation Research Part D-transport and Environment*, 94:102775, 2021.

[304] E.L. Korn. The maritime commons : Digital repository of the world maritime university chapters library 2009 scatterplots with survey data. 2017.

[305] Å Wilske. Examining the commercial viability of cold ironing.

[306] G.A. Livanos, G. Theotokatos, and D.N. Pagonis. Techno-economic investigation of alternative propulsion plants for ferries and roro ships. *Energy Conversion and Management*, 79:640–651, 2014.

[307] Maja Perčić, Lovro Frković, Tomislav Pukšec, Boris Ćosić, Oi Lun Li, and Nikola Vladimir. Life-cycle assessment and life-cycle cost assessment of power batteries for all-electric vessels for short-sea navigation. *Energy*, 251:123895, 2022.

[308] Maja Perčić, Nikola Vladimir, and Ailong Fan. Techno-economic assessment of alternative marine fuels for inland shipping in croatia. *Renewable & Sustainable Energy Reviews*, 148:111363, 2021.

[309] Maja Perčić, Ivica Ančić, and Nikola Vladimir. Life-cycle cost assessments of different power system configurations to reduce the carbon footprint in the croatian short-sea shipping sector. *Renewable and Sustainable Energy Reviews*, 131:110028, 2020.

[310] Jesse D. Maddaloni, Andrew Rowe, and G. Cornelis van Kooten. Wind integration into various generation mixtures. *Renewable Energy*, 34:807–814, 2009.

[311] Robert Fourer. A simplex algorithm for piecewise-linear programming i: Derivation and proof. *Mathematical Programming*, 33:204–233, 1985.

[312] Noam Goldberg, Steffen Rebennack, Youngdae Kim, Vitaliy Krasko, and Sven Leyffer. Minlp formulations for continuous piecewise linear function fitting. *Comput. Optim. Appl.*, 79:223–233, 2021.

[313] C. Nuchturee, T. Li, and H. Xia. Energy efficiency of integrated electric propulsion for ships - a review. *Renewable and Sustainable Energy Reviews*, 134, 110145:1–25, 2020.

[314] H. Tillung, P. Zoglia, and N. Nico Höglund. Hybrid propulsion is part of the future for ropax ferries - environmental and efficiency needs are the drivers. *Journal of the JIME*, 52:40–45, 2017.

[315] E. Sofras and J. Prousalidis. Developing a new methodology for evaluating diesel-electric propulsion. *Journal of Marine Engineering & Technology*, 13:63–92, 2014.

[316] J. Sharples. Lng supply chains and the development of lng as a shipping fuel in northern europe. 2019.

[317] IMO. Energy efficiency for cruise passenger ships. *International Maritime Organization, MEPC 65/4/6*, 2013.

[318] O. Levander. Handy size lng cruise ship concept. *Wartsila Technical Journal: Marine/InDetail*, 01:44–51, 2011.

[319] Y. Bui. Machinery concepts and lng for meeting imo tier iii rules. *Wartsila Technical Journal: Marine/InDetail*, 01:31–38, 2011.

[320] Rainer Kurz and Klaus Brun. Gas turbine performance - what makes the map? 2000.

[321] J. H. Warner and Henrik Nielsen. Combined - cycle gas & steam turbine power plants. 1999.

[322] Alfredo Gimelli and Massimiliano Muccillo. Regulation problems of combined cycle gas-steam turbine power plant in a liberalized market: Part i - experimental investigation and energetic analysis. *International Review on Modelling and Simulations*, 9:295–305, 2016.

[323] Roberto Carapellucci and Lorena Giordano. Studying the effects of combining internal and external heat recovery on techno-economic performances of gas-steam power plants. *Energy Conversion and Management*, 107:34–42, 2016.

[324] Asim Sinan Karakurt and Yasin Ust. Marine steam turbines. 2014.

[325] T. W. F. Brown, Stanley S. Cook, and F. W. Gardner. Steam and gas turbines for marine propulsion. 1947.

[326] https://www.fincantieri.com/it/prodotti-servizi/sistemi-componenti/turbine/.

[327] DNV-GL Maritime. Maritime forecast to 2050-energy transition outlook. 2019.

[328] Rasmus Nielsen, Fredrik Haglind, and Ulrik Larsen. Design and modeling of an advanced marine machinery system including waste heat recovery and removal of sulphur oxides. *Energy Conversion and Management*, 85:687–693, 2013.

[329] Mohammed Al-Breiki and Yusuf Biçer. Investigating the technical feasibility of various energy carriers for alternative and sustainable overseas energy transport scenarios. *Energy Conversion and Management*, 209:112652, 2020.

[330] Piet Meyer, Frank Maes, and Annemie Volckaert. Emissions from international shipping in the belgian part of the north sea and the belgian seaports. *Atmospheric Environment*, 42:196–206, 2008.

[331] Ernestos Tzannatos. Ship emissions and their externalities for the port of piraeus - greece. *Atmospheric Environment*, 44:400–407, 2010.

[332] C. Whall, D. Cooper, K. Archer, L. Twigger, N. Thurston, D. Ockwell, A. McIntyre, and A. Ritchie. Quantification of emissions from ships associated with ship movements between ports in the european community. final report 0617702121. Entec UK Limited, Norwich, UK, 2002.

[333] https://www.fincantieri.com/it/prodotti-servizi/navi-crociera.

[334] David Amaya-Vías, Enrique Nebot, and Juan Antonio López-Ramírez. Comparative studies of different membrane distillation configurations and membranes for potential use on board cruise vessels. *Desalination*, 429:44–51, 2018.

[335] https://www.alfalaval.com.

[336] Paolo Gnes, Piero Pinamonti, and Mauro Reini. Bi-level optimization of the energy recovery system from internal combustion engines of a cruise ship. *Applied Sciences*, 10:6917, 2020.

[337] DNVGL. Guidance for safe return to port projects. 2016.

[338] Konstantinos Sfakianakis and Dracos Vassalos. Design for safety and energy efficiency of the electrical onboard energy systems. *2015 IEEE Electric Ship Technologies Symposium (ESTS)*, pages 150–155, 2015.

[339] IMO. Guidelines to the method of calculation of the attained energy efficiency design index (eedi) for new ships. *MEPC 212 (63/23), Annex 8*, 2012.

[340] Norihiko Iki, Osamu Kurata, Takayuki Matsunuma, Takahiro Inoue, Masato Suzuki, Taku Tsujimura, and Hirohide Furutani. Power generation and flame visualization of micro gas turbine firing ammonia or ammonia-methane mixture. *13-th Annual NH3 Fuel Conference, September 18-21, Los Angeles*, 2016.

[341] https://www.ammoniaenergy.org/articles/ammonia-turbine-power-generation/.

[342] Dongkyu Kim and Changhee Lee. Scr performance evaluations in relation to experimental parameters in a marine generator engine. *Journal of Marine Science and Engineering*, 2019.

[343] Kati Lehtoranta, Hannu Vesala, Päivi Koponen, and Satu Korhonen. Selective catalytic reduction operation with heavy fuel oil: Nox, nh3, and particle emissions. *Environmental science & technology*, 49 7:4735–41, 2015.

[344] A.D. Korberg, S. Brynolf, M. Grahn, and I.R. Skov. Techno-economic assessment of advanced fuels and propulsion systems in future fossil-free ships. *Renewable and Sustainable Energy Reviews*, 142:110861, 2021.

[345] Julia Hansson, Selma Brynolf, Erik Fridell, and Mariliis Lehtveer. The potential role of ammonia as marine fuel-based on energy systems modeling and multi-criteria decision analysis. *Sustainability*, 2020.

[346] Gregor Erbach and Liselotte Jensen. Eu hydrogen policy hydrogen as an energy carrier for a climate-neutral economy. *BRIEFING Towards climate neutrality, EPRS European Parliamentary Research Service*, 2021.

[347] Felix Schorn, Janos Lucian Breuer, Remzi Can Samsun, Thorsten Schnorbus, Benedikt Heuser, Ralf Peters, and Detlef Stolten. Methanol as a renewable energy carrier: An assessment of production and transportation costs for selected global locations. *Advances in Applied Energy*, 2021.

[348] Gerhard Lammel and Hartmut Grassl. Greenhouse effect of nox. *Environmental Science and Pollution Research*, 2:40–45, 1995.

[349] Victor Bolbot, Nikoletta L Trivyza, Gerasimos Theotokatos, Evangelos Boulougouris, Athanasios Rentizelas, and Dracos Vassalos. Cruise ships power plant optimisation and comparative analysis. *Energy*, 196:117061, 2020.

[350] Thant Zin Oo, Yan Ren, Adams Wai-Kin Kong, Yi Wang, and Xiong Liu. Power system design optimization for a ferry using hybrid-shaft generators. *IEEE Transactions on Power Systems*, 37:2869–2880, 2022.

[351] Francesco Baldi, Fredrik Ahlgren, Francesco Melino, Cecilia H Gabrielii, and Karin Andersson. Optimal load allocation of complex ship power plants. *Energy Conversion and Management*, 124:344–356, 2016.

[352] I. Tsiropoulos, D. Tarvydas, and N. Lebedeva. Li-ion batteries for mobility and stationary storage applications - scenarios for costs and market growth. 2018.

[353] Mika Lehmusto and Annukka Santasalo-Aarnio. Mathematical framework for total cost of ownership analysis of marine electrical energy storage inspired by circular economy. *Journal of Power Sources*, 528:231164, 2022.

[354] Nikoletta L. Trivyza, Athanasios A. Rentizelas, and Gerasimos Theotokatos. A comparative analysis of eedi versus lifetime co2 emissions. *Journal of Marine Science and Engineering*, 8:61, 2020.

[355] Aymen Abdaoui. Feasibility study of cold ironing from renewable sources in the nordic region: case study : Port of kapellskar in stockholm. 2022.

Appendix A

Cruise routes

Table A.1 C1 cruise route in the Mediterranean sea.

LOCATION	PHASE	t [h]	V_{ship} [knots]
Genoa	M	0.5	0
Genoa-Civitavecchia	N1	13	15
Civitavecchia	M	0.5	0
Civitavecchia	P	10	0
Civitavecchia	M	0.5	0
Civitavecchia-Palermo	N2	15	17
Palermo	M	0.5	0
Palermo	P	7	0
Palermo	M	0.5	0
Palermo-Malta	N3	16	18
Malta	M	0.5	0
Malta	P	8	0
Malta	M	0.5	0
Malta-Barcelona	N4	38	18
Barcelona	M	0.5	0
Barcelona	P	10	0
Barcelona	M	0.5	0
Barcelona-Marseille	N5	13	15
Marseille	M	0.5	0
Marseille	P	8	0
Marseille	M	0.5	0
Marseille-Genoa	N6	14	16
Genoa	M	0.5	0

Table A.2 C2 cruise route: Mediterranean

LOCATION	PHASE	t [h]	V_{ship} [knots]
Genoa	M	0.5	0
Genoa-Naples	N1	19	18
Naples	M	0.5	0
Naples	P	6	0
Naples	M	0.5	0
Naples-Messina	N2	13	13
Messina	M	0.5	0
Messina	P	6	0
Messina	M	0.5	0
Messina-Tunis	N3	16	18
Tunis	M	0.5	0
Tunis	P	6	0
Tunis	M	0.5	0
Tunis-Barcelona	N4	43	12
Barcelona	M	0.5	0
Barcelona	P	8	0
Barcelona	M	0.5	0
Barcelona-Marseille	N5	14	14
Marseille	M	0.5	0
Marseille	P	7	0
Marseille	M	0.5	0
Marseille-Genoa	N6	15	14
Genoa	M	0.5	0

Table A.3 C3 cruise route: North Sea

LOCATION	PHASE	t [h]	V_{ship} [knots]
Hamburg	M	0.5	0
Hamburg-Southaption	N1	34	15
Southapton	M	0.5	0
Southapton	P	12	0
Southapton	M	0.5	0
Southapton-Le Havre	N2	10	11
Le Havre	M	0.5	0
Le Havre	P	13	0
Le Havre	M	0.5	0
Le Havre-Stavanger	N3	37	15
Stavanger	M	0.5	0
Stavanger	P	9	0
Stavanger	M	0.5	0
Stavanger-Bergen	N4	12	14
Bergen	M	0.5	0
Bergen	P	10	0
Bergen	M	0.5	0
Bergen-Olden	N5	13	7
Olden	M	0.5	0
Olden	P	9	0
Olden	M	0.5	0
Olden-Alesund	N6	14	6
Alesund	M	0.5	0
Alesund	P	9	0
Alesund	M	0.5	0
Alesund-Hamburg	N7	37	17
Hamburg	M	0.5	0

Table A.4 C4 cruise route: Caribbean

LOCATION	PHASE	t [h]	V_{ship} [knots]
Miami	M	0.5	0
Miami-San Juan	N1	61	15
San Juan	M	0.5	0
San Juan	P	18	0
San Juan	M	0.5	0
San Juan-Charlotte	N2	10	16
Charlotte	M	0.5	0
Charlotte	P	5	0
Charlotte	M	0.5	0
Charlotte-Nassau	N3	39	22
Nassau	M	0.5	0
Nassau	P	11	0
Nassau	M	0.5	0
Nassau-Ocean Cay MSC	N4	10	11
Ocean Cay MSC	M	0.5	0
Ocean Cay MSC	P	17	0
Ocean Cay MSC	M	0.5	0
Ocean Cay MSC-Miami	N5	8	7
Miami	M	0.5	0
Miami	P	10	0
Miami	M	0.5	0
Miami-Ocho Rios	N6	36	21
Ocho Rios	M	0.5	0
Ocho Rios	P	9	0
Ocho Rios	M	0.5	0
Ocho Rios-George Town	N7	16	16
George Town	M	0.5	0
George Town	P	6	0
George Town	M	0.5	0
George Town-Cozumel	N8	16	21
Cozumel	M	0.5	0
Cozumel	P	9	0
Cozumel	M	0.5	0
Cozumel-Ocean Cay MSC	N9	36	16
Ocean Cay MSC	M	0.5	0
Ocean Cay MSC	P	17	0
Ocean Cay MSC	M	0.5	0
Ocean Cay MSC-Miami	N10	6	9
Miami	M	0.5	0

Table A.5 C5 cruise route: Red Sea

LOCATION	PHASE	t [h]	V_{ship} [knots]
Dubai	P	46	0
Dubai	M	0.5	0
Dubai-Abu Dabi	N1	8	9
Abu Dabi	M	0.5	0
Abu Dabi	P	15	0
Abu Dabi	M	0.5	0
Abu Dabi-Salalah	N2	56	18
Salalah	M	0.5	0
Salalah	P	12	0
Salalah	M	0.5	0
Salalah-Aqaba	N3	117	16
Aqaba	M	0.5	0
Aqaba	P	2	0
Aqaba	M	0.5	0
Aqaba-Eraklion	N4	61	14
Eraklion	M	0.5	0
Eraklion	P	7	0
Eraklion	M	0.5	0
Eraklion-Civitavecchia	N5	40	20
Civitavecchia	M	0.5	0